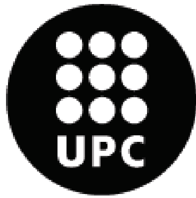
UNIVERSITAT POLITÈCNICA DE CATALUNYA
BARCELONATECH
Departament d'Enginyeria Electrònica

Interdigitated Back-contacted(IBC) c-Si solar cells based on laser processed dielectric layers

Thesis submitted in partial fulfillment of the requirement for the PhD Degree issued by the Universitat Politectnica de Catalunya (UPC), in its Electronic Engineering Program

Gema López Rodríguez

Co-directors: Dr. Pablo Rafael Ortega Villasclaras
Dr. Isidro Martín García

October 2016

Electronic Engineering Department

Agradecimientos

En primer lugar quiero agradecer a mis directores de tesis, los profesores Pablo Ortega e Isidro Martín la dirección y supervisión de este trabajo de tesis. "Gracias a los dos por resolver mis infinitas dudas, por toda vuestra ayuda, dedicación y apoyo. -Gracias Pablo por esa energía infinita".

Gracias a Ramón Alcubilla, a Cristobal Voz y a Michael Vetter por haber confiado en mi y haberme brindado la primera oportunidad de trabajar con el grupo. Gracias también por todo vuestro apoyo a lo largo de estos años.

A los técnicos de la Sala Blanca Miguel y Xavi. Quiero agradecer muy especialmente, tanto a nivel profesional como personal a Miguel García. A nivel profesional porque considero que es incuestionable el excelente trabajo que realiza en la sala blanca, por toda su ayuda técnica, profesional y por todo lo aprendido de él y a nivel personal por su amistad y por todos los buenos momentos "-Gracias Miguel".

A David Muñoz y Carlos Molpecedes del *Centro Laser* de la UPM. Su inestimable coraboración ha sido clave para conseguir el 20% de eficiencia.

A Trifon Trifonov del *Centre de Recerca en Nanoenginyeria* CRne, por su gran trabajo con el FIB/SEM y su tiempo para obtener siempre la mejor imagen posible.

A Luis Enrique Romero y a Javier Pérez del *Instituto de Ciencies Fotóniques,* ICFO, por horas y horas de ALD en las que siempre han estado disponibles para solventar cualquier duda y problema.

Quisiera agradecer a los doctorandos del pasado y del presente, todos los buenos momentos dentro y fuera de la universidad. Gracias por haber hecho y hacer más agradable los días de trabajo: David Molinero, Gerard Villar, Jordi, Rafa, Lukasz, Denis, Moises, Delfina, Kike, Enrique, Maziar, Vito, Carmina, Martín, Gerard Masmitja, Rasha, Guillermo, Chen y Chenna.

A Santi Pérez (por ayudar siempre), Arnau, Teresa, Eric y Sergi por la in-

finidad de horas compartidas "working and post-working".

Finalmente y ya fuera del ámbito de la universidad quiero expresar mi sincera gratitud a Kiko Rodriguez, Mónica DelaPirriera, Mónica Colina, Anna Belen, David Hernandez y Juan Carlos por todos estos años de amistad. Y por último gracias a mi familia por su apoyo incondicional, a mis padres, mis herman@s (JL, JM y MA), cuñad@s y a mi sobrino Pablo.

This work has been supported by the MINECO under project TEC 2014-59736-R and ENE2013-48629-C4-1-R and by the European UnionÂťs Seventh Framework Programme for research, technological development and demonstration under project HERCULES (Grant agreement: 608498).

Abstract

The goal of this thesis is the fabrication of high-efficiency interdigitated back-contact (IBC) crystalline silicon (c-Si) solar cell at low temperature and low-cost manufacturing technology. This thesis proposes a new concept and at the same time a simple and elegant fabrication process that has been fully developed and culminated with the fabrication of a "cold" IBC solar cell as a proof-of-concept. To carry out this proposal, we focus our research on the study and application of low-temperature processes such as Atomic Layer Deposition (ALD) and Plasma-enhanced Chemical Vapor Deposition (PECVD) to deposit dielectric layers. A process based on laser techniques was also developed to be applied on these dielectric layers to form p^{++} and n^{++} regions into the c-Silicon sample. The laser highly-doped regions are defined in a point-like structure avoiding the classical high-temperature diffusion process. The dielectrics used, Al_2O_3 and $SiC_x(n)$ stack, play the role of aluminum and phosphorous dopant sources respectively. A detailed study is reported to find the best laser parameters and obtain the optimal p/n^{++} and n/p^{++} junctions. At the same time, these layers work as excellent surface passivating films and improve rear reflectance. To get the film which better fulfills these tasks, an extensive investigation has been performed to optimize the deposition and post-deposition processes in terms of temperature, time and layer thickness.

The acquired knowledge is applied to finished devices. In order to fabricate this "cold" IBC cell, we firstly developed an IBC cell performed on p-type FZ c-Si with a conventional phosphorous diffusion. The a-$SiC_x(n)$ stack passivates the n-type emitter surface as well as provides phosphorous atoms to create n^{++} regions or selective emitter structures after laser processing. The aluminium atoms supplied by the Al_2O_3 layer form a p^{++} region or Back-surface field (BSF) after the laser processing and simultaneously passivates the p-type surface. A

promising efficiency of 18.7% (J_{sc} = 39.1 mA/cm^2, V_{oc} = 638 mV, FF = 75.3%) was obtained as a result of this new concept.
The first "cold" IBC cell was obtained on n-type substrate. The conventional phosphorous diffusion is eliminated and the fabrication steps are rearranged in order to reduce the thermal budget and the complex photolithographic steps. The laser employed was a pulsed Nd-YAG lamp-pumped working at 1064 nm in the nanosecond regime. The efficiency achieved was 18.0% (J_{sc} = 39.2 mA/cm^2, V_{oc} = 647 mV, FF = 71.1%) on 280 μm thick 2.5± 0.5 Ωcm n-type FZ c-Si with a designated area of 9 cm^2. Finally, the efficiency achieved of the "Cold" IBC cell was boosted to 20% (J_{sc} = 40.5 mA/cm^2, V_{oc} = 650 mV and FF= 76.4%), changing the employed laser by a pulsed Nd:YVO4 laser operating at 355 nm (UV) with a better laser power control and improving the FF by decreasing de pitch from 250 μm to 125 μm.

Contents

I

Agradecimientos **III**

Abstract **V**

1 Introduction **1**

1.1 Market Overview 1
1.2 Thesis motivation 6
1.3 Thesis Outline 8

2 Fundamental Background **17**

2.1 Fundamental parameters of solar cells 17
2.1.1 Introduction 17
2.1.2 p-n junction 18
2.1.3 The solar cell 19
2.1.4 Intrinsic losses limitations 22
2.2 Review of back-contact silicon solar cells 23
2.2.1 Metallization and Emitter Wrap Through (MWT and EWT) solar cells 25
2.2.2 Back-contact back-junction (BC-BJ) solar cells 27
2.2.3 Technological challenges of BC-BJ solar cells 28
2.3 State-of the art of BC-BJ solar cells 30
2.4 Experimental techniques 34
2.4.1 Cleaning and wet texturing 34
2.4.2 Thermal Atomic Layer Deposition, ALD 38
2.4.3 Plasma Enhanced Chemical Vapour Deposition, PECVD 39

2.4.4 Laser . . . 41
2.4.5 Characterization systems . . . 41

3 c-Si surface passivation by Al_2O_3 thin films 53
3.1 Introduction . . . 53
3.2 Recombination in the bulk of c-Si . . . 54
3.2.1 Radiative recombination . . . 55
3.2.2 Auger recombination . . . 56
3.2.3 Recombination through defects in the bandgap, SRH . . . 58
3.3 Recombination at c-Si surface . . . 61
3.4 The Effective lifetime of c-Si . . . 63
3.5 State-of-the-art of c-Si surface passivation . . . 64
3.5.1 Thermally grown silicon dioxide, SiO_2 . . . 65
3.5.2 Amorphous silicon-based compounds . . . 66
3.5.3 Aluminum oxide, Al_2O_3 . . . 68
3.6 c-Si surface passivation by Al_2O_3 thin films . . . 69
3.6.1 Introduction . . . 69
3.6.2 Influence of the ALD deposition temperature and annealing treatment (time and temperature) on surface recombination velocity . . . 70
3.6.3 Influence of Al_2O_3 thickness on surface recombination velocity 72
3.6.4 $Al_2O_3/a-SiC_x$ surface passivating stacks. Experimental . . . 75
3.6.5 $Al_2O_3/a-SiC_x$ stacks. Optical characterization. . . . 78
3.7 CONCLUSION . . . 82

4 Emitter formation using laser doping technique on n- and p-type c-Si substrates 91
4.1 Introduction . . . 91
4.2 Experimental . . . 92
4.2.1 Laser system . . . 92
4.2.2 Sample preparation . . . 93
4.3 Experimental results. J-V measurements . . . 95
4.3.1 Hydrofluoric acid treatment. . . . 97
4.4 Conclusion . . . 101

5 The "Hybrid" IBC solar cell **105**

5.1 Introduction . . . 105
5.2 Precursor samples. Diodes . . . 106
5.3 Emitter saturation current (J_{oe}) study . . . 108
5.4 "Hybrid" IBC Fabrication process . . . 110
5.5 J-V measurements and Suns-V_{oc} . . . 116
5.6 Optical losses analysis and Quantum Efficiency of the "Hybrid" IBC cells . . . 119
5.6.1 Simulation of the solar cell optics . . . 120
5.6.2 External quantum efficiency analysis . . . 123
5.7 Conclusion . . . 127

6 "Cold" Back-contact Back-junction silicon solar cells **131**

6.1 Introduction . . . 131
6.2 Surface passivation and minority diffusion length . . . 133
6.3 Sheet resistance . . . 134
6.4 Precursor samples. Diodes . . . 135
6.4.1 p^{++} region . . . 135
6.4.2 n^{++} region . . . 137
6.5 Emitter saturation current (J_{oe}) . . . 139
6.6 "Cold" IBC structure and fabrication process. . . . 141
6.7 J-V measurements and Suns-V_{oc} . . . 147
6.8 Optical losses analysis and Quantum Efficiency of the "Cold" IBC cells . . . 150
6.8.1 Simulation of the solar cell optics . . . 151
6.8.2 External quantum efficiency analysis . . . 154
6.9 "Cold" IBC fabrication using 400 ns of pulse duration for emitter and BSF formation . . . 156
6.9.1 "Cold" IBC surface passivation . . . 157
6.9.2 Precursor samples. Diodes p^{++}/n . . . 157
6.9.3 Emitter saturation current (J_{oe}) . . . 158
6.9.4 J-V measurements, Suns-V_{oc} and EQE . . . 159
6.10 Conclusion . . . 166

7 One step forward!. Achieving high-efficiency solar cell **169**

7.1 Optimization of laser-doped contacts . . . 170

7.1.1 Laser system 170
7.1.2 Sheet resistance (R_{sheet}) and precursor diodes 170
7.2 "Cold" IBC solar cells characterization 175
7.2.1 J-V measurements and Suns-V_{oc} 176
7.3 Conclusions 180

8 Summary and Future Work 183
8.1 Summary 183
8.2 Future works 186
8.3 List of publications 187
8.3.1 Refereed journal paper 187
8.3.2 Other related publications 187
8.3.3 National and International conferences 188

Chapter 1

Introduction

Solar cells transform sunlight directly into electricity and they are a promising technology for satisfying the current and future energy demands in a sustainable and environmentally friendly way.

1.1 Market Overview

Fossil fuels such a coal, oil and natural gas are and will be in a short term the most used form of energy. However, their relative share in the future energy supply will be significantly decreased. The limited reserves of the fossil fuels as well as climate change caused by the emission of greenhouse gases are the major problems that directly concern the humanity as a cause and effect. Therefore, the transition from fossil energy sources to a clean and renewable energy (wind, biomass, water and solar) is a clear alternative and challenge for the present and the future.

The Earth receives incoming solar radiation from the sun in just one hour to cover the present global annual energy consumption. Solar energy is an abundant and widely available source of energy that can be directly converted into electricity by the photovoltaic cells without any emissions.

Since the first commercial use of solar cells in the late 1950's for powering satellites, the market of solar cells has followed a rapid expansion with a variety of end uses including grid connected systems, consumer products and remote area power supply. The PV market has remarkably progressed and has maintained a continuous growth in the past decade, even during difficult economic times. As it is shown in Fig. 1.1, at the end of 2009, the world's cumulative installed capacity

was more than 23 GW. One year later it was 40.3 GW and by the end of 2014, cumulative photovoltaic capacity reached at least 178 GW, sufficient to supply 1 percent of global electricity demands[1] [1].

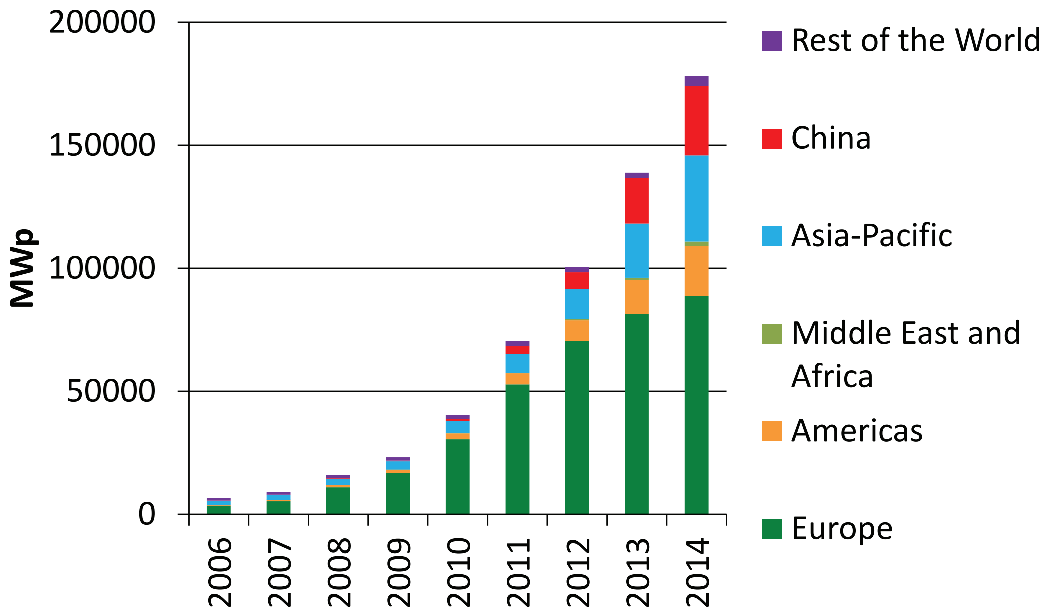

Figure 1.1: Evolution of global PV cumulative installed capacity 2006-2014. Data extrated from The European Photovoltaic Industry Association (EPIA)

However and for the first time in more than a decade, the Europe market lost its leadership to Asia in terms of new installations (China was the top market in 2013 with 11.8GW, Japan with 6.9 GW in front of 3.3 GW from Germany, the top European market) and these non-European markets (among others i.e. USA) are keeping the global PV development on, compensating the European slowdown as a consequence of political decisions to reduce PV incentives and the financial situation [1] (Fig. 1.2).

Figure 1.3 shows the cumulative capacity forecasts for global PV by 2020. Conservative scenario capacity foresee to reach 400GW, assuming declining annual installations from current levels, while more optimistic scenarios project cumulative capacity to grow beyond 500 GW [2].

[1] During the closing months of 2015, the global PV industry grown a 35 percent, global PV installations are forecast to grow an additional 17 percent in 2016, culminating in 21 GW of PV to be installed worldwide in the fourth quarter

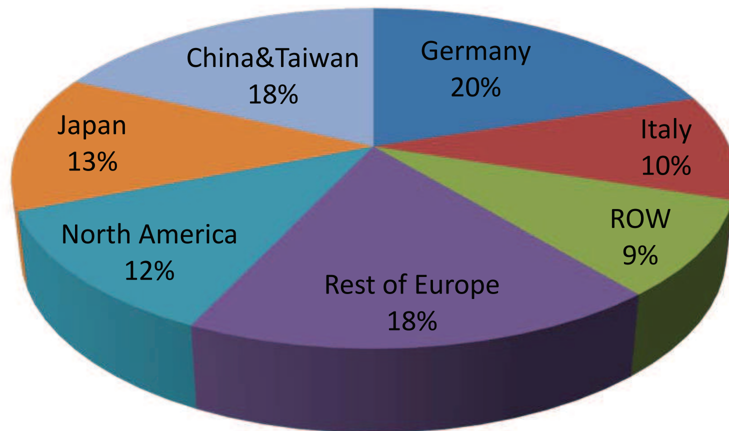

Figure 1.2: The total cumulative installations amounted to 178 GW_p at the end 2014.All percentages are related to total global installations, including off-grid systems.

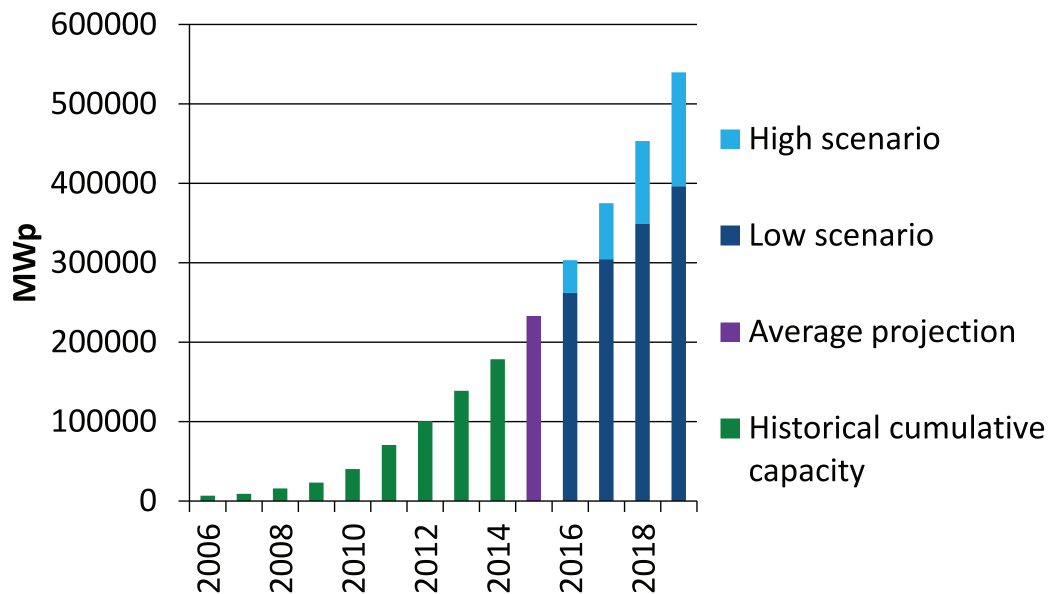

Figure 1.3: Projected global cumulative capacity. Source: EPIA

The International Energy Agency proposed in its latest edition of the Technology Roadmap: Solar Photovoltaic Energy report, a revised long-term scenario for 2050 that would occur if underlying economic, regulatory and political conditions played out. Figure 1.4 envisages up to 16% of global electricity for solar PV with 6300 TWh generated in 2050. In order to achieve IEA's projection, PV deployment of 124 GW and investments of $225 billion are required annually.

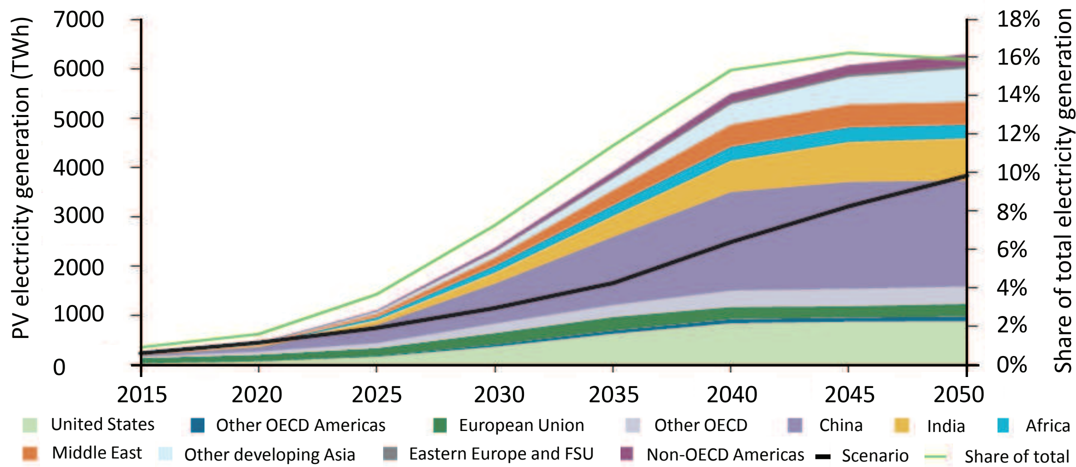

Figure 1.4: Regional production of PV electricity envisioned in the IEA's roapmad [3]

In Europe, photovoltaic energy covers 3.5% of energy demand and 6% of the peak electricity demand [3] and in it could cover between 10% and 15% in 2030 if the political scenario is favourable. However, without major changes of policy, PV contribution to the final electricity demand, could be by 2030, between 7% and 11%. In a short-term prospects for the European markets are stable in the best case, and could even decline. In the worst scenario, without support from policymakers for PV, the transition to a cost-competitive PV market driven less by financial support schemes could be difficult over the five years to come.

Economies of scale, technological improvements and intense competition which lead to module oversupply have been also responsible for achieving continued cost reductions. The average price per watt has dropped drastically for solar cells over the last few decades following the named Swanson's Law (Fig. 1.5) which states that the per-watt cost of solar cells and panels fall by 20% for every doubling of cumulative photovoltaic production.

As it can be seen from the graph, recent solar module prices have experienced a dramatic price reduction. From 2006 to 2014 worldwide average module prices

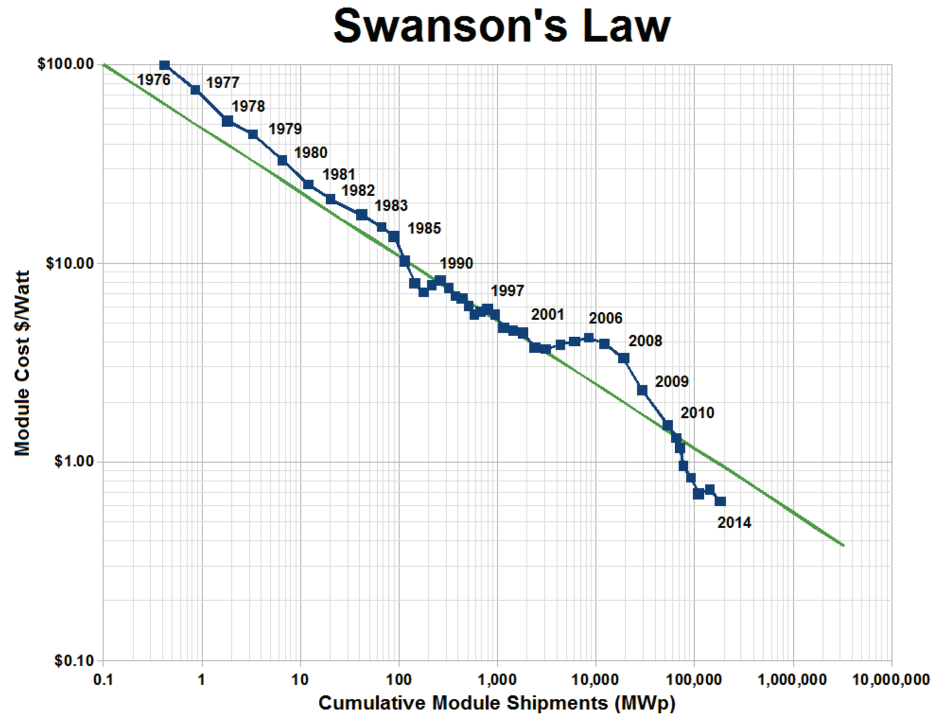

Figure 1.5: PV learning curve

have dropped about 78% from $3.25 per watt to about $0.6 per watt. In 2015, module and cell prices declined even further [4]. The main reason for this decrease was the price of the raw material that dropped notably . Silicon is a very significant part of the total cost and in 2007 there was a world wide polysilicon shortage and prices increased to about $400/kg. From 2008 to 2011 there was a huge polysilicon capacity oversupply and the silicon price dropped to $25/kg.

It is clear that the reduction of silicon prices have remarkably contributed to the expansion of PV market. In fact, silicon wafer based PV technology accounted for 91% of the total production in 2014. Figure 1.6 shows the market share divided by technology. Although multicrystalline technology dominates the market with 55% of the total production [5], monocrystalline technology has started to show a trend of gaining market share benefiting from growth on rooftop installations as well as increasing demand for higher-efficiency products [6].

Silicon technologies are strongly placed to dominate the industry for longer. Progressively thinner wafers of high bulk quality in combination with higher efficiency cell structures will be required keeping at low-cost the manufacturing

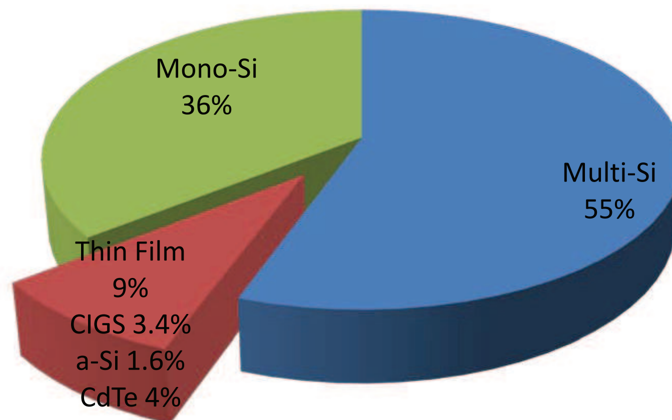

Figure 1.6: Global PV market by technology in 2014. Source: "Photovoltaics Report". Fraunhofer ISE. August 2015

technology.

1.2 Thesis motivation

From the above overview, the short and medium term for industrial solar cells appears to be based on mono and multicrystalline silicon wafers. The substrates will be progressively thinner for costs reasons and surface recombination losses thus become more significant and even dominant for high quality substrates. The minimization of surface recombination losses, known as *surface passivation* is then crucial to achieve high-efficiency solar cells.
An emerging technology that offers high quality passivation at low temperature is *Atomic Layer deposited, (ALD)* aluminum oxide (Al_2O_3) films. The main advantages that ALD technique offers are:

- Ultimate control of film growth and thickness (mono-layer growth control)
- Extremely high conformality/step coverage (very good coverage of textured surfaces
- Good uniformity on large substrates (easily scalable up to $>$ 300mm wafers)

- Relatively low substrates temperatures, typically 200-400°C (even RT)

For the PV industry, high-throughput spatial and batch ALD equipment have been designed in the last few years and are already commercially available [7]. The study of the passivation quality of Al_2O_3 deposited by thermal ALD for a variety of different surface conditions is an important topic in this thesis and is the continuation of previous work developed in a master-thesis work. Furthermore, the optical properties makes Al_2O_3 ideal for photovoltaic applications as a single layer anti-reflection coating. Therefore, Al_2O_3 films deposited by ALD technique offer great potential for increasing the efficiency of industrial crystalline silicon solar cells without increasing the fabrication cost.

On the other hand, conventional high-temperature thermal diffusion to create n^+ and p^+ regions in c-Si solar cells represents one of the most expensive and time-consuming processes in the solar cell fabrication line. Laser appears as a good candidate to achieve highly doped regions at low temperature and low manufacturing cost. Lasers are widely used for different applications in the industry of solar cells such as scribing grooves in buried contact solar cells [8], firing contacts in the laser fired contact (LFC) structure[9],[10], [11],texturing surfaces [12],[13], ablating dielectrics layers [14], among others. Several methods applying laser doping technique (LD) to junction formation have been presented to date and a wide variety of dopant source can be used in gas, liquid or solid form [15],[16],[17],[18].
In the last years our research group (Micro and Nanotechnologies, MNT) at the UPC has developed and optimized a laser process on phosphorus-doped silicon carbide stack a-SiC_x(n) for the creation of n+ region and successfully applied to the rear contact of heterojunction solar cell [19],[20],[21]. Previous group knowledge has been used as starting point and during this thesis laser doped technique has been optimized to create highly-doped regions into c-Si using a-SiC_x(n) stack deposited by PECVD and Al_2O_3 by thermal ALD and consequently reducing the global thermal budget of the solar cell fabrication. The main advantage of these dielectric layers is that, if they are correctly tuned, they can work as c-Si surface passivating layers, dopant source and reduce the optical reflectance simultaneously. Results of this study have been published in several papers [22],[11],[18],[23],[24],[25].

The highest conversion efficiency of crystalline solar cell for one-sun applications is 26.3% and was achieved in a practical size (180 cm^2) by Kaneka Corporation in September 2016. This recent new record was based on Back-contact back-junction structure with heterojunction technology. This achievement breaks the past world record of 25.6% by $\sim$ 0.7 %, achieved by Panasonic (2014) using the same heterojunction back-contact type structure [26].

MNT research group has acquired in the last years an extensive experience on interdigitated back-contact solar cells fabrication [27] and together with Aalto University have achieved the world record in Black Silicon solar cells with interdigitated back-contacts (IBC) [28]. However this cell structure is quite complex and its fabrication involves multiple masking steps, high temperature diffusion and extremely well aligned processes. Due to the potential of high-efficiency devices combined with low-cost fabrication process, the last part of this thesis consists of applying dielectric layers previously studied to fabricate the final IBC solar cell. High surface passivation quality and good antireflection properties in the photovoltaic range are needed. On the other hand, these layers have to provide enough quantity of dopant to originate p^+ and n^+ regions into c-Si either to form a Back-surface field or np^+/pn^+ junction. Thus, optimized laser conditions, i.e. laser power, mode and number of pulses are required. Combining these dielectric layers with laser processing has the potential to drastically simplify the fabrication of IBC c-Si solar cells.

1.3 Thesis Outline

This thesis work has one main and a clear objective: the fabrication of a "cold" IBC, i.e. An interdigitated back-contact solar cell that do not involve the conventional high-temperature diffusion neither time-consuming and complex processes. In order to achieve this final objective, the followed methodology can be seen in figure 1.7 together with the corresponding chapters of the thesis.

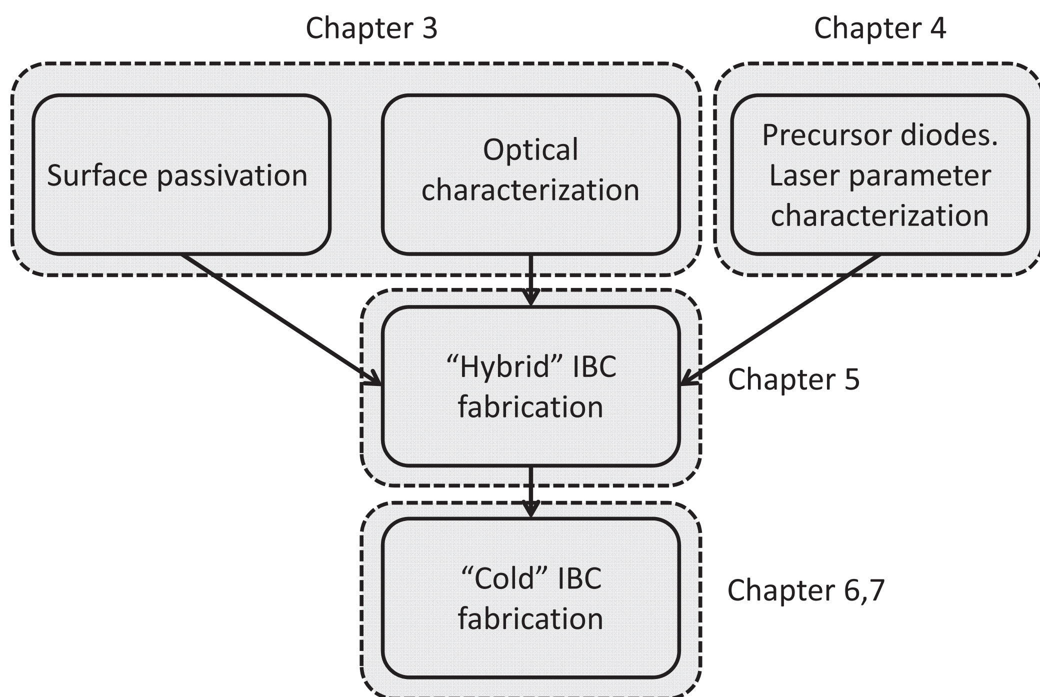

Figure 1.7: Schematic of the experimental flow developed along this thesis work.

Chapter 2 is the starting point of this thesis. Fundamental background as basic concepts and parameters of crystalline silicon solar cells as well as the intrinsic limitations are presented. Back-contacted silicon solar cell designs are briefly introduced and special attention is paid to IBC structure and a short historic overview is given. The last part of this chapter comprises the explanation of the fundamental equipment used in this thesis for processing and characterization.

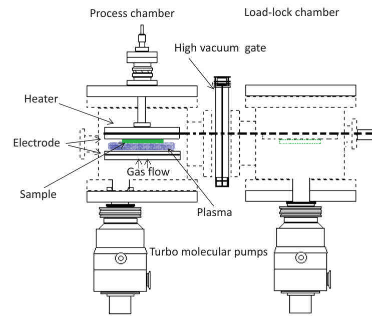

In Chapter 3 basic concepts of recombination mechanisms and surface passivating films in c-Si are presented. Next, we study in detail the Al_2O_3 layer and $Al_2O_3/a-SiC_x$ stacks as passivating films. Surface recombination velocity has been analyzed as a function of deposition temperature, annealing time and temperature and thickness film.

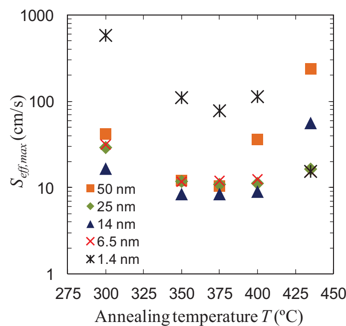

As a second step optical properties of the studied films i.e. Al_2O_3 and $Al_2O_3/a-SiC_x$ stack are also analyzed in this chapter. Reflectance properties on polish and textured c-Si are evaluated in order to find the best film structure that simultaneously fulfills the surface passivation and the antireflection condition needed for the fabrication of an IBC solar cell.

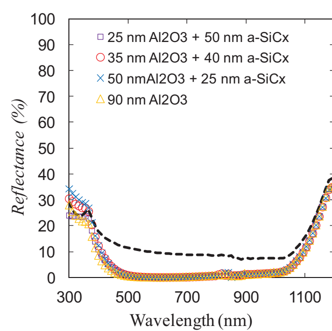

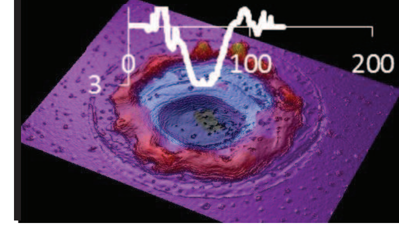

The third stage of the *experimental flow scheme* corresponds to Chapter 4. In this chapter we explore the laser parameters in order to find the ideal conditions to be applied in the formation of the highly doped regions of the solar cell, i.e BSF and emitter. Dark J-V measurements of both n^{++}/p and p^{++}/n diodes under test are analyzed. The p^{++} regions results from applying laser technique through Al_2O_3 layers and their n^{++} counterpart based on Si-rich intrinsic $a-SiC_x(i)$/phosphorous-doped a-Si/stoichiometric $a-SiC_x$ stack laser processing. Additional HF treatment after the laser stage is also evaluated.

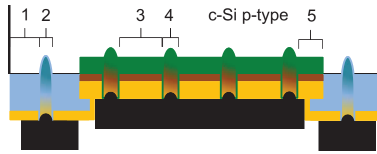

In Chapter 5 we introduce the first approximation to the final "cold" IBC solar cell. In this chapter we fabricate a "hybrid" IBC in which one conventional phosphorous thermal diffusion step is involved. In this structure, the emitter and base region contact are performed by laser technique (IR laser). The knowledge acquired about surface passivation, optical reflectance and laser doped technique applied to the films studied is the starting point of the IBC fabrication. Dark J-V measurement of the precursor diodes involved, J_{oe} measurement, EQE, Suns-V_{oc}, reflectance measurement and simulation of the optical properties of the fabricated IBC solar cells are reported. As a proof of concept, an excellent 18.7% efficiency has been achieved.

In Chapter 6 we describe the fabrication process of our "cold" IBC solar cell. The elimination of the thermal diffusion process and the rearrangement of the layers involved in the process has culminated in a promising 18.0% of efficiency. The simplicity of the fabrication process proposed is explained in detail. Again, Dark J-V measurement of the precursor diodes involved, J_{oe} measurement, EQE, Suns-V_{oc}, reflectance measurement and simulation of the optical properties are used to characterize the devices.

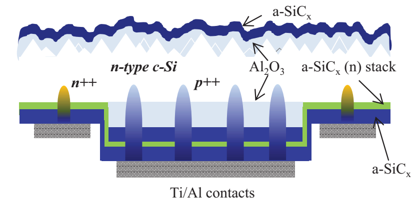

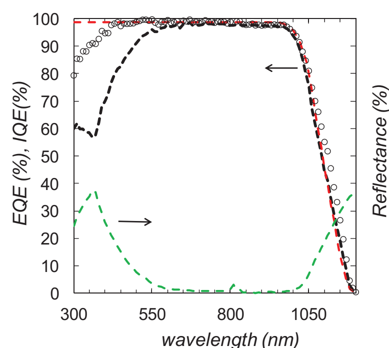

In Chapter 7 we fabricate the final "Cold" IBC solar cells. The laser processing type is changed and UV (355 nm) is applied with better power control trough the dielectric layer studied previously. Efficiencies up to 20% with short-circuit current densities and open circuit voltages of around 40 mA/cm^2 and 650 mV respectively were achieved. Efficiency is mainly limited by series resistance limiting fill factor FF values around 76.5% whit relatively high pseudo-FF (pFF) values over 82% and up to 83.8%.

In chapter 8, conclusions and future work are summarized

It should be mentioned that most of the results reported in this thesis have been published in separate papers in peer-reviewed journals. Each paper corresponds to a chapter as follows:

- Chapter 3
  "Optimization of Al_2O_3 films obtained by ALD to passivate p-type c-Silicon wafers". Presented at 27th European Photovoltaic Solar Energy Conference and Exhibition (Frankfurt, Germany).
  "Surface passivation and optical characterization of $Al_2O_3/a-SiC_x$ stacks on c-Si ". Published in *Beilstein Journal of Nanotechnology*, Vol.4, 726-731, 2013

- Chapter 4
  "Emitter formation using laser doping technique on n- and p-type c-Si ". Published in it Applied Surface Science,
  doi:10.1016/j.apsusc.2014.10.140, 2014

- Chapter 5
  "Base contacts and selective emitters processed by laser doping technique for p-type IBC c-Si solar cells". Published in *Energy Procedia*, Vol. 77, 752-758, 2015

- Chapter 6
  "Cold" process for IBC c-Si solar cells fabrication". Published in *Energy Procedia*,Vol.92; 652-660;2016

Bibliography

[1] EPIA European Photovoltaic Industry Association. Global market outlook for photovoltaics 2014-2018, www.solarpowereurope.org, 2014.

[2] Solar Power. Global market outlook 2015-2019, www.solarpowereurope.org, 2015.

[3] IEA International Energy Agency. Technology roadmap-solar photovoltaic energy, www.iea.org, 2014.

[4] http://pv.energytrend.com/pricequotes.html, 2015.

[5] Fraunhofer Institute for Solar Energy Systems ISE. Photovoltaics report, www.ise.fraunhofer.de/de/downloads/pdf-files/aktuelles/photovoltaics-report-in-englischer-sprache.pdf, 2015.

[6] IHS Technology. Top solar power industry trends for 2015, www.ihs.com/pdf/top-solar-power-industry-trends-for-2015-213963110915583632.pdf, 2015.

[7] G. Dingemans and W. M. M. Kessels. Status and prospects of Al_2O_3-based surface passivation schemes for silicon solar cells. *Journal of Vacuum Science and Technology A: Vacuum, Surfaces, and Films*, 30:040802, 2012.

[8] A. W. Y. Ho and Stuart R. Wenham. Buried contact solar cells with innovative rear localised contacts. *Progress in Photovoltaics: Research and Applications*, 12:297–308, 2004.

[9] E. Schneiderlöchner, R. Preu, R. Lüdemann, and S. W. Glunz. Laser-fired rear contacts for crystalline silicon solar cells. *Progress in Photovoltaics: Research and Applications*, 10:29–34, 2002.

[10] D. Carrió, P. Ortega, I. Martín, G. López, J. M. López-González, A. Orpella, C. Voz, and R. Alcubilla. Rear Contact Pattern Optimization based on 3D Simulations for IBC Solar Cells with Point-like Doped Contacts. *Energy Procedia*, 55:47–52, 2014.

[11] I. Martín, P. Ortega, M. Colina, A. Orpella, G. López, and R. Alcubilla. Laser processing of Al_2O_3 /a-SiC_x:H stacks: a feasible solution for the rear

surface of high-efficiency p-type c-si solar cells. *Progress in Photovoltaics: Research and Applications*, 21:1171–1175, 2012.

[12] Pirozzi L., Vetrella U.B, Falconieri M., and Salza E. A laser system for silicon solar cell processing: design, setup and operation. *Materials Science Forum*, pages 319–324, 1995.

[13] Pirozzi L., Vetrella U.B, and Salza E. Innovative applications of laser technology in photovoltaics. In *Proc. SPIE Conf. Laser Applications in Microelectronic and Optoelectronic Manufacturing II*, 1997.

[14] A. Knorz, M. Peters, A. Grohe, C. Harmel, and R. Preu. Selective laser ablation of SiN_x layers on textured surfaces for low temperature front side metallizations. *Progress in Photovoltaics: Research and Applications*, 17: 127–136, 2009.

[15] G. B. Turner. Solar cells made by laser-induced diffusion directly from phosphine gas. *Applied Physics Letters*, 39:967, 1981.

[16] D. Kray, A. Fell, S. Hopman, K. Mayer, G. P. Willeke, and S. W. Glunz. Laser Chemical Processing (LCP). a versatile tool for microstructuring applications. *Applied Physics A*, 93:99–103, 2008.

[17] E. Fogarassy. Silicon solar cells realized by laser induced diffusion of vacuum-deposited dopants. *Journal of Applied Physics*, 52:1076, 1981.

[18] M. Colina, I. Martín, C. Voz, A. Morales-Vilches, P. Ortega, G. López, A. Orpella, R. Alcubilla, I. Sánchez-Aniorte, and C. Molpeceres. Optimization of laser doping processes for the creation of p+ regions from solid dopand sources. In *27 th EUPVSEC*, pages 1885–1889, 2012.

[19] I. Martín, M. Colina, A. Orpella, C. Voz, S. De Vecchi, T. Desrues, S. Abolmasov, P. Roca i Cabarrocas, and R. Alcubilla. Low recombination n+ regions created by n+ c-si epitaxial layers and laser processing of phosphorus-doped SiC_x films. In *27th European Photovoltaic Solar Energy Conference and Exhibition*, pages 1519–1523, 2012.

[20] A. Morales-Vilches, C. Voz, M. Colina, G. Lopez, I. Martin, A. Orpella, J. Puigdollers, M. Garcia, and R. Alcubilla. Progress in silicon heterojunction

solar cell fabrication with rear laser-fired contacts. In *Proceedings of the 2013 Spanish Conference on Electron Devices, CDE 2013*, pages 345–348, 2013.

[21] A.B. Morales-Vilches, C. Voz, M. Colina, D. Munoz-Martin, I. Martin, P. R. Ortega, G. Lopez-Rodriguez, C. Molpeceres, and R. Alcubilla. Study of the surface recombination velocity for ultraviolet and visible laser-fired contacts applied to silicon heterojunction solar cells. *IEEE Journal of Photovoltaics*, 5:1006–1013, 2015.

[22] P. Ortega, I. Martín, G. Lopez, M. Colina, A. Orpella, C. Voz, and R. Alcubilla. p-type c-Si solar cells based on rear side laser processing of Al_2O_3/SiC_x stacks. *Solar Energy Materials and Solar Cells*, 106:80–83, 2012.

[23] J. M. López-González, I. Martín, P. Ortega, A. Orpella, and R. Alcubilla. Numerical simulations of rear point-contacted solar cells on 2.2 ohm.cm p-type c-si substrates. *Progress in Photovoltaics: Research and Applications*, 23:69–77, 2013.

[24] I. Martín, M. Colina, G. Coll, A.and López, P. Ortega, A. Orpella, and R. Alcubilla. c-si solar cells based on laser-processed dielectric films. *Energy Procedia*, 55:255–264, 2014.

[25] G. López, P. Ortega, M. Colina, C. Voz, I. Martín, A. Morales-Vilches, A. Orpella, and R. Alcubilla. Emitter formation using laser doping technique on n- and p-type c-si substrates. *Applied Surface Science*, 2014.

[26] K. Masuko, M. Shigematsu, T. Hashiguchi, D. Fujishima, M. Kai, N. Yoshimura, T. Yamaguchi, Y. Ichihashi, T. Mishima, N. Matsubara, T. Yamanishi, T. Takahama, M. Taguchi, E. Maruyama, and S. Okamoto. Achievement of more than 25% conversion efficiency with crystalline silicon heterojunction solar cell. *IEEE Journal of Photovoltaics*, 4:1433–1435, 2014.

[27] P. Ortega, E. Calle, G. von Gastrow, P. Repo, D. Carrió, H. Savin, and R. Alcubilla. High-efficiency black silicon interdigitated back contacted solar cells on p-type and n-type c-si substrates. *Progress in Photovoltaics: Research and Applications*, 2015.

[28] H. Savin, P. Repo, G. von Gastrow, P. Ortega, E. Calle, M. Garín, and R. Alcubilla. Black silicon solar cells with interdigitated back-contacts achieve 22.1% efficiency. *Nature Nanotechnology*, 10:624–628, 2015.

Chapter 2

Fundamental Background

In this chapter we present some basic concepts of silicon solar cells. We merely focus on fundamental definitions in order to understand how solar cells work. Additionally, back-contact solar cells and state-of-the-art technology are also described as well as the critical drawbacks involved with IBC solar cell concept. A general overview and a short theoretical background of the methods and equipment used in this thesis are reported.

2.1 Fundamental parameters of solar cells

2.1.1 Introduction

In the photovoltaic effect, the energy of a photon is transferred to charge carriers i.e. converted into electrical energy. In figure 2.1 we plot the AM0[1] and AM1.5[2] spectral irradiance corresponding to the spectrum used as a reference by the spatial industry and photovoltaic earth applications respectively.

The thermodinamic limit of the conversion efficiency for a single band-gap of c-Si (1.12 eV) under AM1.5G solar spectrum and taking into intrinsic recombination was found to be 29.4% [1].
In figure 2.1 in grey color we can see the fraction of the spectrum that can be converted to electrical energy by a single-junction silicon solar cell. Others absorbing materials used in PV field are also shown for comparison.

[1]http://rredc.nrel.gov/solar/spectra/am0
[2]http://rredc.nrel.gov/solar/spectra/am1.5

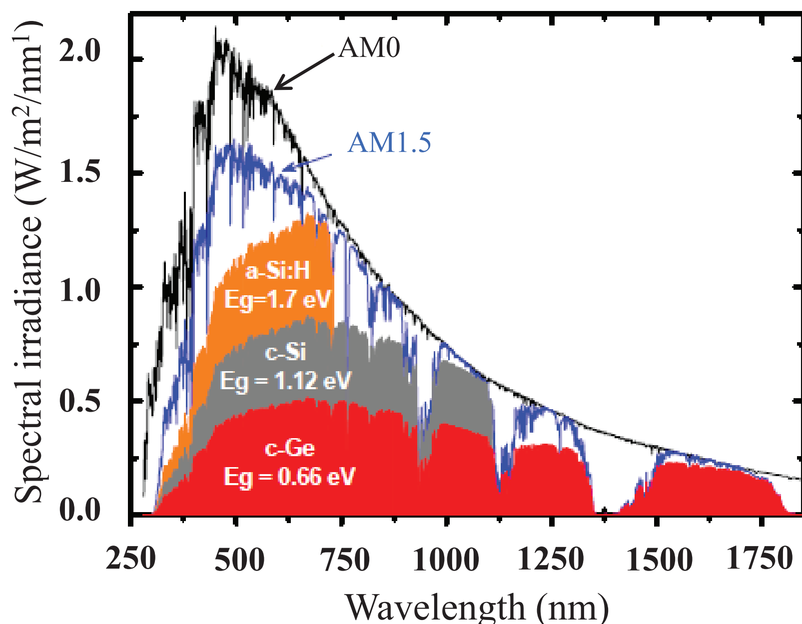

Figure 2.1: Spectral irradiance of the AM0 and AM1.5 solar spectrums, as well as the maximum energy for different absorbing materials. [2]

2.1.2 p-n junction

The p-n junction is the basis of crystalline silicon solar cells as well as of other electronic devices. Such a junction is formed when a n-type semiconductor is brought into contact with a p-type semiconductor. When the material is the same for both semiconductors then the junction is called homojunction. If the material is not the same, then it is called heterojunction.

When the two semiconductor types are placed into contact, majority carriers (electron in n-type and holes in p-type) diffuse from the region where they are in a high concentration towards the region where they are in low concentration leaving behind them ionized atoms; positive ions in n-type semiconductor and negative ions in p-type semiconductor. These ionized atoms are fixed in the crystal lattice and are unable to move. Consequently, an increased electric field (opposed to diffusion) is created until its value stops any further charge transfer. The region affected by this electric field is called the *depletion region* or *space charge region*. A *built-in* potencial (V_{bi}) due to this electric field is formed at the junction. In figure 2.2 the band energy corresponding to a pn junction at thermal equilibrium is shown.

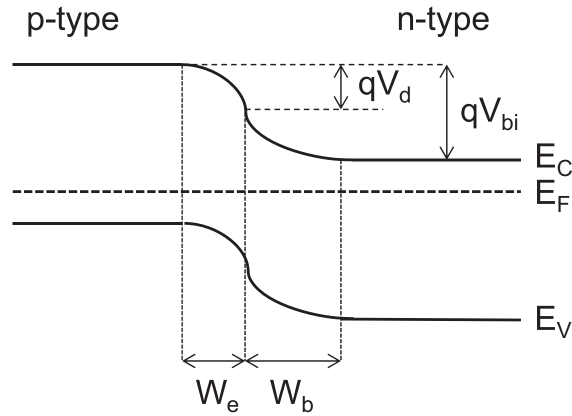

Figure 2.2: Schematic band diagram corresponding to a pn junction (homojunction) in the dark at thermal equilibrium.

The depletion region has a width of $W_e + W_b$ (W_e is width on the emitter side and W_b the width on the base side).

In the dark, the current density can be expressed as a function of the external applied voltage (V) as follows:

$$J_D(V) = J_0 \left[exp\left(\frac{qV}{nkT}\right) - 1\right] \tag{2.1}$$

where J_0 is the recombination current density (diode leakage current density in the absence of light), q the elementary charge, n the ideality factor, k the Boltzmann constant and T absolute temperature. The term kT/q is the so-called *thermal voltage,* V_T, being 25.85 mV at 300K.

2.1.3 The solar cell

Traditionally, photovoltaic energy conversion combines semiconductor materials and a p-n junction. The behaviour of a solar cell in the dark follows the same law described by the equation 2.1. When the solar cell absorbs the energy provided by the photons electron-hole pairs are created. To extract the carriers to the external metal contacts, two carrier-selective contact structures are needed. These structures exhibit efficient transport of one type of carrier blocking the transport of the other type of carrier. Unbalance the number of electrons and holes the recombination in the contact structure is reduced [3]. Electrons are then extracted

by metal contacts to an external circuit where dissipate its energy and return to the solar cell. Consequently, a good ohmic contact is required. This flow of carriers is called photogenerated current.

In short-circuit conditions the carriers are injected to the external circuit generating a current (J_{sc}, short-circuit current density). When the solar cell works under open-circuit conditions the junction energy barrier height decreases. Consequently, the minority diffusion currents increase in such a way that perfectly cancel the photogenerated current leading to no external current, i.e. open-circuit conditions. The voltage required to achieve at this equilibrium is called *open-circuit voltage*, V_{oc}. To understand the electrical properties of a solar cell, it is useful to create a model which is electrically equivalent and based on discrete electrical components. This model describes an illuminated solar cell and includes the initial diode and the photogenerated current density (J_{ph}) flowing in the opposite direction, as it is shown in figure 2.3.

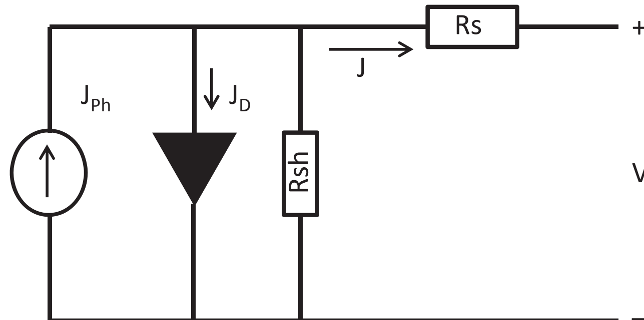

Figure 2.3: Electrical model used to describe a solar cell.

The electrical model above described also includes parasitic series resistance (R_S) that takes into account all the resistive losses in the solar cell (e.g. contact resistance, emitter and base resistance, metallization grid ohmic losses, etc.) and shunt resistance (R_{sh}) causing efficiency drops. Equation 2.2 describes electrical behaviour considering ohmic losses where, r_s and r_{sh} are the normalized resistances considering the cell area in (Ωcm^2) units.

$$J(V) = J_0[exp(\frac{q(V - r_s J)}{nKT}) - 1] + \frac{V - r_s J}{r_{sh}} - J_{ph} \tag{2.2}$$

Losses caused by series resistance increase, in a first approximation, quadratically with the photocurrent. Series resistance losses are therefore most important at high illumination intensities and have to be kept as low as possible. As series resistance increases, the terminal voltage significantly decreases. The short-circuit current, is slightly affected but very high values of R_s could also produce a significant reduction of this parameter.

Low shunt resistance produces a significant reduction in the terminal current and a slight reduction in V_{oc}. Although very low values of R_{sh} could also significantly reduce V_{oc}. Obviously, shunt resistance has to be kept as high as possible. Very high series resistance or/and very low shunt resistance produce a solar cell behaviour similar to those of a resistor.

Physically, reverse saturation current (or recombination current density) is a measurement of the *leakage* of carriers across the p-n junction in reverse bias resulting from the recombination in the neutral regions on either side of the junction. The increase of J_o leads to a reduction of V_{oc} proportional to the inverse of the logarithm of the increase.

The ideality factor (n) is a parameter related to the current mechanism dominating the J-V curve. The ideality factor $n = 1$ implies recombination taking place at the quasi-neutral regions of the diode without recombination within the space-charge region. On the other hand, when recombination in space-region dominates then $n \cong 2$.
The efficiency (η) of the solar cell quantifies the fraction of solar energy that is converted into electrical energy and in mathematical terms is given as:

$$\eta = \frac{P_{out}}{P_{in}} = \frac{FF.J_{sc}.V_{oc}}{P_{in}} \tag{2.3}$$

where P_{in} and P_{out} is the incoming power density and the out maximum power density of the cell respectively. Fill Factor (*FF*) describes the squareness of the current-voltage curve. This parameter is the ratio between the area of the rectangle formed by the maximum power point ($J_{max} \times V_{max}$ and the one formed by V_{oc} and J_{sc} (Figure 2.4).

The J-V measurements is the tool used to characterize the photovoltaic devices and it will be, together with EQE (external quantum efficiency) measurements the main techniques used in the experimental of this thesis to characterize IBC solar cells. The J-V measurements and photovoltaic parameters extraction are carried

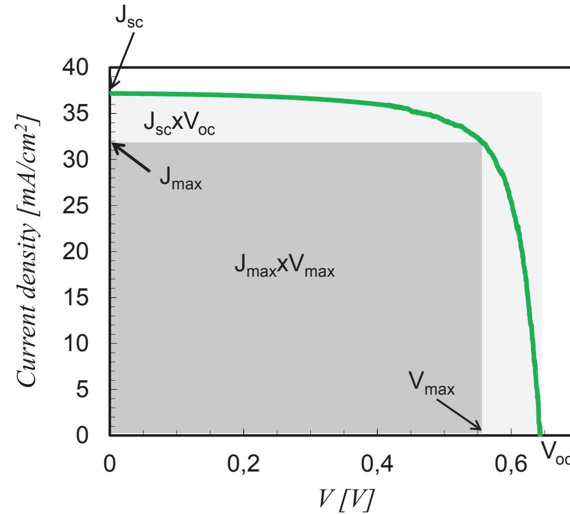

Figure 2.4: Typical J-V curve of a solar cell

out under standard test conditions, i.e. AM1.5G 1 KW/m^2 Solar spectrum and T = 25 °C.

Dark measurements allow to determine J_0 and n parameters while under illumination conditions we get information of V_{oc}, J_{sc} and FF, as well as solar cell efficiency.

2.1.4 Intrinsic losses limitations

The conversion efficiency in a c-Si solar cell is limited in a first approximation by the following intrinsic and unavoidable loss mechanisms:

- Photons with energy higher than the bandgap energy of the material (1.12 eV) will generate electron-hole pairs. However, the exceeding energy will be lost due to thermalization process. This means that the electron will be promoted from valence band to conduction band at an energy level higher than the edge of conduction band. These *hot electrons* release its extra energy via phonon scattering in a very short time compared to the one needed to collect them.

- Photons with smaller energy than the bandgap of silicon will not be absorbed by the material. The photon energy will not be enough to generate electron-hole pairs and its energy will be lost.

- Absorption coefficient of the silicon strongly depends on the photon wavelength. For photons with wavelength higher than 1000 nm the absorption coefficient is very low resulting in absorption lengths longer than device thickness. Then, depending on light-trapping properties, these photons can escape from the device without being absorbed, despite of having the appropriate energy to generate electron-hole pairs.

- The finite maximal average path length of the photons within the silicon is an intrinsic optical loss effect which limits the short-circuit current (J_{sc}) of a solar cell. This maximal average path length (l), considering optimal light trapping scheme, can be approximated by [4],[5]:

$$l \approx 4 \times n_{Si}(\lambda) \times W \tag{2.4}$$

  where $n_{Si}(\lambda)$ is the refraction index of the silicon as a function of the wavelength and W is the wafer thickness.
  Take into account equation 2.4 and the AM1.5G spectrum, the J_{sc} limit for a silicon wafer thickness of 280 μn is calculated about 43.8 mA/cm^2. [6].

- Open-circuit voltage (V_{oc}) of solar cell is limited by the recombination rate of the electrons and holes. Intrinsic recombination are radiative and Auger recombination (explained in detail in chapter 3 (3.2.1 and 3.2.2). A detailed study of the limit of the open-circuit voltage calculated for different wafer thicknesses and different base doping density of an n and p-type solar cell can be found in the thesis work realized by Kerr [6].

All the intrinsic loss mechanisms above explained determine the maximum light-electricity conversion to be achieved by a solar cell, resulted to be about 28.5% ([6]). However, this efficiency will be even more reduced due to technological issues related to solar cell processing.

2.2 Review of back-contact silicon solar cells

Conventional solar cells have metal contacts on both cell sides. The best example of this architecture is the so-called Passivated Emitter Rear Locally diffussed (PERL) cell (see figure 2.5). This structure enabled reaching at 25% of efficiency

of monocrystalline (homojunction) silicon solar cell under one-sun illumination intensity [7]. The features of this cell are:

- A selective doping profiles underneath metal contacts for low contact recombination
- Passivated front and rear surfaces
- Well textured front surface with an antireflection coating for low front surface reflection
- A flat, highly reflective rear for light-trapping
- Low front contact shading

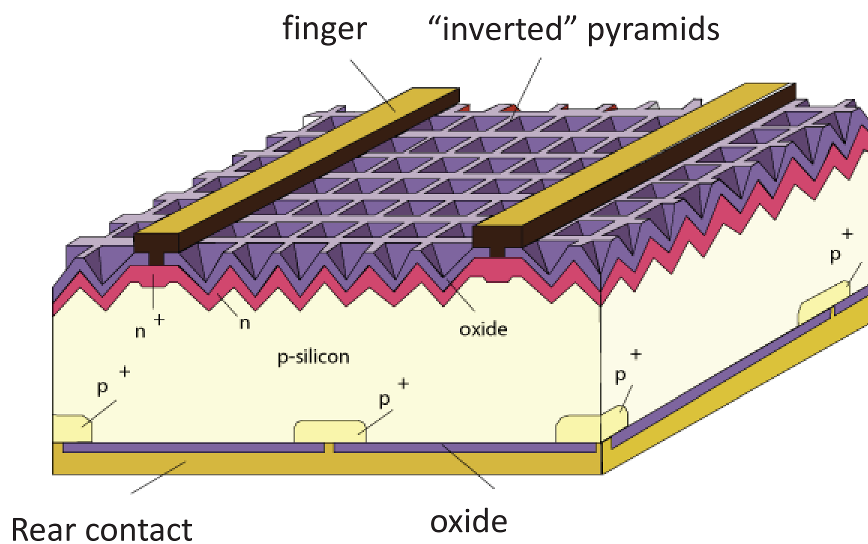

Figure 2.5: The passivated emitter, rear locally-diffused PERL cell. Record efficiency of 25%

These features are required for high-efficiency PERL solar cells but also are required for the back-contact back-junction cell structure. However, the full PERL design is not easy to apply to low-cost industrial production because of the necessity for multiple photolithography steps. On the other hand, a trade-off between resistive losses and optical shading losses due to the front metal grid have to be considered. Such a problem is partially or totally overcame using back contact structures.

Back contact cell design is not a recent concept. Since the first publications by R.J. Schwartz in 1975 [8], interest in back-contact cells has been growing in the last years. Two major advantages which make these cells of great interest are a lack of grid shading loss and a coplanar interconnection.

In April 2014 Panasonic achieved the world's highest energy conversion efficiency of 25.6% at research level (147.7 cm^2) [9]. This new record is an improvement of 0.6 points over the previous record for small area crystalline silicon-based solar cells of 25% (University of New South Wales (Australia)) [10]. Even more recently, in September 2016, Kaneka Corporation has announced a 26.3% of efficiency. This achievement was possible by further development of its heterojunction technology adopted to a back-contact solar cell structure which allows the more efficient utilization of the sunlight.

Back-contact cells developed to date can be divided into three categories:

- Metallization Wrap Through (MWT) solar cells
- Emitter Wrap Through (EWT) solar cells
- Back-Contact Back-Junction (BC-BJ) solar cells, also called Interdigitated Back Contact (IBC) solar cells

2.2.1 Metallization and Emitter Wrap Through (MWT and EWT) solar cells

Metallization wrap-through back-contact cell [11] is the concept that is most closely linked to the conventional cell structure (Figure 2.5). In both cell structures the emitter is located at the front surface, but in the former part of the front metallisation grid is moved from the front to the rear surface. The front side metal fingers are interconnected to the busbar placed at the rear side through the laser drilled holes in the wafer (figure 2.6 a). The MWT cell concept offers some advantages over the conventional solar cell. Removing the busbar from the front side, front contact shading is reduced. Simultaneously, the coplanar interconnection is possible since both contact polarities are placed on the back side.

Many highly efficient metal wrap through solar cell types on monocrystalline *p*-type and *n*-type silicon with efficiencies of about 20% have been reported and a

variety of different MWT structures and contact layouts have been reported over the last years [12]: E. Lohmüller *et al.* (PV-TEC) at Fraunhofer ISE developed metal wrap through passivated emitter and rear solar cells (MWT-PERC) on monocrystalline p-type silicon and on large-area cells with 149 cm^2 wafer size achieving 20.6% on Float-zone (FZ) [13] material. 20.2% was achieved by B. Thaidigsmann *et al.* on mCz-Si substrate and 239 cm^2 with a high-performance HIP-MWT structure solar cells using industrial equipment [14]. W.Yin *et al.* from Canadian Solar developed a MWT structure on p-type, 156 mm x 156 mm cast mono-silicon removing the emitter from via connection and rear side (MWT-BSF+). With this simplified structure achieved 19.6% of efficiency [15]. Lamers *et al.* from ECN group presented mc-Si MWT-BSF with an area of 243 cm^2 and an efficiency of 17.9% [16].

In Emitter Wrap Through concept the emitter is also located at the front surface but in this case all contacts are on the rear surface, remaining the front surface totally free of any metallization. The front surface collecting junction is connected to the interdigitated contacts on the back surface via laser-drilled holes (figure 2.6 b).

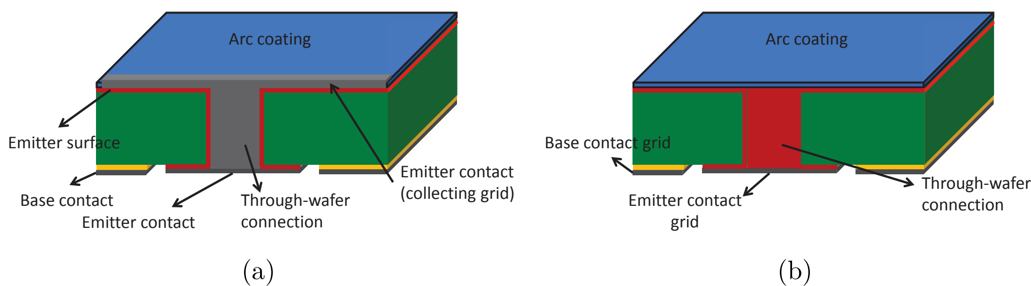

Figure 2.6: a)Schematic representation of metallization wrap-through back contact solar cell and b) emitter wrap-through back contact solar cell.

This structure collects the minority carriers at the front or through the complete thickness of the silicon wafers. The average distance that minority carriers have to travel to the junction is significantly reduced and consequently the requirements for high minority carrier lifetime materials are also relaxed compared to back-contact back junction solar cell structure. The highest efficiency recorded in EWT cell is 21.4% on FZ silicon and 17.2% on multicrystalline substrates [17]

2.2.2 Back-contact back-junction (BC-BJ) solar cells

In Back-contact back-junction solar cell (figure 2.7), the collecting junction together with both contacts are located on the back side of the cell, commonly designed forming an interdigitated (IBC) pattern. A special attention will be given to this structure type since it will be the main topic of this thesis.

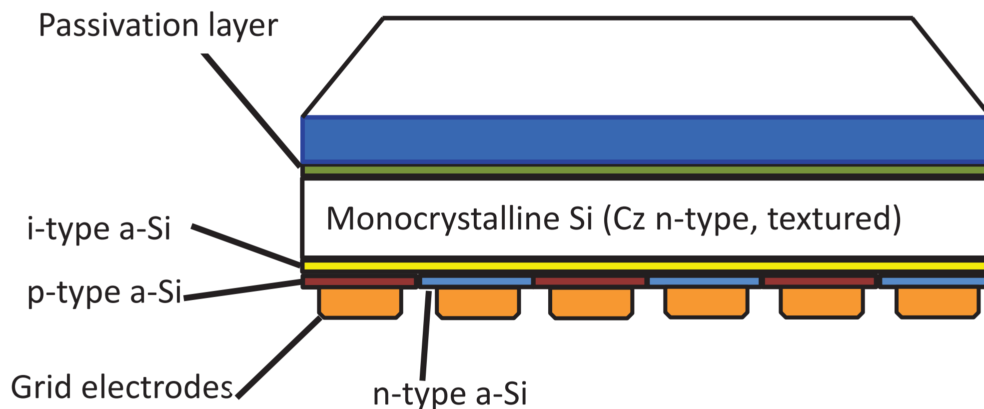

Figure 2.7: Structure of c-Si HIT solar cell with interdigitated back contact. *Panasonic, 2014*

This structure, as in EWT solar cells, eliminates the front surface contact reflection and exhibit the following advantages.

- Higher J_{sc} of the cell due to the absence of the front metal grid to shadow the incident photon flux. Zero shading.
- As a consequence of the absence of the front metal grid, the front surface can be optical and electrically optimized (i.e. light trapping and surface passivation improvements) without the constrains imposed by the conventional trade-off between reflection and series resistance found in front-contacted solar cells.
- Series resistance can be substantially reduced because the backside metallization pattern width is not limited by the shading losses and it can cover nearly half of the back surface for each type of polarization.

- BC-BJ solar cells are well suited for tandem solar cells as bottom cells. The metal-free front surface can be used for epitaxial growth of the top cells or even just as a holder in four terminal configuration.

- Easier co-planar interconnection in the module and increases of the solar cell packaging density.

2.2.3 Technological challenges of BC-BJ solar cells

The advantages related with IBC solar cells make them a potencial low-cost and high-efficiency devices. However, there are some challenges related to BC-BJ solar cells to take into account in solar cells processing:

- Since the emitter is located on the backside of the solar cell, the charge carriers, generated predominantly near the front surface, have to diffuse through the whole thickness wafer. A long minority-carrier diffusion length is a mandatory requirement in the bulk (base) and it can only be provided by either high-quality silicon material or using very thin substrates in order to guarantee high solar cell efficiencies [18].

  In the case of the point-like laser diffusion developed in this thesis, the maximum diffusion distance that the minority carrier have to travel depend on the distance between laser spots (i.e. 250 μm) and wafer thickness ($\sim$ 280 μm. See figure 2.8.

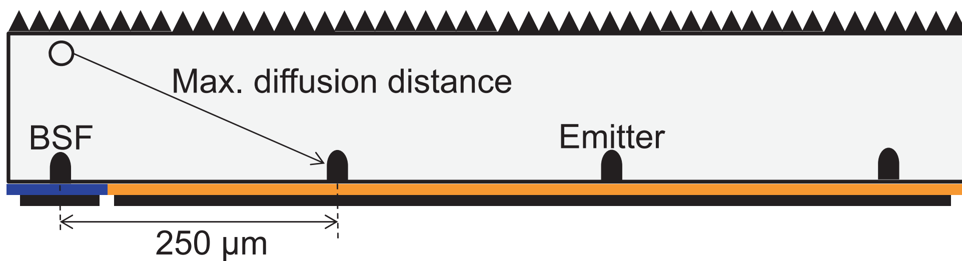

Figure 2.8: Simplified scheme of the IBC solar cell fabricated in this thesis. Punctual diffused regions are defined by laser technique

- Simultaneously, the front surface recombination needs to be kept low and stable in the final device. Otherwise, carriers recombine at this surface strongly reducing the J_{sc}.

- Back surface passivation quality is also needed to avoid carrier recombination. Furthermore, the rear surface hosts the extended termination of the junction and the V_{oc} and the FF of the cell can be lowered by the contribution of the second diode recombination current due to a space-charge region surface recombination [19].

- Surface conductance channels can be formed between the emitter and the base contacts when dielectric layers are applied for passivation schemes based on surface field in the silicon. Thermal SiO_2 or densified deposited oxide are good options [20],[21].

- The processing of back-contact solar cells requires several patterning steps resulting in a complex fabrication process.

- The closely spaced interdigitated fingers of opposite polarity on the backside of the cell, requires careful alignment to avoid risk of fatal shunting between the p- and n- electrodes.

Recombination in the contact areas become dominant once the base lifetime is sufficiently high and all the surfaces are well passivated. Reducing the contact fraction helps to reduce this recombination and the *point contact cell* is the best way to achieve it [22],[23]. The point-contact structure consists of the alternating n- and p-regions in an array pattern on the bottom surface of the device. The IBC solar cells fabricated in this thesis follow this structure (see figure 2.8) and the point-contact base and emitter are formed by laser processing through dielectric layer as it will be explained in chapter 4.

The reduction of the recombination in the contact areas by reducing the fraction results in an increased open-circuit voltage. However, the collection of minority-carrier is also reduced and consequently the short-circuit current and/or fill factor [24],[25]. An accurate solar cell design is needed in order to optimize the trade-off between the improvement of the V_{oc} and the reduction of J_{sc} and FF. On the other hand, by reducing the area of the highly diffused regions, the dark saturation current of the doped areas could be also reduced significantly.

With this idea in mind our group at the UPC (MNT, Micro and Nanotechnologies) has carefully designed and simulated different rear point-contact patterns to be implemented in IBC solar cell, giving a first approximation to the fabrication of our first IBC solar cell [26],[27].

2.3 State-of the art of BC-BJ solar cells

The first BC-BJ silicon solar cell concept suggested by Schwarts and Lammert in 1975 (Stanford University) was originally focused for concentrator applications and the emitter and base were thermally diffused and arranged in an interdigitated pattern. This first version reported an efficiency of 17% under 50 suns concentration. An improved version of the point-contact cell of Swanson *et al.* where the backside diffusion were arranged in arrays of single points [22] was performed by Sinton *et al.* demonstrating an efficiency of 28.4% under 200 suns concentration [28] in 1987. The area of these cells was 0.15 cm^2.

The back-contact back-junction solar cell structure was also optimized for applications under one-sun illumination standard reporting in 1985 an efficiency of 21% [29]. One year later Sinton *et al.* introduced a point contact solar cell with 21.7%. King *et al.* presented a first medium-area (8.5 cm^2) point contact solar cell with the front and back surface field and a novel multi-level metallization scheme introduced by Verlinden *et al.* [30] [31]. In 1990 Sinton *et al.* presented a simplified back-side solar cell [32] in which the *self-aligment method* was applied [33] and the masking step was reduced to one. An efficiency of 21.9% was reported for a 10.5 cm^2 and one-sun illumination. Sunpower Corporation (founded in 1985) commercialized the back-contact silicon solar cells developed by the research group of Stanford University. In 1997 reported a new record one-sun efficiency of 23.2% resulting from the edge passivation and substrate doping improvements [34]. In 2004 Mulligan *et al.* presented a manufacture of large-area (149 cm^2) back-contact solar cells (A-300) with a 21.5% of efficiency [35]. New generation of a high volume production of the A-300 was introduced by De Ceuster *el al.* in 2007 [36].

Additionally to Stanford University and Sunpower, other groups have simultaneously been working on the high-efficiency back-contact back-junction solar cells devices. The Fraunhofer ISE processed a rear-contacted silicon solar cells with line contacts and photolithography masking reporting an efficiency of 22.1% [37]. From UNSW, Guo developed in 2004 the Interdigitated Backside Buried Contact (IBBC), a low-cost approach without the use of photolithography. A maximum one-sun efficiency of 19.2% was obtained [38]. Engelhart *et al.* from ISFH developed between 2006-07 a low-cost BC-BJ solar cells fabricated using a mask-free process in witch the laser ablation of Si and laser ablation of protective

coating were applied. 22% of efficiency was achieved on 4 cm^2 laboratory solar cell [39].

Interdigitated back contact solar cell has long been widely regarded and nowadays with silicon heterojunction (SHJ) technology has surpass the previous world record efficiency of 25% achieved in silicon single-junction solar cell [40]. Panasonic has recently reported a new record of 25.6% of efficiency combining the SHJ technique and IBC structure on 143.7 cm^2 [41]. The same year, Sharp also reported and efficiency of 25.1% on 4 cm^2 based on the same SHJ-IBC architecture [42]. Last Septembre (2016) Kaneka announced an efficiency of 26.3%. SunPower reported a 25.2% for its IBC solar cells using more standard surface passivation methods and manufactured on an industrial pilot line [43]. ANU/Trina and LG reported and efficiency of 24.4 and 23.4% respectively using thermal diffusion and SHJ technique in each case [44],[45]. Table 2.1 shows a summary of the state-of-the-art.

More than twenty years ago, our research group (MNT,UPC) started its adventure in the solar cell world. Among others, a research line of PERC-solar cells was developed, concluding with an excellent 21% of efficiency. The PERC solar cell developed was backside passivated with Al_2O_3 and rear contacted by laser processing [46]. Other important developments in $a-Si/a-SiC_x$, laser doping technique and heterojunction solar cells contributed to group solar cell knowledge.

Five years ago, the MNT group started its research in IBC-BJ solar cells. Since then, many focus of interest have opened different research lines. Conventional diffused IBC, "Hybrid" IBC, "Cool" IBC, IBC based on carrier-selective heterocontacts (TMO's, TiO_2, Tunnel oxides and alkaline metal salts). Today, an excellent 22% of efficiency have been obtained in conventional diffused IBC solar cells improved with a front surface black-silicon textured [47], a 20.8% efficiency in *n*-type "Hybrid" IBC [48]. The work of this thesis has contributed with a 18.8% of efficiency in *p*-type "Hybrid" IBC, with a 18% in our first "Cold" IBC [49] (laser IR) and with a 20% of efficiency in the last "Cold" IBC cells developed with UV laser.

Reported by	**Year**	**Junction type**	**Efficiency (%)**	**Others**
Schwartz and Lammert [8]	1975	Thermal Diffusion	17	Concentration (50 suns)
Swanson *et al.*[22]	1984	Point-contacts (Thermal diffusion)	19.7	Concentration (88 suns)
Verlinden *et al.*[29]	1985	Thermal diffusion	21	One-sun
Sinton *et al.*[50]	1986	Point-contacts (thermal diffusion)	27.5	Concentration (100 suns)
Sinton *et al.*[50]	1986	Point-contacts (thermal diffusion)	21.7	One-sun
Sinton *et al.*[33]	1988	Point-contacts (thermal diffusion)	28.4	Concentration (200 suns)
King *et al*[30]	1988	Point-contact	22.3	One-sun FSF multi-level metal
Sinton *et al.*[32]	1990	Self-aligment (thermal diffusion)	21.9	One-sun illumination

Reported by	**Year**	**Junction type**	**Efficiency (%)**	**Others**
King *et al.*[51]	1991	Point-contacts FSF multi-level metal	22.7	One-sun illumination
Verlinden *et al.*[34]	1997	Point-contacts (thermal diffusion)	23.4	One-sun illumination
Dicker (ISE) *et al.*[37]	2002	line contacts (thermal diffusion)	22.1	One-sun (illumination)
Guo (UNSW)[38]	2004	Buried contacts (thermal diffusion)	19.2	One-sun illumination
Mohr (ISE)[52]	2005	line contacts (thermal diffusion)	25	Concentration (100 suns)
Engelhart *et al* [39] (ISFH)	2006	Laser ablation (thermal diffusion)	22	One-sun illumination
ANU/Trina[44]	2013	Thermal diffusion	24.4	one-sun illumination

Reported by	**Year**	**Junction type**	**Efficiency (%)**	**Others**
Morris *et al.* [53] (IPV)	2013	Sputter and Diffusion Laser doping	22	One-sun illumination
Sharp[42]	2014	Carrier selective a-Si:H	25.1	One-sun illumination
Panasonic [41]	2014	Carrier selective a-Si:H	25.6	One-sun illumination
SunPower [43]	2014	Carrier selective type not disclosed	25.2	One-sun illumination

Table 2.1: State-of-the-art of Back-junction Back-contact c-Silicon solar cells

Once the IBC solar cells background have been defined, in the next section we focus our attention on the description of the experimental techniques mostly used in this work.

2.4 Experimental techniques

2.4.1 Cleaning and wet texturing

RCA cleaning

Contaminants on surface can act as recombination centers and diffuse when the substrate is submitted to high temperature process. Thus, the RCA cleaning sequence is fundamental before deposition process. Prior ALD dielectric deposition, TMAH texturing or any high temperature process (e.g. diffusion, thermal

oxidation) wafers are cleaned following a complete RCA sequence [54].
RCA cleaning consists in four steps:

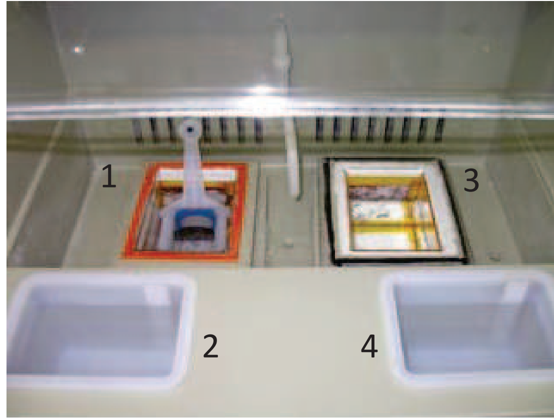

Figure 2.9: RCA cleaning sequence. Step 1: RCA1 cleaning. Step 2: SiO_2 etching. Step 3: RCA 2 cleaning. Step 4: SiO_2 etching

- 1. Base cleaning (RCA1), $H_2O(DI) : H_2O_2 : NH_3$ (5:1:1), at 70 °C. This step basically removes organic contaminants from the c-Si surface. After this first step wafers are cleaning under rising DI (deionized) water.

- 2. Silicon oxide etching. This layer is grown during the first step and it is removed dipping the wafer in diluted hydrofluoric acid at 1% for 1 minute

- 3. Acid cleaning (RCA2), $H_2O(DI) : H_2O_2 : HCl$ (6:1:1), at 70 °C. This bath removes heavy metals, alkali ions and metal hydroxides. After this third step wafers are again cleaning under rising DI water.

- 4. Silicon oxide etching. Again, SiO_2 is grown during the third step and it is removed submerging the wafer in hydrofluoric acid at 1% for 1 minute

The whole RCA sequence is no exactly followed in two steps of the fabrication solar cell process. In case of ALD process we leave the oxide grown ($\sim$ 15 Å) on the c-Si surface in the last chemical treatment because, from our experience, this film leads to a better interface than a H-terminated surface for its electronic passivation. In case of TMAH etching, samples only need to be cleaned following the two first steps of the total RCA sequence

Wet texturing

Reduction of light reflected from the solar cell surface is of paramount importance to get high efficiency devices. These reflection losses can be significantly reduced by application of the so-called antireflection coating (ARC) and/or texturing the c-Si wafer surface. Random pyramidal texturing is commonly achieved by chemical anisotropic etching in potassium hydroxide (KOH) or sodium hydroxide (NaOH) and isopropyl alcohol (IPA), but it can contaminate the surface with K+ and Na+ metal ions . To avoid this contamination, the non-pollutant and non-toxic alternative used in this work is tetramethyl ammonium hydroxyde (TMAH) and IPA used as a surfactant to diminish the adherence of hydrogen bubbles to the etched surface. Figure 2.10(a) illustrates how a pyramidal structure can reflect incident rays onto a neighbouring pyramid giving the photons two or more opportunities to be transmitted into the cell's absorber. Texture also helps absorption by increasing a cell 's capacity to “trap”reflected light from the rear surface of the silicon wafer [55].
Conditions applied in this experimental research for texturing c-Si surface are depicted in the following table. Texturing process is carried out in one silicon side while the other one remains protected by thermal SiO_2.

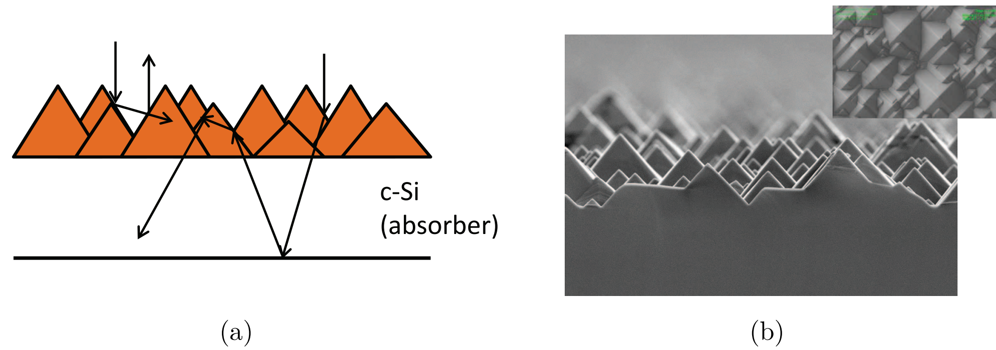

(a) (b)

Figure 2.10: (a) Schematic of light behavior towards textured front surface.(b) SEM image of resulted random pyramidal texturing

Process	Conditions	Results
Thermal oxidation	Temperature: 1060 °C t = 60 min	60 nm SiO_2 thickness
Protection side (If needed)	Photoresist SPR220 7.0 and Bake at 105 °C, 15 min	Side with photoresist protected from SiO_2 etching step
SiO_2 etching	NH_4F t = 2 min	SiO_2 removed from non-protected side
Stripping Photoresist (If needed)	Acetone and IPA ultrasonic bath and DI H_2O	Photoresist stripped
RCA1 cleaning	DI H_2O : H_2O_2 (30%): NH_3 (25%) 6 : 1 : 1 At 75 °C +Rising DI H_2O for 5 min and native SiO_2 etching in HF (1%) for 1 min	Wafer cleaning
TMAH etching	DI H_2O : TMAH (25%) : IPA 83 : 9 : 8 At 80 °C for 73 min	Random pyramids 6 μm height
SiO_2 etching (If needed)	NH_4F, t = 2 min	SiO_2 removed

Table 2.2: Complete sequence of random texturing surface

2.4.2 Thermal Atomic Layer Deposition, ALD

ALD system used for Al_2O_3 deposition is the Savannah S200 from Cambridge Nanotech and located at the ICFO (Institute of Photonic Science) clean room. ALD method relies on alternate pulsing of the precursor gases transported to the reactor where a primary vacuum has been done and where the substrate surface reacts with these precursors. These materials have to have a sufficiently high vapour pressure at the temperature of their vaporization and must not decompose thermally, neither at the vaporization temperature nor at the ALD growth temperature.

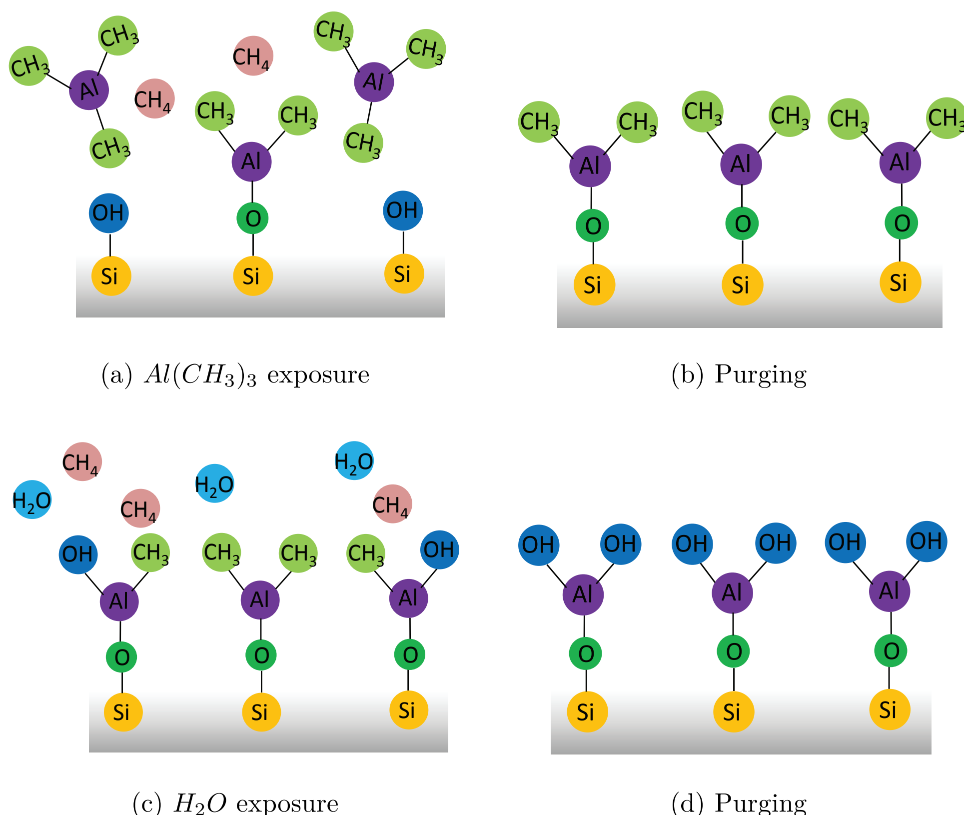

(a) $Al(CH_3)_3$ exposure (b) Purging

(c) H_2O exposure (d) Purging

Figure 2.11: Schematic illustration of one Al_2O_3 ALD reaction cycle

Four repeating steps define sequential self-terminating gas-solid reactions (one cycle) and provide conformal thin film with accurate and uniform thickness down to the nanometer range. Each self-terminating reaction is followed by a purge or evacuation step. Figure 2.11, illustrates one ALD reaction cycle for Al_2O_3 deposition. The sample in the reactor is hydroxilated from exposure to air. Vapour

H_20 is adsorbed on the surface and with silicon surface form: Si-O-H. The four steps defined in the reactor are: (a)Self-terminating reaction of the first reactant. A 0.05 sec pulse of trimethylaluminum ($[Al(CH_3)_3]$,TMA) (Al precursor) reacts with hydroxyl groups, -OH. (b) Then a 5 sec of purge or evacuation with inert N_2 removes the non-reacted TMA and gaseous reaction by-products (CH_4, Ammonia). (c) Self-terminating reaction of 0.015 sec of the second reactant (H_2O)(oxygen precursor) reacts with the dangling methyl groups on the new surface, creating aluminium-oxygen (Al-O) bridges an hydroxyl surface groups. (d) Finally a 5 sec of purge or evacuation with N_2 removes non-reacted H_2O and CH_4. The amount deposited per cycle (step 1 to 4) is expressed as *growth rate*, GPC (Growth per cycle) and is 1.1 Å. Reaction cycles are repeated until the desired amount of material has been deposited.

2.4.3 Plasma Enhanced Chemical Vapour Deposition, PECVD

Plasma-enhanced chemical vapour deposition is a subset of chemical vapour deposition techniques to deposit thin films from vapour phase to solid state on substrates. Process gas is decomposed aided (enhanced) by a plasma created by radio-frequency (13.56 MHz) discharge between two flat and parallel electrodes. In the frame of this work, RF PECVD from Elettrorava S.p.A was used to deposit intrinsic a-SiC_x, a-Si(n-type, doped with phosphorous) and stoichiometric a-SiC_x as antireflection coating using SiH_4, CH_4 and $SiH_4 + PH_3$ as precursor gases. As it is schematically illustrated at figure 2.12 the equipment consists of a Load-Lock chamber and one unique chamber reservoir physically separated by a high vacuum gate. The base pressure of each chamber is ensured by a turbomolecular pump, backed by a rotary vane pump. The substrate is placed in the load-lock chamber and it is evacuated by the pumping unit while the process chamber remain at $1 - 3 \times 10^{-6}$ mbar and at working temperature of 250 ^oC. Then the substrate is transferred into the process chamber by opening the high vacuum gate. In this chamber we introduce the process gas mixture via Mass Flow Controllers and the pressure is kept constant by a variable conductance valve. Gas is continually pumped out of the chamber so that a constant process pressure is maintained inside the reactor during the deposition. Plasma is then ignited between the upper and the lower electrode by an RF generator and

the process gas is decomposed in ions and radical which reacts on the sample depositing thin films. The process variables are shown in table 2.3.

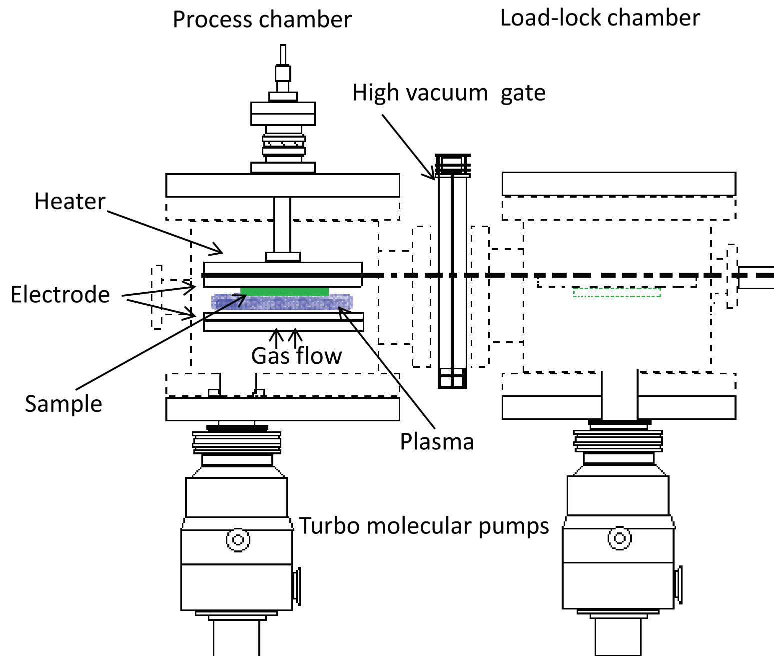

Figure 2.12: Schematic diagram of PECVD. The sample is placed in the load-lock chamber and driven to the process chamber

Film	Precursors	Temperature display/real ($500^oC/300^oC$) [sccm]	P[mbar]	Power [W]	Time	Result
a-SiC_x	SiH_4/CH_4	36/12	0.5	6	30"	∽ 4 nm Intrinsic layer
a-$Si(n-type)$	SiH_4/PH_3	36/4	0.5	6	2’	∽ 15 nm phosphorous doped a-Si
a-SiC_x	SiH_4/CH_4	1.2/60	1	18	9’	∽ 35 nm stoichiometric layer

Table 2.3: Deposition parameters of films deposited by PECVD.

2.4.4 Laser

During this thesis, laser processing has been used for locally doping p+ and n+ c-Si regions on IBC solar cells. The laser employed is a pulsed Nd-YAG lamp-pumped working at 1064 nm in nanosecond regime in TEM00 mode (Starmark SMP100 II Rofin-Baasel). Laser parameters such as power, pulse duration and number of pulses, are varied in order to find the conditions leading to the optimal electrical behavior of the formed junctions. The frequency is fixed to 4Khz and two different laser pulse duration: 100 ns and 400 ns. Regarding the beam characteristics, an objective lens with a focal length of 31.4 cm is used leading to a beam waist radius of 70 μm with a Gaussian profile and a round shape. All the experiments were performed at the same focal distance, as close as possible to the beam focus. The energy of the laser beam can be adjusted by varying the current intensity of the continuous lamp that pumps the Nd:YAG crystal. Power measurements are realized just before every surface treatment with a Ophir power meter F150 equipped with a thermal power sensor.

2.4.5 Characterization systems

Carrier lifetime measurement through photoconductance technique

The effective lifetime of photogenerated carriers quantifies the recombination rate occurring within a solar cell. Among them, non-contacting techniques are very useful to examine the surface recombination at passivated surface of partially processed samples, which are free of metal contacts. To generate the excess carrier density and measure their effective lifetime, optical sources such as laser, led arrays [56] or a simple flash-lamp [57] are used.
Photoconductance methods are based in the measurement of two parameters:

- Sample photoconductance, $\Delta\sigma$
- The light intensity

In this thesis, the effective lifetime was measured using the photoconductance tool WTC-120 commercialized by Sinton Consulting [57]. In this experimental setup (See Fig. 2.13), the measured c-Si sample is illuminated by a Xenon flash lamp generating the excess carriers within the sample which leads to an excess

of conductance. The photoconductance, $\Delta\sigma$, is measured contactless by using inductive coupling. At the same time, the light intensity is measured through a calibrated solar cell placed next to the measured sample. The excess carrier density, Δn, in the sample is calculated from $\Delta\sigma$. The electron-holes photogenerated within the sample under measurement can be estimated, $G_{ext}(t)$. Reflection losses of the sample are defined by an *effective optical transmission factor*, f_{opt}, to accurately determine $G_{ext}(t)$ from the light intensity that is monitored by the reference solar cell. After determination both Δn and G_{ext}, τ_{eff} can be calculated as a function of Δn using the following equation [57]

$$\tau_{eff} = \frac{\Delta n}{G_{ext} - \frac{d\Delta n}{dt}} \tag{2.5}$$

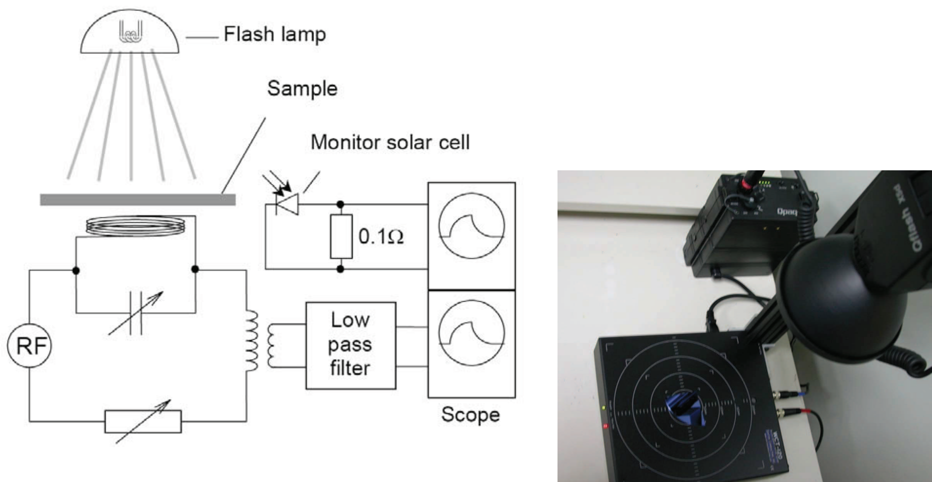

Figure 2.13: Schematic and image of the carrier lifetime measurement system (WCT-120) used in this thesis

This method operates in quasi-steady-state (QSS-PC) and photoconductance decay (PCD) regimes. The latter involves an abrupt pulse of illumination and subsequent determination of the excess carrier density without illumination. A very short flash ($\sim 15\ \mu s$) creates an excess carriers which recombines depending on recombination parameters of the bulk and surface. The advantage of this method is that the only magnitude needed is the photoconductance of the sample since $G_{ext} = 0$ (see equation 2.5). However relatively high τ_{eff} values are also required to obtain reliable values. In QSS-PC regime the intensity of the

illumination varies monotonically with time with a slow decay time ($\sim$ 2.3 ms). This allows the photogeneration rate to be balance by the total recombination within the sample at every instant of time sweeping a range of different injection levels.

Spectrophotometry measurement

Quantitative measurements of the reflection and transmission properties are necessary in order to characterize optical losses in solar cells. These parameters are measured as a function of wavelength in the 300 nm to 1200 nm range with UV-visible-NIR Spectrophotometer (Shimadzu 3600) equipped with ISR 3100 integrating sphere (Fig. 2.14) and UV-probe software.

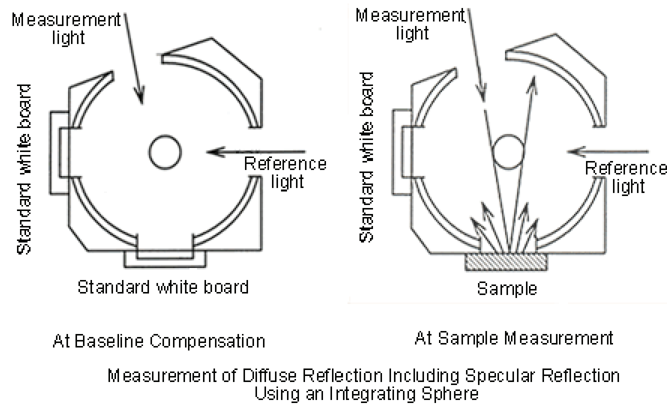

Figure 2.14: Schematic ISR 3100 integrating sphere. Total reflectance (diffuse and specular is measured by placing the sample 8° with respect to the incident light.

Reflectance measurements of the layers involved on the front surface IBC solar cell are performed by placing the sample in front of the incident light window, and concentrating the light reflected from the sample on the detector using a sphere with a barium sulfate-coated inside. The incident light is directed at the sample at an angle of 8°. The obtained value becomes the reflectance (relative reflectance) with respect to the reflectance of the reference standard white board, which is assumed to be 100%. Transmittance is measured by placing the sample under test in reference window and covering the other two with the standard white board. Spectrophotometers measure the light beam's intensity as a function of its wavelength.
Reflection and transmission measurements of the layer involved in our IBC solar cells front side have been done using this technique.

Thickness measurements. Ellipsometry

Ellipsometry is commonly used to determine optical properties and thickness of thin films. We use an Ellipsometer Plasmos SD for measuring refractive index and thickness of Al_2O_3 and a-SiC_x films (Chapter 3). The technique consist of measuring the change in polarization of the incident light upon reflection from a sample. A collimate beam of 632 nm wavelength is directed at the sample to measure. The system use a rotating analyzer to measure ellipsometric angles Ψ (related with the amplitude ratio after reflection) and Δ (phase shift) at the fixed wavelength. The obtained Ψ and Δ are compared with result of simulation to calculate film thickness and refractive index. The film thickness is determined by interference between light reflecting from the surface and light travelling through the film and reflecting from the surface between the thin film and the substrate. Figure 2.15 shows and schematic drawing of an ellipsometry setup.

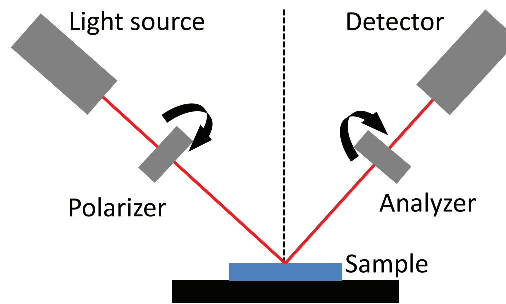

Figure 2.15: Schematic of ellipsometry setup

External Quantum Efficiency, EQE measurements

EQE is defined as the ratio of the collected carriers from a solar cell divided by the number of incident photons at every wavelength. The system used is QEX10 Model from PVmeasurement. It uses a xenon arc lamp source, monochromator, filters and reflective optics to provide a stable monochromatic light. The system wavelength range is 300 nm to 1200 nm and the beam spectral bandwidth can be obtained by adjusting the monochromator slits.

Before starting every measurement session, the system is calibrated with a reference photodiode to maximize accuracy. The measurement wavelength interval is selected at 10 nm. Light is modulated at 66 Hz by an adjustable mechanical

chopper. Figure 2.16 shows the schematic setup. The sample is also illuminated with a bias light to simulate end-use conditions and it is adjusted from 0.1 to 0.3 sun intensity. The measurement progress is monitored by means a graphical user interface. J_{sc} is also estimated using spectrum AM1.5G applying the following equation:

$$J_{sc} = q \cdot \int_{300}^{1200} EQE(\lambda) \cdot S(\lambda) \cdot d\lambda \tag{2.6}$$

where S (λ) is the irradiance using the spectrum AM1.5G.

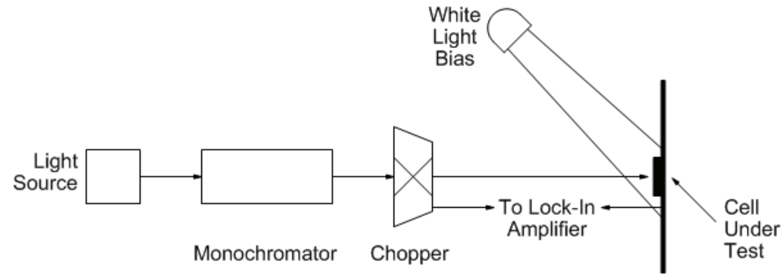

Figure 2.16: Schematic of External quantum efficiency setup

Bibliography

[1] A. Richter, S.W. Glunz, F. Werner, J. Schmidt, and A. Cuevas. Improved quantitative description of auger recombination in crystalline silicon. *Physical Review B: Condens. Matter Mater. Physc.*, 86:165202, 2012.

[2] M. Labrune. *Silicon surface passivation and epitaxial growth on c-Si by low temperature plasma processes for high efficiency solar cells.* PhD thesis, Ecole Polytechnique, 2011.

[3] C. Battaglia, A. Cuevas, and S. De Wolf. High-efficiency crystalline siliocn solar cells: status and perspectives. *Energy and Environmental Science*, 9: 1552–1576, 2016.

[4] T. Tiedje, E. Yablonovitch, G.D. Cody, and B.G. Brooks. Limiting efficiency of silicon solar cells. *IEEE Transactations on Electron Devices*, 5:711–716, 1984.

[5] R. Brendel. *Thin-Film Crystalline Silicon Solar Cells: Physics and Technology.* 2011.

[6] M.J. Kerr. *Surface, emitter and bulk recombination in silicon and development of silicon nitride passivated solar cells.* PhD thesis, 2002. URL `https://digitalcollections.anu.edu.au/handle/1885/47459`.

[7] J. Zhao, A. Wang, and MA. Green. 24.5% efficiency PERT silicon solar cells on SEH MCZ substrates and cell performance on other SEH CZ and FZ substrates. *Solar Energy Materials and Solar Cells*, 66:27–36, 2001.

[8] R.J. Schwartz. Silicon solar cells for high concentration applications. In *IEEE International Electron Devices Meeting, Washington D.C*, pages 350–352. IEEE, 1975.

[9] M. Green, K. Emery, Y. Hishikawa, W. Warta, and E. Dunlop. Solar cell efficiency tables (version 47). *Progress in Photovoltaics: Research and Applications*, 24:3–11, 2015.

[10] M. Green, K. Emery, Y. Hishikawa, W. Warta, and E. Dunlop. Solar cell efficiency tables (version 43). *Progress in Photovoltaics: Research and Applications*, 22:1–9, 2014.

[11] E. Van Kerschaver, R. Einhaus, J. Szlufcik, J. Nijs, and R. Mertens. A novel silicon solar cell structure with both external polarity contacts on the back surface. In *2nd World Conference Photovoltaic Energy Convers, Vienna, (Austria)*, pages 1479–1482, 1998.

[12] E. Lohmuller, M. Thanasa, B. Thaidigsmann, and F. Clement. Electrical properties of the rear contact structure of MWT silicon solar cells. *Solar Energy Materials and Sola cells*, 137:293–302, 2015.

[13] E. Lohmuller, B. Thaidigsmann, M. Pospischil, U. Jager, S. Mack, J. Specht, J. Nekarda, M. Retzlaff, A. Krieg, F. Clement, A. Wolf, D. Biro, and R. Preu. 20% efficient passivated large-area metal wrap through solar cells on boron-doped cz silicon. *IEEE Electron Device Letters*, 32:1719–1721, 2011.

[14] T. Benjamin, L. Michael, W. Andreas, C. Florian, B. Daniel, and P. Ralf. The path to industrial production of highly efficient metal wrap through silicon solar cells. *GREEN*, 2:171–6, 2012.

[15] W. Yin, X. Wang, F. Zhang, and L. Zhang. 19.6% cast mono-mwt solar cells and 268 w modules. In *38th Photovoltaic Specialists Conference (PVSC)*, pages 1–5. IEEE, 2012.

[16] M. W. P. E. Lamers, C. Tjengdrawira, M. Koppes, I. J. Bennett, E. E. Bende, T. P. Visser, E. Kossen, B. Brockholz, A. A. Mewe, I. G. Romijn, E. Sauar, L. Carnel, S. Julsrud, T. Naas, P. C. de Jong, and A. W. Weeber. 17.9% metal-wrap-through mc-si cells resulting in module efficiency of 17.0%. *Progress in Photovoltaics: Research and Applications*, 20:62–73, 2012.

[17] M.K. Mat Desa, S. Sapeaia, Sopiana K. Azharia, A.W., M.Y. Sulaimana, N. Amina, and S.H. Zaidia. Silicon back contact solar cell configuration: A pathway towards higher efficiency. *Renewable and Sustainable Energy Reviews*, 60:1516–1532, 2016.

[18] O. Nichiporuk, A. Kaminski, J. Kraiem, S. Quoizola, A. Fave, and M. Lemiti. Realisation of interdigitated back contacts solar cells on thin epitaxially grown silicon layers on porous silicon. In *19th Photovoltaic Specialists Conference (PVSC)*, pages 1127–1130. IEEE, 2004.

[19] R. Kühn, A. Boueke, M. Wibral, C. Zechner, P. Fath, G. Willeke, and E. Buchner. Investigation of the effect of p/n-junctions bordering on the surface of silicon solar cells. In *2nd WCPSEC, Vienna*, pages 1390–1393, 1998.

[20] A. Schonecker, A.W. Weeber, W.C. Sinke, C. Zechner, Kress A., and P Fath. Attacking limiting factors in 10 x 10 cm^2 multicristalline silicon, emitter wrap-through solar cell design and processing. In *2nd WCPSEC, Vienna*, pages 1677–1680, 1998.

[21] D.D. Smith and J.M. Gee. Review of back-contact silicon solar cells for low cost application. In *16th EPVSC, Glassgow*, pages 1104–1107, 2000.

[22] R.M. Swanson, S.K. Beckwith, R.A. Crane, W.D. Eades, Y.H. Kwark, R.A. Sinton, and S.E. Swirhun. Point contact silicon solar cells. *IEEE, Transaction on Electron Devices*, 32(5):661–664, 1982.

[23] R.M. Swanson. Point contact silicon solar cells. In *17th IEEE PVSEC*, pages 1294–1296, 1984.

[24] G. Stehelin, J.P David, F. Floret, and P. Verlinden. Comparison of the open-circuit voltage for point contact and linear contact ibc solar cells. In *7th EPVSC, Sevilla*, pages 865–869, 1986.

[25] P. Verlinden, F. Van De Wiele, G. Stehelin, F. Floret, and J.P David. High efficiency interdigitated back contact silicon solar cells. In *19th IEEE PVSEC, New Orleans*, pages 405–410. IEEE, 1987.

[26] D. Carrió, P. Ortega, I. Martín, G. López, J. M. López-González, A. Orpella, C. Voz, and R. Alcubilla. Rear Contact Pattern Optimization based on 3D Simulations for IBC Solar Cells with Point-like Doped Contacts. *Energy Procedia*, 55:47–52, 2014.

[27] J. M. López-González, I. Martín, P. Ortega, A. Orpella, and R. Alcubilla. Numerical simulations of rear point-contacted solar cells on 2.2 ohm.cm p-type c-si substrates. *Progress in Photovoltaics: Research and Applications*, 23:69–77, 2013.

[28] R.A. Sinton and R.M. Swanson. Design criteria for si point-contact concentrator solar cells. *IEEE, Transaction on Electron Devices*, 34(10):2116–2123, 1987.

[29] P. Verlinden, F. Van de Wiele, G. Stehelin, and J.P. David. An interdigitated back contact solar cell with high efficiency under concentrated sunlight. In *18th IEEE Photovoltaic Specialists Conference, Las Vegas*, pages 55–60, 1985.

[30] R.R. King, R.A. Sinton, and Swanson R.M. Front and back surface fields for point-contact solar cells. In *20th IEEE Photovoltaic Specialist Conference PVSEC, Las Vegas*, pages 538–544. IEEE, 1988.

[31] P. Verlinden, R.A. Sinton, and R.A. Swanson. High efficiency large area back contact concentrator solar cells with a multilevel interconnection. *International Journal of Solar Energy*, 6(6):347–366, 1988.

[32] R.A. Sinton and R.M. Swanson. Simplified backside-contact solar cells. *IEEE, Transaction on Electron Devices*, 37(2):348–352, 1990.

[33] R.A. Sinton, P. Verlinden, D.E. Kane, and R.M. Swanson. Development efforts in silicon backside-contact solar cells. In *8th European Photovoltaic Solar Energy Conference, EU-PVSEC, Florence*, pages 1472–1476, 1988.

[34] P.J. Verlinden, R.A. Sinton, K. Wickham, R.A. Crane, and R.M. Swanson. Backside-contact silicon solar cells with improved efficiency for the '96 world solar challenge. In *14th European Photovoltaic Solar Energy Conference, EU-PVSEC, Barcelona*, pages 96–99, 1997.

[35] W.P. Mulligan, D.H. Rose, M.J. Cudzinovic, D.M. De Ceuster, K.R. McIntosh, D.D. Smith, and R.M. Swanson. Manufacture of solar cells with 21% efficiency. In *19th European Photovoltaic Solar Energy Conference, EU-PVSEC, Paris*, pages 387–390, 2004.

[36] D. De Ceuster, P. Cousins, D. Rose, D. Vicente, P. Tipones, and W. Mulligan. Low cost, high volume production of $>22\%$ efficiency silicon solar cells. In *22nd European Photovoltaic Solar Energy Conference, EU-PVSEC, Milan*, pages 816–819, 2007.

[37] J. Dicker, J.O. Schumacher, W. Warta, and S.W. Glunz. Analysis of one-sun monocrystalline rear-contacted silicon solar cells with efficiencies of 22.1%. *Journal of Applied Physics*, 91(7):4335–4343, 2002.

[38] J.H. Guo, B.S. Tjahjono, and J.E. Cotter. 19.2% efficiency n-type laser-grooved silicon solar cells. In *31sth IEEE Photovoltaic Specialist Conference PVSEC, Orlando*, pages 983–986. IEEE, 2005.

[39] P. Engelhart, N.P. Harder, R. Grischke, A. Merkle, R. Meyer, and R. Brendel. Laser structuring for back junction silicon solar cells. *Progress in Photovoltaics: Research and Application*, 15:237–243, 2006.

[40] J. Zhao, A. Wang, M.A. Green, and F. Ferrazza. Novel 19.8% efficient "honeycomb "textured multicrystalline and 24.2% monocrystalline silicon solar cells. *Applied Physics Letters*, 73:1991–1993, 1998.

[41] K. Masuko, M. Shigematsu, T. Hashiguchi, D. Fujishima, M. Kai, N. Yoshimura, and T. *et al.* Yamaguchi. Achievement of more than 25% conversion efficiency with crystalline silicon heterojunction solar cell. *IEEE journal of photovoltaics*, 4(6):1433–1435, 2014.

[42] J Nakamura, N. Asano, T Hieda, C. Okamoto, H. Katayama, and K. Nakamura. Development of heterojunction back contact si solar cells. *IEEE journal of photovoltaics*, 4(6):1491–1495, 2014.

[43] D. Smith, P. Cousins, S. Westerberg, R. De Jesus-Tabajonda, G. Aniero, and Y-C. Shen. Toward the practical limits of silicon solar cells. *IEEE journal of photovoltaics*, 4(6):1465–1469, 2014.

[44] E. Franklin, K. Fong, K. McIntosh, A. Fell, A. Blakers, T. Kho, D. Walter, and D. *et al.* Wang. Design, fabricationand charactisation of a 24.4% efficient interdigitated back contact solar cell. *Progress in Photovoltaics: Research and applications*, DOI 10.1002 pip.2556, 2014.

[45] K.S. Ji, J. Syn, H.and Choi, H.M. Lee, and D. Tech. Digest Kim. In *21st International Photovoltaic Science and Engineering Conference, Fukuoka, Japan*, pages 3A–1O–06, 2011.

[46] P. Ortega, I. Martín, G. Lopez, M. Colina, A. Orpella, C. Voz, and R. Alcubilla. p-type c-Si solar cells based on rear side laser processing of Al_2O_3/SiC_x stacks. *Solar Energy Materials and Solar Cells*, 106:80–83, 2012.

[47] H. Savin, P. , Repo, G. von Gastrow, P. Ortega, E. Calle, M. Garín, and R. Alcubilla. Black silicon solar cells with interdigitated back-contacts achieve 22.1% efficiency. *Nature Nanotechnology*, 10:624–628, 2015.

[48] G. Masmitja, P. Ortega, I. Martín, G. López, and R. Voz, C.and Alcubilla. IBC c-Si(n) Solar Cells Based on Laser Doping Processing for Selective Emitter and Base Contact Formation. *Energy Procedia*, 92:956–961, 2016.

[49] G. López, G. Ortega, i: Marín, C. Voz, A. Orpella, and R. Alcubilla. "Cold" process for IBC c-Si solar cells fabrication. *Energy Procedia*, 92:652–660, 2016.

[50] R.A. Sinton, Y. Kwark, and R.M. Gan, J.Y. abd Swanson. 27.5 percent silicon concentration solar cells. *IEEE Electron Devices Letter*, EDL-7:567–569, 1986.

[51] R.R. King, R.A. Sinton, and R.M. Swanson. One-sun, single-crystalline silicon solar cell research. *Technical Report, Solid-State Electronics Lab.*, 1991.

[52] A Mohr. *Silicon concentrator cells in a two-stage photovoltaic system with a concentration factor of 300X*. PhD thesis, Universiät Freiburg, 2005.

[53] M. Dahlinger, B. Bazer-Bachi, Köhler J.R. Röder, T.C. and, R. Zapf-Gottwick, and J.H Werner. 22.0% Efficient laser doped back contact solar cells. *Energy Procedia*, 38:250–253, 2013.

[54] W. Kern and D. Puotinen. Cleaning solutions based on hydrogen peroxide for use in silicon semiconductor technology. *RCA review*, 31:187–206, 1970.

[55] K McIntosh and Luke P. Recombination at textured silicon surfaces passivated with silicon dioxide. *Journal of Applied Physics*, 105:124520, 2009.

[56] J. Schmidt and Armin G. Aberle. Accurate method for the determination of bulk minority-carrier lifetimes of mono- and multicrystalline silicon wafers. *Journal of Applied Physics*, 81:6186, 1997.

[57] Ronald A. Sinton and A. Cuevas. Contactless determination of current-voltage characteristics and minority-carrier lifetimes in semiconductors from quasi-steady-state photoconductance data. *Applied Physics Letters*, 69:2510, 1996.

Chapter 3

c-Si surface passivation by Al_2O_3 thin films

The improvement of the electrical quality of the c-Si surface is crucial in the development of high efficiency c-Si solar cells. This chapter introduces fundamental recombination mechanisms in c-Si and the conventional surface passivating films used in solar cells fabrication. The second part is focused on the study and optimization of Al_2O_3 film deposited by thermal-ALD used as passivating c-Si surface. The experimental is carried out depositing Al_2O_3 and $Al_2O_3/a-SiC_x$ stacks at different conditions on both random textured and polished surfaces. Optical properties are also measured and analyzed

3.1 Introduction

Generation in semiconductors is the process whereby electron-hole pairs are created. The implied energy comes from thermal activity, electrical excitation, or through the absorption of photons, as occurs in solar cells. *Recombination* is the opposite effect in which an electron from the conduction band is combined with a hole from the valence band and consequently a electron-hole pair is annihilated. This process liberates energy in form of photons or phonons. *Recombination rate*, U, quantifies this process and its minimization is crucial in high efficiency solar cell development. As the recombination rate decreases, the photo generated carries increase their contribution to the photo-current and therefore the *conversion efficiency* of the solar cell also increases.

Experimentally, the recombination rate can not be directly measured and instead it is used the *recombination lifetime* (τ) defined as the average time of a carrier between its generation and its recombination. This term is applied when the solar cell works under mid-injection or even high-injection conditions. Under low-injection conditions recombination lifetimes are referred to minority carriers and the term used is *minority carrier lifetimes*. In this thesis lifetime is studied for a wide range of injection conditions and we always use the term *recombination lifetime* to refer any carrier lifetime.

The relationship between recombination rate and lifetime is given by:

$$U = \frac{\Delta n}{\tau} \tag{3.1}$$

where Δn is the excess minority carrier density per unit volume and $\Delta n = n - n_0$ (n_0 is the minority carrier density under thermal equilibrium)[1].

3.2 Recombination in the bulk of c-Si

Under thermal equilibrium and at temperatures higher than absolute zero the recombination and thermal generation are equal and consequently the excess carrier density is zero. In the case of solar cells we are interested in study the device exposed to an external source of light. Assuming a constant light intensity and steady-state conditions, an excess carrier density is present in the semiconductor and for every recombination process a net recombination rate (U) can be defined as (3.1)

Three fundamental recombination mechanisms occur in the bulk of crystalline silicon (c-Si):

- Radiative recombination
- Auger recombination, and

[1] Δn can be referred to both electron or hole excess carrier density, since we assumed $\Delta n \cong \Delta p$ in quasi-neutral regions

- Recombination through defects in the bandgap, or Shockley-Read-Hall recombination

Radiative and Auger recombination are semiconductor intrinsic processes and therefore, unavoidable. Shockley-Read-Hall recombination (SRH) is an extrinsic recombination via defect states and hence it can significantly be reduced by improving the material quality. The use of high quality thin substrates considerably minimizes the recombination processes into the bulk. Therefore, the recombination at the silicon surface becomes dominant and the reduction of such surface recombination is a requirement for high efficiency solar cells development.
The total recombination rate within the bulk is defined as the sum of each recombination mechanisms:

$$U = U_{Rad} + U_{Aug} + U_{SRH} = \frac{\Delta n}{\tau_{Rad}} + \frac{\Delta n}{\tau_{Aug}} + \frac{\Delta n}{\tau_{SRH}} = \frac{\Delta n}{\tau_{bulk}} \tag{3.2}$$

The corresponding recombination lifetime can be calculated as:

$$\frac{1}{\tau_{bulk}} = \frac{1}{\tau_{Rad}} + \frac{1}{\tau_{Aug}} + \frac{1}{\tau_{SRH}} \tag{3.3}$$

3.2.1 Radiative recombination

Radiative or *band to band* recombination (U_{rad}) is the direct annihilation of an electron from the conduction band and a hole from valence band releasing the excess energy (energy close to that of the bandgap) as a photon [1], as schematically depicted in Fig. 3.1. This recombination mechanism in c-Si is a process with relative low probability due to the indirect band gap of c-Si and it is normally of minor importance for solar cells made with this material [2].
This recombination mechanism is dominant in direct bandgap semiconductor (e.g.,CdTe y GaAs) and depends on the density of electrons and holes, since one of each is needed in this process. The net recombination rate can be expressed by:

$$U_{rad} = \frac{\Delta n}{\tau_{rad}} = B\Delta n(N_{dop} + \Delta n) \tag{3.4}$$

where N_{dop} is the corresponding doping density (acceptor or donor) and B is the recombination radiative coefficient.
Accordingly to 3.1, τ_{rad} is defined as follow:

$$\tau_{rad} = \frac{1}{B(N_{dop} + \Delta n)} \tag{3.5}$$

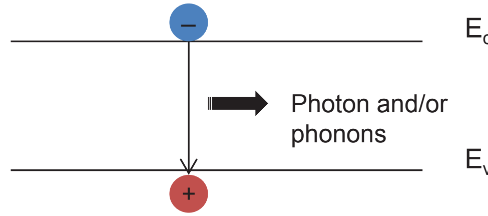

Figure 3.1: Radiative recombination in a semiconductor

In silicon, many authors have reported on the determination of this coefficient. At room temperature, Michaelis and Pilkuhn determined a $B = 1.7\times10^{-15} cm^3 s^{-1}$ [3], Ruff *et al.* a $B = 7 \times 10^{-15} cm^3 s^{-1}$ [4] and Schlangenotto *et al.* a $B = 0.95 \times 10^{-14} cm^3 s^{-1}$ [5]. More recently a complete study comes from the work done by T. Trupke *et al.*[6]. This paper include a discussion about the previous research and determined $B = 4.73 \times 10^{-15} cm^3 s^{-1}$

3.2.2 Auger recombination

Auger recombination is a three-particle interaction where an electron from conduction band recombines with a hole from valence band. The energy and momentum conservation are assured by a third particle (electron in the conduction band or hole in the valence band)[7], as it is shown in Fig. 3.2. The total Auger recombination U_{Auger} is given by:

$$U_{Auger} = C_n(n^2p - n_0^2p_0) + C_p(np^2 - n_0p_0^2) \tag{3.6}$$

where n(p) is the electron (hole) density, $n_0(p_0)$ the electron (hole) density at equilibrium and C_n, C_p are Auger coefficients.

Many works concerning the determination of these coefficients can be found

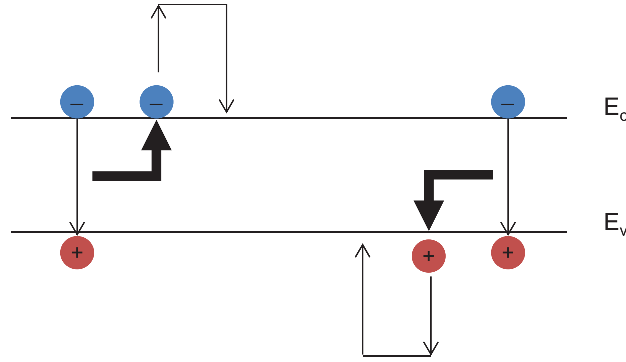

Figure 3.2: Auger recombination in a semiconductor

in the literature and one of the most commonly used value for the Auger coefficients are those determined by Dziewior and Schmid ($C_n = 2.8 \times 10^{-31} cm^6 s^{-1}$ and $C_p = 0.99 \times 10^{-31} cm^6 s^{-1}$) for silicon with a doping concentration higher than $5 \times 10^{18} cm^3$ [8]. Sinton and Swanson accurately measured C_a ($C_a = C_n + C_p$ is the ambipolar Auger coefficient) in the Δn range between 10^{15} and 2×10^{17} cm^{-3}, which was found to be 1.66×10^{-30} $cm^{-6} s^{-1}$.
A review of the various parametrizations can be found in [9] where a general parametrization based on experimentally determined minority carrier lifetime data is given by *Kerr and Cuevas* and reproduced here in equation 3.7. In this study the surface recombination is neglected and then limited by the quality of surface passivation. However, over the last years, surface passivation has significantly been improved which allows the investigation of the silicon bulk recombination with a better precision. A recently and more accurate study done by *Richter et al.* introduce an advanced parametrization for the intrinsic lifetime of crystalline silicon at 300K where empiric measurements of samples with very high surface passivation level and coulomb-enhanced Auger recombination are taken into account[10]. Equation 3.8 shows the simplified model for Auger lifetime for low dopant concentrations ($N_{dop} < 6\times^{16}$ cm^{-3}).

$$\tau_{Auger} = \frac{\Delta n}{np(1.8 \times 10^{-24} n_0^{0.65} + 6 \times 10^{-25} p_0^{0.65} + 3 \times 10^{-27} \Delta n^{0.8})} \qquad (3.7)$$

$$\tau_{Auger} = \frac{\Delta n}{np(8.7 \times 10^{-29} + n_0^{0.91} + 6 \times 10^{-30} p_0^{0.94} + 3 \times 10^{-29} \Delta n^{0.92})} \tag{3.8}$$

Auger recombination is typically the dominant intrinsic bulk recombination mechanism in solar cells. Both intrinsic recombinations (Auger and radiative) are dependent on the c-Si doping level and charge carrier density [9].

3.2.3 Recombination through defects in the bandgap , SRH

The presence of defects within the silicon crystal due to impurities or crystallographic imperfections creates a number of states within the bandgap. These defect levels act as carrier traps for free electrons or holes and greatly facilitate recombination through a two-step process resulting in the dominant mechanism in indirect bandgap semiconductors. The recombination happens when an electron from conduction band (or a hole from valence band) is trapped firstly at this defect level and then released to the valence band (or conduction band). There are four interactions between the defect center and the charge carrier as it can be seen in figure 3.3:

- 1. Capture of an electron from conduction band
- 2. Emission of an electron from defect level to conduction band
- 3. Capture of a hole from valence band
- 4. Emission of a hole from defect level to valence band

Carrier recombination does not happen when the charge carrier is released into the same band where it was captured. That is, when the electron is released to conduction band (step 1 and 2) or the hole is released to valence band (step 3 and 4).

Recombination through defects is an extrinsic process and was described by Shockley and Read [1] and Hall [11] in 1952. SRH recombination rate U_{SRH}, for a single defect level is described by the following equation:

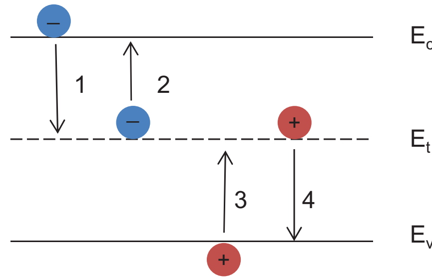

Figure 3.3: Four fundamental interactions between a charge carrier and a defect center with energy E_t

$$U_{SRH} = \frac{np - n_i^2}{\tau_{po}(n + n_t) + \tau_{no}(p + p_t)} \tag{3.9}$$

From equation 3.1, the SRH lifetime τ_{SRH}, can be expressed as:

$$\tau_{SRH} = \frac{\tau_{no}(p_o + p_t + \Delta n) + \tau_{p_o}(n_o + n_t + \Delta n)}{n_o + p_o + \Delta n} \tag{3.10}$$

where τ_{po} and τ_{no} are the fundamental hole and electron lifetime that can be defined in terms of the trap density at the energy level N_t (E_t), the mean thermal velocity $(v_n(v_p))$ and the capture cross section of the traps for electrons or holes $(\sigma_n(\sigma_p))$ as follow:

$$\tau_{n0} = \frac{1}{N_t \sigma_n v_n} \qquad and \qquad \tau_{p0} = \frac{1}{N_t \sigma_p v_p} \tag{3.11}$$

and n_t and p_t can be expressed as:

$$n_t = n_i e^{\frac{E_t - E_i}{KT}} \qquad and \qquad p_t = p_i e^{\frac{E_i - E_t}{KT}} \tag{3.12}$$

where E_i is the intrinsic Fermi level

We must underline that when the defect is close to E_i level, i.e. close to the midgap, the SRH recombination will be the highest one. Contrariwise, if the defect energy is located close to conduction or valence band (shallow defects), the defect will act more like a trap for electrons or holes rather like a recombination center. These shallow defects become more active at high-injection level.

Finally, all these recombination processes lead to a total effective bulk lifetime previously described at the equation 3.3.

Figure 3.4, shows the Auger, radiative and SRH recombination lifetime as a function of the excess carrier density, Δn (injection level) for 2.5 Ωcm n- and p-type substrates used in this thesis (a and b respectively) corresponding to a donor density of $1.88 \times 10^{15}\ cm^{-3}$ and a acceptor density of $5.7 \times 10^{15}\ cm^{-3}$. The resulting τ_{bulk} is also shown is black line. To calculate τ_{rad} and τ_{Auger} equation 3.5 the constant value $B = 4.73 \times 10^{-15}\ cm^3 s^{-1}$ and 3.8 have been used. In the case of τ_{SRH}, we consider one defect located in the middle of the bandgap ($E_t = E_i$) and $\tau_{n0} = \tau_{p0} = 2.5$ ms [12]. The radiative lifetime is constant at low injection, but then decreases and continues decreasing as the injection level increases. At high injection depends on the inverse of the carrier density ($\tau_{rad} \propto \frac{1}{\Delta n}$). Auger lifetime depends on the inverse of the carrier density squared ($\tau_{Auger} \propto \frac{1}{\Delta n^2}$) and hence it shows a stepper slope with the injection level than τ_{rad}. In fact, Auger recombination is dominant in highly doped c-Si, e.g. in emitters) and under light concentration.

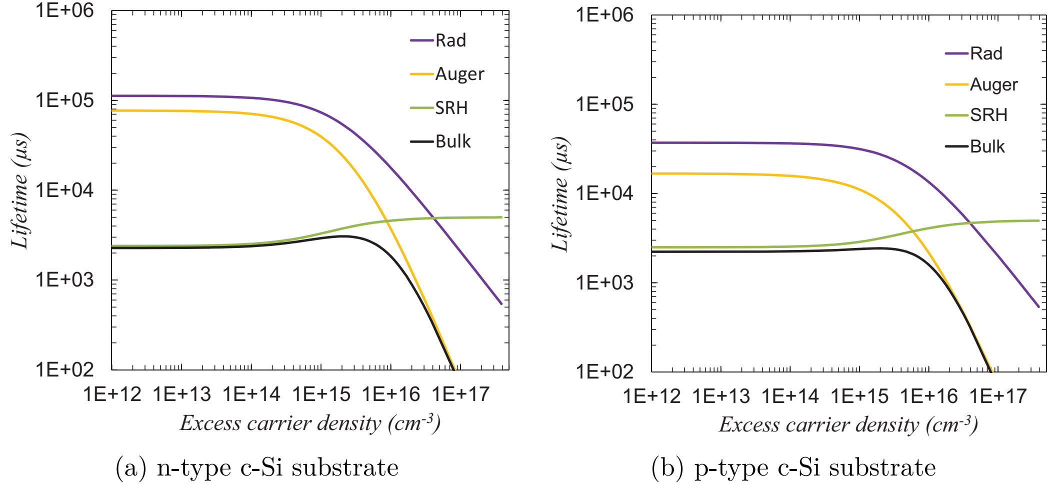

(a) n-type c-Si substrate

(b) p-type c-Si substrate

Figure 3.4: Fundamental recombination mechanism in the bulk of a *n*-type and *p*-type c-Si substrate at 300 K ($n_i = 9.65 \cdot 10^9\ cm^{-3}$, $\rho_{p-type} = \rho_{n-type} = 2.5\ \Omega cm$, $\tau_{n0} = \tau_{p0} = 2.5ms$)

3.3 Recombination at c-Si surface

The continuity of the crystal lattice is completely lost at the surface of any crystalline material [13]. The large number of partially bonded silicon atoms gives rise to many dangling bonds and therefore, a high amount of defect states are present within the bandgap leading to a high recombination rate. Recombination at c-Si surface can be described similar as bulk SRH recombination by replacing the bulk carrier density by the surface carrier density. The net recombination rate per unit area, can be defined as follow:

$$U_s = \frac{n_s p_s - n_i^2}{\dfrac{n_s + n_1}{S_{po}} + \dfrac{p_s + p_1}{S_{no}}} \tag{3.13}$$

where n_s and p_s are the concentrations of electrons and holes at the surface ($n_s = \Delta n_s + n_o$, $p_s = \Delta n_s + p_o$), and S_{po} and S_{po} are related to the density of surface states per unit area, N_{st}, the capture cross-sections, σ_p and σ_n and thermal velocity, v_{th} for the specific defect as follow:

$$S_{no} \equiv \sigma_n v_{th} N_{st} \qquad \text{and} \qquad S_{po} \equiv \sigma_p v_{th} N_{st} \tag{3.14}$$

Equation 3.13 shows that surface recombination depends on the properties of the surface states, on the injection level and on the doping density. The energy level of the defects dependence is the same to the Shockley-Read-Hall lifetime. Surface recombination can be characterized by the surface recombination velocity in cm/s, S, as:

$$U_s = S\Delta n_s \tag{3.15}$$

where Δn_s is the minority carrier density at the surface. An electric field is usually found at c-Si surface and Δn_s could be far away from Δp_s since the electric field creates large differences between n_s and p_s [14]. Hence, an effective surface recombination velocity, S_{eff}, is defined as:

$$U_s = S_{eff}.\Delta n \tag{3.16}$$

where $\Delta n \cong \Delta p$ is the minority carrier density at the quasi-neutral bulk region and easily measured by changing the illumination level.

The surface recombination is the dominant recombination mechanism in silicon and the reduction of such parameter, i.e. surface passivation, is of paramount importance to maintain the minority carrier high and achieve high efficiency solar cells.
There are two fundamental passivation mechanisms:

- Reducing the density of the interface states
- Modifying the relative concentration of photogenerated electrons and holes near the surface.

Saturation of defects

The high amount of defects at the surface can be reduced by saturating the remaining silicon dangling bonds. This strategy represents the direct reduction of S_{no} and S_{po} described by equation (3.13). By depositing or growing an appropriate dielectric layer over the c-Si surface, $D_{it}(E)$[2] is decreased and consequently

[2]Instead of N_{st}. $D_{it}(E)$ defines a density of states as function of energy level. There is a large number of levels within the bandgap, each of them with a determinated density and capture cross-section

U_s. This strategy is more sensitive to the presence of defects at the silicon surface than the field effect passivation.

Modification of the photogenerated carriers

When the population of the two types of carriers (electrons and holes) is equal, the recombination rate at the surface is maximum. This strategy consists of reducing one type of carriers at the interface by shielding the action of one type of carriers and therefore strongly reduce the recombination rate. This can be achieved by doping the semiconductor surface to repel the minority carriers such as in an emitter region or a back-surface-field (BSF). Another strategy consists in depositing or growing a charged film which also repels one type of carriers, electrons or holes depending on the type of fixed charge in the overlying dielectric film.
The films employed in solar cells for passivating the c-Si surface use a combination of both passivating strategies and usually is achieved by dielectric material (SiO_2, SiN_x, SiC_x, Al_2O_3) or semiconductor such a a-Si:H.

3.4 The Effective lifetime of c-Si

The total losses in the c-Si bulk and at the c-Si surface results in the so-called effective lifetime of the minority charge carriers (τ_{eff}) and can be experimentally measured. In general, the recombination processes can be considered to occur independently and the total recombination is the sum of the individual recombination mechanisms and therefore:

$$\frac{1}{\tau_{eff}} = \frac{1}{\tau_{bulk}} + \frac{1}{\tau_{surface}} \tag{3.17}$$

where the first term correspond to:

$$\frac{1}{\tau_{bulk}} = \frac{1}{\tau_{rad}} + \frac{1}{\tau_{Auger}} + \frac{1}{\tau_{SRH}} = \frac{1}{\tau_{int}} + \frac{1}{\tau_{SRH}} \tag{3.18}$$

where τ_{int} is the intrinsic recombination parameter combining both Auger and radiative mechanisms.

A c-Si sample symmetrically passivated with identical dielectric film the τ_{eff}

can be written as:

$$\frac{1}{\tau_{eff}} = \frac{1}{\tau_{bulk}} + \frac{2S_{eff}}{W} \tag{3.19}$$

where W is the c-Si sample thickness.
In all the experiments performed in this thesis Float Zone silicon wafers of very high quality are employed. Therefore, the presence of defects within the bulk is extremely low and the corresponding SRH lifetime will be assumed to be infinite. Consequently, expression 3.19 can be simplified as follow:

$$\frac{1}{\tau_{eff}} = \frac{1}{\tau_{int}} + \frac{2S_{eff}}{W} \tag{3.20}$$

From this expression, we can extract the maximum surface recombination ($S_{eff,max}$) assuming the bulk lifetime as infinite.

$$S_{eff,max} = \frac{W}{2 \times \tau_{eff}} \tag{3.21}$$

Equation 3.21 will be the expression used in this thesis and it results from the effective lifetime measurements using the photoconductance technique explained in section 2.4.5.

3.5 State-of-the-art of c-Si surface passivation

In the 1980s an intense research and development in the field of passivation layers was carried out due to the successful implementation of passivating layers for high-efficiency devices (higher than 20%). According to their main passivation mechanism these layers can be divided into three groups:

- Thermally grown silicon dioxide (SiO_2)
- Amorphous silicon based compounds: Amorphous hydrogenated silicon nitride (a-SiN_x:H), silicon carbide(a-SiC_x:H) and intrinsic amorphous silicon (i a-Si:H)
- Aluminum oxide (Al_2O_3)

3.5.1 Thermally grown silicon dioxide, SiO_2

It is the state-of-the-art surface passivation layer on lightly doped *n*- and *p*-type c-Si. It was the passivation layer employed for the first solar cells with efficiencies higher than 20%. On highly doped *n*-type c-Si (e.g. n^+ emitter) the level of surface passivation results excellent [15]. However, the passivation quality of *p*-type emitters is poorer [14].

The excellent surface passivation achieved with this film is mainly attributed to high quality of the c-Si/SiO_2 interface that reduces the density of states at the interface ($\sim 10^9 cm^{-2}eV^{-1}$). In addition, positive charge densities within the dielectric layer (up to $10^{11}cm^{-2}$) [2],[16] cause a weak field effect passivation [17] and contribute to lead to S_{eff} values as low as 2 cm/s (substrate *n*-type) and 12 cm/s (*p*-type) [18]. Due to the positive sign of these charges, electron are drifted to the c-Si surface and holes are rejected. As a consequence, at the surface of low resistivity p-type c-Si and p-type emitters, electron density equals hole density resulting in an increasing in surface recombination.

The high quality interface is due to the fact that thermal SiO_2 is grown onto the silicon wafer by oxidation at elevated temperatures (1000-1100 °C) guaranteeing an unaffected final interface by initial c-Si surface conditions. A post-deposition anneal in H_2 atmosphere further improves the electrical passivation by supplying H to the interface. Another method is the deposition of a sacrificial/structural Al film in the SiO_2 followed by a anneal process at 400 °C typically. This so-called *Alneal* generates atomic hydrogen, which effectively reduces the Si/SiO_2 interface states density [14].

The high growth temperatures employed are the main limitation for the application thermal SiO_2 as passivating layer requiring high purity c-Si to avoid significant bulk time degradation [19]. Moreover, the high temperature is a clear disadvantage from production cost and throughput point of view. On the other hand, the SiO_2 refractive index (1.47) is rather low to be applied as single antireflection coating on the front side of c-Si solar cells.

3.5.2 Amorphous silicon-based compounds

Between such compounds we can find amorphous silicon (a-Si), silicon nitride (a-SiN_x), silicon carbide (a-SiC_x). Deposition conditions of these layer strongly affects the optical and electronic properties. High content of silicon presents strong optical absorption in visible-ultraviolet range and when the content of Si is low, light absorption and conductivity decrease, thus exhibiting transparency and very good dielectric properties.
Methods based on decomposition of hydrogenated gases are usually used ensuring a high content of hydrogen that improves the surface passivation by saturating dangling bonds. Plasma excitation systems are the most widespread methods.

Amorphous silicon nitride, $a - SiN_x : H$

Extensive research has been led during last decades to produce silicon nitride with excellent surface passivation properties. The positive fixed charge density is particularly beneficial in the passivation of *n*-type c-Si as the minority carriers (i.e. holes) are effectively shielded from c-Si surface and wherein an accumulation of majority carriers takes place. A substantial problem of a-SiN_x passivation layers with their high built-in positive charge is that they yield inversion layers for low-doped *p*-type c-Si which can lead to a parasitic shunting between contacts [20]. S_{eff} as low as 6 cm/s and 22 cm/s have been reported on 1.5 Ωcm *n*-type and 1 Ωcm *p*-type passivated by a-SiN_x:H, respectively [21].

In order to reduce this shunting effect, some authors suggest the use of a thin SiO_2 layer between Si and SiN_x [22]. Thermally grown SiO_2/SiN_x stacks provide a high level of passivation due to a low interface density [23],[24]. The combination of such stacked films on *p*-type, 1 Ωcm wafers resulted in S_{eff} values lower than 3 cm/s. More recently, low-temperature SiO_x/a-SiN_x synthesized by plasma enhanced chemical vapor deposition (PECVD) has demonstrated a good alternative to thermal oxidation and very low S_{eff} has been obtained (i.e. 6 cm/s and 11 cm/s for *n*- and *p*-type c-Si on 3.5 Ωcm and 2.2 Ωcm respectively)[25].

Apart from its excellent passivation properties, silicon nitride shows two more advantages:

- Its refractive index can be widely tuned in the range of 1.9 to 2.3 controlled by the quantity of Si within the layer. More quantity of Si involves higher

refractive index. The available range allows to use SiN_x as optimum anti-reflection coating (ARC) with n = 1.9 [26]. Schmidt *et al.* showed that films with a refractive index equal to 2.1 enhanced the effective lifetime after a short treatment at 900°C, while the index was slightly higher (n=2.4) and therefore more rich in silicon, the tendency was inverted [27],[28].

- SiN_x deposited by PECVD is characterized by high quantity of hydrogen. During annealing steps, atomic hydrogen can diffuse into the c-Si bulk passivating its bulk defects

Amorphous silicon carbide, a-SiC_x:H

Amorphous silicon carbide (a-SiC_x:H) is a feasible process that has shown very good passivation results and good antireflection coating properties. Refractive indexes in the range 2.25-2.7 and a widely tunable band gap 1.5-3 eV, have been reported [29], [22]. Optical characteristics strongly depend on film and can be tuned by quantity of carbon in the film [30]. Surface passivation is dependent on hydrogen content which promotes saturation of dangling bonds. Silicon-rich films have yielded S_{eff} values at 1 sun-illumination below 3 and 2 cm/s on 1 Ωcm on *p*- and *n*-type c-Si , respectively [31]. Dopability (n or p), thermal and mechanical stability are other qualities of a-SiC_x. It is widely deposited by (PEVCD) technique through the decomposition of silane (SiH_4) and methane (CH_4) gases and can be doped by phosphorous or boron phosphine (PH_3) or diborane (B_2H_6) gases, respectively. Phosphorus-doped amorphous silicon carbide (a-$SiC_x : H(n)$)has also demonstrated the ability to passivate p-type c-Si substrates and highly doped n-type emitters in solar cells [32].

Our research group (Micro and Nanotechnology, MNT at UPC) has extensively explored the c-Si passivation properties of a-$SiC_x : H$ films deposited by PECVD with excellent results on p- and n- type c-Si [30], [32], [33]. More recently phosporous-doped silicon carbide stack has successfully implemented as passivating layer and dopand source at the rear side of heterojuntion solar cell [34], [35] and DopLA (Doped by Laser) concept [36]. Stoichiometric a-SiC_x has also been applied as capping layer (ARC) on the rear side of *p*-type PERC c-Si solar cell. In the second part of this chapter, we focus on the optical study results obtained from stoichiometric a-SiC_x implemented as ARC deposited on Al_2O_3 layers.

Amorphous silicon, a-Si:H

This material has been widely studied for several applications in the microelectronics industry and effectively exploited in the HIT (Heterojunction with Intrinsic Thin-layer) c-Si solar cell developed by Sanyo electric Co. a-Si:H has demonstrated an excellent level of c-Si surface passivation and it has also been used as active part in solar cells.

The principle of passivation of amorphous silicon is based on defects saturation, like silicon oxide. To provide such low interface states density good hydrogenation of the interface is critical. However, if the substrate temperature is too high hydrogen effusion may occur due to its high mobility, leaving dangling bonds at the interface and therefore decreasing the surface passivation quality.

a-Si:H film is produced from decomposition of silane (SiH_4), with optional addition of molecular H_2. The films can be *n* or *p*-type doped by introducing phosphine (PH_3) or diborane (B_2H_6) together with silane.

Effective surface recombination velocities of around 2 to 5 cm/s were typically shown in literature deposited by PECVD technique [37], [38],[39]. [40].

The main challenge in the application of a-Si:H in solar cell devices is related to its relatively low thermal stability and its high absorption in the UV part of the solar spectrum. To reduce optical losses, thickness should be kept as low as possible when applied at the front of c-Si solar cells. Moreover, optical properties of a-Si:H are not optimal when is applied at the rear side.

3.5.3 Aluminum oxide, Al_2O_3

The main difference of Al_2O_3 in comparison to other passivation schemes is its high fixed negative charge density Q_f ($10^{12} - 10^{13}\ cm^{-2}$) located at Al_2O_3/Si interface which produces effective field-effect passivation by shielding electrons from the interface [41]. Moreover, the significant reduction in the interface defect density D_{it} ($10^{10} - 10^{12} eV^{-1} cm^{-2}$) during post-deposition annealing is vital for c-Si surface passivation performance. Hydrogen content around 2-3% seems to play an important role in passivating defects at the Si/SiO_x interface which is formed when Al_2O_3 is applied on an H-terminated Si surface.

Al_2O_3 has demonstrated a good alternative for passivating both lightly and highly doped *n*- and also *p*-type c-Si substrates [42],[43],[44]. S_{eff} values below

3 cm/s have been achieved depositing Al_2O_3 by Atomic Layer Deposition (ALD) system.

Al_2O_3 layers are essential in the developing work of this thesis. Special attention will be paid in the next section where experiments will be focused on the study of the passivation quality and optical properties of Al_2O_3 films deposited by thermal ALD (explained in detail in chapter 2). Deposition temperature, film thickness, annealing temperature and time have been analyzed in order to know how these parameters affect surface passivation quality.

3.6 c-Si surface passivation by Al_2O_3 thin films

3.6.1 Introduction

Back-contact solar cells exhibit some advantages over the conventional solar cell with metal contact on the front side (see chapter 5 for more details). However, there are also some challenges related to its fabrication and structure. Due to the fact that both emitter and base metal contacts are placed on the back cell side, the photo generated carriers need to diffuse through the wafer thickness before be collected by the contacts. Then high minority carrier diffusion lengths are required. As a rule of thumb it can be assumed that the diffusion length of the minority carriers should be at least four times greater than the wafer thickness in order to allow high efficiencies in IBC solar cells [45]. High front surface recombination velocities (S_{front}) due to a poorly passivated front surface and/or low minority carrier lifetime in the bulk (τ_{bulk}) cause carrier losses by recombination. Therefore, (S_{front}) and (τ_{bulk}) are the two most critical parameters to achieve high-efficiency solar cells.

In this section we optimize Al_2O_3 films deposited by thermal ALD to obtain low surface recombination velocity. We study the influence of the deposition temperature from 150 to 250 ^oC and the post-annealing treatments needed to activate the surface passivation. We also analyze the surface passivation of $Al_2O_3/a{-}SiC_x$ stacks on both p-type and n-type polished and textured c-Si substrates. Different thicknesses of Al_2O_3 are deposited at 200 ^oC and complemented up to a total

thickness of 75 nm (corresponding to the optimum antireflection coating, ARC) with a-SiC_x film deposited by PECVD. Both passivation and a high-quality ARC plays a vital role in high efficiency solar cells [46]. We experimentally determine the optimum thickness of the stack for photovoltaic applications by minimizing reflection losses over a wide wavelength range (300-1200 nm), without compromising the passivation properties of Al_2O_3 films. The effective surface recombination velocity (S_{eff}) is calculated from the measured effective lifetime (τ_{eff}) by applying the quasi-steady-state photo-conductance (QSS-PC) method and assuming an infinite bulk lifetime leading to an upper limit of the surface recombination velocity ($S_{eff,max}$). This parameter is evaluated at a carrier injection level corresponding to 1-sun illumination. In order to assess the optical properties, a UV-VIS-NIR spectrometer equipped with an integrating sphere was used to measure the diffuse and specular reflection and absorption spectra (See section 2.4.5) of our antireflection stacks.

3.6.2 Influence of the ALD deposition temperature and annealing treatment (time and temperature) on surface recombination velocity

Samples processed for determining the surface recombination velocity are FZ *p*-type c-Si with a resistivity of 2.5± 0.5 Ωcm and 290 μm thickness. Prior ALD deposition films, the silicon samples are cleaned using a RCA sequence as it was explained in section 2.4. Once the substrate is in the reactor, it is preheated at the deposition temperature for 5 min before the ALD process starts. 50 nm of Al_2O_3 is deposited on both sides at 150, 200 and 250 ^oC. After deposition, samples are annealed 20 minutes in H_2/N_2 atmosphere at different temperatures (300, 350, 375, 400 and 435 ^oC). Additionally, annealing time is varied (10, 20 and 30 min) in order to evaluate its impact on surface passivation quality. $S_{eff,max}$ is calculated before and after annealing from equation 3.22 using the effective lifetime (τ_{eff}) measured by quasi-steady-state photoconductance (QSSPC) technique and assuming infinite bulk lifetime.

$$S_{eff,max} = \frac{W}{2 \times \tau_{eff}} \tag{3.22}$$

where W is the substrate thickness. The obtained results are shown in figure 3.5

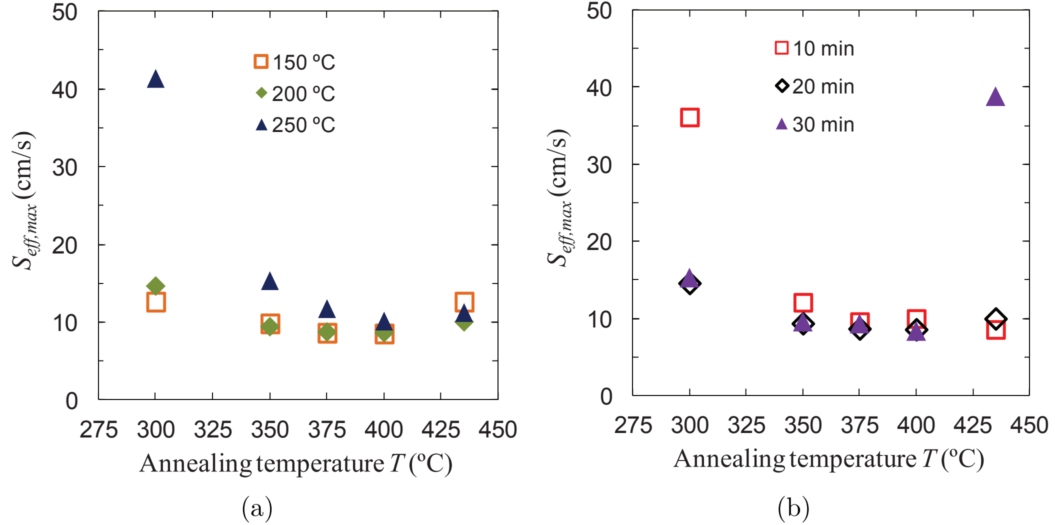

Figure 3.5: (a) $S_{eff,max}$ as a function of the annealing temperature from 300 to 435 °C for 20 min. 50 nm of Al_2O_3 layers are symmetrically deposited at 150, 200 and 250 °C. (b) $S_{eff,max}$ as a function of the annealing temperature from 300 to 435 °C and different times (10, 20 and 30 min). 50 nm of Al_2O_3 layers are symmetrically deposited at 200 °C.

Before annealing, the $S_{eff,max}$ measured was $\sim$ 480 cm/s, $\sim$ 90 cm/s and $\sim$ 45 cm/s in the samples deposited at 150, 200 and 250 °C respectively. After the annealing process all the samples show a strong improvement of their passivation quality. As it can be seen in the graph 3.5a the best level of surface passivation is achieved in the samples processed at 150 and 200 °C followed by an annealing step from 350 to 400 °C range obtaining a $S_{eff,max} < 10$ cm/s. Analyzing the annealing time, samples processed between 350 and 400 °C for 20 and 30 minutes exhibited the best result presenting a $S_{eff,max} < 10$ cm/s corresponding to a τ_{eff} of $\sim$ 1.7 ms (at 1 sun) (figure 3.5b).

The high surface passivation quality after annealing step can be explained by a local reconstruction of Al_2O_3 at the interface which increases the negative built-in charges. The fixed negative charge density, Q_f, shields the minority carrier (electrons) unbalance the number of electrons and holes resulting in exceptional low surface recombination velocities. Previous works have demonstrated that Al_2O_3 films contain a high fixed negative charge density in the order of $10^{12} - 10^{13}$ cm^{-2} [43],[47],[48],[49],[50]. Furthermore, chemical passivation at the $c - Si/Al_2O_3$ interface provided by the diffusion of hydrogen from the bulk of the Al_2O_3 layer,

reduces defect related recombination [47],[48],[49],[50],[51] improving even more the passivation.

Another important fact that should be mentioned is the blistering effect detected at the samples processed at 150 °C followed by a post-annealing temperature higher than 350 °C and at the remaining samples annealed above 435 °C (Figure 3.6). This effect consists of the partial delamination of the Al_2O_3 film and the corresponding bubble formation is attributed to the local accumulation and release of gaseous hydrogen and/or H_2O from the layer upon thermal treatments above a critical temperature [52],[53],[54]. The higher the annealing temperature is, the higher the bubble density and bubble radii are. Despite the blistering phenomenon in some samples, effective lifetime measurements still evidenced a good passivation quality after the annealing step.

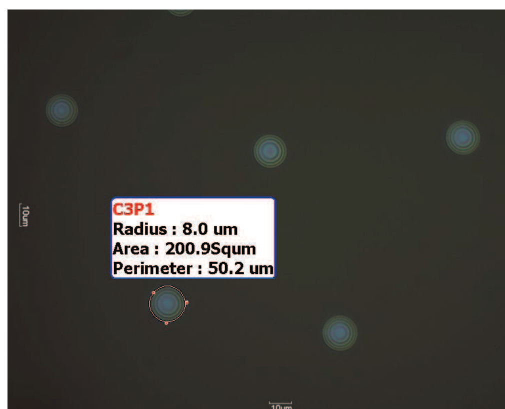

Figure 3.6: Optical microscope images of the blistering effect. The sample with 50nm of Al_2O_3 was deposited at 150 ^oC. Image shows bubbles of 8 μm radius and 200 $bubbles/mm^2$ density

3.6.3 Influence of Al_2O_3 thickness on surface recombination velocity

Influence of Al_2O_3 thickness on the passivation quality is also studied. Samples under test are ALD processed at 200 °C and 1.4, 6.5, 14, 25 and 50 nm (corresponding to 13, 59, 127, 227 and 455 cycles) of Al_2O_3 are deposited after a RCA cleaning. Then, the samples are annealed at different temperatures and time. $S_{eff,max}$ results are displayed in Figure 3.7.

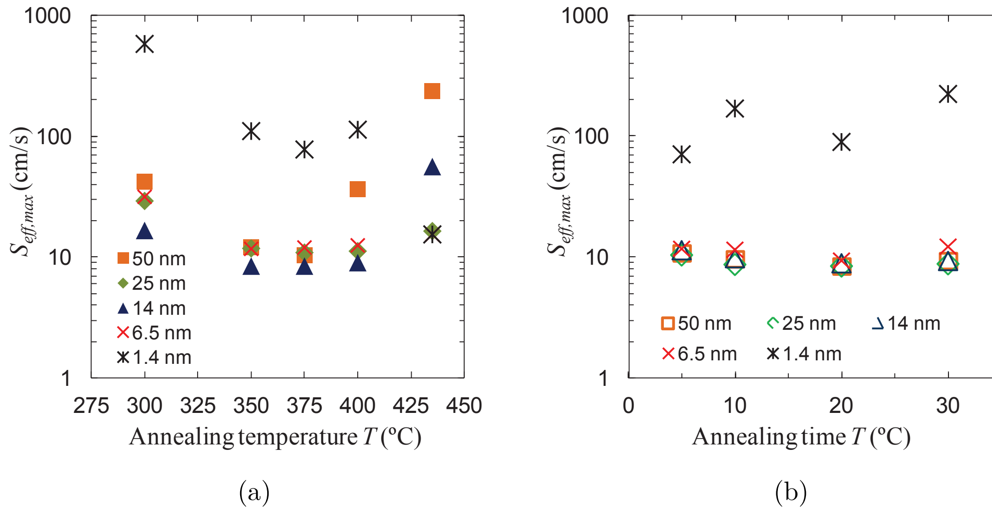

Figure 3.7: (a) $S_{eff,max}$ as a function of the annealing temperature from 300 to 435 ^oC and different Al_2O_3 thicknesses. Al_2O_3 is deposited at 200 ^oC and annealed for 20 min.(b) $S_{eff,max}$ as a function of the annealing time (5 to 30 min) and for different Al_2O_3 layer thicknesses, deposited at 200 ^oC and annealed at 375 ^oC.

Results show a clear relationship between the passivation quality, the annealing temperature and the thickness of the Al_2O_3 layer. Excellent $S_{eff,max} < 10$ cm/s is obtained for 6.5, 14, 25 and 50 nm annealed from 350 to 400 ^oC, while the worst results is found for the thinnest Al_2O_3 layer (1.4 nm). This behaviour can be attributed to a deterioration of the chemical passivation (i.e high surface state densities) for very thin layers. Since the fixed negative charges are located at the interface between the Al_2O_3 and c-Si, field-effect passivation would be likely less affected by the thickness [55].

Regarding the impact of the annealing time in the passivation quality, from 3.7b we can observe that there are no significant differences in $S_{eff,max}$ in the samples annealed from 5 to 30 min and thicknesses higher than 6.5 nm. The lowest $S_{eff,max}$ (~ 8 cm/s) was achieved for the sample with 25 nm of Al_2O_3 and annealed for 20 min. However, the sample deposited with 1.4 nm of Al_2O_3 layer the $S_{eff,max}$ is clearly higher for all the annealing time tested showing values beyond 100 cm/s.
In the samples with thicknesses below 25 nm blistering is not observed and neither in any of the other samples annealed below 435 °C.

In order to evaluate the minority diffusion length, the τ_{eff} at $\Delta n = 1 \times 10^{15}$ is

chosen as a reference. The effective lifetime of the minority carriers is measured for the sample symmetrically passivated with 50 nm Al_2O_3 deposited at 200 °C and annealed at 375 °C for 20 min. Result is presented in figure 3.8.

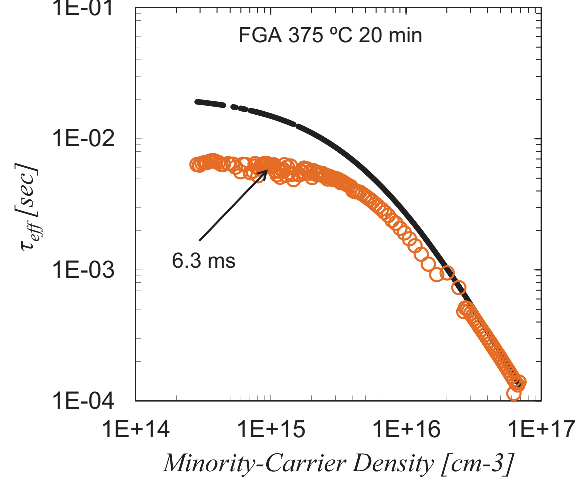

Figure 3.8: Minority carrier lifetime of c-Si (p-type) sample symmetrically deposited with 50 nm of Al_2O_3 at 200 ^oC and annealed at 375 ^oC for 20 min (rounded shape). Intrinsic lifetime applying simplified model parametrization of *Richter et Al.* is also shown (black line)

Effective minority diffusion length the L_{eff} is related to the carrier lifetime by the diffusivity according to:

$$L_{eff} = \sqrt{D \times \tau_{eff}} \tag{3.23}$$

where D is electron diffusivity and is equal to 30.59 cm^2/s. Then, L_{eff} for p-type FZ c-Si with base resistivity of 2.5 $\Omega.cm$ symmetrically deposited with 50 nm of Al_2O_3 is 4389 μm. Thus, c-silicon material selected is of very high quality and suitable for processing high-efficiency IBC solar cells

We conclude that remarkably low $S_{eff,max}$ 10 cm/s and $\tau_{eff} > 1,7$ ms are achieved for a wide range of variables, i.e. Al_2O_3 layer thicknesses from 6.5 to 50 nm range deposited at 200 °C and annealed between 350 and 400 °C for the explored times (5, 10, 20 and 30 min). Similar results are also obtained at 150 °C and 250 °C process temperature for the 50 nm Al_2O_3 film. For the lowest deposition temperature we can observe a blistering phenomenon after the annealing process at temperature higher than 350 ^oC, but the passivation quality

is not apparently affected. It is also important to highlight that a good passivation level is achieved ($S_{eff,max} < 100\ cm/s$) for ultra-thin Al_2O_3 layers ($\backsim$ 1.4 nm).

3.6.4 $Al_2O_3/a-SiC_x$ surface passivating stacks. Experimental

In the previous experiment, we showed that Al_2O_3 on p-type polished c-Si substrates annealed between 350 and 400 °C (< 435 °C) from 10 to 20 min is enough to obtain an excellent passivation . The aim of this experimental is to complement the preceding work studying the surface recombination velocity on both n- and p-type polished and randomly textured wafers passivated with Al_2O_3/a-SiC_x stacks as well as their optical characterization. The reason to include the stoichiometric a-SiC_x as capping layer on Al_2O_3 is because it has been demonstrated that it improves the laser contact formation on p-type c-Si solar cells in comparison to the typical Laser Fired Contact (LFC) process [56],[57]. Additionally, SiC_x layer is needed for chemical protection purposes of the Al_2O_3 films in cleaning/etching steps during the IBC fabrication process.

Samples under test where symmetrically deposited with 25, 35, 50 and 90 nm of Al_2O_3 and complemented up to 75 nm total with stoichiometric $a-SiC_x$ deposited by PECVD. As exception, the sample with 90 nm of Al_2O_3 will be evaluated without the extra capping layer as a reference of antireflection without SiC_x. Test structures are shown in Figure 3.9.

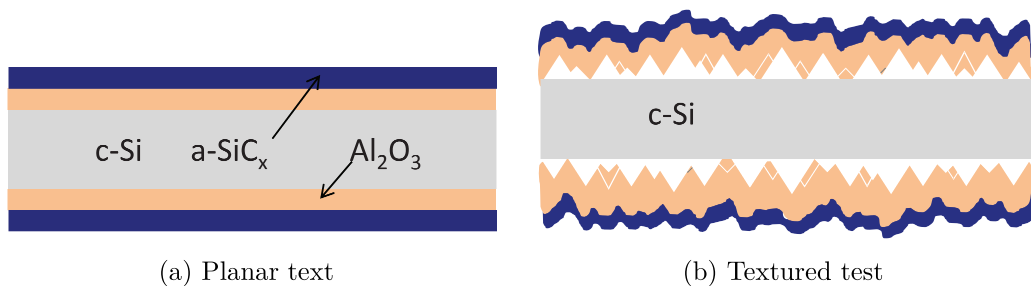

(a) Planar text (b) Textured test

Figure 3.9: Symmetrical test structures for the measurements of τ_{eff}

The experimental starts with four FZ c-Si wafers (4 inches). Two are p-type and two n-type. For both types the resistivity is about 2.5± 0.5 Ωcm and 280 μm thickness. One p-type and one n-type wafers are both side randomly textured

after RCA cleaning[3] (see conditions in Table 2.2). Then, all of them are cut in four quarters and cleaned following the RCA sequence. Al_2O_3 film is deposited on both sides at 200 ^oC followed by an stoichiometric carbon rich $a-SiC_x$ as capping layer deposited on both sides by PECVD (See 2.3 table conditions). The thickness of the layers are achieved changing the process time while the rest of conditions remain unchanged. Finally, an annealing at 425 ^oC for 10 min in a N_2/H_2 ambient activates the passivation. The following table displays a summary of the samples.

c-Si		Al_2O_3 **(nm)**	$a-SiC_x$ **(nm)**
p-type	Polished and Textured	25	50
		35	40
		50	25
		90	-
n-type	Polished and Textured	25	50
		35	40
		50	25
		90	-

Table 3.1: Samples properties for surface passivation and optical characterization .

Passivating characteristics of the $Al_2O_3/a-SiC_x$ stacks are tested after Al_2O_3 deposition, $a-SiC_x$ deposition, and after the final annealing process (Figure 3.10). Moderate $S_{eff,max}$ values are achieved for as-deposited Al_2O_3 layers with better results on polished than on randomly textured samples. This level of surface passivation can be explained by the relatively low D_{it} ($\sim 10^{11}$ $eV^{-1}.cm^{-2}$)) prior to the annealing step [58],[54], which is responsible for the chemical passivation.

Higher $S_{eff,max}$ values are obtained for textured samples. The reason is the increased surface area due to the pyramid-shaped texturation and the large D_{it} value on the exposed [111] planes [59],[60],[61]. After the $a-SiC_x$ deposition by PECVD, it is observed a general improvement of the $S_{eff,max}$. Values close to 10 cm/s are achieved on polished *n*- and *p*-type samples. This effect can be attributed to a partial in-situ annealing effect that takes place in the PECVD chamber (deposition temperature T_{dep} = 300 °C). Textured samples show also an important improvement of $S_{eff,max}$ values. However, it seems that this in-situ

[3] Samples that are TMAH etched only need to complete the two first steps of the total RCA cleaning

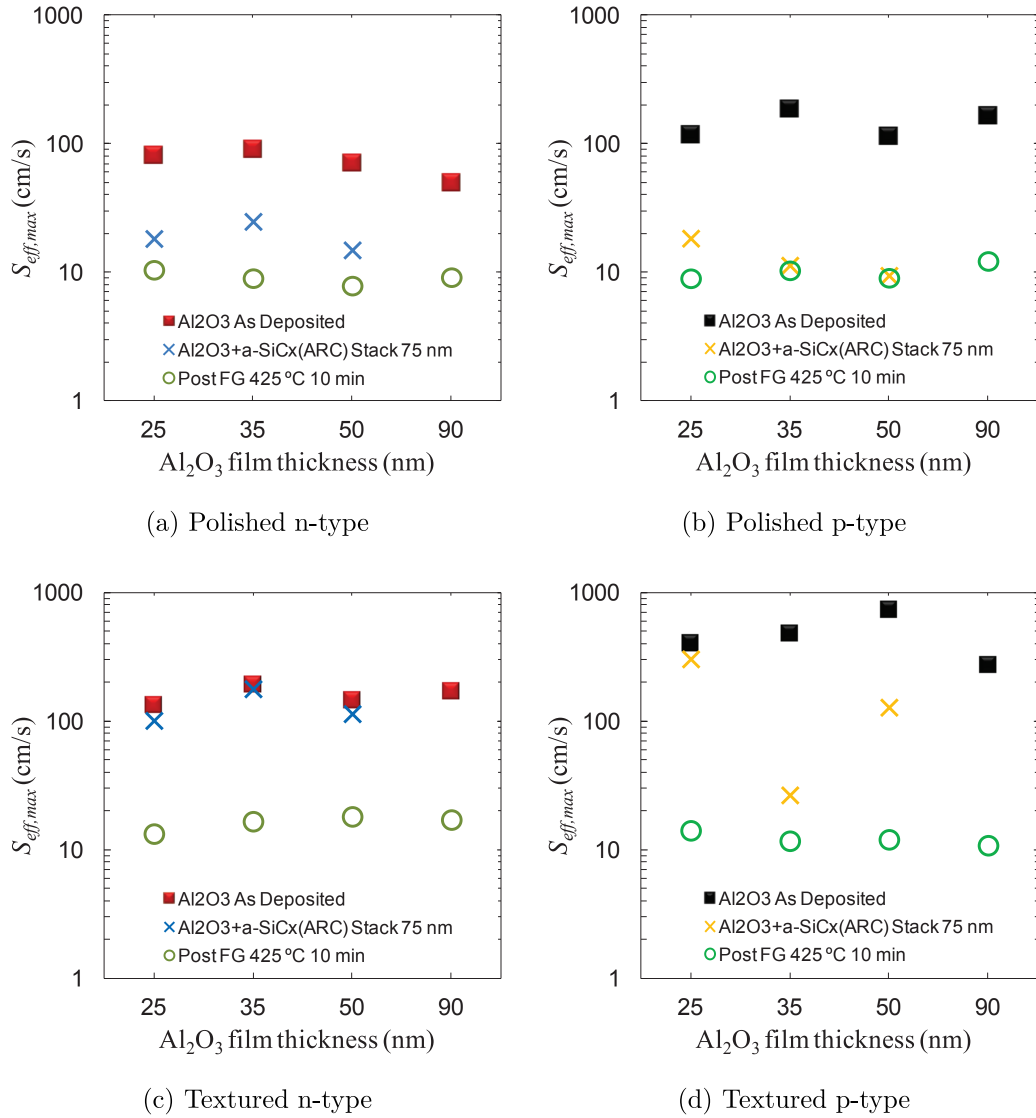

(a) Polished n-type

(b) Polished p-type

(c) Textured n-type

(d) Textured p-type

Figure 3.10: Surface recombination velocity, $S_{eff,max}$ (cm/s). (a) and (b) calculated values for n and p-type polished samples respectively. (c) and (d) calculated values for for n and p-type randomly textured samples respectively. $S_{eff,max}$ was determined at 1-sun injection level as a function of the Al_2O_3 thickness. Al_2O_3 layers were complemented up to 75 nm with an $a-SiC_x$ film. The sample with 90 nm of Al_2O_3 is shown as a reference

annealing is not enough to totally activate the passivation of textured samples. The final annealing step at $T_{ann} = 425$ °C for 10 min leads to a further improvement of the surface passivation of all samples. As a result, outstanding $S_{eff,max}$ values of less than 15 cm/s, i.e. τ_{eff} (1 sun) > 1.3 ms, are achieved independently of doping type and surface morphology. We have to point out that the randomly

textured sample require higher annealing temperatures (425 °C) than polished ones to achieve similar $S_{eff,max}$.

The previous experimental demonstrates that T_{ann} = 375 °C is enough to activate the surface passivation on polished substrates. In fact, some polished samples already showed an optimum passivation quality just after the PECVD process due to the in-situ annealing. On the other hand, an annealing of 425 °C is the critical limit to avoid a blistering effect, which we have previously observed on polished samples with Al_2O_3 films.

Regarding the effect of the film thickness, it is interesting to note that a rather constant high level of surface passivation is obtained after the annealing of the whole range of Al_2O_3 thicknesses with $a-SiC_x$ capping layer agreeing with the study realized in previous section with only Al_2O_3 . It can be deduced that fixed negative charges located at the interface between Al_2O_3 are not affected by the introduction of the additional layer.

3.6.5 $Al_2O_3/a-SiC_x$ stacks. Optical characterization.

Optical losses in IBC solar cells are heavily reduced due to the absence of the metal finger grid on the front side. However, there are still other remaining optical losses that include surface reflectance and film parasitic absorption.

In order to achieve an optimal conversion efficiency of IBC solar cells the application of a so-called antireflection coating (ARC) in combination with surface texturing techniques plays an important role in reducing reflection losses [62]. The minimum reflectance should be located at about $\lambda = 600$ nm where the maximum photon flow for spectrum AM 1.5g occurs.

In this study, the antireflection behaviour of the different combinations of Al_2O_3 and Al_2O_3/ stoichiometric a-SiC_x stack deposited on c-Si substrates proposed in the previous section is evaluated.

Refractive index is measured by ellipsometry resulting in
$n_{Al_2O_3} = 1.6$ and $n_{a-SiC_x} = 2.0$. Simple simulations demonstrate that the optimum thickness for the total stack is 75 nm. Figure 3.11 shows the simulated reflectance for three thickness combinations on polished c-Si surface.

Reflectance measurements corresponding to samples described in Table 3.1 are measured with UV-VIS-NIR spectrometer equipped with an integrating sphere over the wavelength range from 300 to 1200 nm. These measurements are taken after the Al_2O_3 deposition and after $a-SiC_x$ deposition. Both results are pre-

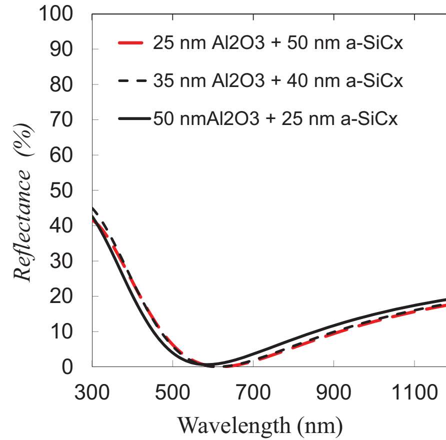

Figure 3.11: The graph shows the simulated reflectance of double layer antireflection coating. Different thickness of Al_2O_3 and a-SiC_x are displayed resulting in a total stack thickness of 75 nm. Source *www.pveducation.org/pvcdrom/design/dlarc*

sented in Figure 3.12. It must be mentioned that no significant differences were found between *n*- and *p*-type c-Si substrates.

As it can be observed the textured sample without ARC exhibits an integrated reflectance average of 13.3%, much lower than that of polished c-Si substrates. For a randomly textured surface, the reduced reflection is explained by a second reflection of the incident light at the side walls of an opposite pyramid [63]. After coating the silicon substrates, optical reflectance was further reduced in all cases. When a single layer antireflection coating covers the polished c-Si samples (Graph 3.12a) the reflectance yields to a minimum of 3.2% at 600 nm wavelength in case of 90 nm thick quickly increasing for wavelengths shorter and longer. Furthermore, reflectance properties are worse as the film thickness decreases. However, when the single layer ARC is deposited on textured c-Si samples reflectance is strongly reduced (Graph 3.12b). We can observe a flattering response of the reflectance curves on the whole studied range. The values measured are $< 2\%$ from 460 nm to 1000 nm when a textured c-Si sample is coated by 90 nm of Al_2O_3. Reflectance slightly increases when ARC thickness decreases.

When 75 nm of double-layer antireflection coatings are deposited on c-Si samples (polished (Graph 3.12c) and textured (Graph 3.12d), the whole range of reflection measurements are clearly lower (the total stack have the optimum thickness). In the case of textured samples, reflectance is lower than 2% from 460 nm to 1050 nm for all the stack configurations.

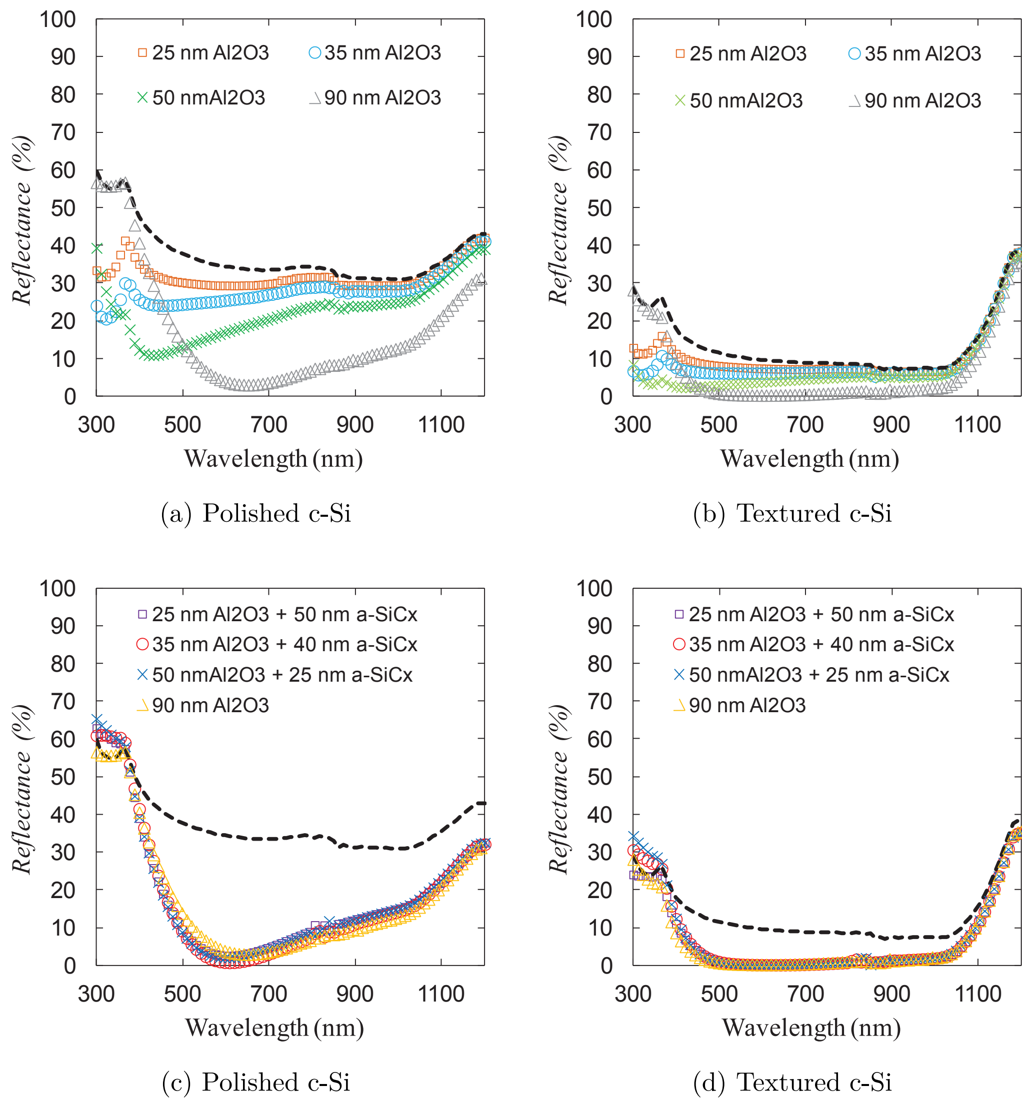

(a) Polished c-Si

(b) Textured c-Si

(c) Polished c-Si

(d) Textured c-Si

Figure 3.12: Reflectance curves of Al_2O_3 coated on (a)polished c-Si and (b) randomly textured c-Si for different film thickness. Reflectance curves of $Al_2O_3/a-SiC_x$ coated on (c) polished c-Si and (d) randomly textured c-Si (d). As a reference, bare polished and textured c-Si reflectance is also included (black line). Samples do not include a back reflector scheme.

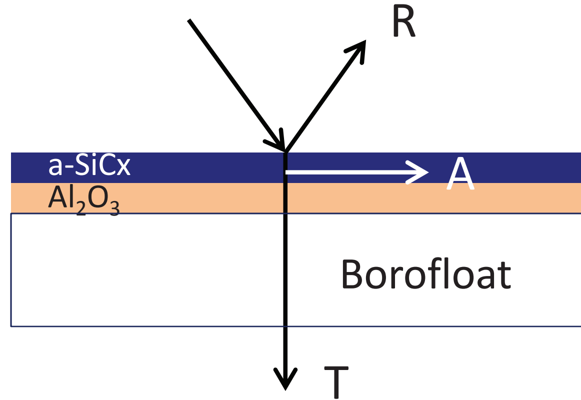

Figure 3.13: Borofloat test structure for absorbance measurements

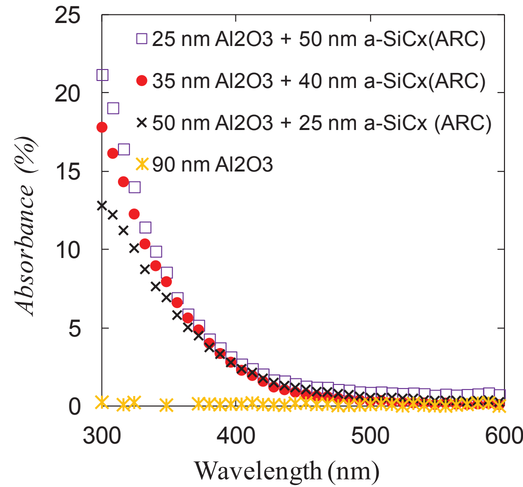

Figure 3.14: Absorbance as a function of the wavelength in the range of 300 to 600 nm of different stacks configurations and 90 nm Al_2O_3.

Absorbance is another optical parameters studied in order to know the quantity of light absorbed by the $Al_2O_3/a-SiC_x$ stacks. To do so, borofloat substrates are one side deposited with the different stacks configurations and analysed between 300 to 600 nm range (Figure 3.13). The absorbance stack is calculated from the reflectance and transmittance measurements and the results are shown in figure 3.14.

Other works have previously reported an optical bandgap of $E_{opt} = 6.4 \pm 0.1$ eV for as-deposited and annealed ALD Al_2O_3 films [54], which means that this material is transparent for wavelengths above 200 nm. Therefore, absorption of light by the Al_2O_3 layer does not occur in the wavelength range relevant for

photovoltaic applications. This property is experimentally confirmed by the 90 nm Al_2O_3 sample results (see figure 3.14). For the sake of clarity, only the 300 to 600 nm wavelength range is depicted, i.e. where a relevant absorbance can exist. However, it can be seen that as the $a-SiC_x$ layer thickness increases, the optical absorbance also increases up to a value of 21.1% at 300 nm. Then, the SiC_x capping layer is less attractive to be used as an antireflection layer on the illuminated side of the solar cell compared to a single 90 nm Al_2O_3 film.

3.7 CONCLUSION

Al_2O_3 layers and $Al_2O_3/a-SiC_x$ stacks with different thickness were deposited on polished and randomly textured *p*- and *n*-type c-Si substrates by combining thermal ALD and PECVD technique. Outstanding $S_{eff,max}$ values below 15 cm/s were achieved independently of the surface morphology and doping type of the samples. This value is low enough to obtain highly efficient c-Si IBC solar cells.

Concerning the optical properties, the absorbance of Al_2O_3 layers with different thickness and also of different $Al_2O_3/a-SiC_x$ stacks was calculated by evaluating reflectance and transmittance measurements. We found that optical losses due to the absorption of $a-SiC_x$ layers in the range of short wavelengths is the reason for the superior overall optical performance of a single 90 nm thick Al_2O_3 film. Therefore, the latter represents the better option as an antireflection coating compared to $Al_2O_3/a-SiC_x$ stacks. This result is supported by the reflectance measurements of Al_2O_3 films with different thickness and $Al_2O_3/a-SiC_x$ stacks on polished and textured c-Si substrates in the wavelength range from 300 to 1200 nm. In any case, the measured reflectance was less than 2% for all the $Al_2O_3/a-SiC_x$ stacks and also for the single 90 nm layer of Al_2O_3. Nevertheless, an $a-SiC_x$ capping layer could be useful if the Al_2O_3 layer needs to be protected from some chemical treatment during the solar cell fabrication. Moreover, on the rear side of a c-Si solar cell, where the optical absorbance is not critical, an $a-SiC_x$ layer on top of the passivated Al_2O_3 film acts as a back reflector that reflects photons towards the c-Si bulk. This $a-SiC_x$ capping layer on the Al_2O_3 also improves the laser contact formation on c-Si solar cells.

Bibliography

[1] W. Shockley and W. Read. Statistics of the recombinations of holes and electrons. *Physical Review*, 87:835–842, 1952.

[2] Armin G. Aberle. *Crystalline Silicon Solar Cells: Advanced Surface Passivation and Analysis.* 1999.

[3] W. Michaelis and M. H. Pilkuhn. Radiative recombination in silicon p-n junctions. *physica status solidi (b)*, 36:311–319, 1969.

[4] M. Ruff, M. Fick, R. Lindner, U. Rössler, and R. Helbig. The spectral distribution of the intrinsic radiative recombination in silicon. *Journal of Applied Physics*, 74:267–274, 1993.

[5] H. Schlangenotto, H. Maeder, and W. Gerlach. Temperature dependence of the radiative recombination coefficient in silicon. *Physica Status Solidi (a)*, 357(21):357–367, 1974.

[6] T. Trupke, M. A. Green, P. Wurfel, P.P. Altermatt, A. Wang, J. Zhao, and R. Corkish. Temperature dependence of the radiative recombination coefficient of intrinsic crystalline silicon. *Journal of Applied Physics*, 94: 4930–4937, 2003.

[7] A. Hangleiter and R. Häcker. Enhancement of band-to-band auger recombination by electron-hole correlations. *Physical Review Letters*, 65:215–218, 1990.

[8] J. Dziewior and W. Schmid. Auger coefficients for highly doped and highly excited silicon. *Applied Physics Letters*, 31:346, 1977.

[9] M. Kerr and A. Cuevas. General parameterization of auger recombination in crystalline silicon. *Journal of Applied Physics*, 91:2473, 2002.

[10] A. Richter, S.W. Glunz, F. Werner, J. Schmidt, and A. Cuevas. *Physical Review B.*

[11] R. Hall. Electron-hole recombination in germanium. *Physical Review*, 87: 387–387, 1952.

[12] J. Schmidt and A.G. Aberle. Accurate method for the determination of bulk minority-carrier lifetimes of mono- and multicrystalline silicon wafers. *Journal of Applied Physics*, 81:6186, 1997.

[13] M.A. Green. *Advanced Principles and Practice.* Sydney:UNSW, 1995.

[14] Armin G Aberle. Surface passivation of crystalline silicon solar cells: a review. *Progress in Photovoltaics: Research and Applications*, 8:473–487, 2000.

[15] Pietro P. Altermatt, Jürgen O. Schumacher, A. Cuevas, M.J Kerr, S. W Glunz, Richard R. King, G. Heiser, and A. Schenk. Numerical modeling of highly doped si:p emitters based on fermi- dirac statistics and self-consistent material parameters. *Journal of Applied Physics*, 92(6):3187, 2002.

[16] Armin G. Aberle, S. Glunz, and W. Warta. Impact of illumination level and oxide parameters on shockley-read-hall recombination at the si-sio_2 interface. *Journal of Applied Physics*, 71:4422, 1992.

[17] S. W Glunz, D. Biro, S. Rein, and W. Warta. Field-effect passivation of the sio_2-si interface. *Journal of applied Physics*, 86:683, 1999.

[18] M. Kerr and A. Cuevas. Very low bulk and surface recombination in oxidized silicon wafers. *Semiconductor Science and Technology*, 17:35–38, 2002.

[19] J Zhao, A Wang, and M.A Green. 24.5% efficiency pert silicon solar cells on seh mcz substrates and cell performance on other seh cz and fz substrates. *Solar Energy Materials and Solar Cells*, 2001.

[20] R. Hezel and K. Jaeger. Low-temperature surface passivation of silicon for solar cells. *Journal of the Electrochemical Society*, 136:518–523, 1989.

[21] M. Kerr and A. Cuevas. Recombination at the interface between silicon and stoichiometric plasma silicon nitride. *Semiconductor Science and Technology*, 17:166–172, 2002.

[22] M. Hofmann, S. Janz, C. Schmidt, S. Kambor, D. Suwito, N. Kohn, J. Rentsch, R. Preu, and S.W Glunz. Recent developments in rear-surface passivation at fraunhofer ise. *Solar Energy Materials and Solar Cells*, 93: 1074–1078, 2009.

[23] M. Schmidt, J.and Kerr and A. Cuevas. Surface passivation of silicon solar cells using plasma-enhanced chemical-vapour-deposited sin films and thin thermal sio_2 /plasma sin stacks. *Semiconductor Science and Technology*, 16: 164–170, 2001.

[24] Y. Larionova, V. Mertens, N.P Harder, and R. Brendel. Surface passivation of n-type Czochralski silicon substrates by thermal-SiO_2/plasma-enhanced chemical vapor deposition SiN stacks. *Applied Physics Letters*, 96:1–3, 2010.

[25] G Dingemans and M.M Mandoc. Effective passivation of Si surfaces by plasma deposited SiO_x/a-SiN_x: H stacks. *Applied Physics Letters*, 98: 222102, 2011.

[26] P. Doshi, Gerald E. Jellison, and A. Rohatgi. Characterization and optimization of absorbing plasma-enhanced chemical vapor deposited antireflection coatings for silicon photovoltaics. *Applied Optics*, 36:7826, 1997.

[27] J. Schmidt, J.D. Moschner, J. Henze, S. Dauwe, and R. Hezel. Recent progress in the surface passivation of silicon solar cells using silicon nitride. In *19th European Photovoltaic Solar Energy Conference*, Paris, France, 7-11 June 2004.

[28] Mark John Kerr. *Surface, Emitter and Bulk Recombination in Silicon and Development of Silicon Nitride Passivated Solar Cells.* PhD thesis, 2002.

[29] S. Kerdiles, R. Madelon, and R. Rizk. Spectroscopic ellipsometry analysis of nanocrystalline silicon carbide obtained at low temperature. *Applied surface Science*, 184:150–155, 2001.

[30] I. Martin, M. Vetter, A. Orpella, C. Voz, J. Puigdollers, and R. Alcubilla. Characterization of p-type c-si surface passivation by n-doped a-sic_x:h films. In *Proceedings of the 17th European Photovoltaic Solar Energy Conference, Munich*, pages 2954–2957, 2001.

[31] R. Ferre, A. Orpella, D. Munoz, I. Martin, F. Recart, C. Voz, J. Puigdollers, P. Cabarrocas, and R Alcubilla. Very low surface recombination velocity of crystalline silicon passivated by phosphorus-doped a-$sic_x n_y$:h(n) alloys. *Progress in Photovoltaics: Research Appl.*, 16:123–127, 2008.

[32] R. Ferre, I. Martin, P. Ortega, M. Vetter, I. Torres, and R. Alcubilla. n-type emitter surface passivation in c-si solar cells by means of antireflective amorphous silicon carbide layers. *Journal of Applied Physics*, 100:073703–073710, 2006.

[33] R. Ferre, I. Martín, P. Ortega, and M. Vetter. n-type emitter surface passivation in c-si solar cells by means of antireflective amorphous silicon carbide layers. *Journal of Applied Physics*, 100:073703, 2006.

[34] A. Morales-Vilches, C. Voz, M. Colina, G. Lopez, I. Martin, A. Orpella, J. Puigdollers, M. Garcia, and R. Alcubilla. Progress in silicon heterojunction solar cell fabrication with rear laser-fired contacts. In *Proceedings of the 2013 Spanish Conference on Electron Devices, CDE 2013*, pages 345–348, 2013.

[35] I. Martín, M. Colina, A. Orpella, C. Voz, S. De Vecchi, T. Desrues, S. Abolmasov, P. Roca i Cabarrocas, and R. Alcubilla. Low recombination n+ regions created by n+ c-si epitaxial layers and laser processing of phosphorus-doped sic_x films. In *27th European Photovoltaic Solar Energy Conference and Exhibition*, pages 1519–1523, 2012.

[36] I. Martín, M. Colina, A. Coll, G. López, P. Ortega, A. Orpella, and R. Alcubilla. c-si solar cells based on laser-processed dielectric films. *Energy Procedia*, 55:255–264, 2014.

[37] S. Dauwe, J. Schmidt, and R. Hezel. Very low surface recombination velocities on p- and n-type silicon wafers passivated with hydrogenated amorphous silicon films. In *Conference Record of the Twenty-Ninth IEEE Photovoltaic Specialists Conference, 2002*, pages 1246–1249. IEEE, 2002.

[38] S.W. Glunz, A. Grohe, M. Hermle, and et Al. Comparison of different dielectric passivation layers for application in industrially feasible high-efficiency crystalline silicon solar cells. In *20th European Photovoltaic Solar Energy Conference 2005. Proceedings*, pages 572–577, 2005.

[39] A. Bentzen, A. Ulyashin, A. Suphellen, E. Sauar, D. Grambole, D.N. Wright, E.S. Marstein, B.G. Svensson, and A. Holt. Surface passivation of silicon solar cells by amorphous silicon/silicon nitride dual layers. In *15th International Photovoltaic Science & Engineering Conference (PVSEC-15)*, pages 316–317, 2005.

[40] H. Plagwitz, Y. Takahashi, B. Terheiden, and R. Brendel. Amorphous si/sin double layers: A low temperature passivation method for diffused phosphorus as well as boron emitters. In *21st European Photovoltaic Solar Energy Conference*, page 688, 2006.

[41] F. Werner, B. Veith, V. Tiba, P. Poodt, F. Roozeboom, R. Brendel, and J. Schmidt. Very low surface recombination velocities on p- and n-type c-si by ultrafast spatial atomic layer deposition of aluminum oxide. *Applied Physics Letters*, 97:162103, 2010.

[42] B. Hoex, M. C. M. Van de Sanden, J. Schmidt, R. Brendel, and W. M. M. Kessels. Surface passivation of phosphorus-diffused n^+-type emitters by plasma-assisted atomic-layer deposited al_2o_3. *physica status solidi (RRL) - Rapid Research Letters*, 6:4–6, 2012.

[43] G. Agostinelli, A. Delabie, P. Vitanov, Z. Alexieva, H.F.W. Dekkers, S. De Wolf, and G. Beaucarne. Very low surface recombination velocities on p-type silicon wafers passivated with a dielectric with fixed negative charge. *Solar Energy Materials and Solar Cells*, 90:3438–3443, 2006.

[44] B. Hoex, J. Schmidt, R. Bock, Pietro P. Altermatt, MCM Van de Sanden, and WMM Kessels. Excellent passivation of highly doped p-type Si surfaces by the negative-charge-dielectric Al_2O_3. *Applied Physics Letters*, 91(11): 112107, 2007.

[45] F. Granek. *High-Efficiency Back-Contact Back-Junction Silicon Solar Cells*. PhD thesis, Fraunhofer Institut fur Solare Energiesysteme (ISE), July 2009.

[46] M.A. Green, A.W. Blakers, J. Shi, E.M. Keller, and S.R. Wenham. High-efficiency silicon solar cells. *IEEE Transactions on electron devices*, 5:679–683, 1984.

[47] B. Hoex, J. Schmidt, P. Pohl, M. C. M. van de Sanden, and W. M. M. Kessels. Silicon surface passivation by atomic layer deposited al_2o_3. *Journal of Applied Physics*, 104:044903, 2008.

[48] G. Dingemans, M. C. M. van de Sanden, and W. M. M. Kessels. Influence of the Deposition Temperature on the c-Si Surface Passivation by Al_2O_3 Films Synthesized by ALD and PECVD. *Electrochemical and Solid-State Letters*, 13:H76, 2010.

[49] J. Schmidt, F. Werner, B. Veith, D. Zielke, S. Steingrube, P.P. Altermatt, S. Gatz, T. Dullweber, and R. Brendel. Advances in the surface passivation of silicon solar cells. *Energy Procedia*, 15:30–39, 2012.

[50] B. Hoex, S. B. S. Heil, E. Langereis, M. C. M. van de Sanden, and W. M. M. Kessels. Ultralow surface recombination of c-Si substrates passivated by plasma-assisted atomic layer deposited Al_2O_3. *Applied Physics Letters*, 89: 042112, 2006.

[51] M. Cho, HB. Park, J. Park, C.S. Hwang, JC. Lee, SJ. Oh, J. Jeong, K.S. Hyun, HS. Kang, YW. Kim, and JH. Lee. Thermal annealing effects on the structural and electrical properties of HfO_2/Al_2O_3 gate dielectric stacks grown by atomic layer deposition on Si substrates. *Journal of applied physics*, 94:2563–257, 2003.

[52] B. Vermang, H. Goverde, A. Lorenz, A. Uruena, G. Vereecke, J. Meersschaut, E. Cornagliotti, A. Rothschild, J. John, J. Poortmans, and R. Mertens. On the blistering of atomic layer deposited Al_2O_3 as Si surface passivation. In *2011 37th IEEE Photovoltaic Specialists Conference*, pages 003562–003567, jun 2011.

[53] B. Vermang, H. Goverde, A. Uruena, A. Lorens, E. Cornagliotti, Rothschild A., J. John, J. Poortmans, and R. Mertens. Blistering in ALD Al_2O_3 passivation layers as rear contacting for local Al BSF Si solar cells. *Solar Energy Materials and Solar Cells*, pages 204–209, 2012.

[54] G. Dingemans and W. M. M. Kessels. Status and prospects of Al_2O_3 based surface passivation schemes for silicon solar cells. *Journal of Vacuum Science & Technology A: Vacuum, Surfaces, and Films*, 30:040802, 2012.

[55] G. Dingemans, R. Seguin, P. Engelhart, M. C. M. van de Sanden, and W. M. M. Kessels. Silicon surface passivation by ultrathin Al_2O_3 films synthesized by thermal and plasma atomic layer deposition. *physica status solidi (RRL) - Rapid Research Letters*, 4:10–12, 2010.

[56] P. Ortega, I. Martín, G. Lopez, M. Colina, A. Orpella, C. Voz, and R. Alcubilla. p-type c-Si solar cells based on rear side laser processing of Al_2O_3/SiC_x stacks. *Solar Energy Materials and Solar Cells*, 106:80–83, 2012.

[57] I. Martín, P. Ortega, M. Colina, A. Orpella, G. López, and R. Alcubilla. Laser processing of $Al_2O_3/a-SiC_x : H$ stacks: a feasible solution for the rear surface of high-efficiency p-type c-Si solar cells. *Progress in Photovoltaics: Research and Applications*, 21:1171–1175, 2012.

[58] G. Dingemans, N.M. Terlinden, D. Pierreux, H.B. Profijt, M.C.M. van de Sanden, and W. M. M. Kessels. Influence of the Oxidant on the Chemical and Field-Effect Passivation of Si by ALD Al_2O_3. *Electrochemical and Solid-State Letters*, 14:H1–H4, 2011.

[59] Keith R. McIntosh and Luke P. Johnson. Recombination at textured silicon surfaces passivated with silicon dioxide. *Journal of Applied Physics*, 105: 124520, 2009.

[60] H. Angermann. Passivation of structured p-type silicon interfaces: Effect of surface morphology and wet-chemical pre-treatment. *Applied Surface Science*, 254:8067–8074, 2008.

[61] P.A. Basore. Numerical modeling of textured silicon solar cells using PC-1D. *IEEE Transactions on Electron Devices*, 37:337–343, 1990.

[62] Martin Green. *High efficiency silicon solar cells*. Trans Tech, 1987.

[63] J. Zhao and M.A. Green. Optimized antireflection coatings for high-efficiency silicon solar cells. *IEEE Transactions on Electron Devices*, 38:1925–1934, 1991.

Chapter 4

Emitter formation using laser doping technique on n- and p-type c-Si substrates

In this chapter laser doping technique is used to create highly-doped regions defined in a point-like structure to form n^+/p and p^+/n junctions. In particular, phosphorous-doped amorphous silicon (a-Si (n-type)) and aluminum oxide (Al_2O_3) layers are used as dopant sources. Laser power and number of pulses per spot are explored to obtain the optimum electrical behaviour of the junctions. The junctions are electrically contacted and characterized by means of dark J-V measurements. Additionally, a diluted HF treatment previous to front metallization has been explored in order to know its impact on the junction quality. The objective of this study is to apply the best laser condition on the rear side of the IBC solar cell to form the BSF and emitter in a point-like structure.

4.1 Introduction

Lasers are widely used for different applications in the industry of solar cells such as scribing grooves in buried contact solar cells [1], firing contacts in the laser fired contact (LFC) structure [2],[3],[4], texturing surfaces [5],[6], ablating dielectrics layers [7], among others. The introduction of laser processes to create doped regions into crystalline silicon (c-Si) can avoid the use of dopant diffusion

in conventional high temperature furnaces that represents one of the most expensive and time-consuming processes in the fabrication line. Laser doping diffusion (LD) relies upon laser ability to heat locally the semiconductor surface. Doping happens during the melting phase of the silicon in which dopant is incorporated (diffused) into the silicon structure [6],[8]. Several methods applying laser doping technique (LD) to junction formation have been presented to date and a wide variety of dopant source can be used in gas, liquid or solid form [9],[10],[11],[12]. In this experimental we apply the LD technique to create highly-doped regions defined in a point-like structure to form n^+/p and p^+/n junctions applying a pulsed Nd-YAG 1064 nm laser in the nanosecond regime. Dielectric layers deposited at low temperature have been used as dopant sources, particularly a phosphorous-doped silicon carbide stack ($a - SiC_x(i)/a - Si : H$ (n-type)) deposited by PECVD and Al_2O_3 layer deposited by ALD. These layers have the advantage that, if correctly tuned, they can also work as c-Si passivating layers and reduce optical reflectance as it has been demonstrated in previous chapter [13],[14]. Parameters such as pulse power and number of pulses are varied in order to find the conditions leading to the optimal electrical behaviour of the formed junction. The fabricated n^+/p and p^+/n junctions are electrically characterized by means of dark J-V measurements. We analyze how the laser parameters and the HF treatment previous metallization step impact on the J-V curves.

4.2 Experimental

4.2.1 Laser system

Laser doping is carried out using a pulsed Nd:YAG laser (Star-Mark SMP100 II Rofin-Baasel) working at 1064 nm wavelength in TEM00 mode, with a fixed frequency of 4 kHz and a pulse duration fixed at 100 ns. The power of the laser beam can be adjusted by varying the intensity of the continuous lamp that pumps the Nd:YAG crystal. In this study, we explore the quality of the laser doped regions varying the laser power from 0.8 W to 1.4 W and the number of pulses per spot: 3, 6 and 9 pulses.

4.2.2 Sample preparation

All the samples processed by LD are $\sim 280\ \mu m$ thick float zone n- and p-type c-Si wafers with a resistivity of $1.4 - 2.5\ \Omega cm$. The experimental starts with a complete RCA cleaning sequence. Then, the p-type wafer is introduced in the PECVD chamber and a phosphorous-doped $a - SiC_x$ stack is deposited directly on the front c-Si surface. The stack consists of an a-Si-rich intrinsic ($a - SiC_x(i)$) passivating film ($\sim 4nm$) plus a phosphorus-doped a-Si film ($\sim 15nm$)(from now on both layers will be call $a - SiC(n)$ stack). A final stoichiometric $a - SiC_x$ film (n = 2.0, 75 nm) as capping layer is deposited for chemical protection purposes and laser stage improvement. Then, 90 nm Al_2O_3 films are symmetrically grow by ALD. The Al_2O_3 film of the front side is removed with HF at 1% previous rear side protection with a photoresist film. This photoresist film is eliminated after the etching process. Finally, a 50 nm thick of stoichiometric $a - SiC_x$ film is deposited on the rear side.

In order to create the n^+ regions and study the laser parameters which lead to the optimal electrical behavior of the junction, the front surface of the sample is irradiated with the laser simultaneously enabling the diffusion of the dopant atoms and opening the dielectric layer. Several hexagonal matrices of spots separated a distance (pitch) of 300 μm are done. Each matrix corresponds to one device with a total area of 0.42 cm $\times$ 0.42 cm and the laser conditions (power and number of pulses) are fixed within the same array and varied between them (see Figure 4.1). In this way the processed surface is ready to be contacted.

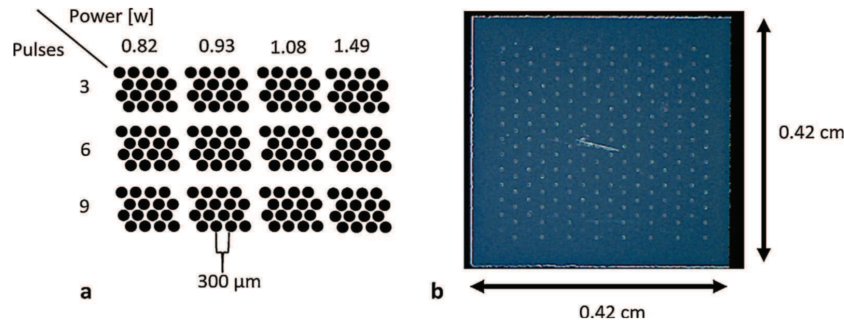

Figure 4.1: (a) Illustration of laser spots arranged in hexagonal matrices. Parametrization of the n^+/p junction (p-type substrate) varying the laser power and the number o pulses. (b) Optical microscopy image of the device front side.

The ohmic contacts of the rear side are also defined with laser in a point-like structure with a pitch of 600 μm, 1.07W and a laser pulse duration of 400

ns. Then, after the laser process both sides are metallized with Ti/Al e-beam evaporated. No HF treatment previous metallization is done unless other-wise stated. Finally, an annealing in N_2/H_2 at 375 ^oC for 10 min is carried out in order to increase the negative fixed charge density located at the $Al_2O_3/c-Si$ interface favouring the passivation quality and improving the metal-silicon contacts.
The same structure is defined for n-type substrates where p^+/n junctions are defined at the front side. The only difference is the position of the dielectric films. Figure 4.2 shows the structure of the sample to be analysed and the fabrication process scheme. In fact, the studied dielectric stacks are chosen to be technologically compatible with the fabrication of interdigitated back contacted c-Si solar cells that impose strong constraints in dielectric configuration.

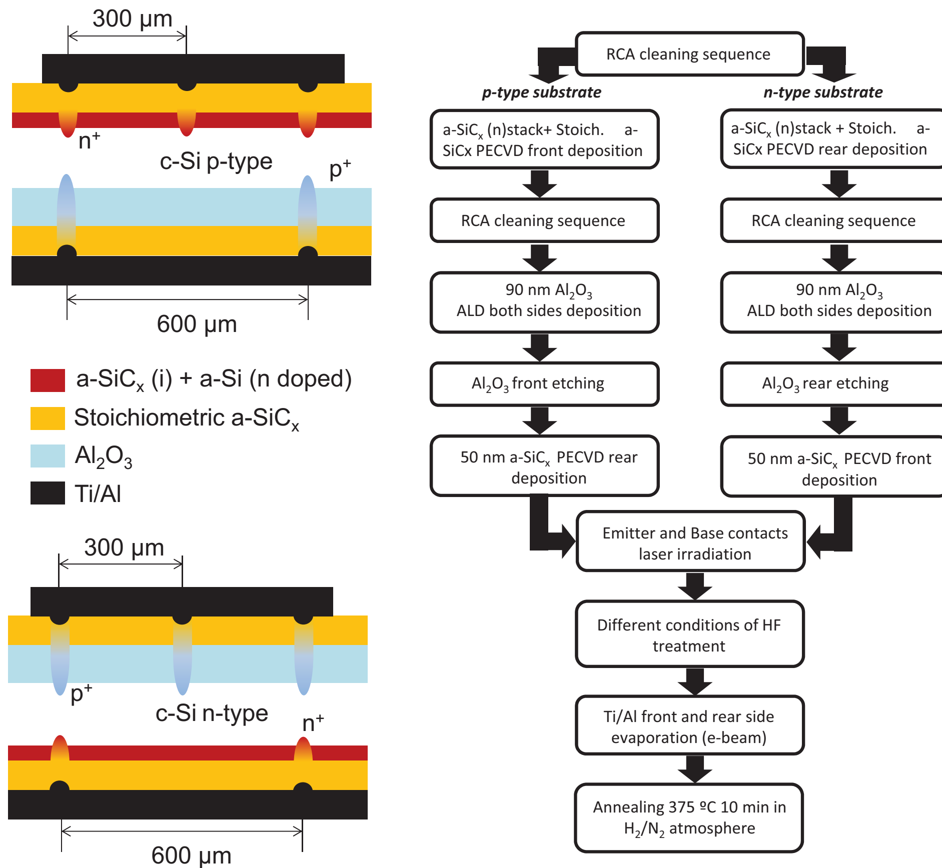

Figure 4.2: On the left, diode schemes. On the top, n^+/p diode scheme. n^+ emitter regions doped with phosphorous atoms from the $a-SiC_x(n)$ stack and p^+ regions (base contacts) from Al_2O_3 layer. On the bottom, p^+/n diode scheme. p^+ emitter regions doped with aluminium atoms from Al_2O_3 layer and n^+ regions (base regions) from $a-SiC_x$(n) stack. On the right, scheme of the diodes fabrication process

4.3 Experimental results. J-V measurements

Surface passivation quality is determined by means of lifetime measurements before the laser stage. All the samples processed on p- and n-type substrates exhibited a high initial lifetime. Over 1 ms at 1 sun (see figure 4.3) corresponding to surface recombination velocities lower than 10 cm/s.

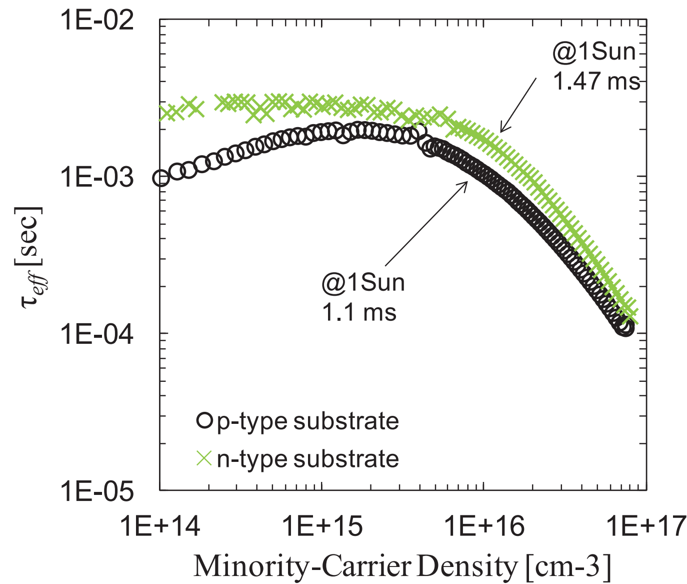

Figure 4.3: Effective lifetime vs. excess carrier density corresponding to *p*- and *n*-type c-Si samples prepared and after laser processing. Fig.4.1

.

Dark J-V measurements are done at 25 °C and the current density is calculated dividing the measured current by the device area.

Figure 4.4 shows J-V characteristics for p^+/n and n^+/p junctions created by laser doping. The comparison between devices irradiated with different laser powers shows a rectifying behaviour in all the diodes with a clear exponential trend at mid-injection, except for the diodes created with the highest power (1.49 W). If the pulse energy is too high, the c-Si material could be ablated introducing damage into the crystal lattice [15]. Moreover, the partially or totally removing of the dopant from the contacts ([16],[17]) can create metal/semiconductor junctions, i.e. Schottky diode.

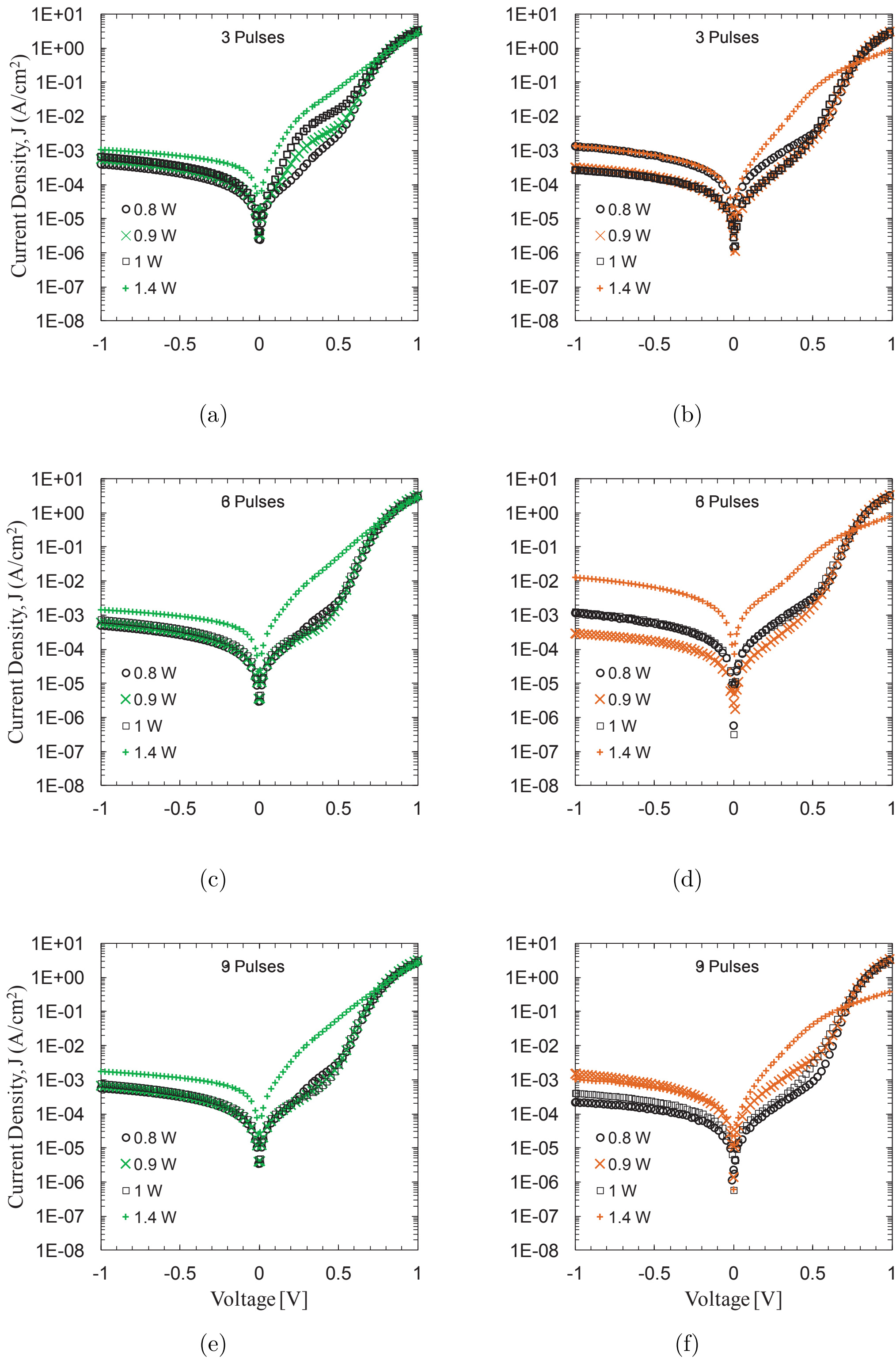

Figure 4.4: Dark J-V characteristics of p^+/n (left) and n^+/p (right) created from Al_2O_3/SiC_x and $a - SiC_x$ (n type) stack respectively for different laser powers. From top to bottom different number of pulses are evaluated

We can observe that the quality of the diodes are very similar indicating a laser parameter window available from 0.8 W to 1.0 W and 3, 6 and 9 pulses to create both p^+ and n^+ regions. However, the optimum behaviour is identified for 0.9 W and 1 W, 6/9 pulses for p^+/n junction and 0.9 W, 3/6 pulses and 0.8 W/9 pulses for n^+/p junction. Major differences in leakage current are found as the laser power increases for the case of n^+/p junction (clearly visible in the reverse bias region), while in the case of p^+/n remains at the same level. On the other hand, the highest energy condition originates a Schottky diode behaviour, probably due to direct contact between metal and a low or non-doped semiconductor region.

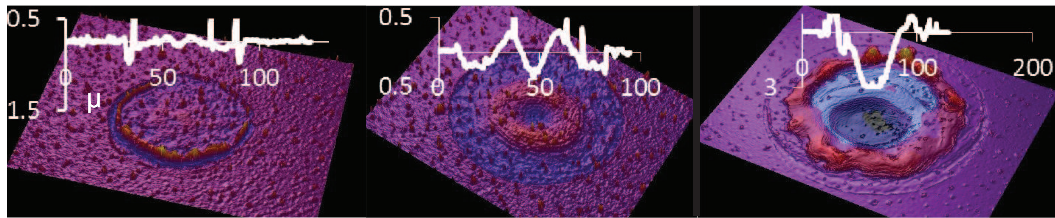

Figure 4.5: Interferometric images for three different spots done at laser powers of 0.93, 1.08 and 1.49 W. Inset curves of profilometer measurements are also shown.

Figure 4.5 shows optical profilometric data for three different laser powers, i.e. 0.93, 1.08 and 1.49 W. The highest laser power leads to a penetration depth in the order of 3 micrometer, causing damage into the silicon structure. This behaviour could be due to an excessive melting during a too powerful laser doping process. Additionally, we can see that the radius of the affected region increases with laser power, ranging from 30 μm to 45 μm.

4.3.1 Hydrofluoric acid treatment.

Additional experiments have been carried out in order to know if a treatment of diluted HF before the metallization step impacts on the electrical behavior of the diodes. This treatment is usually done to remove the native SiO_2 from the Si surface and to ensure a metal-semiconductor ohmic contact. No HF treatment, 20 seg and 35 seg in HF 1% are done for both p- and n-type substrate using a laser power of 0.9 W and 6 pulses for both substrate types. Results are plotted in figure 4.6.

As we can see, the HF treatment has no impact in the electrical characteristic for p^+/n junction. However, and increase in the leakage current is observed for

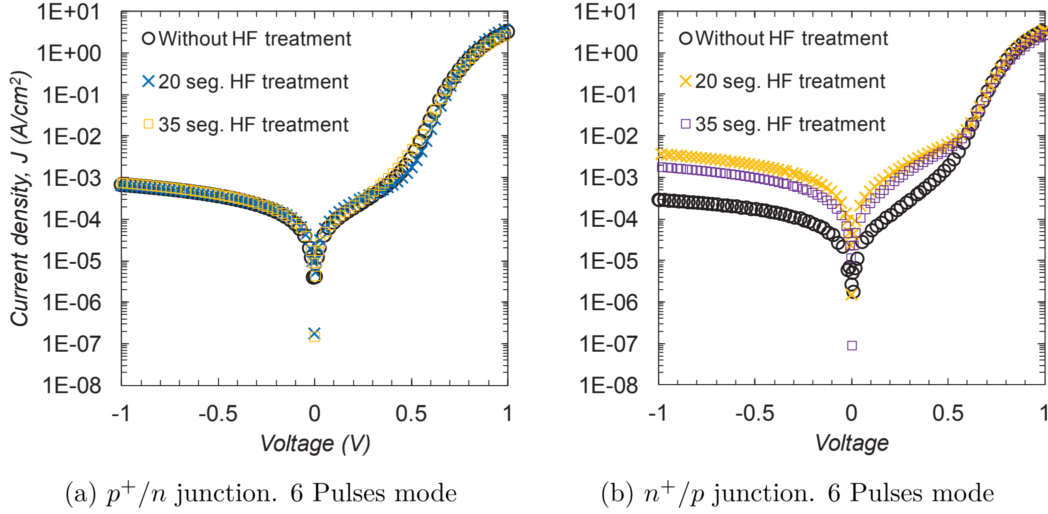

(a) p^+/n junction. 6 Pulses mode

(b) n^+/p junction. 6 Pulses mode

Figure 4.6: Dark J-V characteristics of p+/n (left) and n+/p junction (right). No HF treatment, HF 1% for 20 s and 35 s are done before metallization process.

n^+/p junction when a HF treatment is done. In our opinion, this behaviour is related to pinholes in the $a-SiC_x$ (n)stack/$a-SiC_x$ where the native oxide is removed by the HF treatment and the subsequent metallization results in shunting paths. Notice that more than 90% of device area consists of a metal layer over an insulator film and any absence of it allows the metal to directly contact the c-Si substrate. This effect is strongly reduced in $Al_2O_3/a-SiC_x$ stack since the Al_2O_3 layer is deposited by ALD technique that lead to a much less pin-hole density in the films compared to PECVD one.

In all cases the dark J-V curves flatten at high voltage mainly due to ohmic losses hindering the characterization of the exponential current mechanism. In order to evaluate the quality of this exponential trend, we measure the best p^+/n and n^+/p diode at different temperatures in the 298-363 K range.
J-V curves are fitted using the following two diode expression (4.1) and taking into account that series resistance r_s does not vary with temperature or applied voltage:

$$J(V) = J_{o1}(e^{A(V-J(V)r_s} - 1) + J_{o2}e^{A(V-J(V)r_s} - 1 + \frac{V - J(V)r_s}{r_{sh}} \tag{4.1}$$

where for every exponential trend J_o is the saturation current density, A ($A = q/nKT$) is an exponential factor and n is the ideality factor respectively. From the dependence of A and the corresponding J_o on the temperature, the carrier transport mechanism behind the exponential trend can be identified.
A summary of the basic conduction mechanisms is given in table 4.1.

Transport mechanisms	J_o	**A**	**n**
Diffusion	$J_o \propto exp(-E_g/KT)$	q/nKT	$n = 1$
Recombination	$J_o \propto exp(-E_g/2KT)$	q/nKT	$1 < n \leqslant 2$
Tunneling	$J_o \propto exp(-E_{ac}/KT)$	const.	$n \neq const.$
Thermionic	$J_o \propto exp(-\varphi_B/KT)KT^{3/2}$	q/KT	$n = 1$

Table 4.1: Basic transport mechanisms. E_g is the energy gap, K is the Boltzmann constant, T is the absolute temperature, n the ideality factor, E_{ac} is the activation energy, and φ_B is the barrier energy.

Applying the electrical model and assuming an ideality factor of one for the main current mechanism related to the first exponential dependence in equation 4.1 (n = 1), J_{o1} can be extracted at different temperatures. All these data can be arranged in an Arrhenius plot where the logarithm of J_{o1} is plotted as a function of the inverse of the temperature. In this type of plots, a straight line is expected for current mechanism thermally activated and their activation energy can be extracted from the line slope. As it is shown in figure 4.7 the Arrehnius plot reveals an activation energy of 1.1 eV corresponding to the silicon bandgap. This result together with the ideality factor of 1 indicates that current is controlled by minority carrier recombination at the quasi-neutral c-Si bulk. Additionally, we can conclude that recombination at the space charge region and thus crystal damage is not dominant in the device performance.
Due to the high quality of the laser doped regions and the surface passivation provided by dielectric films, this technique is well suited to c-Si solar cells. Figure 4.8 shows dark J-V measurements and the resulting theoretical curves once the influence r_s has been canceled in order to a correct estimation of V_{oc} from the dark J-V curve (the normalized series resistance considering the diode area is 0.15 Ωcm^2 in both cases). As it can be observed, assuming a photogenerated current

density of 36 mA/cm^2 at 1 sun-illumination, a V_{oc} about 0.63 V and 0.64 V are expected for p^+/n and n^+/p junctions respectively. These values are promising results and can be considered in the state of the art of commercial c-Si solar cells.

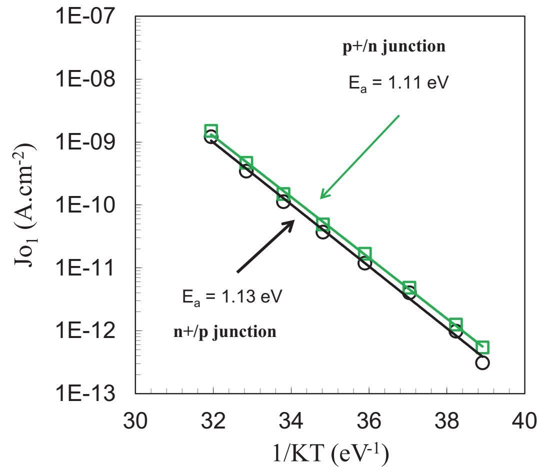

Figure 4.7: Arrehnius plot of the J_{o1} against 1/KT. Dark J-V measurements at different temperatures are done for p^+/n and n^+/p junction formed at 0.9 W, 6 pulses and without HF treatment. The exponential gives activation energy of 1.1 eV corresponding to the silicon E_{gap}.

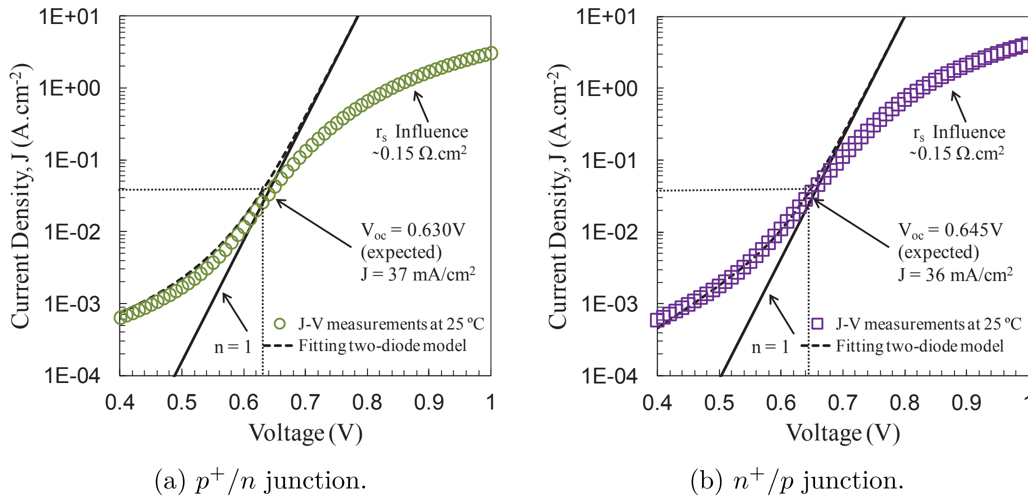

(a) p^+/n junction.

(b) n^+/p junction.

Figure 4.8: Dark J-V measurements at 25 ^oC for p^+/n (a) and n^+/p (b) junctions (symbols). Laser power of 0.9 W (6 pulses) and no HF treatment are considered in both cases. The two-diode model fitting without r_s is displayed in black dashed line. Diffusion diode term considering n = 1 (continuous black line), resulting from the fitting, is also included as a reference.

4.4 Conclusion

In this chapter we have explored different laser conditions, i.e. laser power and number of laser pulses, to create reliable p^+/n and n^+/p junctions on c-Si using Laser doping technique. In this case, dielectric layers (Al_2O_3 and $a - SiC_x$ (n) stack) were applied as both dopant sources and surface passivation layers. Optimum laser conditions were established studying systematically dark J-V measurements. Excellent quality of the p^+ and n^+ regions has been formed from 0.8 W to 1 W and 3/6/9 pulses. Additionally, a study of a diluted HF treatment before the metallization process has been also done concluding that best electrical behavior corresponds to no HF treatment. Finally, dark J-V measurements for different temperatures have demonstrated that the main current mechanism is linked to minority carrier recombination in the quasi-neutral bulk and, thus, that laser damage is not dominant in device performance. The high quality of the junctions and the excellent surface passivation makes laser doping technique using dielectric layers as dopand source suitable for solar cells applications. A promising open circuit voltages at 1 sun-illumination of about 640 mV are expected for this type of solar cells.

Bibliography

[1] A.W.Y. Ho and Stuart R. Wenham. Buried contact solar cells with innovative rear localised contacts. *Progress in Photovoltaics: Research and Applications*, 12:297–308, 2004.

[2] E. Schneiderlöchner, R. Preu, R. Lüdemann, and S. W. Glunz. Laser-fired rear contacts for crystalline silicon solar cells. *Progress in Photovoltaics: Research and Applications*, 10:29–34, 2002.

[3] D. Carrió, P. Ortega, I. Martín, G. López, J. M. López-González, A. Orpella, C. Voz, and R. Alcubilla. Rear contact pattern optimization based on 3D Simulations for IBC Solar Cells with Point-like Doped Contacts. *Energy Procedia*, 55:47–52, 2014.

[4] I. Martín, P. Ortega, M. Colina, A. Orpella, G. López, and R. Alcubilla. Laser processing of $Al_2O_3/a{-}SiCx : H$ stacks: a feasible solution for the rear surface of high-efficiency p-type c-si solar cells. *Progress in Photovoltaics: Research and Applications*, 21:1171–1175, 2012.

[5] L. Pirozzi, U.B. Vetrella, Mauro Falconieri, and E. Salza. A laser system for silicon solar cell processing: Design, setup and operation. *Materials Science Forum*, 173-174:319–324, 1995.

[6] L Pirozzi, U. Besi-Vetrella, and E. Salza. Innovative applications of laser technology in photovoltaics. In *Proc. SPIE Conf. Laser Applications in Microelectronic and Optoelectronic Manufacturing II*, 1997.

[7] A. Knorz, M. Peters, A. Grohe, C. Harmel, and R. Preu. Selective laser ablation of SiN_x layers on textured surfaces for low temperature front side metallizations. *Progress in Photovoltaics: Research and Applications*, 17: 127–136, 2009.

[8] A. Ogane, K. Horiuchi, A. Kitiyanan, Y. Uraoka, and T. Fuyuki. Feasible control of laser doping profiles in silicon solar cell processing using multiple excitation wavelengths. In *2008 33rd IEEE Photovolatic Specialists Conference*, pages 1–4. IEEE, 2008.

[9] G. B. Turner. Solar cells made by laser-induced diffusion directly from phosphine gas. *Applied Physics Letters*, 39:967, 1981.

[10] D. Kray, A. Fell, S. Hopman, K. Mayer, G. P. Willeke, and S. W. Glunz. Laser Chemical Processing (LCP). A versatile tool for microstructuring applications. *Applied Physics A*, 93:99–103, 2008.

[11] E. Fogarassy. Silicon solar cells realized by laser induced diffusion of vacuum-deposited dopants. *Journal of Applied Physics*, 52:1076, 1981.

[12] M. Colina, I. Martín, C. Voz, A. Morales-Vilches, P. Ortega, G. López, A. Orpella, R. Alcubilla, I. Sánchez-Aniorte, and C. Molpeceres. Optimization of laser doping processes for the creation of p+ regions from solid dopand sources. In *27 th EUPVSEC*, pages 1885–1889, 2012.

[13] G. López, P. Ortega, C. Voz, I. Martín, M. Colina, A. Morales-Vilches, A. Orpella, and R. Alcubilla. Surface passivation and optical characterization of $Al_2O_3/a - SiC_x$ stacks on c-Si substrates. *Beilstein journal of nanotechnology*, 4:726–31, 2013.

[14] I. Martín, M. Colina, A. Coll, G. López, P. Ortega, A. Orpella, and R. Alcubilla. c-si solar cells based on laser-processed dielectric films. In *4th International Conference on Silicon Photovoltaics, Silicon PV*. Energy Procedia, 2014.

[15] M. Okanovic, U. Jäger, M. Ahrens, U. Stute, A. Grohe, and R. Preu. Influence of different laser parameters in laser doping from phosphosilicate glass. In *24th European PV Solar Energy Conference and Exhibition, EUPVSEC, Hamburg (Germany)*, 2009.

[16] A. Fell, E. Franklin, D. Walter, D. Suh, and K. Weber. Laser doping from Al_2O_3 layers. In *27th European PV Solar Energy Conference and Exhibition, EUPVSEC, Frankfurt (Germany)*, 2012.

[17] Z. Hameiri, L. Mai, T. Puzzer, and S.R. Wenham. Influence of laser power on the properties of laser doped solar cells. *Solar Energy Materials and Solar Cells*, 95:1085–1094, 2011.

Chapter 5

The "Hybrid" IBC solar cell

This chapter corresponds to the experimental work related to IBC solar cell fabrication. This is a first approximation to the final "cold" IBC solar cell (developed in chapter 6) in order to apply the knowledge acquired in the previous experiments and about the laser doped technique. We introduce the selective emitter concept that includes one thermal step (phosphorous diffusion) with punctual highly doped regions created by laser, predecessor of the punctual emitters of the "cold" IBC cell. The BSF regions are developed entirely with laser doped technique in a point-like structure. This IBC structure mixes one high-temperature step with laser technique and will be called from now on "hybrid" IBC solar cell.

5.1 Introduction

In this section, we describe a novel fabrication process of p-type interdigitated back contact (IBC) silicon solar cell developed by means of laser doping technique. We use dielectric layers as both passivating layers and as dopant sources to create highly-doped regions. In particular, we use phosphorous-doped silicon carbide stacks ($a - SiC_x(i)/a - Si(n)$/stochiometric $a - SiC_x$) deposited by PECVD and Al_2O_3 layer deposited by thermal-ALD. A detailed study of these layers were done in chapter 3 and 4. Emitters are fabricated with a light thermal phosphorous diffusion in order to guarantee good photocarrier collection, i.e. high J_{ph}, and reduce the surface emitter recombination losses. Highly doped regions n^{++} and p^{++} under emitter and base contacts respectively, are simultaneously created

in a single-laser step in a point-like structure using a pulsed Nd-YAG 1064 nm laser in the nanosecond regime, 100ns pulsed mode (6 pulses). By combining these dielectric layers with the laser processing the IBC solar cell fabrication is drastically simplified. A cross-section sketch of the developed IBC cell is shown in figure 5.1.

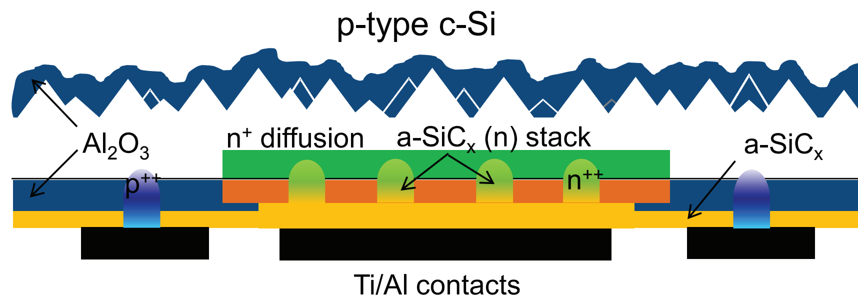

Figure 5.1: Cross-section sketch of a p-type Hybrid-IBC Solar cell processed

5.2 Precursor samples. Diodes

The n^{++} regions implemented in the "Hybrid" IBC solar cell are different than the other analyzed in the previous chapter, since a conventional phosphorous diffusion is carried out at the c-Si surface. Then, the laser power conditions are explored in the similar way than in chapter 4 in order to obtain the optimal electrical behaviour of the formed junctions. The junctions are electrically contacted and characterized by means of dark J-V measurements. The objective of this study is to apply the best laser condition on the rear side of the "Hybrid" IBC solar cell to form the BSF (p^{++}) and the selective emitter in a point-like structure (n^{++}).

The prepared sample consists of c-Si p-type with a thickness of 275 $\pm$ 10 μm and a base resistivity of 2.5$\pm$ 0.5 Ωcm. A sketch of this sample is shown in the figure 5.2. SiO_2 layer is thermally grown in both sides as diffusion mask. A photolithographic step defines 1 cm x 1 cm square areas limiting each devices after a SiO_2 etching. After a RCA cleaning, the sample is introduced into the diffusion furnace at 840 °C. In this way, the diffusion is only carried out where there is not SiO_2 mask. The phosposilicate glass (PSG) and the SiO_2 is eliminated by hydrofluoric acid solution (HF). After a drive-In process in O_2 atmosphere, the sample has a sheet resistance of 65 Ω/sq.

After an RCA cleaning, the sample is introduced into the ALD reactor at

200 °C and 50 nm of Al_2O_3 is deposited on both sides. Then a capping layer 35 nm thick of stoichiometric a-SiC_x is deposited on the rear side. The Al_2O_3 of the front side is etched with a HF solution and after a RCA cleaning, ∼ 20nm a-$SiC_x(n)$[1]/75 nm stoichiometric a-SiC_x stack is deposited on the front side. The backside, with 50 nm of Al_2O_3 is covered with 50 nm of stoichiometric $a-SiC_x$. Rear ohmic contacts are created with laser technique at 1.02W and 400 ns of pulse duration. Spots with a pitch of 600 μm cover the whole rear side in a point-like structure. In the front side, each device is irradiate with the pulsed mode (6 pulses) and 100 ns of pulse duration forming an hexagonal matrix of spots separated a distance of 300 μm. The power laser applied is different for each device in order to study its influence on the diode electrical behaviour. Finally, the front and rear side are Ti/Al evaporated and the sample is annealed at 400 °C in a N_2/H_2 atmosphere for 10 min. The resulting dark J-V measurements are presented in figure 5.3. The current density is calculated dividing the measured current by the device area (1 cm^2).

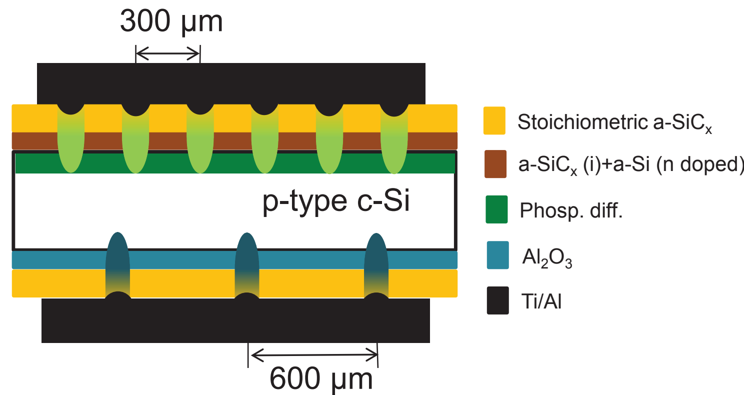

Figure 5.2: Schematic illustration of the "Hybrid" diode sample

In figure 5.3 we can observe that all the diodes show a rectifying behaviour with a clear exponential trend at mid-injection and flatten in the same way at high forward voltages due to series resistance ohmic losses. The best electrical behaviour correspond to the diode done at 0.9 W (yellow dashed lines). Below 0.9W the laser is not stable and the formation of all laser spots is not guaranteed. This diode shows the lowest current leakage, about 0.1 mA/cm^2, as it can be seen

[1] $a-SiC_x(n)$ stack consists of ∼ 4 nm of silicon rich $a-SiC_x(i)$/∼ 15 nm of phosphorous doped $a-Si$

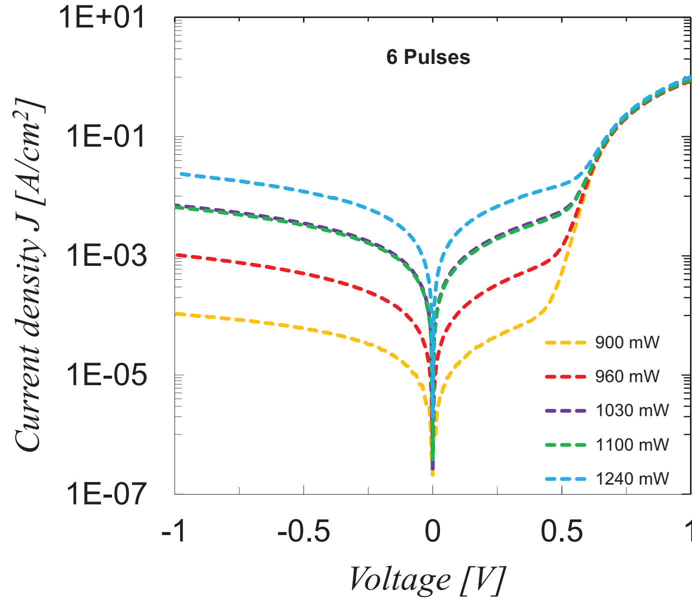

Figure 5.3: Dark J-V measurements of the "Hybrid" diodes at different laser powers

in the reverse bias region as a consequence of the highest r_{shunt}. The r_{shunt} is clearly affected by the laser power. As the laser power increases the r_{shunt} decreases deteriorating the J-V diode response. In the forward bias the exponential trend of the diffusion diode is clearly hidden by the influence of r_{shunt} (being predominant at 1.24 W).

5.3 Emitter saturation current (J_{oe}) study

In the "Hybrid" IBC solar cell, we have to distinguish between three different interfaces in order to study the surface passivation properties, i.e. the front textured surface covered with 90 nm of Al_2O_3, the polished rear base region covered with 90 nm of Al_2O_3 as passivating layer and covered with 35 nm of stoichiometric a-SiC_x and the polished emitter region thermally phosphorous doped and covered with a-Si(n) stack + 75 nm stoichiometric $a - SiC_x$. The latter will be the focus of the next passivation study. The other two passivated interfaces were previously studied in detail in chapter 3.

The sample under study consists of a p-type c-Si with a thickness of 275 $\pm$ 10 μm and a base resistivity of 2.5$\pm$ 0.5 Ωcm. The sample is cleaned with the RCA

sequence before a phosphorous diffusion performed at 840°C. The phosphosilicate glass grown is etched with HF solution. Then, the sample is again cleaned with RCA and submitted to a thermal drive-in in O_2 atmosphere, achieving a final sheet resistance of $\sim$ 65 Ω/sq. The SiO_2 is etched and the sample is introduced in the PECVD chamber to deposit on both sides a $a-SiC_x(n)$ stack/75 nm stoichometric $a-SiC_x$.

Emitter saturation current (J_{oe}) is determined measuring effective lifetime on the symmetrical c-Si sample processed. Test structure n^+pn^+ is shown in figure 5.4a. The carrier lifetime is measured before laser processing. Then, we irradiate only one surface with laser spots with a pitch of 250 μm covering 4.5% of the total surface area and τ_{eff} is measured again. J_{oe} is extracted from the slope of the $1/\tau_{eff}$ vs. Δn at high injection levels using the method proposed by Kane and Swanson [1] (see Fig. 5.4b). Emitter saturation currents of 36 fA/cm^2 and 42 fA/cm^2 are obtained before and after laser stage respectively. Therefore a J_{oe} can be deduced for each selective emitter point yielding $\sim$150 fA/cm^2. Despite the J_{oe} does not change much before and after laser process, there is a degradation of the bulk lifetime as it can be deduced from the shift between the curves. This deterioration has probably been caused by the damage into the bulk lattice during the laser doping stage.

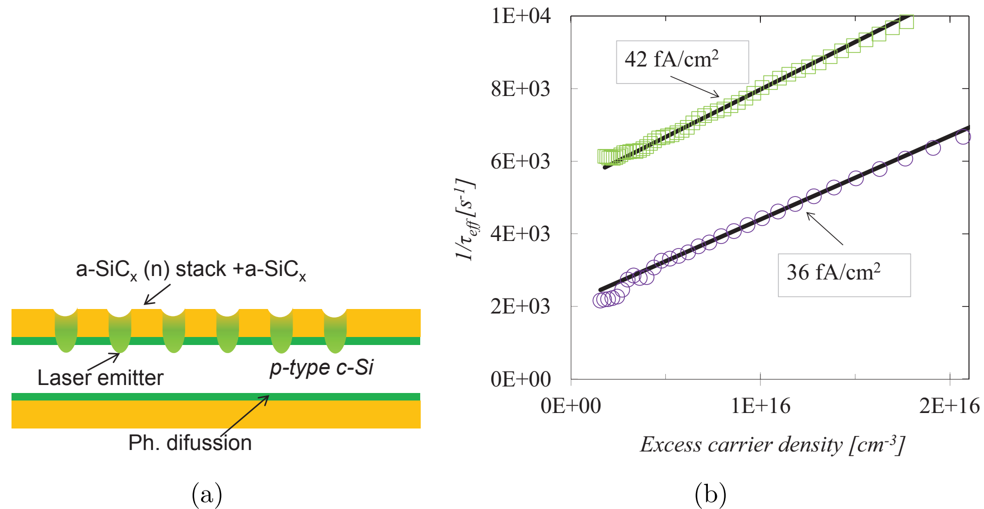

Figure 5.4: (a) Symmetrical test structure for measurements of minority carrier lifetime. (b) Determination of J_{oe} using the "slope method" for a symmetrical sample before (round-shaped) and after laser process (square-shaped) when a point-like selective emitters are created

5.4 "Hybrid" IBC Fabrication process

As starting material, we use p-type float-zone (FZ) silicon wafers with a thickness of 275 ± 10 μm and a base resistivity of 2.5± 0.5 Ωcm (the same substrate used in previous experimental). In figure 5.5 is described step by step the "hybrid" IBC cell fabrication process.

(1) The fabrication starts with a RCA cleaning and a light thermal diffusion performed at 840 °C from solid source. The phosphorous glass grown is etched with HF (5%) Dip.
(2) A subsequent O_2 drive-in (1080°) after an RCA cleaning results in a grow of a SiO_2 layer and in a n^+ emitter with 65 Ω/sq sheet resistance.
(3) The SiO_2 of the front layer is etched side with a commercial SiO_2 etching solution.
(4) The SiO_2 of the backside is used to protect the surface from the subsequent front side random texturation achieved by tetramethyl ammonium hydroxide (TMAH) solution. The front side is textured at the same time that the phosphorous diffusion is etched.
(5) and (6) After removing the back SiO_2 mask layer, we deposit on the whole rear side by PECVD a dielectric $a-SiC_x$ (n) stack and 25 nm stoichiometric $a-SiC_x$ for chemical protection purposes.
(7) and (8) Emitter regions are defined through standard photolithography followed by plasma dry etching (CF_4) to remove the stoichiometric $a-SiC_x$ and the $a-SiC_x(n)$ stack from the undesired areas. A subsequent isotropic etching removes the c-Si phosphorous doped from the base regions. This isotropic etching consist of 200 ml HNO_3 + 8 ml HF (50%)+ 200 ml H_2O(DI) for 4 minutes.
(9) The photoresist is stripped and after a RCA cleaning, we deposit 90 nm of Al_2O_3 by thermal-ALD at 200 °C on both sides. This layer plays the role of passivating front and rear base surface , antireflection coating and as aluminium source for a later BSF formation (p^{++}).
(10) and (11) Base regions are defined by photolithography and the Al_2O_3 is wet etched from the emitter regions.
(12) After removing the photoresist, an additional stoichiometric $a-SiC_x$ film (50 nm thick) is deposited on the whole device rear side to optimize the back reflector and improve the laser process.
(13) Next, the rear of the solar cells are laser irradiated in one single laser step applying 6 pulses per spot (laser pulse duration of 100 ns) in a point-like square

matrix arrangement with a pitch of 250 μm. In this way, laser beam simultaneously ablates the dielectric layers and diffuses the dopant atoms creating highly doped n^{++} (selective emitter) and p^{++} (BSF) regions. These highly doped regions underneath the contacts helps for the formation of a good ohmic contact. 0.9 W is the laser power selected considering the results obtained in the study of the precursor p^{++}/n done in the chapter 4 and diffused n^{++}/p in section 5.2 of this chapter.
(14) Just after the laser stage, the rear side is totally covered by e-beam evaporated Ti/Al film stack.
(15) and (16) A photolithographic step and Ti and Al wet etching define both emitter and base metal contacts in an interdigitated pattern.
(17) Finally, an annealing at 400 °C for 10 min in H_2/N_2 atmosphere recovers the damage produced during the e-beam evaporation and activates the negative charge in the Al_2O_3/c-Si interface.

The illuminated area on the front side is defined using an extra aluminium thermal evaporation on the front surface. This aluminium layer is properly patterned and aligned face to face with the rear side (electrode side) to act as a shadow mask defining light windows of 3 cm x 3 cm (the busbar is not take into account).

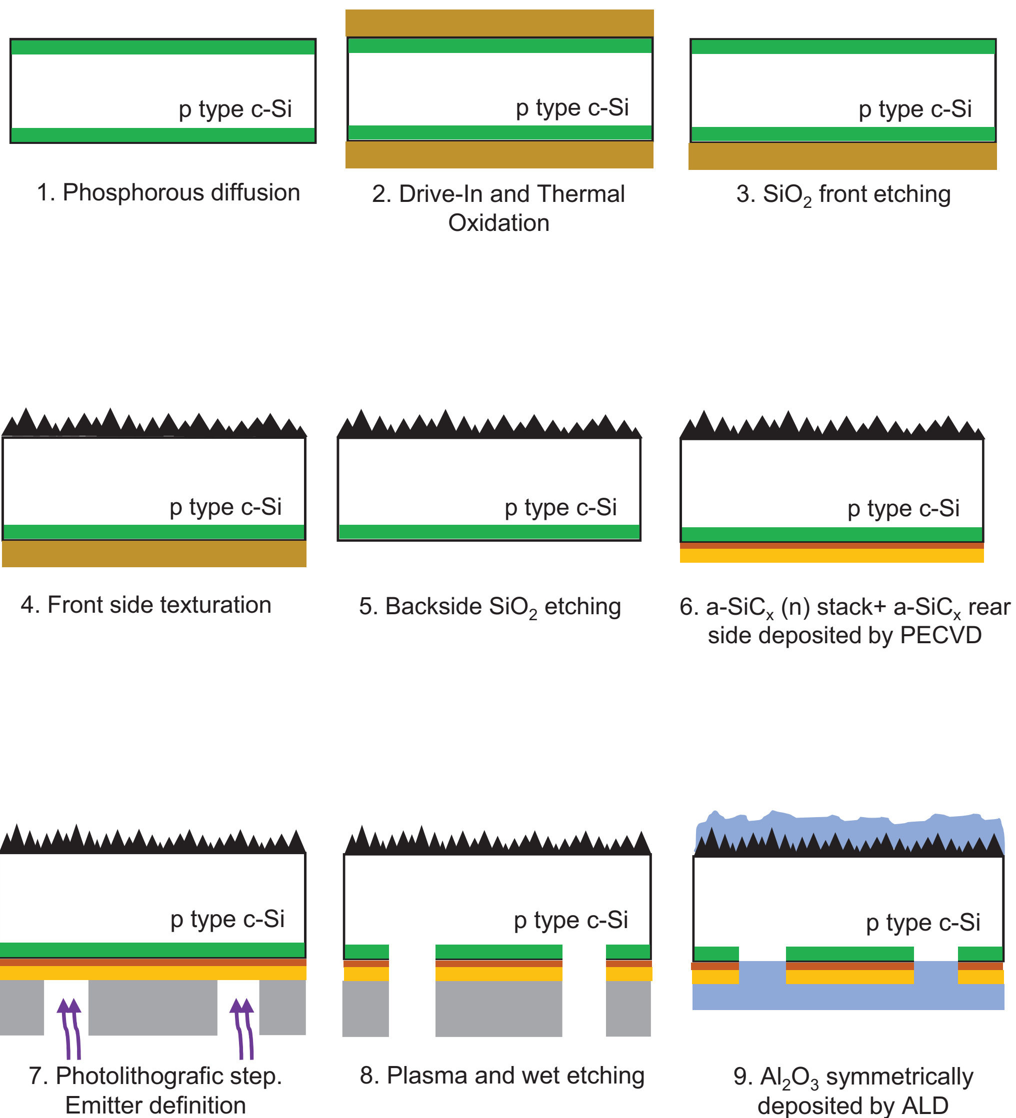
p type c-Si
1. Phosphorous diffusion
p type c-Si
2. Drive-In and Thermal Oxidation
p type c-Si
3. SiO2 front etching
p type c-Si
4. Front side texturation
p type c-Si
5. Backside SiO2 etching
p type c-Si
6. a-SiCx (n) stack+ a-SiCx rear side deposited by PECVD
p type c-Si
7. Photolithografic step. Emitter definition
p type c-Si
8. Plasma and wet etching
p type c-Si
9. Al2O3 symmetrically deposited by ALD

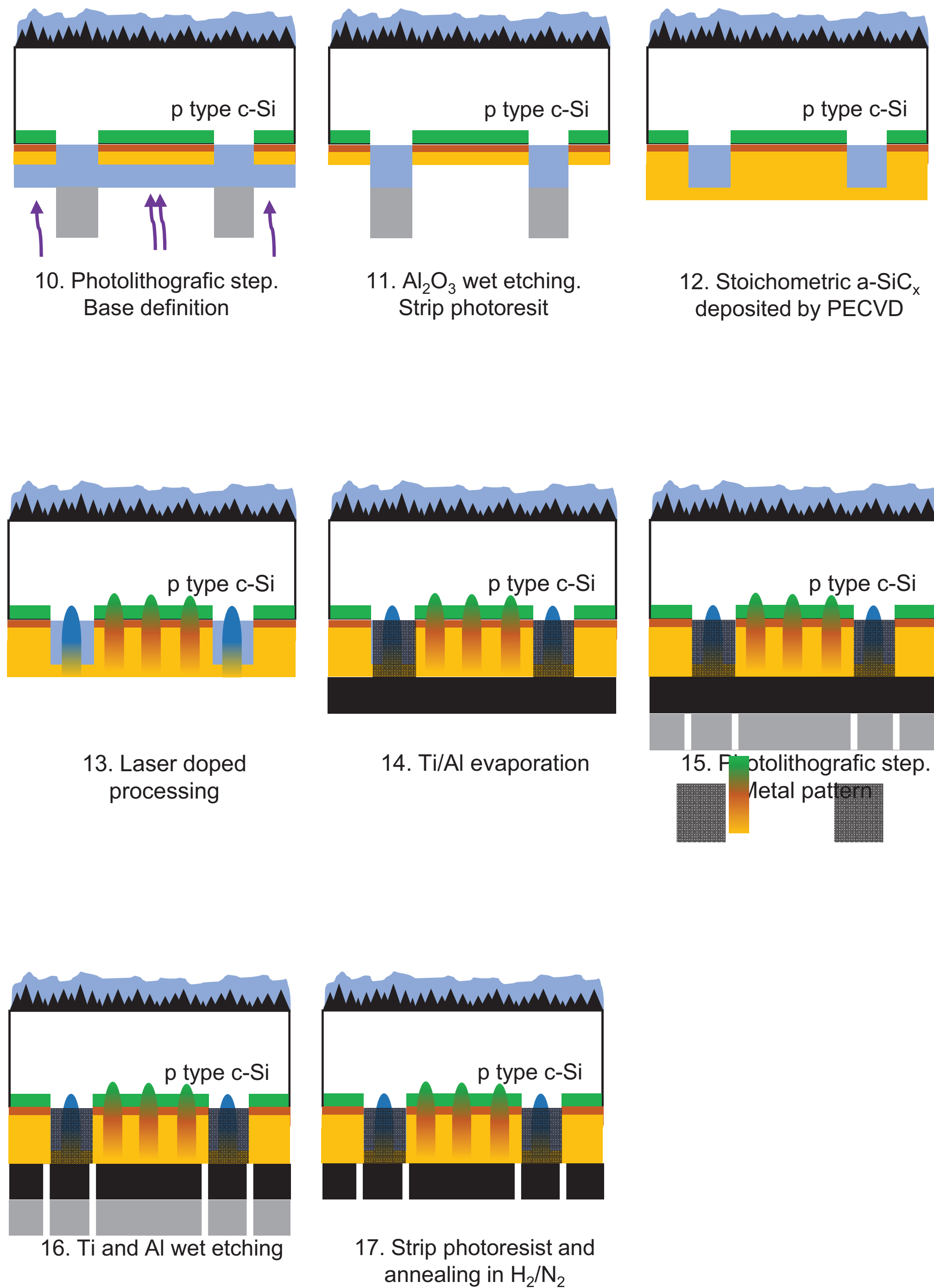

Figure 5.5: Schematic illustration of *Hybrid* IBC fabrication process

Laser spots are defined in a square matrix shape with a pitch of 250 μm determined by the optimization by simulation of trade-off between base resistance and carrier collecting losses [2]. Additionally, different emitter coverages have been considered in our devices following a pattern of 1 spot per base and 2, 3, 4. and 6 spots per emitter region, corresponding to 66, 75, 80 and 85% emitter coverage. Figure 5.5 shows the four different interdigitated metal pattern of the devices developed in this thesis, supported by the corresponding microscope images.

In this study, the laser power is set to 0.9 W and 6 pulses per spot resulting in a 60 μm diameter spot on the dielectric films (figure 5.6).

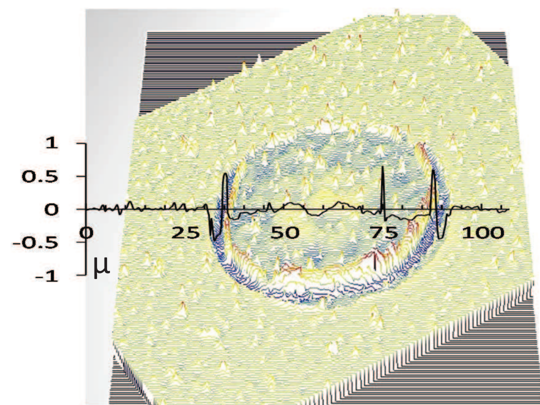

Figure 5.6: Interferometric image of the laser spot int done at 0.9 W. Inset curve of profilometric measurement.

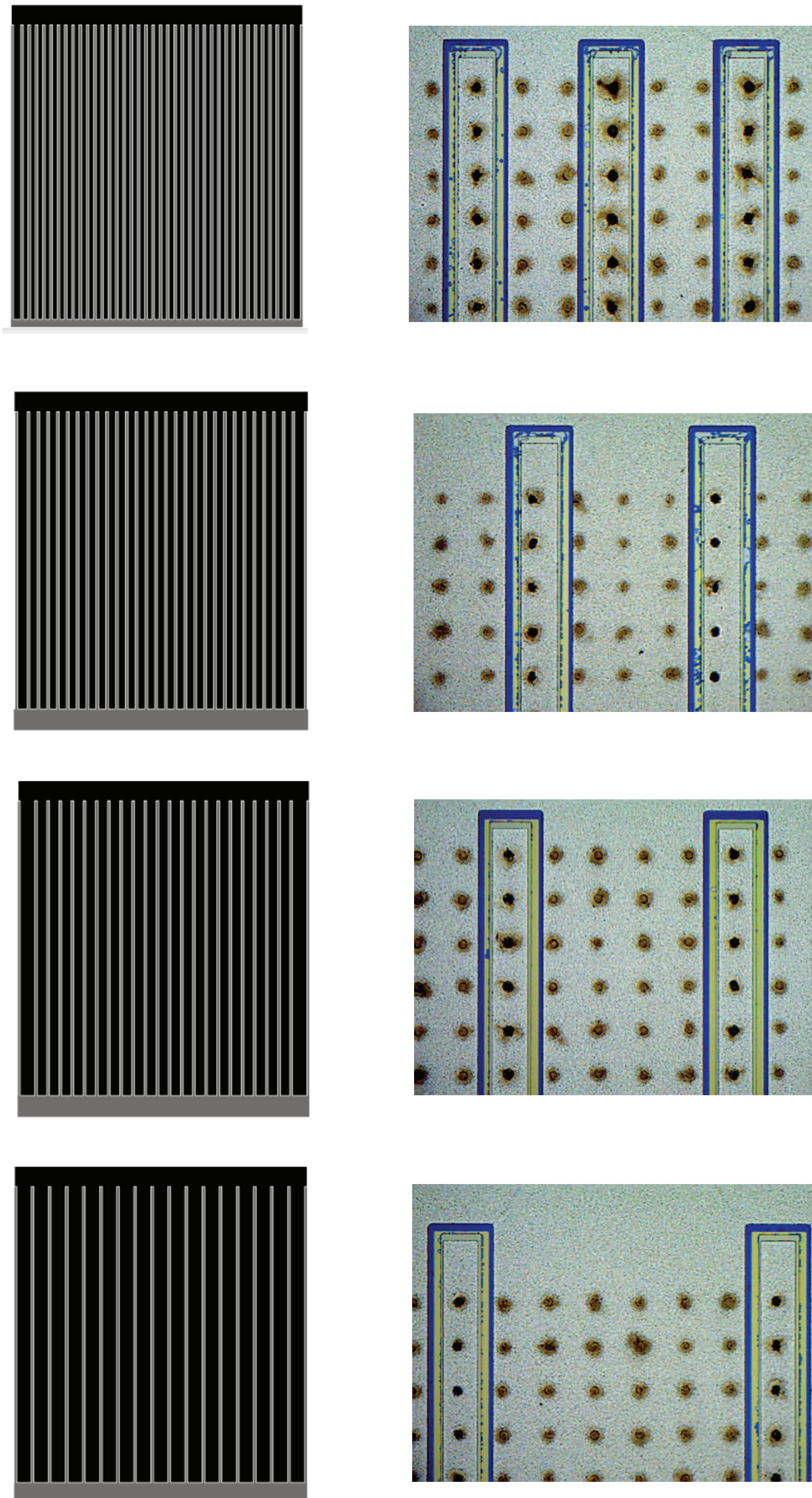

Figure 5.7: Rear interdigitated metal pattern. From top to bottom 66, 75, 80 and 85% emitter coverage. In the right side the corresponding microscopes images.

5.5 J-V measurements and Suns-V_{oc}

In figure 5.8, J-V characteristics and main photovoltaic parameters of the four "hybrid" IBC solar cells are shown. Measurements are taken under standard conditions (AM1.5G, 100 mW/cm^2, 25 °C). Dark measurements and measurements of suns-V_{oc} are also depicted in order to know the influence of the leakage current and the series resistance in the efficiency of the final device [3]. Table 5.1 shows the summary of the results.

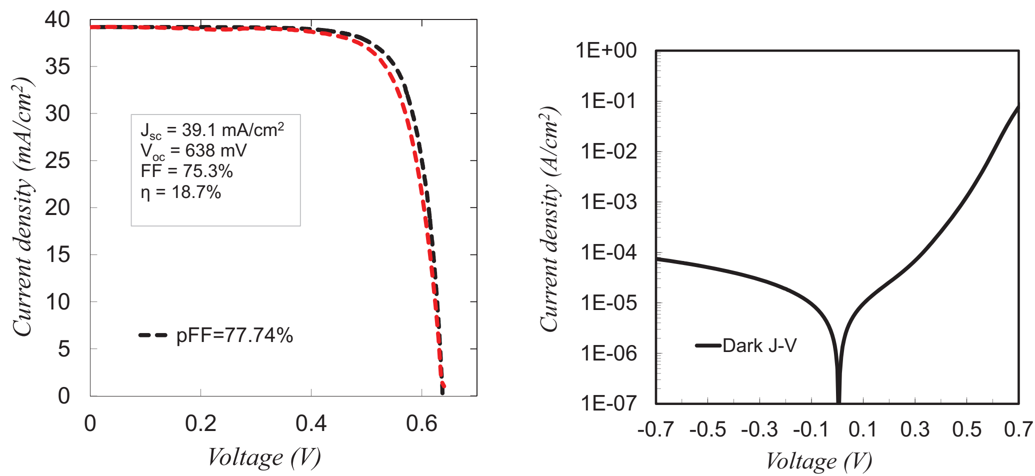

a. Emitter coverage 66%.

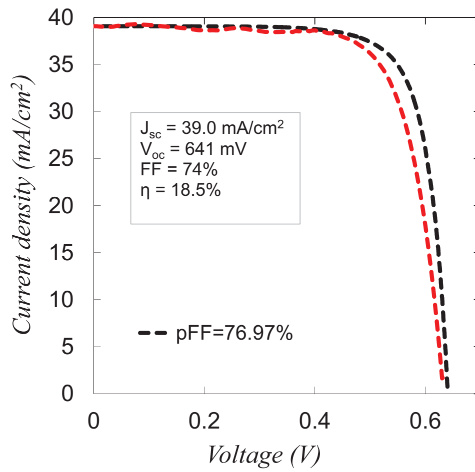

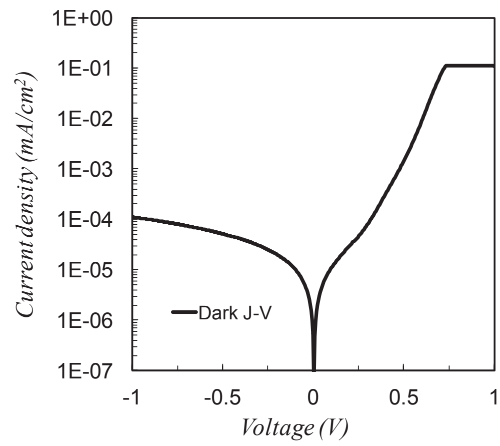

b. Emitter coverage 75%.

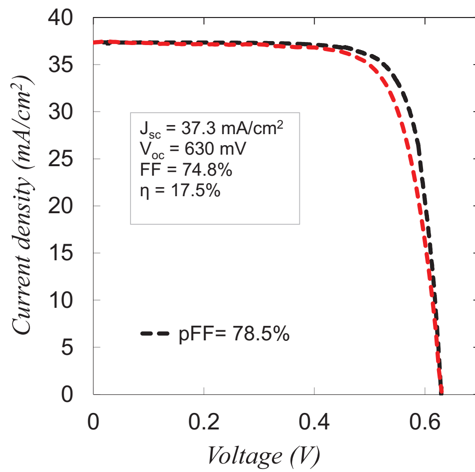

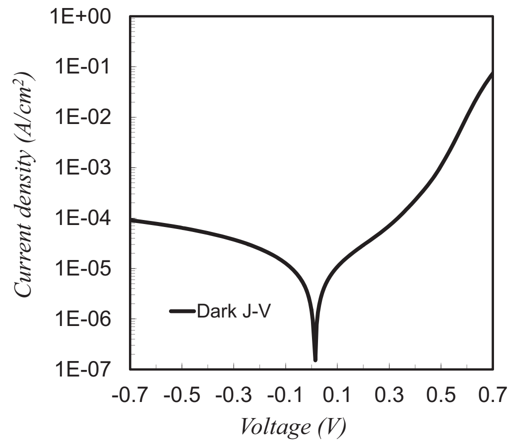

c. Emitter coverage 80%.

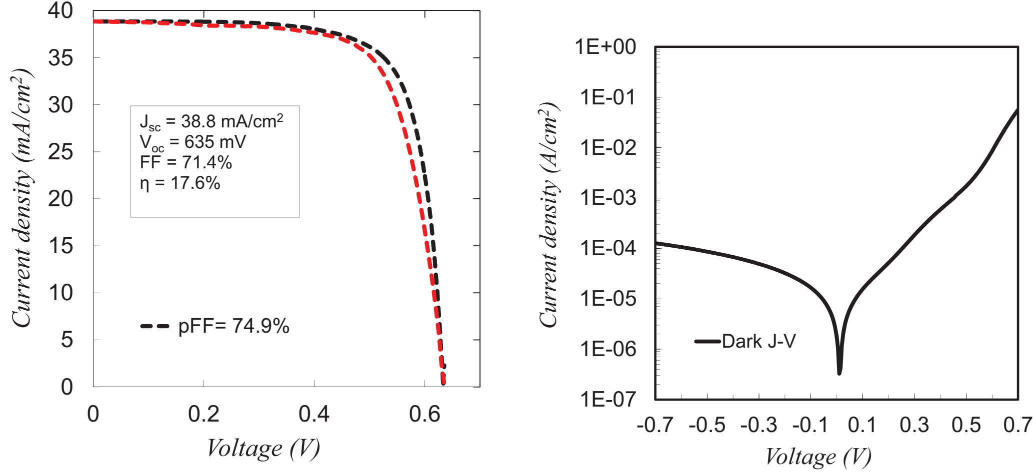

d. Emitter coverage 85%.

Figure 5.8: On the left, J-V measurements of different emitter coverages of "Hybrid" IBC solar cells (red dashed lines) and suns-V_{oc} results (black dashed lines). On the right, J-V Dark measurements results

Emitter coverage (%)	V_{oc} (mV)	J_{sc} (mA/cm^2)	**FF** (%)	**pFF** (%)	η (%)
66	638	39.2	75.4	77.7	18.7
75	641	39.1	74	76.9	18.5
80	630	37.3	74.6	78.6	17.5
85	635	38.8	71.4	74.9	17.6

Table 5.1: Summary of the results of "Hybrid" solar cells with different emitter coverages

For laboratory-scale (9 cm^2 devices) our best efficiency conversion is 18.7% corresponding to the "hybrid" IBC cell with 66% of emitter coverage. From the photovoltaic measurements we can see that low V_{oc} and *FF* are limiting the final efficiency. The difference between *FF* and *pFF* extracted from Suns-V_{oc} measurements indicate some resistance series probably related to the thickness of the metal grid and the lateral resistance of majority carriers. However, this is not the main loss factor. On the other hand, it can be seen a clear relation between leakage currents (identified at the reverse bias) and *FF*. The cell 4 with 85% emitter coverage, presents the highest leakage current density ($\sim$ 0.2 mA/cm^2)

and corresponds to the lowest *FF* (71.4%). This cell has the largest number of emitter spots while the other structures present similar leakage current density and similar *FF*. The increment of the spot increases the probability of shunting and consequently higher current leakages.

5.6 Optical losses analysis and Quantum Efficiency of the "Hybrid" IBC cells

In order to assess the optical properties, a UV-VIS-NIR spectrometer equipped with an integrating sphere is used to measure the diffuse and specular reflection of the "Hybrid" IBC cells fabricated. Reflectance spectra from 300 to 1200 nm is shown in figure 5.9. As it can be seen the reflection losses are nearly zero at a wavelength range from 500 to 1000 nm and the main differences are observed from 1100 nm on corresponding to the photons reaching the rear side of the cell (escape reflectance). Clearly, this difference is related to the emitter coverage of the cells under test. As the emitter coverage increases, the total reflectance decreases (escape reflectance). The calculated lost in J_{sc} related to the optical reflectance is 1.75-1.87 mA/cm^2. In order to analyze in detail the optical losses we perform optical simulations.

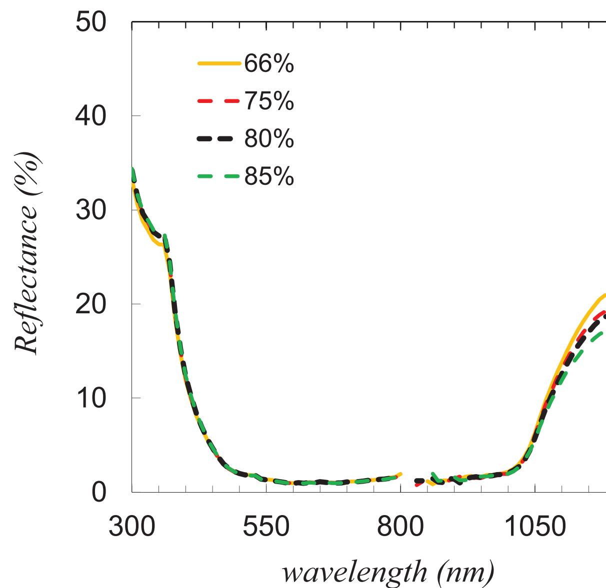

Figure 5.9: Reflectance measurements of the "Hybrid" solar cells fabricated as a function of the wavelength and emitter coverage

5.6.1 Simulation of the solar cell optics

In order to analyze the optical losses, optical simulations are done using the wafer ray tracer tool of PV Lighthouse (*https://www.pvlighthouse.com.au*). The resulting simulation spectra reflectance, absorbance and transmitance are depicted in figure 5.11 as a function of the three different regions involved in the rear side of the "hybrid" IBC cell. Figure 5.10 shows a sketch of the structure for the optical simulations. The front side is considered randomly textured and coated with 90 nm of Al_2O_3. An extrapolated study according to the different IBC structures fabricated and taking into account the percentage of each contribution region as a function of the emitter coverage (see figure 5.7) is also done. The results are shown is the table 5.2 and 5.3 where the J_{sc} reduction due to optical losses are shown.

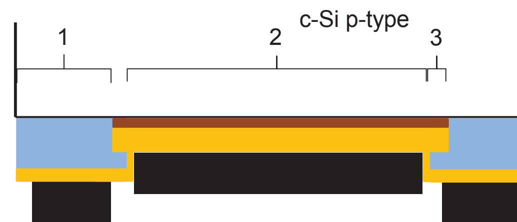

Figure 5.10: Simplified sketch of the "Hydrid" IBC solar cell rear side for optical simulations

- 1. Metallized base region:
  c-Si+90 nm Al_2O_3+50 nm stoichiometric $a-SiC_x$+Ti+Al
- 2. Metallized emitter region:
  c-Si+∼20 nm a-Si(n) stack [2]+75 nm stoichiometric $a-SiC_x$ +Ti+Al
- 3.Non-metallized region:
  c-Si+∼20 nm a-Si(n) stack +25 nm stoichiometric $a-SiC_x$+90 nm Al_2O_3 +50 nm stoichiometric $a-SiC_x$

[2] $a-SiC_x(n)$ stack consists of $\sim$ 4 nm of silicon rich $a-SiC_x(i)/\sim$ 15 nm of phosphorous doped $a-Si$

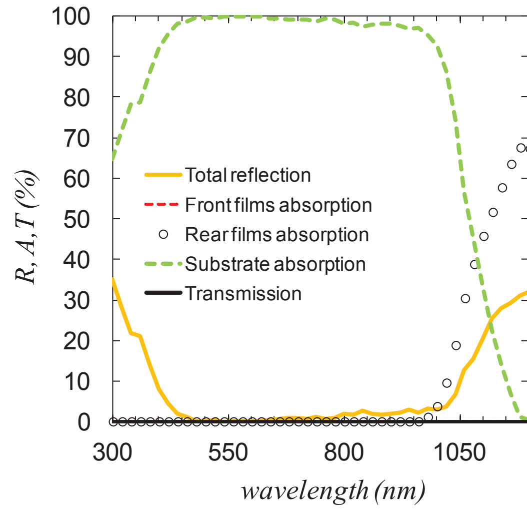

(a) Metallized base region

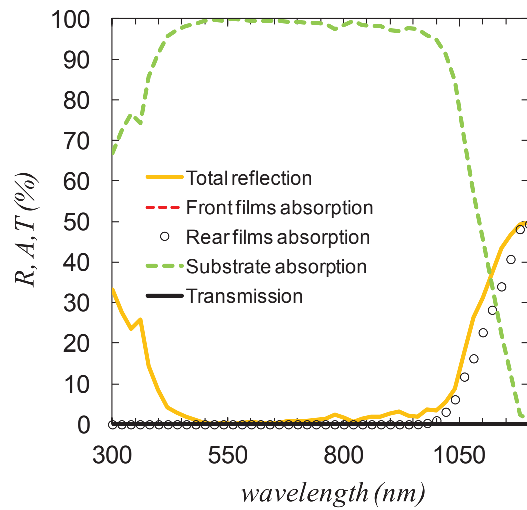

(b) Metallized emitter region

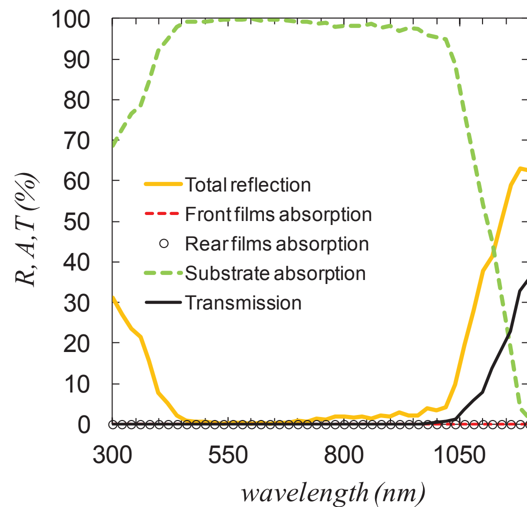

(c) Non-metallized region

Figure 5.11: Optical losses simulation. *https://www2.pvlighthouse.com.au*

		Optical losses $[mA/cm^2]$				
E. cover.	**Distrib.**	**Reflec.**		**Absorp.**		**Trans.**
[%]	Emitter [%] Base[%] Non-metal.[%]	Ext.	Esc.	Front	Rear	
66	50.1	0.51	0.52	$2.53.10^{-15}$	1.55	-
	29.5	0.32	0.52	$1.63.10^{-15}$	0.49	-
	20.4	0.20	0.44	$1.23.10^{-15}$	$3.88.10^{-16}$	0.17
75	63.7	0.65	0.66	$3.21.10^{-15}$	1.96	-
	23.7	0.25	0.41	$1.31.10^{-15}$	0.39	-
	12.6	0.12	0.27	$7.59.10^{-16}$	$2.40.10^{-16}$	0.11
80	68	0.69	0.71	$3.43.10^{-15}$	2.10	-
	20	0.21	0.35	$1.10.10^{-15}$	0.33	-
	12	0.12	0.26	$7.23.10^{-16}$	$2.28.10^{-16}$	0.10
85	79.6	0.81	0.83	$4.02.10^{-15}$	2.46	-
	16.8	0.18	0.29	$9.29.10^{-16}$	0.28	-
	3.6	0.03	0.08	$2.17.10^{-16}$	$6.86.10^{-17}$	0.03

Table 5.2: Optical losses distribution depending on the rear IBC region and emitter coverage

IBC structure **% coverage**	**Reflectance** $[mA/cm^2]$	**Absorption** $[mA/cm^2]$	**Transmitance** $[mA/cm^2]$	**Total loss** $[mA/cm^2]$	**Photogen. (Absorbed)** $[mA/cm^2]$
66	2.51	2.04	0.17	4.72	41.49
75	2.36	2.35	0.11	4.82	41.37
80	2.34	2.43	0.10	4.87	41.34
85	2.22	2.74	0.03	4.99	41.22

Table 5.3: Optical losses distribution depending of rear IBC region and emitter coverage

Major reduction of the optical losses is due to the absence of the front side metallization grid and an adequate design of the front surface texturation and antireflection coating. However, there are still other remaining optical losses that jeopardize the current generation of the solar cell. As it can be seen in graphs (figure 5.11) the largest loss mechanism is the surface reflectance (external and escape) which accounts more than 50% of the total optical losses. The former is caused by non-optimal properties of the antireflection coating, the latter is a result of non-ideal light-trapping, where light rays are reflected out of the cell after multiple internal reflections. As it was obtained in the experimental reflectance, there is a trend in the total reflectance whose value decreases as the emitter coverage increases. The parasitic absorption of the rear films (mainly Ti) participates in an important manner while the transmission losses are considerable in the region without metal.

Taken into account each percentage of the region involved for the different structures and the simulated results (see table 5.2 and 5.3), we can deduce that the non-metallized region is the main responsible of the small difference in the reflectance results. From the optical simulation, it can be seen that escape reflectance loss has a significant weight in the non-metallized region (more than the emitter and base region) and as the size of this region increases, the escape reflectance loss also increases. In other words, as the emitter coverage increases, the non-metallized area decreases and the total reflectance decreases. This result agrees with the experimental reflectance. On the other hand, the losses due to the the rear film absorption and transmitance in the metallized base and non-metallized regions respectively are also very important and then, as the emitter coverage increases the losses due to the rear film absorption and transmitance respectively also decreases.

5.6.2 External quantum efficiency analysis

Figure 5.12a shows the external quantum efficiency EQE values as a function of wavelength of the four IBC structures. Experimental reflectance and internal quantum efficiency (IQE) calculated as $IQE = EQE/(1-R)$ of our best "Hybrid" IBC (66% emitter coverage) are also depicted in figure 5.12b.

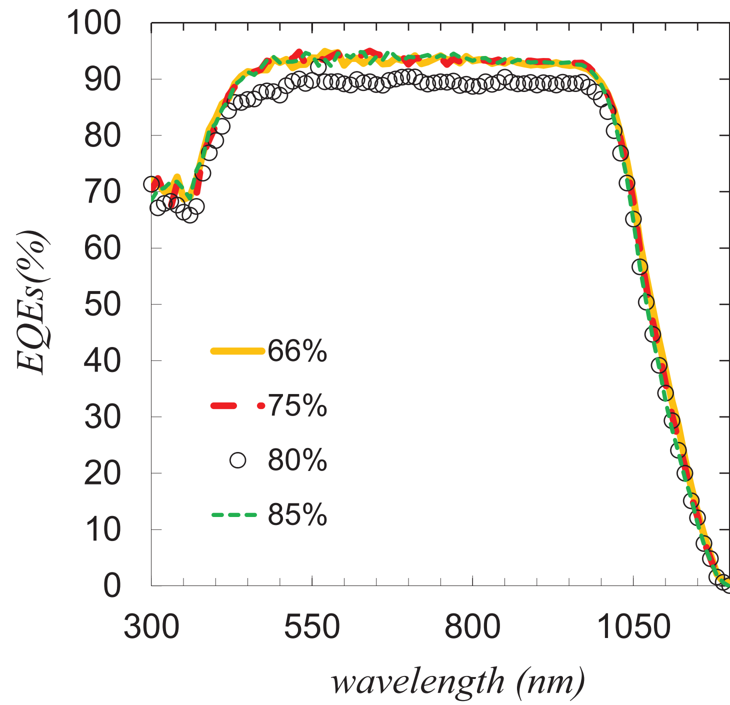

(a)

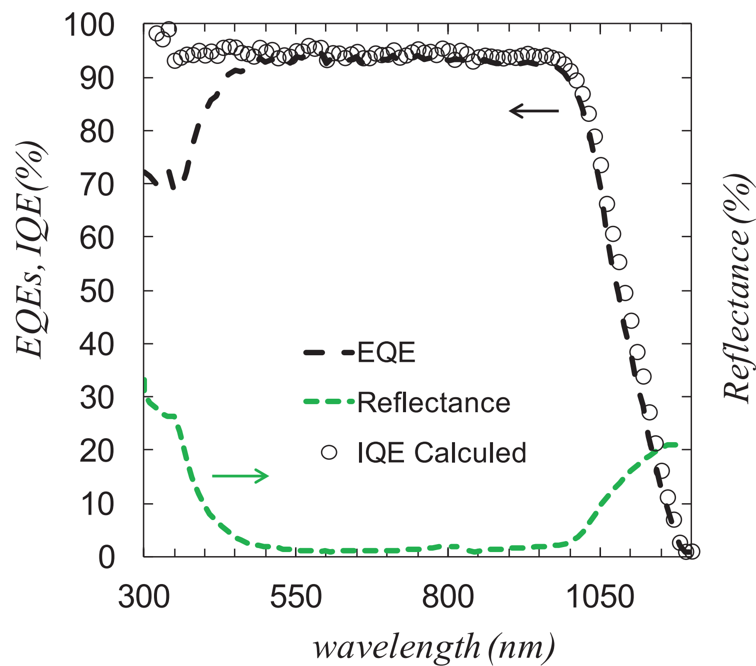

(b)

Figure 5.12: (a) EQEs measurements of the four different "Hybrid" IBC structures (b) EQE, IQE and Reflectance measurements of the "Hybrid" IBC with 66% emitter coverage

The relative high value of EQE in the visible wavelength range (about 95%) involves high J_{sc} ($\sim$ 39 mA/cm^2) in three of the four structures. The lowest EQE corresponds to the IBC with 80 % of emitter coverage (37.3 mA/cm^2). This difference can be partially caused by a non uniform in front surface passivation. The EQE values are strongly impacted by the front surface recombination due to the location of the emitter at the rear side of the cell.

The IQE curve shows a flat response for $\lambda < 960$ nm. No drop is observed at low wavelengths since no front film absorption exits (the Al_2O_3 film does not absorb in the whole photovoltaic range). In order to analyse the impact of the front surface passivation on the V_{oc} values, an approximation to the S_{front} value is obtained by fitting the experimental IQE curve (black circles symbols, figure 5.13) with the simulated IQE values curve done with PC-1D (red dashed lines, in the same figure). The simulated IBC device is simplified by means of a simple back junction structure with the same device features (thickness, substrate doping density and experimental reflectance). Simulations are done for different S_{front} values, 30, 70 and 150 cm/s, resulting 70 cm/s the best choice for the fitting.

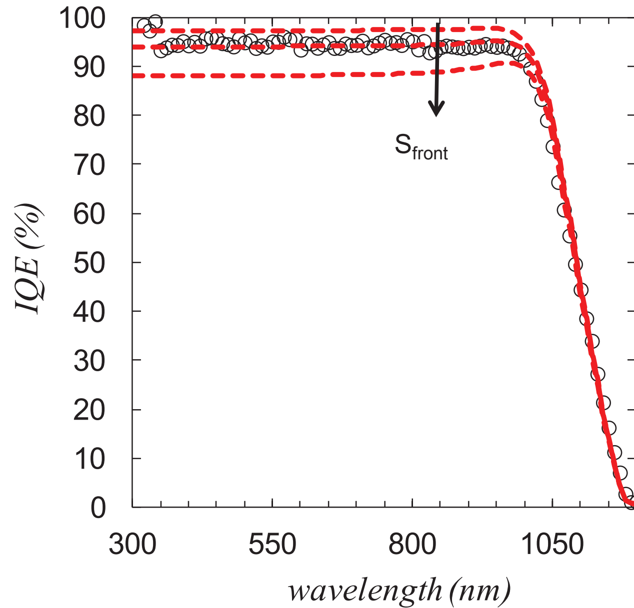

Figure 5.13: Calculated (black circles symbols) and simulated (red dashed line) IQE data of the "Hybrid" IBC cell with 66% of emitter coverage for different S_{front} (30, 70 and 150 cm/s)

We can assume from the S_{front} deduced that the front surface passivation is good enough and the low V_{oc} obtained is probably due to a high recombination

at the rear side. Once the possible influence of a poor passivated front side is eliminated, we are going to focus on the analysis to the rear side of the cells.

The most likely explanation for the low V_{oc} is related the laser-induced crystal damage which can be responsible for limiting the performance of the laser-doped emitter. If the pulse energy is too high, the surface starts being ablated and can introduce damage to the silicon lattice. [4]. These defects are recombination centers locally affecting minority carrier lifetim [5]. On the other hand, during the laser stage, fluctuations in the power laser have been observed and it could be the main cause of having deeper and bigger laser spots than expected resulting in higher lattice damage. This damage strongly increases the recombination rate in the emitter regions.
Furthermore, the final annealing of the devices done at 400 °C to activate the Al_2O_3 passivation can degrade the a-Si(i) increasing the recombination rate at the emitter regions.

Finally, in order to know if the diode ideality factor (n) plays an special role in the final FF, we calculate its value using the experimental dark J-V measurements of the Cell 1 as follow.

$$n = \frac{J}{V_t . \frac{dJ}{dV}} \tag{5.1}$$

We obtain an ideality factor of 1.7 at the maximum power point (see figure 5.14). This value, far away from 1, could be due to either carrier recombination in the space charge region by the laser damage on the crystal lattice or the influence of partial shunting generated during the laser stage. These effects are stronger as the density of laser spots increases in the emitter region.

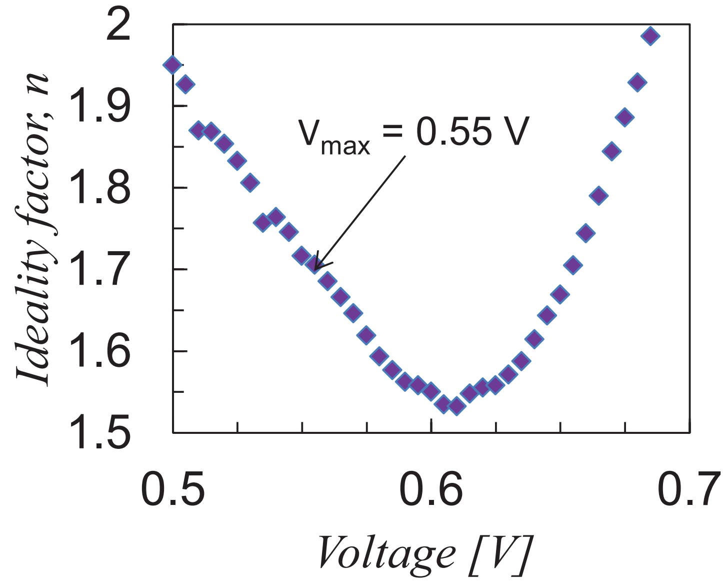

Figure 5.14: Ideality factor of cell 1 as a function of voltage

5.7 Conclusion

In this chapter, a "hybrid" IBC solar cell on p-type substrate has been developed. It was fabricated with laser technology through dielectric layers in a point-like structure for selective emitters and BSF contacts formation. Devices were arranged in four different emitter coverages of 66, 75, 80 and 85%. The selective emitters include an additional thermal phosphorous diffusion step.

The main photocurrent (J_{ph}) loss mechanism is related to a non-ideal front surface passivation (70 cm/s). Furthermore, optical simulation points out to extra J_{ph} losses as a consequence of the back reflector scheme and rear films absorption. Additionally, the low FF and V_{oc} values are also limiting efficiency. Comparing pFF and FF it can be deduced that series resistance is not the main cause for these low values. The relatively high experimental and simulated IQE values demonstrate that the front surface passivation is good enough for not limiting the V_{oc}. Consequently, this parameter is affected by both rear surface recombination and technological issues related to laser processing (parasitic shunting and crystal lattice damage).

As a conclusion, better control of the power laser is needed in order to limit the laser damage in the c-Si lattice. The pulsed mode seems to be more sensitive to instabilities causing fluctuation in the power laser and to increase the pulse duration could be a good alternative to improve the laser stage minimizing the lattice damage. Additionally, the emitter pattern could be modified decreasing the number of spots. That latest suggestion would decrease J_{oe} and would improve the V_{oc}.

Bibliography

[1] D.E Kane and R.M Swanson. Measurement of the emitter saturation current by a contactless photoconductivity decay method. In *18th Photovoltaic Specialists Conference. IEEE*, pages 578–583. IEEE, 1985.

[2] D. Carrió, P. Ortega, I. Martín, G. López, J. M. López-González, A. Orpella, C. Voz, and R. Alcubilla. Rear Contact Pattern Optimization based on 3D Simulations for IBC Solar Cells with Point-like Doped Contacts. *Energy Procedia*, 55:47–52, 2014.

[3] D. Pysch, A. Mette, and S.W. Glunz. A review and comparison of different methods to determine the series resistance of solar cells. *Solar Energy Materials and Solar Cells*, 91:1698–1706, 2007.

[4] M. Okanovic, U. Jäger, M. Ahrens, U. Stute, A. Grohe, and R. Preu. Influence of different laser parameters in laser doping from phosphosilicate glass. In *24th European PV Solar Energy Conference and Exhibition, EUPVSEC, Hamburg (Germany)*, 2009.

[5] M. Abbott, P. Cousins, F. Chen, and J. Cotter. Laser-induced defects in crystalline silicon solar cells. In *31st IEEE Photovoltaic Specialists Conference (PVSC), Orlando*, pages 1241–1244. IEEE, 2005.

Chapter 6

"Cold" Back-contact Back-junction silicon solar cells

The application of the knowledge acquired in previous chapters is the starting point to develop an innovative fabrication process of n-type interdigitated back-contact (IBC) back-junction c-Si solar cells. The main feature is that all the highly-doped regions in the cell have been entirely fabricated through laser processing of dielectric layers, avoiding the high temperature step of the conventional diffusion processes. Combining dielectric layers as both dopant source and passivating layer with laser doping technique drastically simplifies the fabrication process reducing the global thermal budget. Additionally, we have reduced the fabrication process to only two patterning steps. The simplicity of the fabrication process proposed in this chapter significantly reduce time and energy consumption. As a proof of concept, our first "cold" IBC cells have been developed and characterized.

6.1 Introduction

In the first part of this chapter we analyse the minority diffusion length of the samples involved and, as in the same way than in "Hybrid" IBC of the previous chapter, the sheet resistance, the dark J-V measurements of the new precursor diodes to study the dark electrical characteristic at different laser conditions and the optical properties. Due to the power fluctuations detected in the experimental done in chapter 5 and the lattice damage induced into the c-Si structure, two

pulse duration (100 ns and 400 ns) will be compared in order to determine which one provides better results. Special attention will be taken into the study of the layers corresponding to the emitter region, since now no conventional dopant diffusion is carried out. The results of these studies are used to fabricate the "cold" IBC solar cells.

The structure cross-section of the "cold" IBC cell designed and fabricated is depicted in figure 6.1.

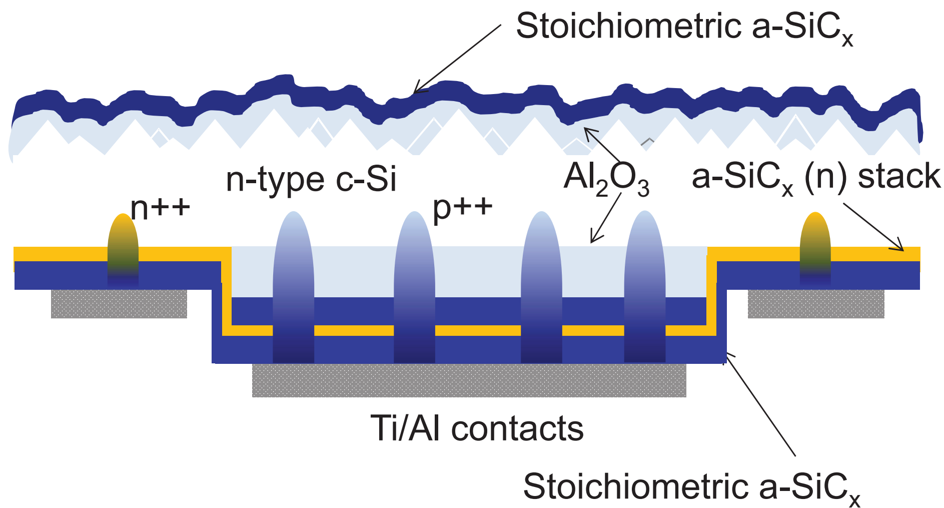

Figure 6.1: Cross-section of the "cold" IBC structure

The second part of this chapter is focus on the fabrication and characterization of a "cold" IBC applying the pulsed laser mode with a pulse duration of 100 ns trough the stack developed to form punctual emitter regions (p^{++}). Additionally, a pulse duration of 400 ns is employed for the BSF formation (n^{++}). Thus, two laser stage are needed to define both contacts. In the third part, we apply a laser pulse duration of 400 ns in either punctual emitter and punctual BSF formation. In this case, two laser stages are also needed in order to apply the power laser condition that best suits to each layer stack.

Fundamental parameters of the fabricated solar cell are obtained from EQE, IQE, suns-V_{oc} and J-V measurements and as a function of the different emitter coverages.

6.2 Surface passivation and minority diffusion length

Samples used for the different experiments consist of a c-Si n-type substrates with a thickness of 275 ± 10 μm and a base resistivity of 2.5± 0.5 Ωcm.
On one test sample we emulate the Al_2O_3 passivated surfaces that can be found in the final device by defining, one side randomly textured and both faces symmetrically passivated with 50nm Al_2O_3 and 35 nm of stoichiometric $a-SiC_x$. Another sample is used to assess the surface passivation provided by the intrinsic Si-rich $a-SiC_x$ film. The upper limit to the surface recombination velocity ($S_{eff,max}$) is estimated in 9.5 cm/s and 13 cm/s respectively, which corresponds to one-sun effective lifetimes of 1.4 ms and 1 ms as it can be seen in figure 6.2.

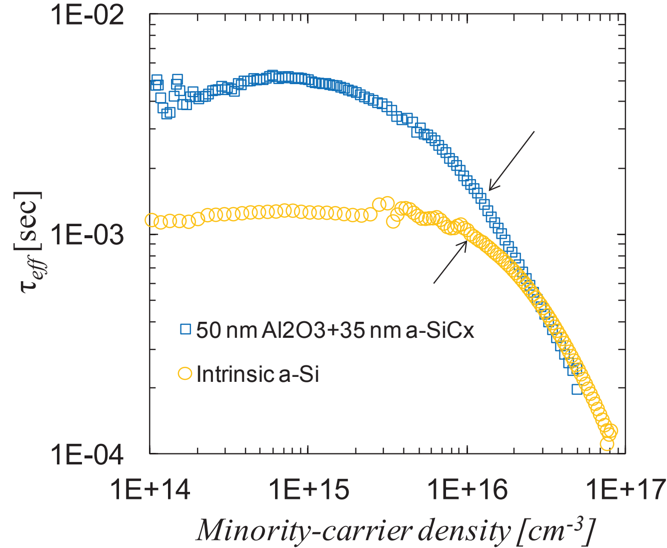

Figure 6.2: Effective minority-carrier lifetime as a function of the carrier density. - Arrows show the values for 1 sun injection level)

In order to assure a high quality substrate suitable for the fabrication of high-efficiency IBC solar cells, we calculated the effective minority diffusion length (L_{eff}) in the bulk considering that it must be at least four times longer than the wafer thickness [18]. Accordingly to equation 3.23 and using the τ_{eff} values at 10^{15} cm^{-3} and a hole diffusivity of 11.93 cm^2/s, L_{eff} is calculated as 2442 μm in the case of the sample with Al_2O_3 and 1245 μm in the case of $a-SiC_x(i)$ sample. Therefore, the surface passivation and the high quality of the c-Si sample

guarantee the conditions for the IBC fabrication.

6.3 Sheet resistance

Sheet resistances as a function of the laser power measured with four-point probe are shown in figure 6.3b. For this experimental a sample is specially prepared depositing on the front surface of a n-type c-Si sample, 50 nm of Al_2O_3 + 35 nm of stoichiometric $a - SiC_x + a - SiC_x(n)$ + 35 nm of stoichiometric $a - SiC_x$ (figure 6.3a). This surface is irradiate with the laser overlapping pulses to avoid any undoped area that could disrupt the current flow between the probes. Six areas of 1 cm x 1 cm with different power laser conditions are irradiated.

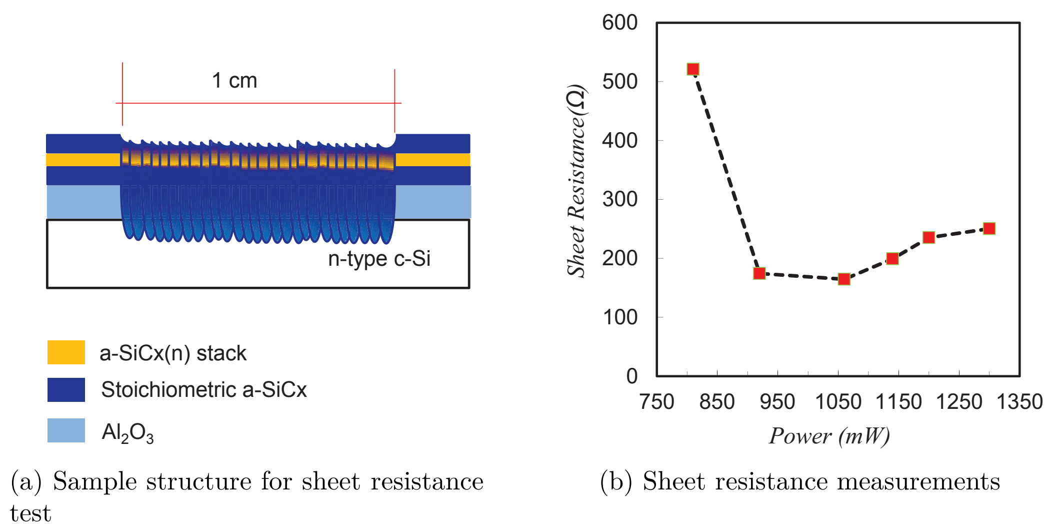

(a) Sample structure for sheet resistance test

(b) Sheet resistance measurements

Figure 6.3: Study of the sheet resistance as a function of the laser power. The number of pulses and the pulse duration is fixed to 6 and 100 ns respectively

The result of these measurements should not be assumed as precise values of doping level, but can be used to compare the trend between different laser parameters and give us a power laser approximation. In this experimental laser powers between 920 to 1050 mW show the lowest sheet resistance and consequently the most doped region.

6.4 Precursor samples. Diodes

The diodes under test consist of devices of 0.42 cm x 0.42 cm size. The objective of this experimental is determine the optimum power laser conditions to create the p^{++} (laser pulse duration fixed at 100 ns) and n^{++} (laser pulse duration fixed at 400 ns) regions. The electrical behaviour is evaluated from the results of dark J-V measurements. The experimental starts with c-Si sample of 275 ± 10 μm thickness and a resistivity of 2.5 Ωcm. After and RCA cleaning the samples are ready for layer depositions.

6.4.1 p^{++} region

The sample (n-type) is double side deposited with 50 nm of Al_2O_3. The sample is annealed at 375 °C for 10 min in order to activate the surface passivation. Then, a 35 nm of stoichiometric $a-SiC_x$ following by $a-SiC_x(n)$[1] stack and 35 nm stoichiometric $a-SiC_x$ is deposited by PECVD on the front side. On the rear side, the Al_2O_3 is etched and we deposit the $a-SiC_x(n)$ stack and 35 nm of stoichiometric $a-SiC_x$ as capping layer. Figure 6.4 shows a cross-section of the sample for testing the laser process.

The front side of the sample is laser-processed with pulsed laser mode (6 pulses and 100 ns of pulse duration) forming a hexagonal matrix of spots separated a distance (*pitch*) of 300 μm. Each matrix corresponds to one device. The laser power is modified in each device to elucidate those that lead to higher quality junctions. Notice that, despite the intermediate a-Si(n-doped) layer included in such multilayer, punctual p^{++} regions could be formed after the laser step. This is a very remarkable result, as it allows to simplify the IBC fabrication process by eliminating one photolithographic step, i.e. p^{++} regions can be created without eliminating the phosphorous source layer. As it can be seen in figure 6.4, the Al_2O_3 layer is directly onto c-Si surface, while the a-$SiC_x(n)$ stack is on the 35 nm thick stoichiometric a-SiC_x layer. The laser process melts the c-Si surface mostly incorporating the closer aluminium atoms.
The rear side is processed to create ohmic point contacts with 600 μm pitch and a laser pulse duration of 400 ns.

After the laser processing steps, the sample is ready to be contacted with

[1] $a-SiC_x(n)$ stack consists of $\sim$ 4 nm of silicon rich $a-SiC_x(i)$ and $\sim$ 15 nm phosphorous doped a-Si

evaporated Ti/Al stack. A final annealing step at 275 °C in N_2/H_2 atmosphere is done in order to recover the damage due to e-beam evaporation and to improve the contacts.

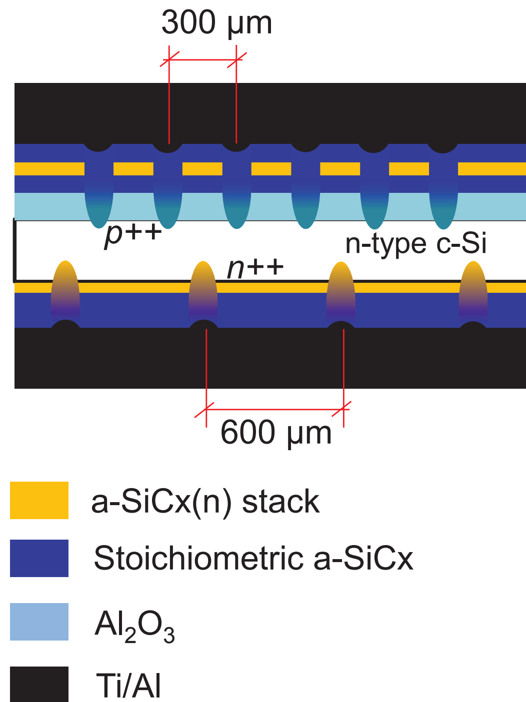

Figure 6.4: p^{++}/n diode scheme of the test sample fabricated for measuring the electrical behaviour and to identify the optimum laser power conditions with pulsed laser mode (6 pulsed and 100ns)

The results of the dark J-V measurements of the p^{++}/n junctions are presented in figure 6.5. The current density is calculated dividing the measured current by the device area.

The results obtained show a rectifying behaviour in all the diodes irradiated from 810 mW to 1100 mW confirming the p-type character of the laser processed regions.

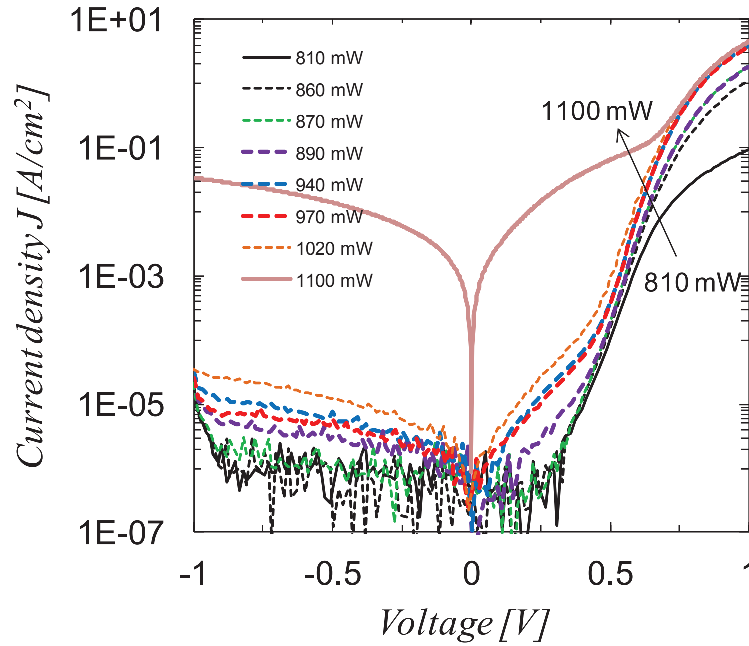

Figure 6.5: Dark J-V measurements of diodes done with pulsed mode (6 pulses and laser pulse duration of 100 ns) and at different power laser conditions

The leakage current observed in the reverse biased region was also rather low except for the 1100 mW case in which the r_{shunt} is clearly hiding the diode curve in forward voltages. In all cases the dark J-V curves flatten at high forward voltages. This behavior due to ohmic losses in the series resistance typically hinders the exponential region of the diode characteristic. The series resistance decreases as the power laser is increased in the range under evaluation. Considering both series resistance and level of leakage current, the diodes show optimum electrical behavior in the range of 940 mW to 970 mW .

6.4.2 n^{++} region

A similar sample is fabricated with the p-type substrate where we define punctual n^{++} regions. Notice that in the final device these regions will play the role of base contacts creating n^{++}/n junctions. However, n^{++}/p junctions are more sensitive to the quality of the n^{++} regions. The sample is double side deposited with 50 nm of Al_2O_3. An annealing step at 375 °C at 10 min activate the surface

passivation. Then, a 35 nm of stoichiometric $a - SiC_x$ is deposited on the rear side and the Al_2O_3 of the front side is etched with HF solution dip. After another RCA cleaning, the front surface is ready to be deposited with an $a - SiC_x(n)$ stack and 35 nm of stoichiometric $a - SiC_x$ as capping layer (figure 6.6).

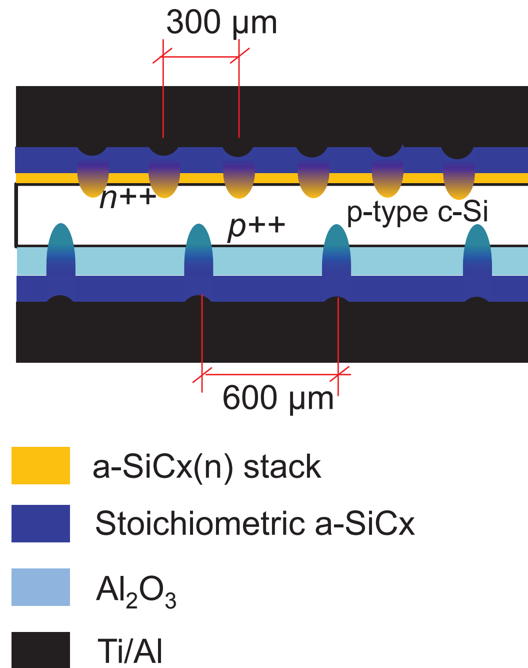

Figure 6.6: n^{++}/p diode scheme of the test sample fabricated for measuring the electrical behaviour and to identify optimal laser power conditions

The front side is laser-processed with a laser pulse duration of 400 ns and different powers forming the same matrix structure than in the previous sample. The rear side is processed to create ohmic point contacts with 600 μm pitch and 400 ns of pulse puration. After the laser processing steps, the sample is metal contacted with evaporated Ti/Al stack and annealed at 275 °C for 10 min.

Dark J-V measurements are presented in figure 6.7. Similar results are obtained from the whole range of power laser studied. Nevertheless, we can distinguish the best behaviour in the diodes done from 1000 to 1170 mW. The influence of the series resistance at high forward voltage flat all the curve in a similar way corresponding to a very similar ohmic losses.

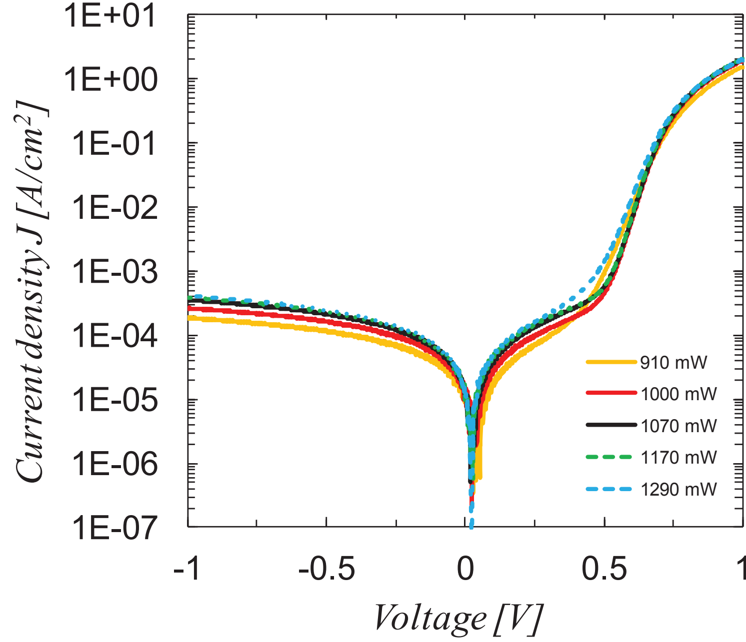

Figure 6.7: Dark J-V measurements of n^{++}/p diodes done with a fixed laser pulse duration of 400 ns and at different power laser conditions

6.5 Emitter saturation current (J_{oe})

Emitter saturation current density (J_{oe}) is determined measuring effective lifetime before and after the laser stage. The sample consists of a n-type c-Si in which the front side is covered with 50 nm of Al_2O_3 + 35 nm stoichiometric $a-SiC_x$ + ∼ 20 nm $a-Si(n)$ stack + 35 nm stoichiometric $a-SiC_x$ as in the final solar cell. The rear side is passivated with 50 nm Al_2O_3. The test structure is shown in figure 6.8. Then, we irradiate the front surface following a squared pattern with a pitch of 600 μm. Laser conditions are the optimum ones determined in the previous section: pulsed laser mode (6 pulses), pulse duration of 100 ns and 970 mW of laser power. The observed loss of the τ_{eff} after the laser stage can be assumed caused by the recombination induced by the laser processed regions.

J_{oe} is determined from the slope of the $1/\tau_{eff}$ vs. Δn (excess carrier density, cm^{-3}) at high injection using the "slope" method [1] (see Fig. 6.9). The slope of the inverse lifetime is then proportional to J_{oe} according to the equation:

$$\frac{1}{\tau_{eff,f}} = \frac{1}{\tau_{eff,o}} + \frac{J_{oe}}{qn_i^2W}\Delta n \qquad (6.1)$$

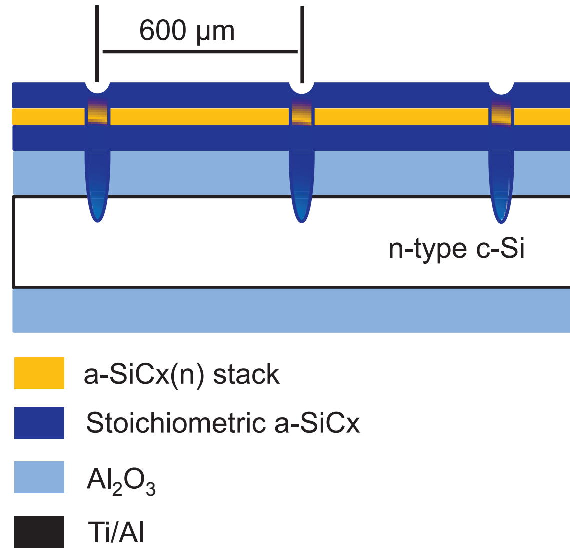

Figure 6.8: Test structure of the emitter region for the measurement of the minority carrier lifetime and determination the J_{oe}

where $\tau_{eff,f}$ is the final effective carrier lifetime (after the laser stage), $\tau_{eff,o}$ is the initial effective carrier lifetime (before the laser stage), q is the elementary charge, n_i the intrinsic carrier concentration, Δn is the excess minority carrier density per unit volume and W the wafer thickness.

Emitter saturation current density of 8 fA/cm^2 is obtained (see figure 6.9) and the J_{oe} of the laser processed area ($J_{oe,cont.}$) can be deduced taking into account the density of laser spots (related to the pitch). The number of spots per cm^2 involved in the sample is 266 spots. On the other hand, the contacted area is not clearly defined as it can be seen in figure 6.9. By the inspection of the spot, we determine a contacted area of 30.10^{-6} $\pm$3.10^{-6} cm^2.

Then, $J_{oe,cont.}$ can be calculated as follow.

$$J_{oe,cont.} = \frac{J_{oe}}{NA_{cont.}} \tag{6.2}$$

where N is the numbers of spots per cm^2 and $A_{cont.}$ is the contacted area, resulting in:

$$J_{oe,cont.} = 1.0 \pm 0.1pA/cm^2$$

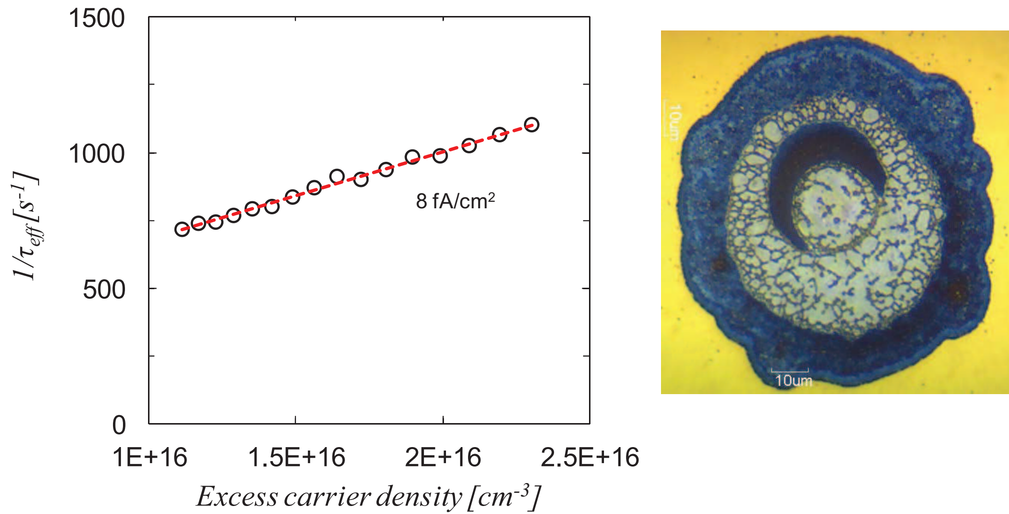

Figure 6.9: Determination J_{oe} using the "slope method" for the sample processed with fixed pulse duration of 100 ns, 6 pulses and 970 mW. On the right, optical image of the spot. The gray area corresponds to the contacted region.

6.6 "Cold" IBC structure and fabrication process.

Solar cells are fabricated on n-type float zone (FZ) c-Si wafers. The starting thickness is 275± 10 μm and a base resistivity of 2.5± 0.5 Ωcm. The detailed fabrication process is presented in figure 6.10.

1. The front side is randomly textured with a TMAH solution, while the rear side is protected by thermally grown SiO_2.
2. Then, the SiO_2 is removed and the wafer is cleaned following a RCA sequence.
3. Both sides are coated with a 50 nm thick of Al_2O_3 layer grown by thermal-ALD.
4. The sample is annealed at 400 °C for 10 min in H_2/N_2 atmosphere, in order to activate the negative charge in the Al_2O_3/c-Si interface to improve the passivation. After that, a 35 nm thick of stoichiometric $a-SiC_x$ layer is deposited on both sides by PECVD. As in the case of the "hybrid" IBC fabrication, the reason to include $a-SiC_x$ as a capping layer on Al_2O_3 is chemical protection of the Al_2O_3 films during cleaning/etching steps and to improve the laser contact formation on c-Si solar cells.
5. A photolithographic step defines the emitter regions.
6. The rear $a-SiC_x$ layer is removed from undesired regions (base regions) with

plasma etching (CF_4).
7 and 8. The rear Al_2O_3 layer is wet etched from the base region with a HF solution and the photoresist is stripped.
9. After a RCA cleaning, we deposit on the entire rear side the $a-SiC_x(n)$ stack and 35 nm thick of stoichiometric $a-SiC_x$.
10. BSF (n^{++}) and emitter (p^{++}) regions result from the laser irradiation of these dielectric layers applying a pulsed Nd-YAG 1064 nm laser in the nanosecond regime. Contacts are defined in a point-like structure with a pitch of 250 μm. The laser conditions are 100 ns of pulse duration, 6 pulses per spot and 1100 mW of laser power for the point-like emitter formation and 400 ns of pulse duration and 1070 mW of laser power for the point-like BSF formation. The reason to apply 1100 mW instead of the optimum laser power for the emitter formation, i.e. 940-970 mW is because during the laser stage most of the spots were not formed at this power and it was necessary to increase it in order to form all the punctual emitters. That means that the energy delivered per unit of area (fluence) also increases and consequently its effects on the crystal lattice.
Following the same structure that in the "Hybrid" IBC, four emitter coverage are defined: one base laser spot per 2, 3, 4 or 6 emitter spots, corresponding to 66, 75, 80 and 85 % emitter coverage respectively (see figure 6.11).
11. A Ti/Al stack is deposited on the whole rear side.
12 and 13. The metal interdigitated pattern is defined by photolithographic step and wet etching in H_3PO_4 solution. 14. Finally, the photoresit is stripped and the wafer is annealed in a N_2/H_2 atmosphere at 275 °C for 10 minutes.

The illuminated area on the front side is defined using an extra aluminium thermal evaporation on the front surface. This aluminium layer is properly patterned and aligned face to face with the rear side (electrode side) to act as a shadow mask defining light windows of 3 cm x 3 cm as in the same way than "Hybrid" solar cells.

Step 1. Front surface texturation

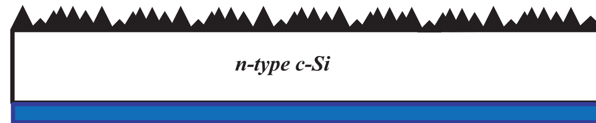

Step 2. Rear SiO_2 etching

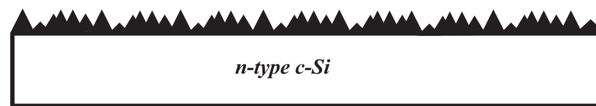

Step 3. 50 nm Al_2O_3 both sides deposition

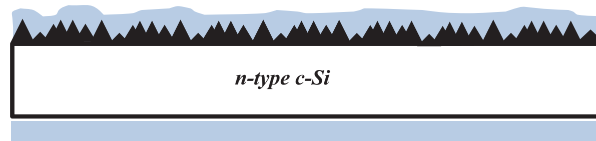

Step 4. 35 nm Stoichiometric $a-SiC_x$ both sides deposition

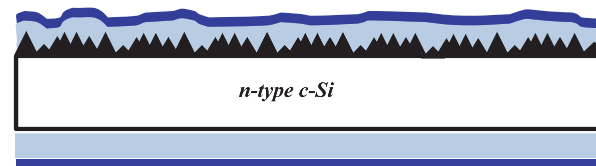

Step 5. Photolithograpic step. Emitter definition

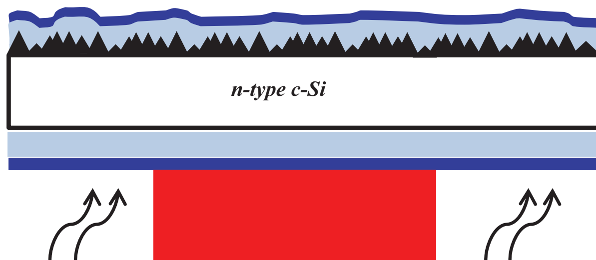

Step 6. Plasma (CF_4) Stoichiometric $a - SiC_x$ etching

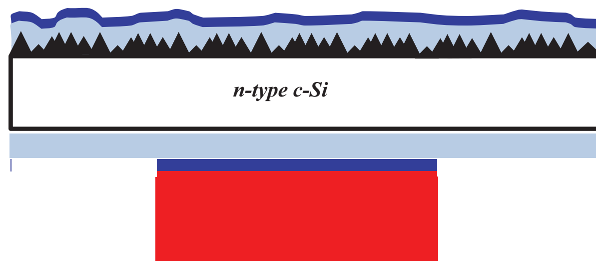

Step 7. Al_2O_3 etching

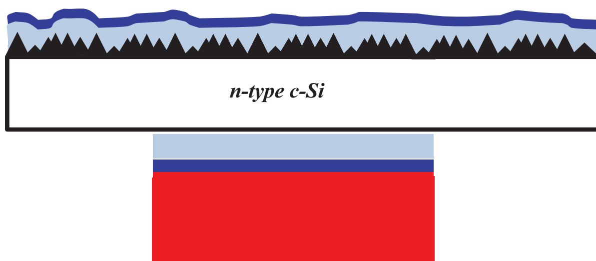

Step 8. Photoresist stripping

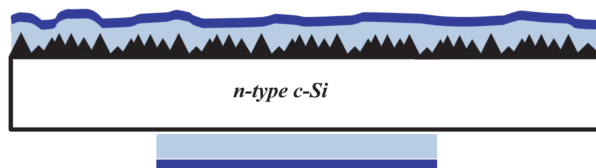

Step 9. $a - SiC_x(n)$ stack and 35 nm Stoichiometric $a - SiC_x$ deposition

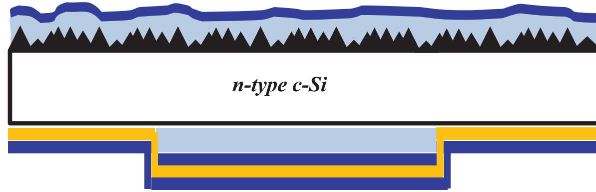

Step 10. Laser stage. Highly doped region formation

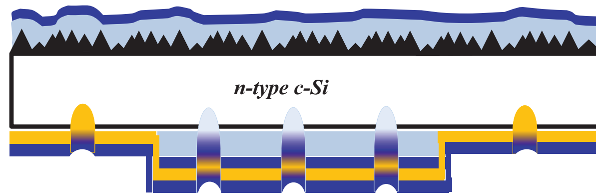

Step 11. Ti/Al e-beam evaporated

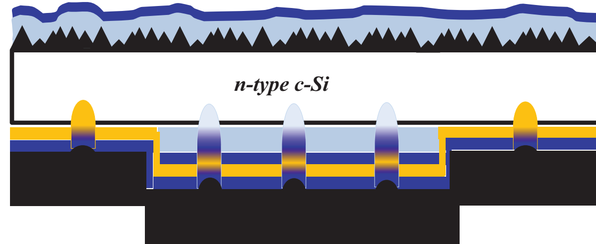

Step 12. Photolithografic step. Metal contact definition

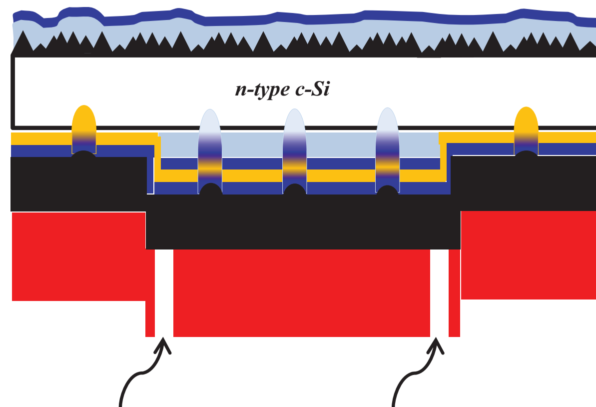

Step 13. Ti/Al etching

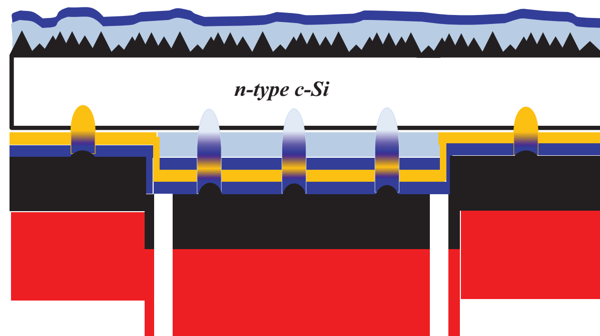

Step 14. Photoresist stripping

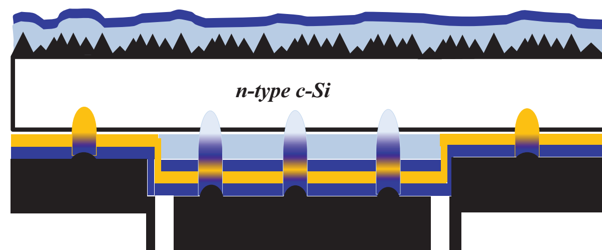

Figure 6.10: Fabrication process of the "cold" IBC solar cell

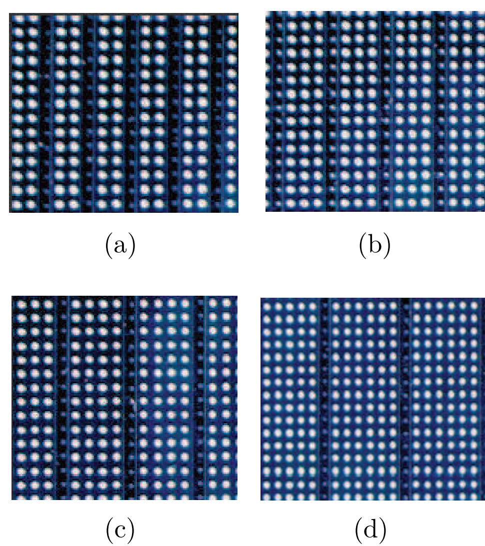

(a) (b)

(c) (d)

Figure 6.11: IBC solar cell images done under magnifying glass corresponding to different emitter coverages. (a) 66%. (b) 75%. (c) 80% and (d) 85%

We have to highlight that the whole fabrication of the "cold" IBC process implies no thermal steps beyond 400 °C. Furthermore, the innovative layer structure designed allows to form p^{++} regions despite the presence of n-type layer (a-$SiC_x(n)$) in the laser process. This fact is particularly remarkable because it drastically simplifies the IBC fabrication process requiring just one photolithographic step in addition to the metal pattern definition.

6.7 J-V measurements and Suns-V_{oc}

In this section present the electrical results of the four "cold" IBC solar fabricated. In figure 6.12 dark J-V measurements and main photovoltaic parameters are shown together with Suns-V_{oc} in order to compare and to analyze the effect of the series resistance on the FF. Measurements are taken under standard conditions (AM1.5G, 100 mW/cm^2, 25 °C) and summarized in the table 6.1.

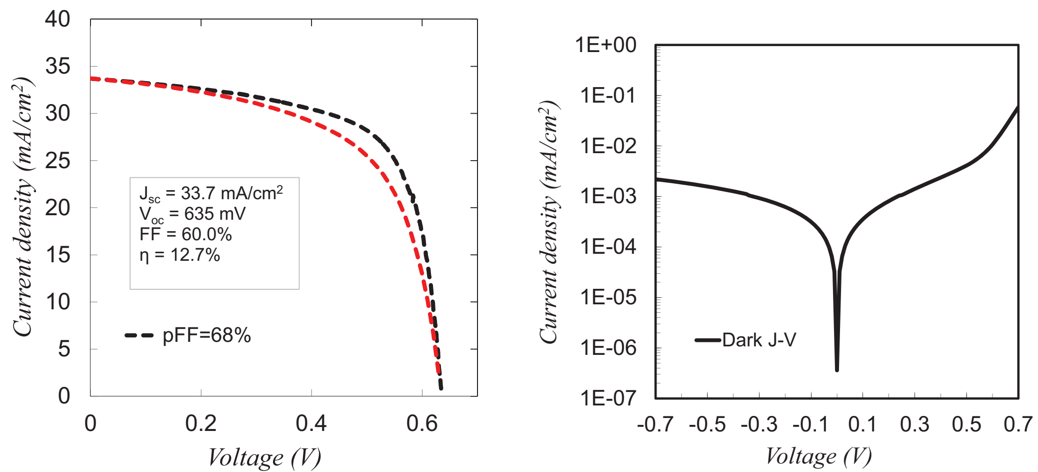

a. Emitter coverage 66%.

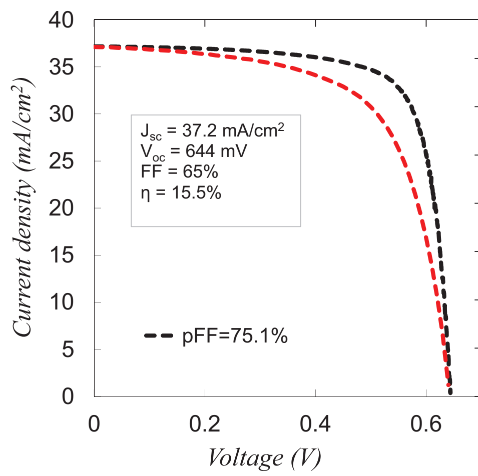

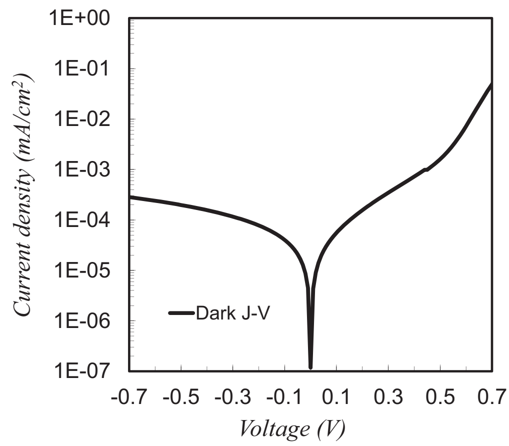

b. Emitter coverage 75%.

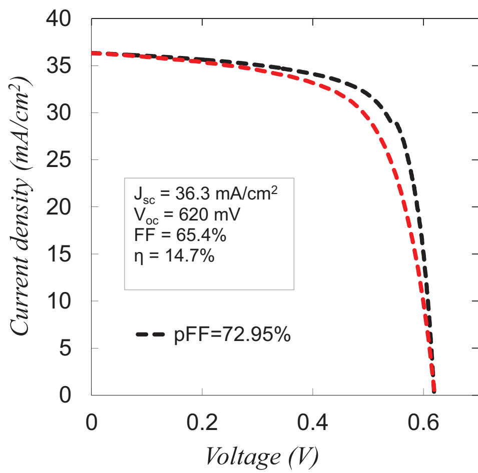

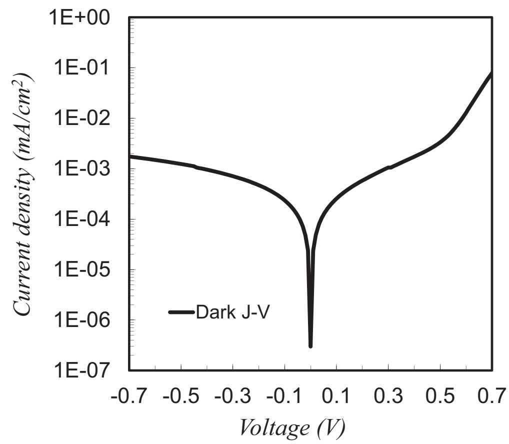

c. Emitter coverage 80%.

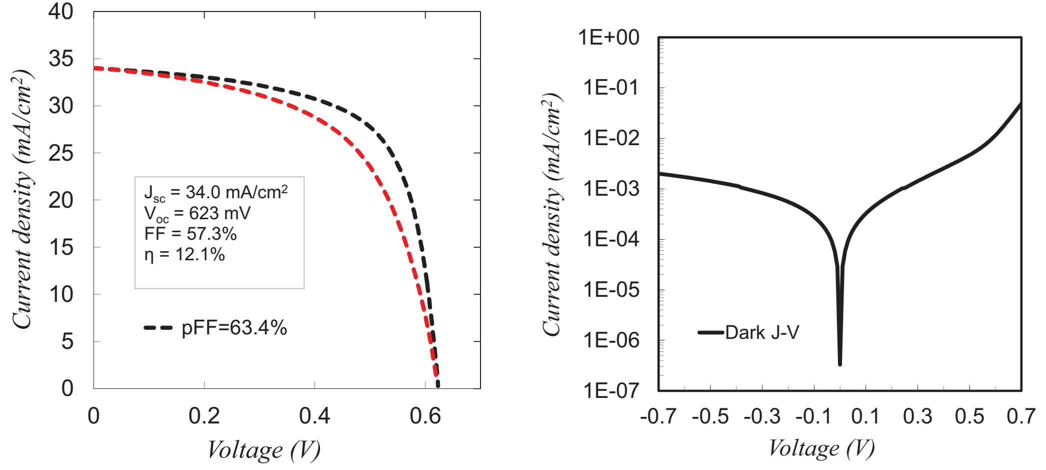

d. Emitter coverage 85%.

Figure 6.12: On the left, J-V measurements (red dashed curves) and suns-V_{oc} results (black dashed curves) of the four "Cold" IBC fabricated with different emitter coverages. On the right, J-V dark measurements results.

Emitter coverage (%)	V_{oc} (mV)	J_{sc} (mA/cm^2)	**FF** (%)	**pFF** (%)	η (%)
66	635	33.7	60	68	12.7
75	644	37.2	65	75.1	15.5
80	620	36.3	65.4	73	14.7
85	623	34	57.3	63.4	12.1

Table 6.1: Summary of the results of "cold" IBC solar cells with different emitter coverages done with pulsed laser mode

For laboratory-scale devices (9 cm^2), our best conversion efficiency is 15.5% corresponding to the "cold" IBC cell with 75% emitter coverage. From the photovoltaic measurements we can see that low V_{oc} and FF are limiting the final efficiency of the four devices. The low pFF obtained from the suns-V_{oc} measurements indicates that resistance series are not the main factor of this limitation. The origin is related to the high current flow observed at 0-0.5 V range in forward bias in the dark J-V curves. The influence of this current mechanism in the forward voltages hides the exponential behaviour and is responsible of the low

FF values.

6.8 Optical losses analysis and Quantum Efficiency of the "Cold" IBC cells

Reflectances of the four "cold" IBC fabricated are measured using the UV-VIS-NIR Spectrophotometry with the integrating sphere. The results are shown in figure 6.13. As it can be seen, non significant differences are observed between final devices. From 680 to 980 nm reflectance values are very close to 0 and increases outside this range due to a non-perfect front antireflection coating and back reflector scheme. The J_{sc} loss due to reflectance is calculated to be about 2.78 mA/cm^2 representing more than the 50% of the total optical losses. This results is surprising, since the rear surface is covered with different layers depending on the proportion of emitter, base and non-metallized regions and the proportion between them changes. In order to get a deeper insight, we perform again optical simulations.

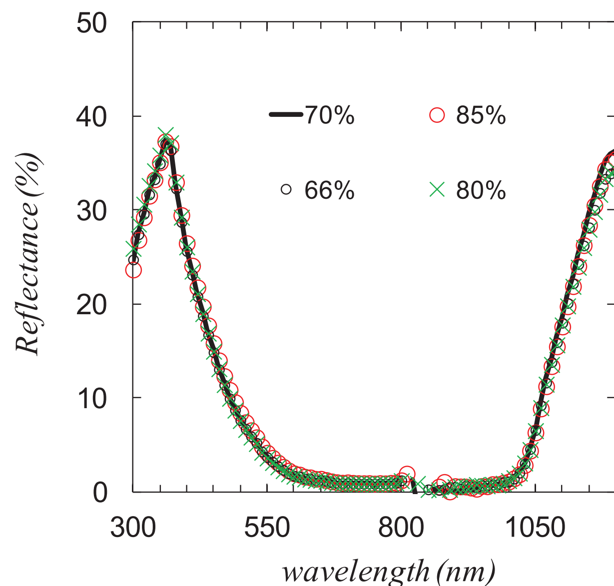

Figure 6.13: Reflectance measurements of the different IBC structures as a function of wavelength and emitter coverage

6.8.1 Simulation of the solar cell optics

Figure 6.14 shows the structure to be simulated with the ray tracer tool of *PV Lighthouse* and the resulting simulation spectra reflectance, absorbance and transmitance are depicted in figure 6.15. Detailed optical study taking into account the different IBC structures fabricated and the percentage of region contribution is show in table 6.2 and 6.3.

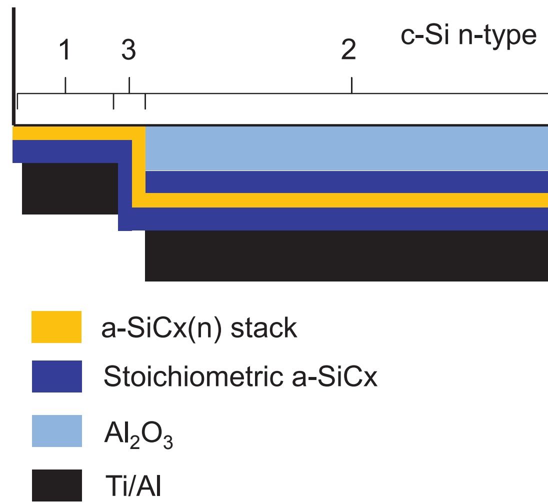

Figure 6.14: Simplified sketch of the "Cold" IBC solar cell rear side for optical simulations)

- 1. Metallized base region consist of c-Si+ $\sim$ 4 nm intrinsic $a-SiC_x$+$\sim$ 15 nm phosphorous doped a-Si (together forming the $a-SiC_x(n)$ stack)+35 nm stoichiometric $a-SiC_x$+$\sim$3 μm of Ti/Al metallization
- 2. Metallized emitter region consist of c-Si+50 nm of Al_2O_3+35 nm stoichiometric $a-SiC_x$+$\sim$ 4 nm intrinsic $a-SiC_x$+$\sim$ 15 nm phosphorous doped a-Si (together forming the $a-SiC_x(n)$ stack)+35 nm stoichiometric $a-SiC_x$+$\sim$3 μm of Ti/Al metallization
- 3. Non-metallized region consist of c-Si+50 nm of Al_2O_3+35 nm stoichiometric $a-SiC_x$+$\sim$ 4 nm intrinsic $a-SiC_x$+$\sim$ 15 nm phosphorous doped a-Si (together forming the $a-SiC_x(n)$ stack)+35 nm stoichiometric $a-SiC_x$

The front surface is considered randomly textured and covered with 50 nm of Al_2O_3 and 35 nm of stoichiometric $a-SiC_x$ as in the final device.

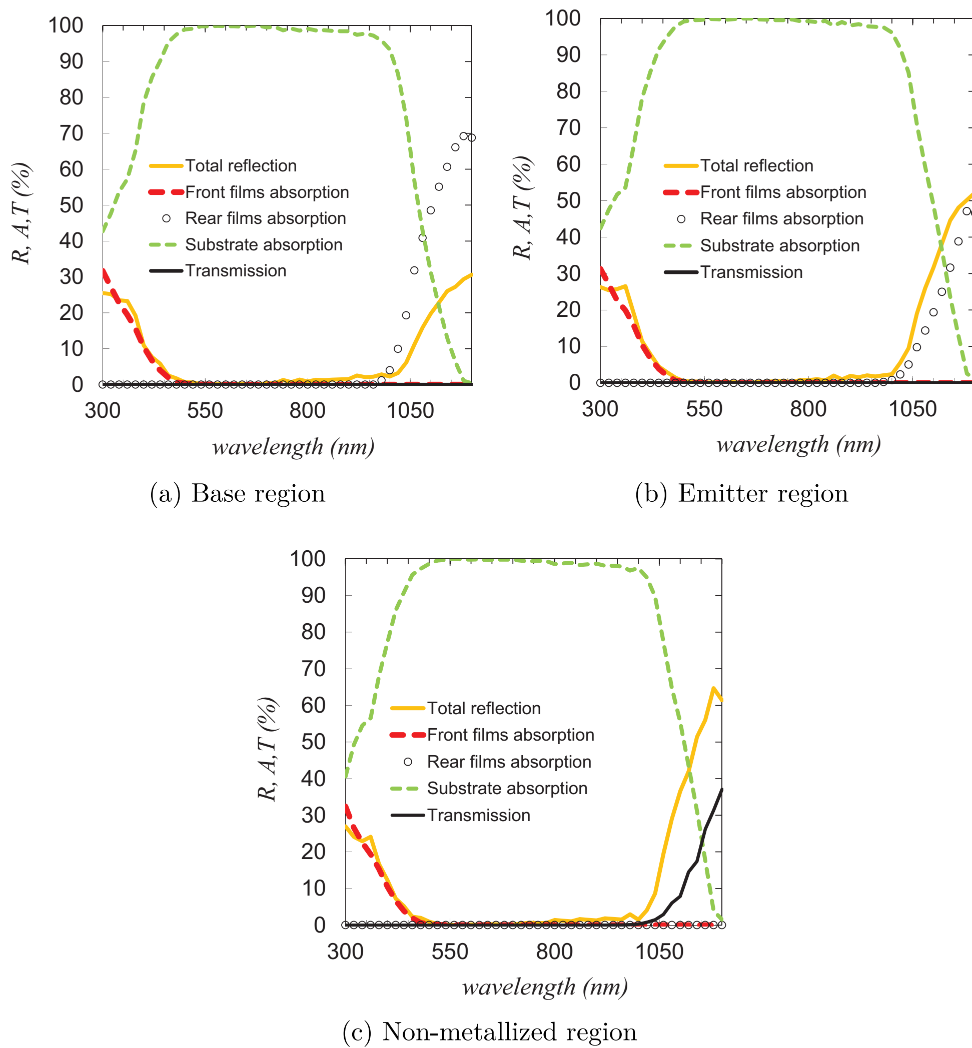

(a) Base region

(b) Emitter region

(c) Non-metallized region

Figure 6.15: Optical losses simulation results using the wafer ray trace tool of PVlighthouse. *https://www2.pvlighthouse.com.au*

		Optical losses $[mA/cm^2]$				
E. cover.	**Distrib.**	**Reflec.**		**Absorp.**		**Trans.**
[%]	Emitter [%] Base[%] Non-metal.[%]	Ext.	Esc.	Front	Rear	
66	50.1	0.50	1.04	0.20	0.86	-
	29.5	0.30	0.34	0.12	1.04	-
	20.4	0.20	0.49	0.08	$3.16.10^{-16}$	0.21
75	63.7	0.63	1.32	0.26	1.1	-
	23.7	0.24	0.27	0.09	0.83	-
	12.6	0.12	0.30	0.05	$1.9.10^{-16}$	0.13
80	68	0.67	1.41	0.28	1.17	-
	20	0.20	0.23	0.08	0.70	-
	12	0.12	0.29	0.05	$1.8.10^{-16}$	0.12
85	79.6	0.79	1.65	0.32	1.37	-
	16.8	0.17	0.19	0.07	0.59	-
	3.6	0.03	0.08	0.01	$5.58.10^{-17}$	0.04

Table 6.2: Optical losses distribution depending on rear IBC region and emitter coverage

IBC % coverage	**Reflect.** $[mA/cm^2]$	**Absorp.** $[mA/cm^2]$	**Transmit.** $[mA/cm^2]$	**Total loss** $[mA/cm^2]$	**Ph. (Absorbed)** $[mA/cm^2]$
66	2.87	2.30	0.21	5.38.	41.28
75	2.88	2.33	0.13	5.34	41.30
80	2.92	2.28	0.12	5.32	41.33
85	2.91	2.36	0.04	5.31	41.33

Table 6.3: Optical losses distribution depending of rear IBC region and emitter coverage

The largest loss mechanism is the escape surface reflectance together with the transmission losses in the non-metallized zone. The escape surface reflectance is caused by non-ideal light-trapping and is also considerable in the base and emitter region together with parasitic absorption of the rear films, mainly due to the titanium film. The external reflectance is related to non-optimal properties of the antireflection coating (Al_2O_3 and stoichiometric $a-SiC_x$) that is common for the three zones. The parasitic front film absorption losses is due to the absorption of the stoichiometric $a-SiC_x$ below 450 nm. Al_2O_3 does not absorbs in the whole evaluated range.

Table 6.2 and 6.3 show a detailed analysis of the optical losses as a function of the emitter coverage. The study reveals that the J_{sc} current density loss due to the optical losses is very similar between the different IBC structures ($\sim$ 5.3 mA/cm^2) most of them related to the emitter regions. As we can see from the simulated results (table 6.3), the total reflection losses are between 2.8 and 2.9 mA/cm^2 that agrees with the value obtained from the experimental measurement. In general, we can say that different regions contribute with similar values to the optical losses resulting in a weak dependence on the emitter coverage.

6.8.2 External quantum efficiency analysis

In figure 6.16a the measured external quantum efficiency (EQE) of the "cold" IBC cells are depicted. The EQE responses are strongly impacted by the front surface recombination velocity and the non-ideal front surface passivation is responsible of the major photocurrent (J_{ph}) loss mechanism. Best results are achieved for the "cold" IBCs with 75 and 80% emitter coverage, probably due to a better front surface passivation. Additionally, IQE and reflectance of the best "cold" IBC fabricated (75% emitter coverage) is calculated from experimental data as $IQE = EQE/(1-R)$ and represented in figure 6.16b. The drop observed below the 500 nm wavelength is due to the parasitic absorption of the 35 nm thick of stoichiometric a-SiC_x in the front of the cell as it was concluded in the study carried out in the chapter 3.

In order to compare the impact of S_{front} in the IQE response, we have simulated IQE curves assuming different front surface recombination velocities as in the same way than in the "Hybrid" solar cells. The approximation to the S_{front} value is obtained by fitting the experimental IQE curve (black circles symbols, figure 6.17) with the simulated IQEs curve calculated with PC-1D (red dashed

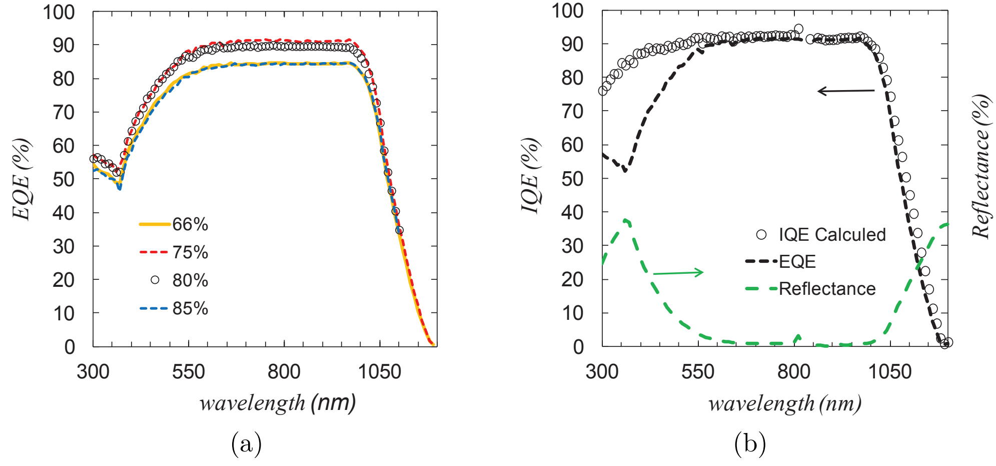

(a) (b)

Figure 6.16: (a) EQEs measurements of the four different "Cold" IBC structures (b) EQE, IQE and Reflectance measurements of the "Cold" IBC with 75% emitter coverage

lines, in the same figure). The simulated IBC device is simplified by means of a simple back junction structure with the same device features (thickness, substrate doping density and experimental reflectance). Simulations are done for different S_{front} values, 20, 40 and 60 cm/s, resulting 40 cm/s the best choice for the fitting. From the comparative between experimental and simulated IQE curves it can be seen that, as in the case of "Hybrid" IBC, front surface passivation is good enough (S_{front}=40 cm/s) to assume that the low V_{oc} obtained is again probably due to a high recombination at the rear side.

The laser-induced crystal damage is partially responsible of the low V_{oc} values. The pulse energy had to be increased above the optimal power to form all the punctual emitters. The high energy can ablate the surface introducing damage to the silicon lattice. These defects are recombination centers that affect the lifetime of the minority carriers resulting in low V_{oc} [2]. Another cause of these low V_{oc} values could be the poor rear surface passivation either in base regions and emitter region. During the fabrication process, specially after the CF4 dry etching (step 6 of the fabrication process) the surface passivation substantially worsens and it is just partially recovered after an annealing step.

It is clear that the loss in the surface passivation quality (due to the plasma etching with CF_4 at the rear side) and the damage introduced by the laser are the two main factors to be improved for better V_{oc} and FF values and consequently

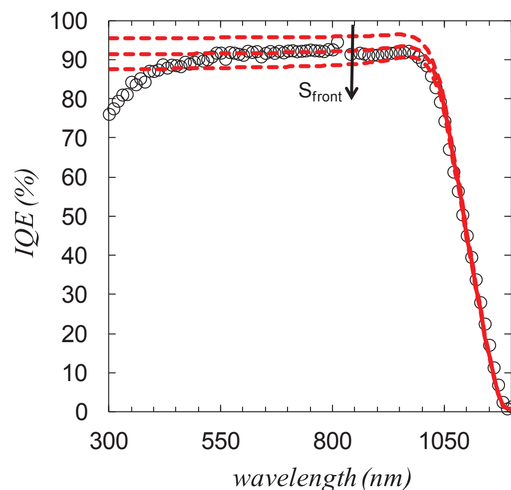

Figure 6.17: Calculated (black circles symbols) and simulated (red dashed line) IQE data of the "Cold" IBC cell with 75% of emitter coverage for different S_{front} (20, 40 and 60 cm/s)

to increase the efficiency of the final IBC.

To preserve the quality of the surface passivation during the CF_4 plasma etching seems to be a good solution placing an insulator (ex. glass) under the sample when the plasma etching is carrying out in the PECVD chamber and submit the sample to a post-annealing treatment at 375 °C for 10 min.

Due to the limit imposed by the laser available for this thesis work (i.e. infrared laser, and not fine power control), minimization the damage in the silicon lattice does not have an easy solution. As a first approximation, the next experimental will consist in applying a pulse duration of 400 ns for doping both punctual emitter and BSF. The increment of the pulse duration can avoid the high peak power that induced the damage into the silicon.

6.9 "Cold" IBC fabrication using 400 ns of pulse duration for emitter and BSF formation

Simulations of the optical losses, reflectance measurements, diode n^{++}/p characterization and fabrication process analysed in previous sections do no change in this new experiment. Consequently, in this section we just analyse the surface passivation during the whole fabrication process (in particular after the CF_4

plasma etching and post-annealing step) and the p^{++}/n diodes done with a pulse duration of 400 ns at different laser powers. Finally, we fabricate and characterize the "Cold" IBCs using the new optimized laser parameters.

6.9.1 "Cold" IBC surface passivation

The $S_{eff,max}$ is affected in every fabrication step. In figure 6.18 we show the $S_{eff,max}$ values calculated after each fabrication step. We can observe that $S_{eff,max}$ strongly increases after CF_4 plasma etching. Then, after the annealing step at 400 °C for 10 min, the passivation quality is recovered.

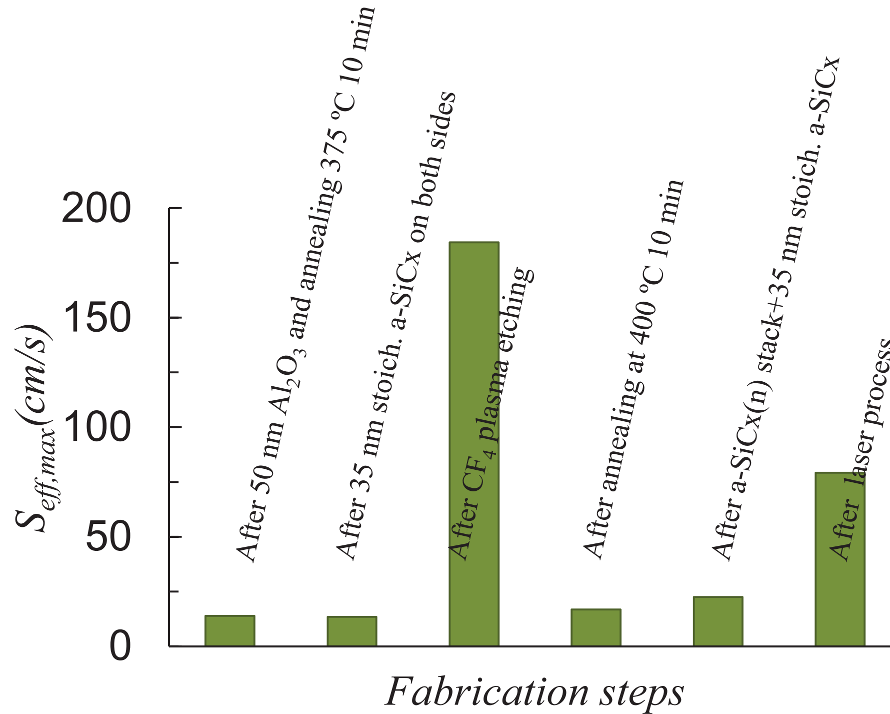

Figure 6.18: $S_{eff,max}$ value at one-sun illumination during the "cold" IBC solar cell fabrication

6.9.2 Precursor samples. Diodes p^{++}/n

Diodes precursor done for this experimental follow the same structure and fabrication process than in previous section (6.3.1). The only difference is the laser processing. In this experimental the front side of the precursor diodes are done with a laser pulse duration of 400 ns and at different laser powers.

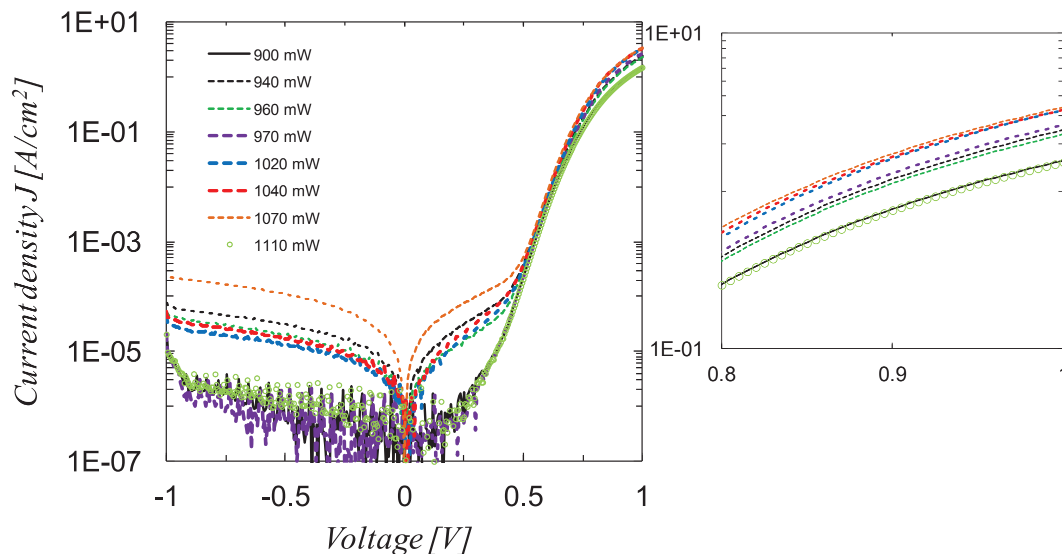

Figure 6.19: Dark J-V measurements of diodes done with a pulse duration of 400 nm at different power laser conditions. On the right, graph magnification of the high forward voltage

In figure 6.19 we show the dark J-V measurements results. On the right, the same curve at high forward voltage shows the influence of series resistance in each diode curve. The lowest series resistances are obtained in the diodes done between 1020 and 1070 mW but also good diodes are obtained from 940 to 970 mW. The highest series resistances are found in the diodes done at 900 mW and 1100 mW. The former is probably related to a shallower and a very small spot (even not formed) increasing accordingly the series resistance. The latter is probably due to the partially or totally removal of the dopant by high laser power [3],[4].

The scattered behaviour shown in the reverse bias can be explain by random leakage caused by pin-holes in the layer stack before the laser process.

6.9.3 Emitter saturation current (J_{oe})

Again, J_{oe} parameter is extracted using the "slope method" (equation 6.1). The sample test prepared and the laser pattern follow the same structure than previous experimental (see section 6.4). The front surface is irradiated with a pulse duration of 400 ns at 1020 mW and a pitch of 400 μm. The observed loss of the τ_{eff} after the laser stage can be assumed caused by the damage induced by the laser. Figure 6.20 (left) shows the $1/\tau_{eff}$ as a function of Δ n. From "the slope method" J_{oe} is calculated to be 60 fA/cm^2

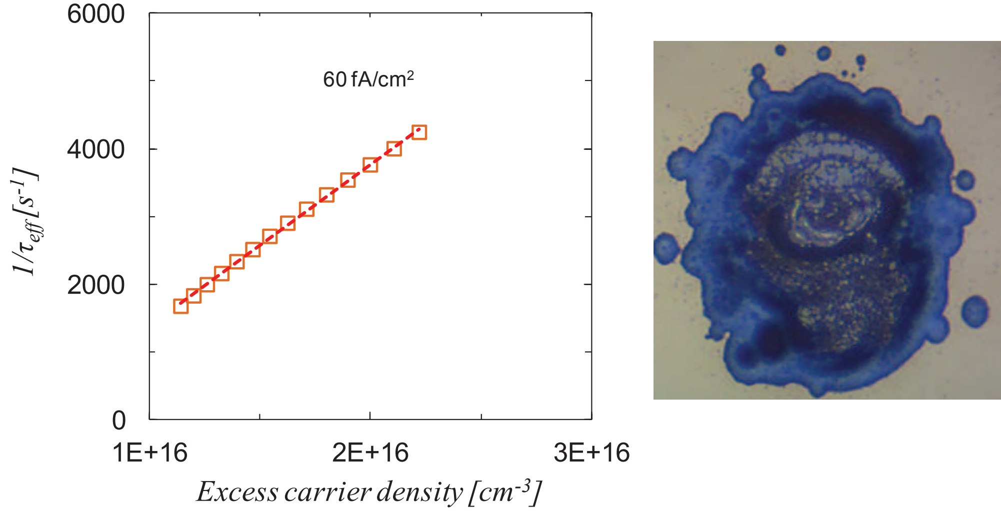

Figure 6.20: Determination J_{oe} using the "slope method" for the sample processed with a pulse duration of 400 ns and 1020 mW. On the right, optical image of the spot.

From equation 6.2 $J_{oe,cont.}$ is determined taking into account that the number of spot per cm^2 are 625 spots and the contacted area is estimated in $28.0.10^{-6} \pm 2.8.10^{-6}$ cm^2. Then

$$J_{oe,cont.} = 3.4 \pm 0.35 pA/cm^2$$

6.9.4 J-V measurements, Suns-V_{oc} and EQE

Finally, we fabricate the four different structures of "cold" IBC solar cells following the same fabrication processes than in the previous experiment (section 6.6) using a power laser of 1020 mW (pulse duration of 400 ns) to define the punctual emitter contacts while 1070 mW is the power laser used to define the punctual BSF regions. As it was previously commented, fluctuations in the laser power results in a higher laser power employed for the IBC contact formation than that used for the diodes fabrication in order to assure all the spots formation. This means that the final result will not correspond with the optimal behaviour achieved in the precursor diodes. The IBC cells are characterized by means of J-V measurements, Suns-V_{oc} and EQE. The illuminated J-V characteristics together with Suns-Voc results are depicted together in order to compare FF vs pFF. Dark J-V curves are show in figure 6.21. In this experiment two c-Si wafers n-type, with the same characteristics than in previous "Cold" IBC cells, are used to fabricate two

"Cold" IBC of 80% and 85% of emitter coverage in one wafer and 66, 75, 80 and 85 % emitter coverage in the other one. The photovoltaic parameter results are summarized in the table 6.4.

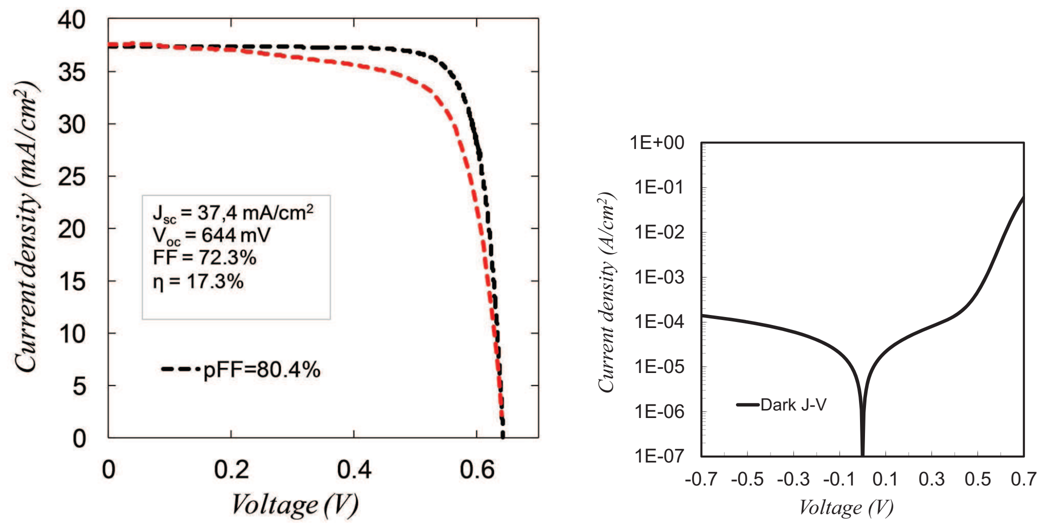

a. Emitter coverage 66%.

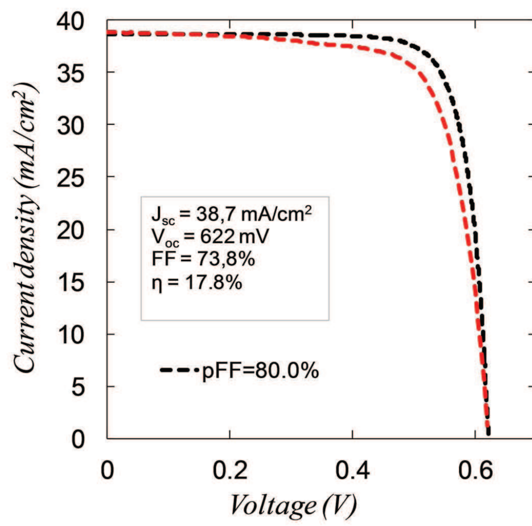

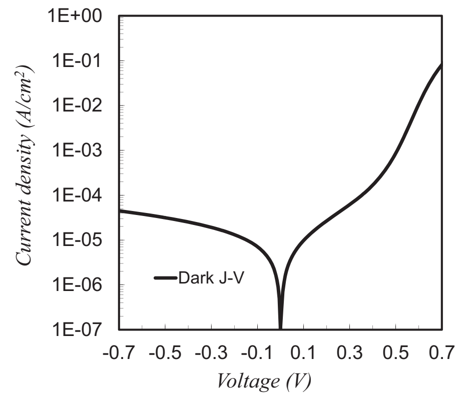

b. Emitter coverage 75%.

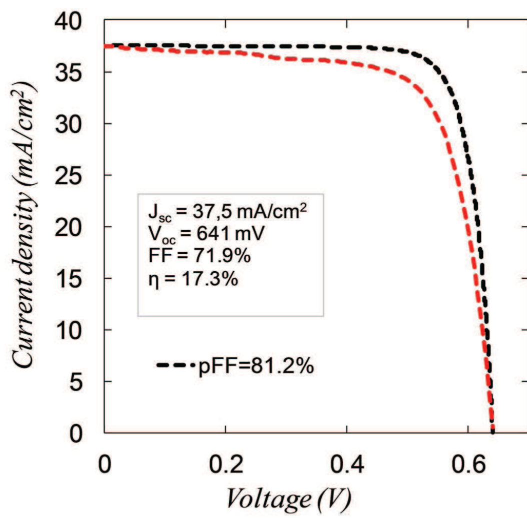

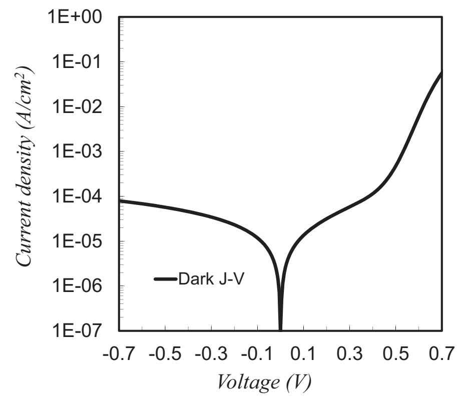

c. Emitter coverage 80%.

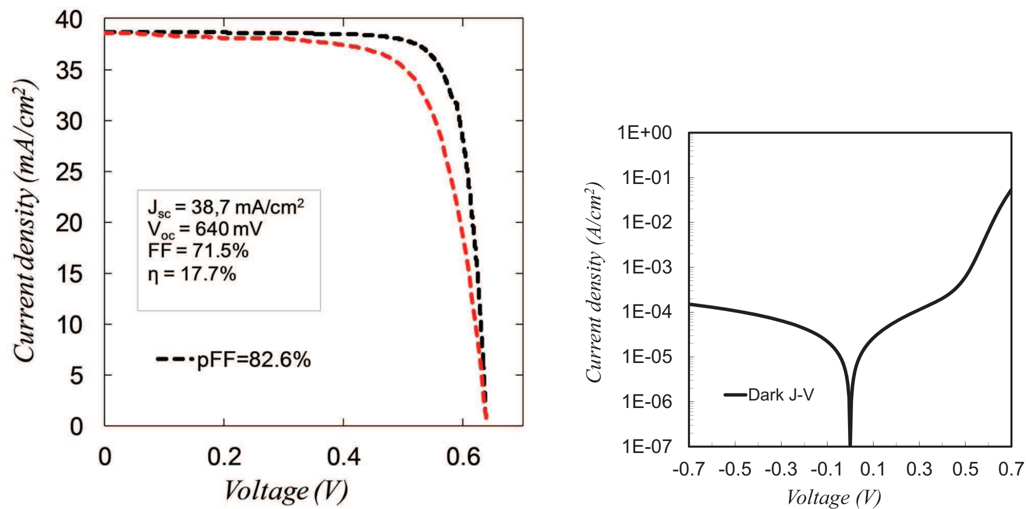

d. Emitter coverage 85%.

Figure 6.21: Wafer 1. On the left, J-V measurements of different emitter coverage of "Cold" IBC solar cells (red dashed lines) and suns-V_{oc} results (black dashed lines). On the right, J-V Dark measurements results.

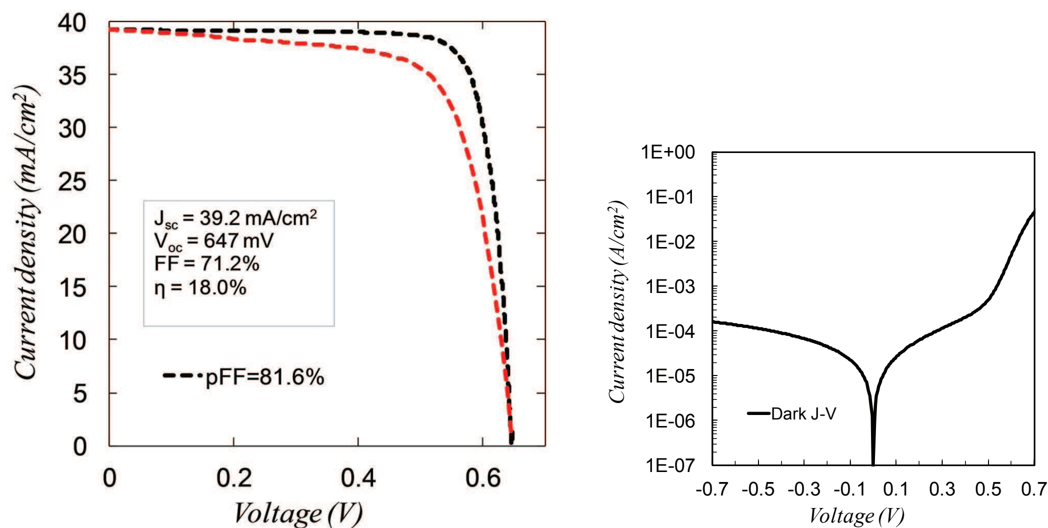

c. Emitter coverage 80%.

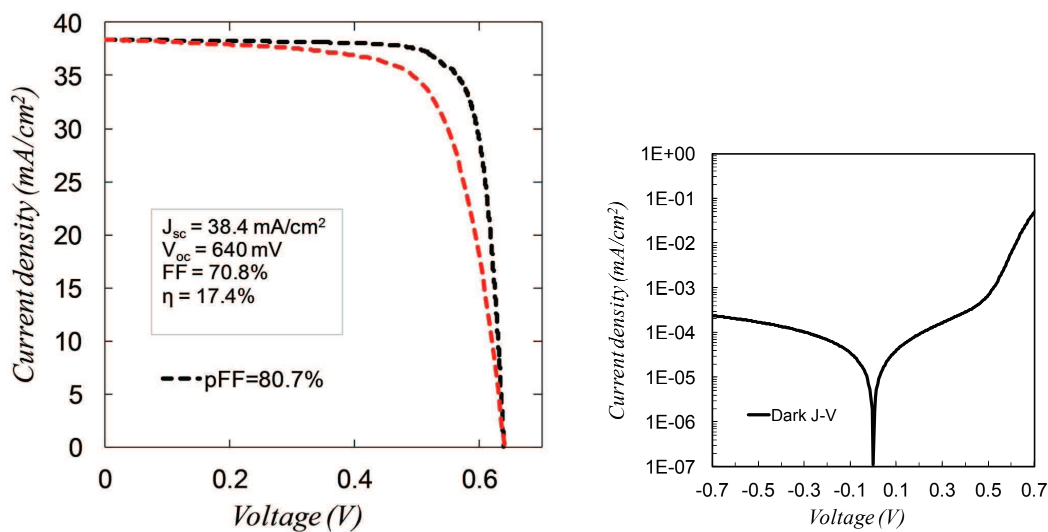

d. Emitter coverage 85%.

Figure 6.22: Wafer 2. On the left, J-V measurements of different emitter coverage of "Cold" IBC solar cells (red dashed lines) and suns-V_{oc} results (black dashed lines). On the right, J-V Dark measurements results.

Wafer №	Emitter coverage. (%)	V_{oc} (mV)	J_{sc} (mA/cm^2)	FF (%)	pFF (%)	η (%)
1	66	644	37.4	72.3	80.4	17.3
	75	622	38.7	73.8	80.0	17.8
	80	641	37.5	71.9	81.2	17.3
	85	640	38.7	71.5	82.6	17.7
2	80	647	39.2	71.2	81.6	18.0
	85	640	38.4	70.8	80.7	17.4

Table 6.4: Summary of the results of "cold" IBC solar cells with different emitter coverages done with 400 ns of pulse duration

As it can be seen in the above table, there is a general increment of the efficiency in all the IBC cell obtaining the 18.0% in our best device. The increment of the J_{sc} values agree with the improvement of the EQE responses (see figure 6.23a) .

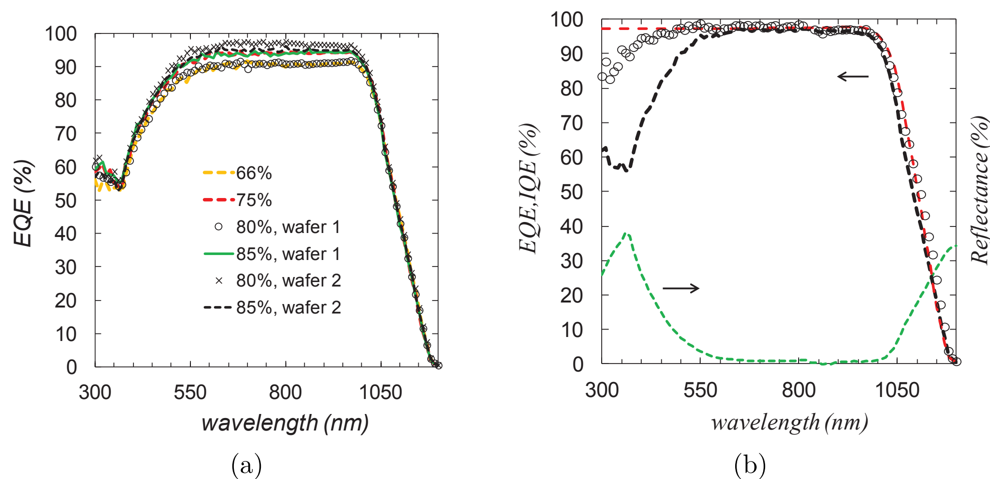

Figure 6.23: a) EQEs measurements of the "Cold" IBC cell with different emitter coverages. b) EQE (black dashed), calculated IQE (black circles), simulated IQE (red dashed) and Reflectance (green dashed) measurements of the "Cold" IBC with 80% emitter coverage

The surface passivation achieved in the wafer 2 was better than in the wafer

1. This improvement is clearly translated to a better EQE results (in all the wavelength range) for the same emitter coverage cells. A remarkable 97% is achieved from 620 nm to 960 nm. The difference in the EQE responses of the different cells can be attributed to differences in the quality of the surface passivation among them. The better surface passivation results in a decrease of the surface recombination velocity helping photogenerated carriers to get to the collecting contact. Again, the reduction in the EQE curve below 560 nm is due to the front cell reflectance. The optical losses do not play a especial role in the general improvement since the "Cold" IBCs developed with a pulse laser duration of 400 ns follow exactly the same cell structure than those "Cold" IBCs with a laser pulse duration of 100 ns and the latter cells have not achieved so high J_{sc} values. Furthermore, we can also observe a remarkable increase of the V_{oc} values evidencing a clear improvement of surface passivation. In the figure 6.23b we show the EQE, IQE and reflectance of the best "Cold" IBC obtained,i.e. 80% of emitter coverage and the drop in the IQE below 450 nm indicate a parasitic absorption of the front c-SiC_x layer.

From the IQE fitting (figure 6.23b) we deduce a very low S_{front} of 12 cm/s and therefore the relative still low V_{oc} values are affected by the rear surface passivation. On the other hand, the damage in the passivation quality after the laser processing (see section 6.10) point to the spot laser depassivation due to the dielectric ablation. Additionally, we can say that the increase of the pulse duration to a 400 ns decreases the laser-induced defects into the silicon structure (a laser with longer pulsed allow to the silicon to recrystallize in a proper manner avoiding the defect formation [5]). Consequently, and as it can be seen in the reverse voltage in the dark J-V measurements the leakage current is considerably reduced since the number of shunting path between the metal and the bulk is decreased.
However, there is still some efficiency limitation mainly due to the low FF. The high value of the pFF indicates that the main loss in the FF is due the R_s. Apart from the IBC with emitter coverage of 75%, the results indicate that as the emitter coverage increases the R_s reducing the pFF. The origin of this R_s can be in the bulk resistance since the base contacts are more and more separated. As the emitter coverage increases, the mean transport path of the electrons to the base also increases and hence the resistance series. Another important contribution to

this series resistance can be related with a very resistive p- channel surrounding p^{++} emitter contacts induced by the negative charge in the Si/Al_2O_3 interface.

6.10 Conclusion

In this chapter, we have developed our first "cold" IBC solar cells with different emitter coverages on n-type c-Si substrates. We have eliminated any conventional diffusion and simplified the fabrication process by removing photolithografic steps. The dielectric layers employed as dopant source are the same than those used in the "Hybrid" IBC, i.e. Al_2O_3 to dope the emitter regions (p^{++}) and a-SiC_x(n) stack the BSF regions (n^{++}). Additional stoichiometric a-SiC_x was used for chemical protection and to reduce the lattice damage induced during the laser step. Optical losses have been also analyzed in order to know the main way of photocurrent loss. We have demonstrated that the surface passivation and the laser conditions are crucial to achieve high efficiency. The increment of the pulse duration from 100 to 400 ns has reduced the laser-induced defects. In a first approximation, the punctual emitters were created with a pulsed mode of 6 pulses (100 ns) while the BSF with a pulse duration of 400 ns achieving an efficiency of 15.5% in our best cell. The final "Cold" IBC solar cells were fabricated using a pulse duration of 400 ns to create both punctual emitter and BSF regions achieving an impressive 18.0% of efficiency.

Finally we must point out that the instability of the laser system causes missing pulse effect. Moreover, the difficult to achieve a good laser power control for an infrared laser, leads to a very narrow processing windows and the small increased in the beam energy, in order to avoid missing pulses, causes additional crystal damage. Thus, the simplest way to prevent this damage is to avoid melting an excessive volume of silicon, by controlling the laser power, difficult to achieve in the infrared laser. The change to shorter laser wavelengths would lead to shallower photon absorption and better power control. Consequently, less silicon would be melted with less lattice damage.

Bibliography

[1] D.E Kane and R.M Swanson. Measurement of the emitter saturation current by a contactless photoconductivity decay method. In *18th Photovoltaic Specialists Conference. IEEE*, pages 578–583. IEEE, 1985.

[2] M. Abbott, P. Cousins, F. Chen, and J. Cotter. Laser-induced defects in crystalline silicon solar cells. In *31st IEEE Photovoltaic Specialists Conference (PVSC), Orlando*, pages 1241–1244. IEEE, 2005.

[3] A. Fell, E. Franklin, D. Walter, D. Suh, and K. Weber. Laser Doping from Al_2O_3 layers. In *27th European Photovoltaic Solar Energy Conference and Exhibition, (Frankfurt), Germany*, pages 706–708, 2012.

[4] Z. Hameiri, L. Mai, T. Puzzer, and S.R. Wenham. Influence of laser power on the properties of laser doped solar cells. *Solar Energy Materials and Solar Cells*, 95:1085–1094, 2011.

[5] B. Santoso. *Laser doped selective emitter solar cells.* PhD thesis, 2010.

Chapter 7

One step forward!. Achieving high-efficiency solar cell

In this final chapter, we have developed the "Cold" IBC solar cells following the same fabrication process used in the previous chapter, but just changing the laser stage method. The main goal in this experiment is to increase the solar cell efficiencies avoiding the lattice damage induced by the infrared laser. We have optimized the laser-doped contacts employing UV laser (355 nm) through the dielectric stacks to create the highly-doped regions (p^{++} and n^{++}) in one single laser step. The laser power is controlled by means of an external attenuator in the 20-200 mW range as a free parameter to be optimized. Additionally, sheet resistance (R_{sheet}) and precursor diodes (p^{++}/n and n^{++}/p) are analyzed in the same way that previous chapters to optimize the laser conditions. The final devices are characterized by EQE, Suns-V_{oc}, and J-V measurements. Short-circuit densities and open-circuit voltages about 40 mA/cm^2 and 650 mV respectively and efficiencies up to 20% have been obtained using this simplified baseline process.

7.1 Optimization of laser-doped contacts

7.1.1 Laser system

The laser employed is located in *Centro Laser*, UPM (Universidad Politécnica de Madrid) facilities. The laser is a diode-pumped, ns-pulsed, Nd:YVO4 system (Spectra-Physics Hippo H10-355QW) operating at wavelength of 355 nm (UV). and emitting with a TM0 gaussian mode beam with radius at focus of 15 μm. Pulse duration and frequency are 12 ns and 20 kHz respectively. The laser power is controlled by means of an external attenuator in the 20-200 mW and adjusted just before each experiment thanks a thermocouple sensor. The laser beam can be swept thanks to a galvo scanner (ScanLAB HurryScan II) up to 125 mm x 125 mm area and is focused using a z-theta lens (250 nm focal length). Samples were mounted in a four axis manual stage, allowing 25 mm travel in the XY horizontal directions, 12.5 mm travel in the Z vertical direction, and 360° rotation around Z axis. Both the optical scanner and the manual stages have a position and angle accuracy of ±10 μm and 0.01° respectively.

7.1.2 Sheet resistance (R_{sheet}) and precursor diodes

In order to optimize UV laser system for IBC manufacturing some test samples are fabricated using *n*- and *p*-type high quality float zone FZ <100> c-Si 4 inch wafers (2.5 ± 0.5 Ωcm, 275 ± 10 μm thick). The p^{++} doped regions are formed into *n*-type c-Si processing the laser through Al_2O_3/stoichiometric a-SiC_x/a-$SiC_x(n)$ stack [1]/stoichiometric a-SiC_x stack layers (figure 7.2a) while the n^{++} doped regions are processed into *p*-type c-Si through a-$SiC_x(n)$/stoichiometric a-SiC_x (figure 7.2b).

Laser power tuning

Spot diameter as a function of laser power considering the two different stacks involved in the IBC solar cell fabrication is shown in figure 7.1. Laser crater morphology exhibits a circular-like shape with two different regions. On the one hand an inner circular region with an internal diameter D_{in} where dielectric stack is fully removed and the silicon is clearly melt. On the other hand one ring

[1] $a - SiC_x(n)$ stack consists of $\sim$ 4 nm of silicon rich $a - SiC_x(i)$ and $\sim$ 15 nm phosphorous doped a-Si

region with an inner and outer diameter D_{in} and D_{out} respectively, where material is partially ablated and surface/bulk recombination is significantly affected [1]. Nevertheless, from an electrical contact point of view, we consider that only the inner circle is contacted in the subsequent metallization stage and its area allows define the contact fraction area f_c.

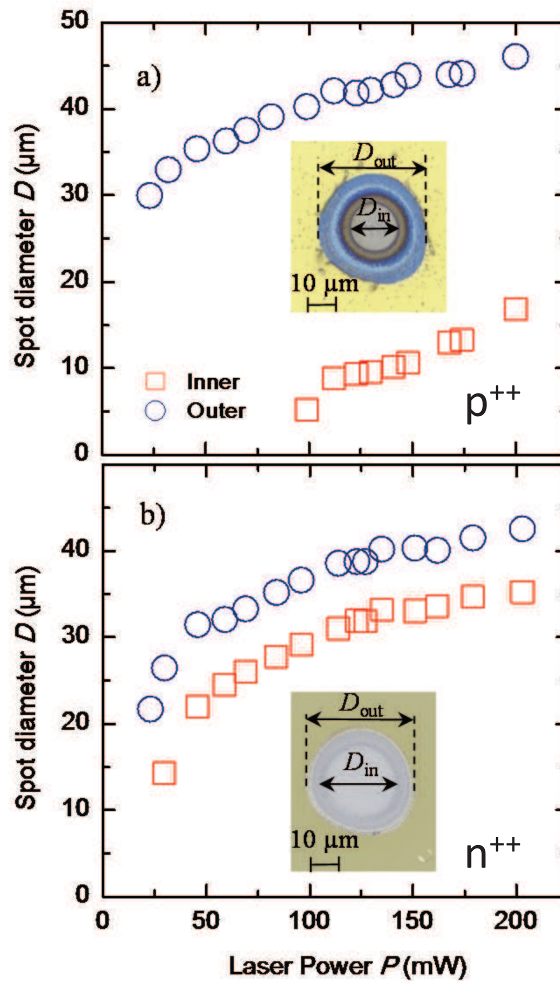

Figure 7.1: Spot diameter vs. laser power P. The above figure corresponds to p-type doping and below to the n-type doping. Laser spot images corresponding to P $\sim$ 125 mW are also shown in the insets.

As it is expected from results shown in 7.1, higher laser powers result in higher D_{in} and D_{out} values. Inner spot diameters are in the 5-17 and 14-35 μm range for the stacks with and without Al_2O_3 layer respectively. It is important to remark that p-type doping needs higher powers to form the contacts ($> \sim$90 mW) than n-type doping counterparts ($> \sim$20 mW). In all cases, crater depths in the melted

region are well below 800 nm in the whole laser power range, indicating that UV irradiation superficially affects silicon material minimizing potential deep bulk damage after laser stage.

Sheet resistance

Samples are fabricated to explore the sheet resistances R_{sh} on large laser-doped areas of 1 cm x 1 cm using the UV laser. Only the front side of the samples are processed with the corresponding stacks (see figure 7.2). The contact pitch is also adjusted to overlap laser spots to form continuous doped regions in order to measure the R_{sh} using the four-point probe technique

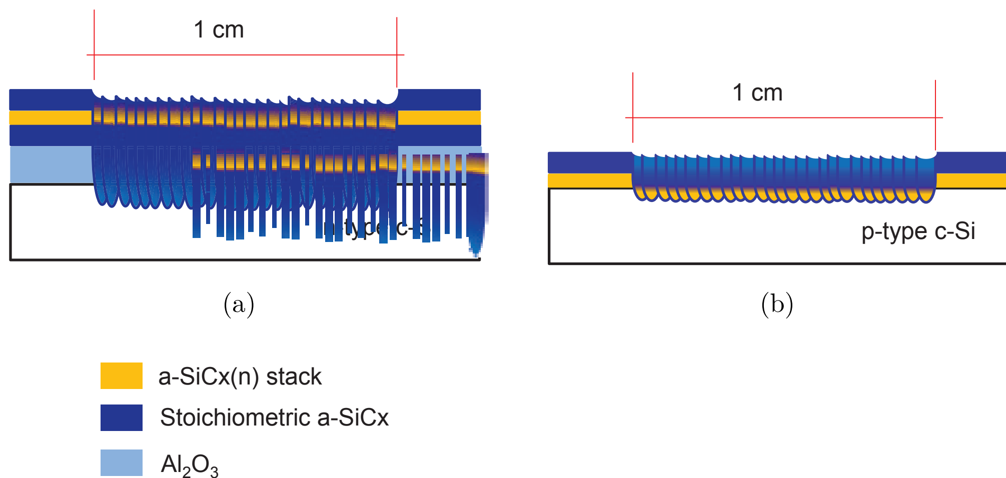

Figure 7.2: Sample structures for sheet resistance test. a) p-type doping b) n--type doping

R_{sh} measurements allow to determine a coarse laser power range to perform the laser doping stage as it is shown in figure 7.3. It is clear that formation of n^{++} emitters involves a broad window of useful powers in the 40-200 mW range, however powers higher than ∼100 mW are necessary to form reliable p^{++} regions ($R_{sh} < 200\Omega/sq$).

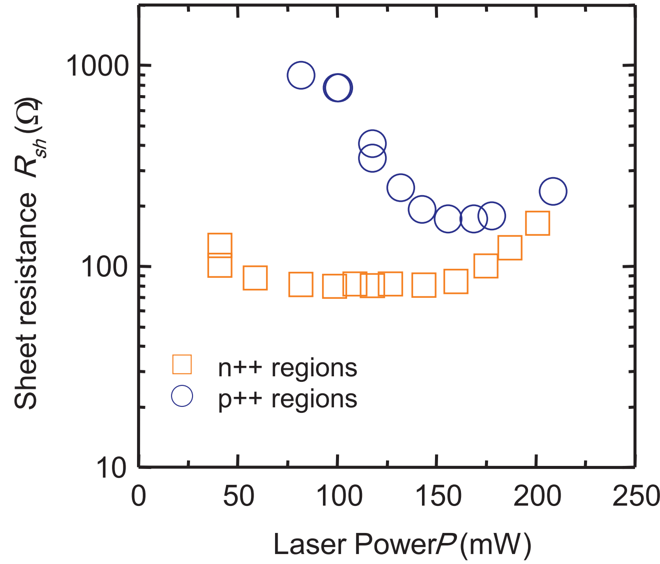

Figure 7.3: Sheet resistance R_{sh} vs. laser power P for *p*- and *n*-stacks.

Notice that this laser power optimization method do not take into account neither contact quality, i.e. contact resistance and existence of leakage currents, nor excessive lattice damage during the laser stage, i.e. high recombination -emitters. In order to obtain a fine-tuning of laser power to form doped contacts we analyze in the next section dark current-voltage (J-V) characteristics of vertical test diodes for different P values.

Precursor diodes

The samples fabricate to test the electrical characteristics of the diodes (p^{++}/n and n^{++}/p) follow the sample structure and fabrication process than in the previous chapter (section 6.3). In figure 7.4 the dark J-V characteristics results of p^{++}/n and n^{++}/p diodes are shown. Table 7.1 summarizes fitting parameters using a double-diode model. Where J_{o1} is the diffusion current density in base and emitter regions assuming a diode ideality factor of n=1. J_{o2} is the space-charge-region recombination current density considering n=2, whereas r_s and r_{sh} are the series and shunt specific resistances respectively in Ωcm^2 units. It is clear that low laser powers create very poor emitter contacts with high contact resistances, i.e. high r_s values, or alternatively on p^{++} emitters with excessive leakage current, i.e. low r_{sh} values. Furthermore, high laser powers increases J_o values decreasing at the same time r_s, arising a trade-off between low recombination

emitters with reasonable ohmic losses.

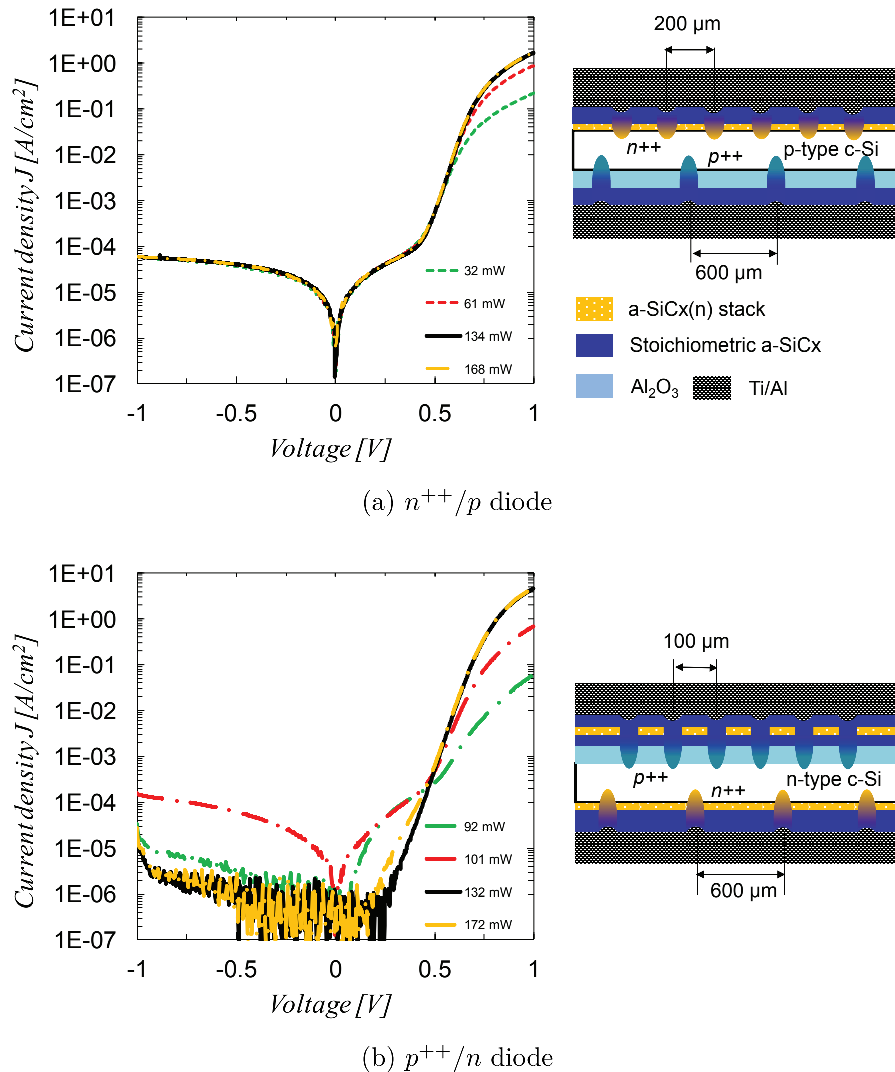

(a) n^{++}/p diode

(b) p^{++}/n diode

Figure 7.4: On the left, Dark J-V characteristics for different laser powers. The best curve is shown in black continuous line. On the right, the diode test structures

Optimum laser powers around 130 mW are a good choice to form emitters independently of substrate polarity, resulting in inner diameter D_{in} values about 30 and 12 μm for n^{++} and p^{++} contacts with a similar outer diameter D_{out} in both cases of $\sim$40 μm.

P (mW)	f_c (%)	J_{o1} (fA/cm^2)	J_{o2} (nA/cm^2)	r_s ($m\Omega cm^2$)	r_{sh} ($K\Omega cm^2$)
			n^{++}/p diodes		
32	0.4	439	21.5	1882	7.0
61	1.2	579	17.7	476	7.0
134	1.9	571	16.4	249	7.0
168	2.2	769	15.5	285	7.0
			p^{++}/n diodes		
102	0.3	133	23.0	867	5.51
132	1.2	565	13.0	200	700
172	1.6	676	25.8	196	400

Table 7.1: Summary of fitting parameters of dark J-V curves using a double-diode model. Notice that data related to p++n diode sample irradiated at 92 mW is missed in the table because of it was not possible to fit its curve using this simple model.

7.2 "Cold" IBC solar cells characterization

The "cold" IBC solar cells fabricated follow the same structure and fabrication process that in the chapter 6 (section 6.6) and the substrate used is *n*- type float zone FZ <100> c-Si with a resistivity of 2.5 ± 0.5 Ωcm and 275 ± 10 μm thick. In this experimental, we develop four cell geometries defined as number of emitter spots per each base contact (see figure 7.5), namely: 3, 5, 7 or 11 emitter spots per base contact, corresponding to 66, 75, 80 and 85 % emitter coverage respectively.

The laser doping stage was performed using a power of 130 mW to create both n^{++} back surface field (BSF) and p^{++} emitter regions. Contacts are arranged in an array point-like structure with a pitch of 100 and 125 μm on vertical and horizontal axis respectively. A gap of 250 μm between base and surrounding emitter lines of contacts was established in accordance with mask alignment requirements involved in our baseline fabrication process. The laser beam simultaneously ablates the dielectric layer and diffuses dopant atoms into the c-Si; aluminium from Al_2O_3 and phosphorous from a-$SiC_x(n)$ creating at the same laser step both p^{++}

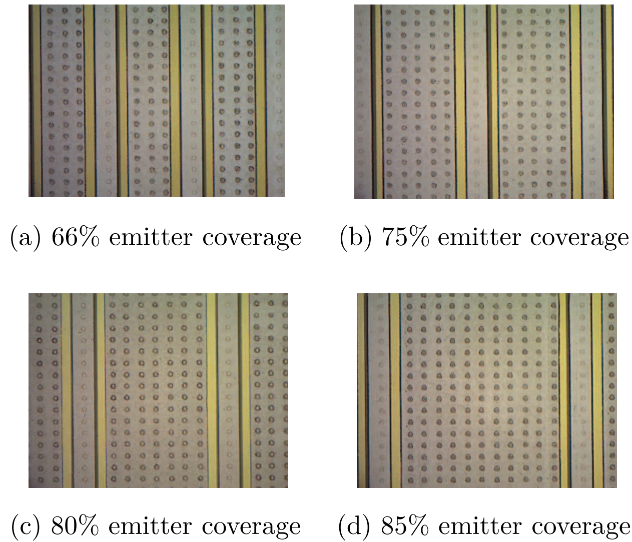

(a) 66% emitter coverage (b) 75% emitter coverage

(c) 80% emitter coverage (d) 85% emitter coverage

Figure 7.5: Optical images of the four cell topologies used in this work.

and n^{++} regions respectively.

7.2.1 J-V measurements and Suns-V_{oc}

One wafer with four devices was successfully processed and each solar IBC cell was measured under AM1.5G 1 kW/m^2 solar spectrum (T=25 °C). The illuminated area is defined of 3 x 3 cm^2. The J-V curves resulted are depicted in figure 7.6 and their photovoltaic parameters summarized in table 7.2. In all cells, efficiencies η are around 20% independently of the geometry

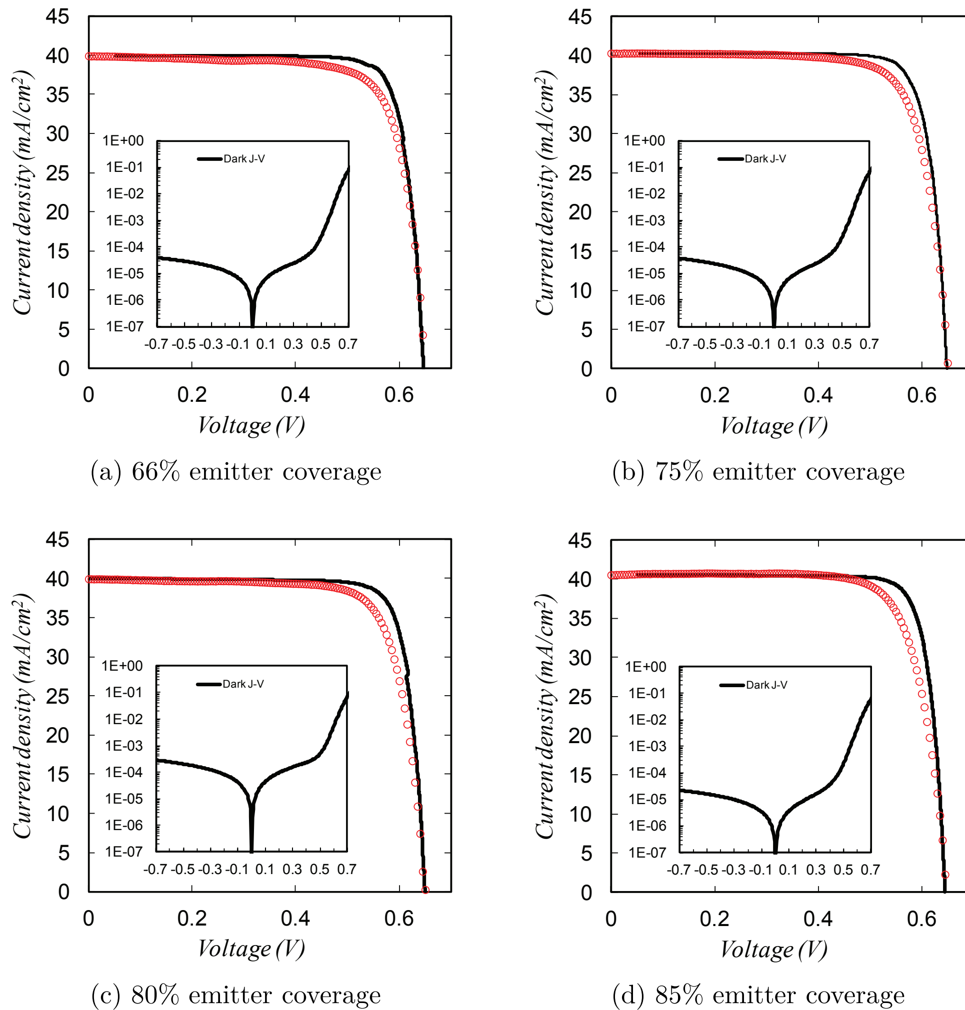

(a) 66% emitter coverage

(b) 75% emitter coverage

(c) 80% emitter coverage

(d) 85% emitter coverage

Figure 7.6: J-V measurements of the four "cold" IBC fabricated as a function of the emitter coverage. Dark J-V characteristics are also included in the inset

The high J_{sc} values achieved suggest that front surface passivation is preserved after the CF_4 etching, the laser-stage and rear e-beam metallization as it is also confirmed by observing the external quantum efficiency EQE curves in figure 7.7a. In figure 7.7b the EQE, reflectance and calculated IQE of the best cell (75% emitter coverage) are shown.

EQE values up to 98% in the visible wavelength range not only require an excellent front surface passivation, but also a negligible electrical shadowing due to a poor passivation at the rear side including the base n^{++} contacts. Excellent rear passivation explains the scarcely influence of emitter coverage in the J_{sc} parameter. The relevant decay in the UV-VIS (300-600 nm) and the near IR (>

E.cover. (%)	J_{sc} (fA/cm^2)	V_{oc} (mV)	**FF** (%)	**pFF** (%)	r_s (Ωcm^2)	η (%)
66	39.9	650	76.3	82.9	1.3	19.8
75	40.3	653	76.2	83.0	1.3	20.0
80	40.0	650	76.5	82.2	1.1	19.9
85	40.5	649	76.4	83.8	1.4	20.0

Table 7.2: Summary of solar cell parameters measured at standard test conditions STC (AM1.5G 1 kW/m^2 solar spectrum, 25 °C) for the four devices topologies (9 cm^2 cells excluding busbars

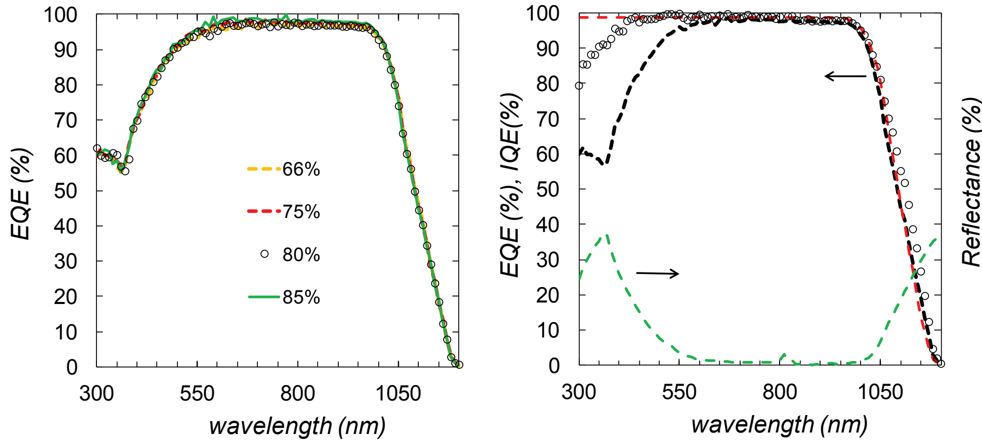

Figure 7.7: a) EQE measurements of the "Cold" IBC cells with different emitter covergares. b) EQE (black dashed curve), calculated IQE (circles shape), simulated IQE (red dashed curve) and reflectance (green dashed curve) of the "Cold" IBC cell with 75 % emitter coverage

1000 nm) wavelength range are due in part by the reflectance of the front surface (see reflectance curve) but also by the absorption in the stoichiometric a-SiC_x front layer (clearly visible in the drop of the calculated IQE below ~ 460 nm) and in the titanium rear metal film respectively. .

However, fill factor FF, with current values around 76.5%, is the main parameter to improve in our solar cells. Pseudo fill factor pFF values obtained by suns-V_{oc} measurements over 82% and up to 83.8% confirm that FF losses are basically due to series resistance in our devices. In fact, specific resistance r_s values in table 7.2, calculated using equation 7.1 [2], are ~ 1.3 Ωcm^2. If we consider that base and emitter electrode contribution (fingers and busbars) are of only ~ 0.3 Ωcm^2, a room for improvement exists.

$$r_s \simeq (1 - \frac{FF}{pFF}) \times \frac{V_{oc}}{J_{sc}} \quad (7.1)$$

In order to find the origin of the high ohmic losses, we compare J-V curves under illumination and normalized by J_{sc}, with a counterpart device where the only difference is the horizontal pitch between emitter contacts of 250 μm (double pitch) (see figure 7.8). It is clear that reducing the pitch by a factor of two improves noticeable the J-V curve and the FF. Note that the current drop for low voltages in the 250 μm pitch curve compared with the 125 μm pitch counterpart is not caused by a hypothetical shunt in that device, as it can be seen in the dark J-V characteristics shown in the inset of 7.8. This fact suggest that the main contribution on series resistance might be due to a very resistive p- channel around emitter p^{++} contacts induced by the negative charge in the Si/Al_2O_3 interface. This induced pn junction around emitter contacts improve photocarrier collection in the cell, but has a negative effect in r_s.

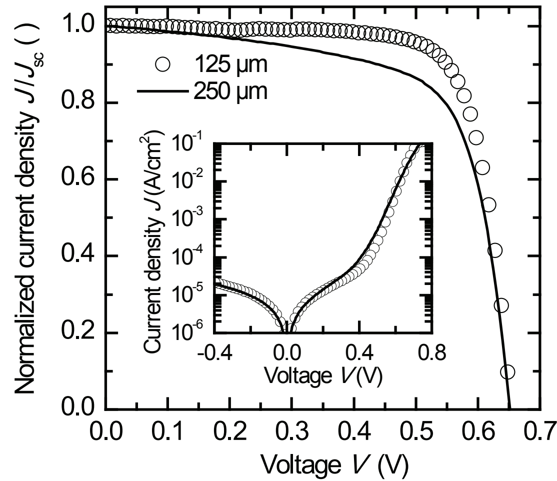

Figure 7.8: Normalized $J/J_{sc} - V$ characteristics of the best IBC cell (75% emitter coverage) compared with a counterpart device with a higher horizontal pitch in emitter regions (250 μm). Dark J-V characteristics for both cells are also included in the inset.

This pernicious impact on r_s might be reduced by bringing closer even more emitter contacts (decrease pitch in emitter regions) without jeopardizing recombination current density J_o, i.e. V_{oc}, of the solar cell using for instance even smaller point contacts (reducing D_{in} and/or D_{out}). This aspect is another important point to be study in future works, where the election of the laser system will play a crucial role in the optimization of this type of solar cell structures.

7.3 Conclusions

A novel interdigitated back contacted (IBC) solar cell structure on c-Si(n) substrates has been proposed using a fully low-temperature fabrication process based on laser-doped point-like contacts. Emitter and base contacts are created in a single UV laser processing stage. Low-temperature deposited Al_2O_3 and a-SiC_x(n) stacks provide both the aluminum and phosphorous doping atoms respectively, and excellent front and rear passivation. The fabrication process sequence involved in our lab cells is very simple with only two photolithography patterning stages which might be replaced in an industrial feasible process using standard serigraphy, laser ablation or selective deposition by means of metal masks. The final devices reach to a promising efficiencies up to 20% with short-circuit current densities and open circuit voltages of around 40 mA/cm^2 and 650 mV respectively. Efficiency is mainly limited by series resistance with fill factor FF values around 76.5% and relatively high pseudo-FF (pFF) values over 82% and up to 83.8%. Main ohmic losses are probably due to an induced p-type floating channel surrounding p^{++} emitter contacts provided by the negative charge inherent on Al_2O_3/Si interfaces. Additional efficiency losses are due to reflectance and parasitic absorption of the SiC_x and Ti layers present on front antireflection coating and back reflector stacks respectively.

Bibliography

[1] A. Roigé, J.O. Ossó, I. Martín, C. Voz, P. Ortega, J.M. López-González, and L.F. Alcubilla, R. Vega. Microscale characterization of surface recombination at the vicinity of laser-processed regions in c-Si solar cells. *IEEE Journal of Photovoltaics*, 6(2):426–431, 2016.

[2] Martin Green. *Solar cells: Operating Principles, Technology and System Applications.* UNSW, pp.96, 1998.

Chapter 8

Summary and Future Work

8.1 Summary

In this thesis a new concept of high-efficiency interdigitated back-contact (IBC) solar cells for one-sun applications have been developed. Laser doping technique through dielectric layers has been employed to create highly doped regions (n^{++} and p^{++}) in a point-like structure on c-Si wafers and following four different emitter coverage. A innovative stack of dielectric layers has allowed to simplify the multiple and complex structuring steps traditionally used to form the n- and p-doped regions and the grid metal contacts. The two different dielectric stacks used in this work consisted of:

- Al_2O_3+ stoichiomentric carbon rich a-SiC_x
- intrinsic a-SiC_x+ a-Si phosphorous doped+ stoichiometric carbon rich a-SiC_x

Both layers have been studied and optimized to act simultaneously as passivatting layer and dopant source of aluminum and phosphorous respectively and to form the p^{++} and the n^{++} regions.

Additionally, the total elimination of the conventional high-temperature diffusion combined with the reduction of the complex and costly photolithographic masking steps have allowed to reduce the time-consuming fabrication process and the high cost associated to high temperature.

Special attention has been paid to the surface passivation (polished and textured c-silicon) achievable with Al_2O_3 deposited by thermal ALD. A detailed

studied was carried out in order to know the influence of thickness film, deposition temperature and time/temperature of annealing on the surface recombination velocity. The surface passivation study was also extended to Al_2O_3/stoichiometric carbon rich a-SiC_x stack (the last layer deposited by PECVD) due to its final implementation on the final device. The study has demonstrated an outstanding $S_{eff,max}$ below 15 cm/s independently of the surface morphology and doping type. Additionally, optical properties measurements have revealed that 90 nm of Al_2O_3 deposited on textured c-Si surface are optimal for antireflection purposes while the combination of Al_2O_3+ stoichiometric $a-SiC_x$ with different thickness combination shows some absorption by the capping layer below 460 nm. Although this absorption, all the stack configuration show a low J_{sc} loss lower than 2% between 460 to 1025 nm.

Concerning the electrical quality of the p^+/n and n^+/p junctions, we have fabricated diodes applying different laser conditions to the two dielectric stacks. We have varied the number of pulses and laser power while the pulse duration and frequency were fixed to 100 ns and 4Khz respectively. Systematical dark J-V measurements were done to electrically characterize the diodes concluding that the best diodes were obtained with 0.9 W and 1 W (6/9 pulses) for p^+/n junction and 0.9 W (3/6 pulses) and 0.8 W/9 pulses for n^+/p junction.

As a first approximation, the first p-type IBC solar cells were fabricated using one phosphorous diffusion step and the laser processing was applied through the dielectric layer studied. Accordingly, new precursors diodes were fabricated and analyzed. Efficiencies up to 18.7% and J_{sc} of 39.2 mA/cm^2 were obtained. However, low surface passivation quality and the damage induced by the laser stage onto the silicon lattice limited the final efficiency by reducing the FF and V_{oc}. A calculated ideality factor of ~1.5 agrees with carrier recombination in the space charge region by the laser damage or the influence of parasitic shunting. Additionally, optical simulation demonstrates extra J_{ph} losses as a consequence of the back reflector scheme and rear films absorption.

In a second approach we eliminated the phosphorous diffusion step and we developed the first n-type "Cold" IBC solar cells in which all the highly-doped regions were entirely fabricated by infrared laser processing through the dielectric

layers. Additionally, the dielectric stacks were strategically modified in order to reduce the number of patterning steps to only two. The dielectric layers employed as dopant sources were the same than those used in the "Hybrid" IBC, i.e. Al_2O_3 to dope p^{++} regions and a-SiC_x(n) the n^{++}. "Cold" IBCs were fabricated in two different batches following the same fabrication process. In the first one, the punctual contacts were done in two laser steps. The emitter contacts (p^{++}) were done with 6 pulses and a laser pulse duration of 100 ns. The power applied was 1100 mW. The base contacts were done at 1070 mW with a pulse duration of 400 ns. Efficiencies from 12% to 15.5% depending of the emitter coverage were obtained. However, the low FF, V_{oc} and J_{sc} point to a poor surface passivation and damage-induced laser. The second batch was focused on a better passivation quality control after CF_4 etching and laser stage improvement. The surface passivation quality was maintained along the whole fabrication process and the laser stage was modified applying a pulse duration of 400 ns at 1020 mW in one single step to form both emitter and base contacts. General improvement was achieved in the final devices. Efficiencies from 17.3 to 18.0% and J_{sc} up to 39.2 mA/cm^2 were obtained. Unfortunately, the low FF and V_{oc} still limited the final η mainly due to the laser processing step and the instability of the power laser. Consequently, the used laser power was above the optimum power in order to form all the doped contacts.

Finally, we developed the last "Cold" IBC solar cells changing the laser processing type. We applied UV laser (355 nm), with a pulse duration and frequency of 12 ns and 20kHz respectively in one single laser step to form BSF and emitter regions simultaneously. Due to the smaller spots, the pitch could be decreased to 125 μm. The power laser was controlled by means of an external attenuator and the optimum value was found 130 mW. As a result, the photovoltaic parameters were improved. Efficiencies up to 20% using this simplified baseline process exhibited short-circuit densities and open-circuit voltages about 40 mA/cm^2 and 650 mV respectively. However, efficiencies are mainly limited by series resistance limiting fill factor FF values around 76.5% with relatively high pseudo-FF (pFF) values over 82% and up to 83.8%. Main ohmic losses are probably due to an induced p-type floating channel surrounding p^{++} emitter contacts provided by the negative charge inherent on Al_2O_3/Si interfaces.

8.2 Future works

Efficiencies beyond 22% are feasible by future improvements in the fabrication process addressed to overcome some optical and series resistance losses in our current devices. In particular:

- Overcome optical losses by replacing the front absorbent layer (stoichiometric a-SiC_x) by non-absorbent a-SiN_x and/or introducing new single-side texturing technique based for instance on black silicon which can boost efficiency about 1% absolute in the future.
- Selecting a laser system which allow small contacts and reduce pitches might reduce p-channel effect decreasing series resistance and improving FF accordingly without jeopardizing J_{sc} and V_{oc}.
- Simplify even more the fabrication process avoiding the thermal oxidation texturing simultaneously both surfaces.
- Substitute the rear metal contacts of Ti/Al stack by another metal configuration to avoid the rear film absorption.
- To eliminate the photolithographic step to form the metal pattern and to substitute it by laser ablation.

8.3 List of publications

8.3.1 Refereed journal paper

- G. López, P. Ortega, I. Martín, C. Voz, A. Orpella, R. Alcubilla, "Cold process for IBC c-Si solar cells fabrication" Energy Procedia, 92:652-660, 2016.

- G. López, P. Ortega, I. Martín, C. Voz, A. Morales-Vilches, A. Orpella, R. Alcubilla, "Base contacts and selective emitters processed by laser doping technique for p-type IBC c-Si solar cells" Energy Procedia, 77:752-758, 2015

- G. López, P. Ortega, C. Voz, I. Martín, A. Morales-Vilches, A. Orpella, R. Alcubilla, " Emitter formation using laser doping technique on n- and p-type c-Si substrates" Applied Surface Science, 336:182-187, 2015

- G. López, P. Ortega, C. Voz, I. Martín, M. Colina, A. Morales-Vilches, A. Orpella, and R. Alcubilla "Surface passivation and optical characterization of $Al_2O_3/a-SiC_x$ stacks on c-Si substrates. Beilstein journal of nanotechnology, 4:726-31, 2013

8.3.2 Other related publications

Falta publicacion de Isi y Gerard

- G. Masmitja, P. Ortega, I. Martín, G. López, C. Voz, R. Alcubilla, "IBC c-Si(n) solar cells based on laser doping processing for selective emitter and base contact formation", Energy Procedia, 92C:956-961, 2016

- A. Morales-Vilches, C. Voz, M. Colina, D. Munoz-Martin, I. Martin, P. Ortega, G. Lopez, C. Molpeceres, and R. Alcubilla. "Study of the surface recombination velocity for ultraviolet and visible laser-fired contacts applied to silicon heterojunction solar cells". IEEE Journal of Photovoltaics, 5:1006-1013, 2015

- M. Colina, A. Morales-Vilches, C. Voz, I. Martín, P. Ortega, A. Orpella, G. López, R. Alcubilla. "Laser Induced Forward Transfer for front contact improvement in silicon heterojunction solar cells". Energy Procedia, 336:89-95, 2015

- I. Martín, A. Coll, G. López, P. Ortega, T. Desrues, A. Orpella, R. Alcubilla. "TCO-free Low-temperature p^+ Emitters for Back-junction c-Si Solar Cells". Energy Procedia, 77:296-303, 2015

- I. Martín, M. Colina, A. Coll, G. López, P. Ortega, A. Orpella, R. Alcubilla. "c-Si solar cells based on laser-processed dielectric films". Energy Procedia, 55:255-264, 2014

- M. Colina, I. Martín, C. Voz , A. Morales-Vilches , P. Ortega, G. López, A. Orpella, M. García-Molina, D. MuÃśoz-Martín, M.I. Sánchez-Aniorte, C. Molpeceres, R. Alcubilla. " Optimization of Laser Processes for Local Rear Contacting of Passivated Silicon Solar Cells". Energy Procedia, 44:234-243, 2014

- D. Carrió, P. Ortega, I. Martín, G. López, J. M. López-González, A. Orpella, C. Voz, R. Alcubilla. "Rear contact pattern optimization based on 3D simulations for IBC solar cells with point-like doped contacts". Energy Procedia, 55:47-52, 2014

- A. Morales-Vilches, C. Voz, M. Colina, G. López, I. Martín, P. Ortega, A. Orpella, R. Alcubilla. "Recovery of Indium-tin-oxide/silicon Heterojunction Solar Cells by Thermal Annealing". Energy Procedia, 44:3-9, 2014

- P. Ortega, I. Martin, G. Lopez, M. Colina, A. Orpella, C. Voz, R. Alcubilla. "p-type c-Si solar cells based on rear side laser processing of Al_2O_3/SiC_x stacks". Solar energy materials and solar cells, 106:80-83, 2012

- I. Martín, P. Ortega, M. Colina, A. Orpella, G. López, R. Alcubilla."Laser processing of $Al_2O_3/a-SiC_x:$ H stacks: a feasible solution for the rear surface of high-efficiency p-type c-Si solar cells". Progress in Photovoltaics:Research and Applications, 21:1171-1175, 2012

- P. Ortega, A. Orpella, I. Martin, M. Colina, G. Lopez, C. Voz, I. Sánchez, C. Molpeceres, R. Alcubilla. "Laser-fired contact optimization in c-Si solar cells". Progress in photovoltaics, 20(2):173-180, 2012

8.3.3 National and International conferences

- G. López, P. Ortega, I. Martín, C. Voz, A. Orpella, R. Alcubilla, "Cold process for IBC c-Si solar cells fabrication", SiliconPV 2016, the 6th Inter-

national Conference on Silicon Photovoltaics, 7-9 March 2016, Chambéry (France)

- G. Masmitja, P. Ortega, I. Martín, G. López, C. Voz, R. Alcubilla, "IBC c-Si(n) solar cells based on laser doping processing for selective emitter and base contact formation", SiliconPV 2016, the 6th International Conference on Silicon Photovoltaics, 7-9 March 2016, Chambéry (France)

- E. Calle, P. Ortega, G. Lopez, I. Martin, D. Carrió, C. Voz, A. Orpella, J. Puigdollers, R. Alcubilla. "High efficiency interdigitated back-contact c-Si solar cells". 10th Spanish Conference on Electron Devices, CDE 2015, 11-13 February 2015, Aranjuez-Madrid (Spain)

- G. López, P. Ortega, I. Martín, C. Voz, A. Morales-Vilches, A. Orpella, R. Alcubilla, "Base contacts and selective emitters processed by laser doping technique for p-type IBC c-Si solar cells", SiliconPV 2015, 5th International Conference on Silicon Photovoltaics, 23-25 March 2015, Konstanz (Germany)

- I. Martín, A. Coll, G. López, P. Ortega, T. Desrues, A. Orpella, R. Alcubilla. "TCO-free Low-temperature p^+ Emitters for Back-junction c-Si Solar Cells", SiliconPV 2015, 5th International Conference on Silicon Photovoltaics, 23-25 March 2015, Konstanz (Germany)

- I. Martín, M. Colina, A. Coll, G. López, P. Ortega, A. Orpella, R. Alcubilla. "c-Si solar cells based on laser-processed dielectric films", SiliconPV 2014, 4th International Conference on Silicon Photovoltaics, 25-27 March 2014, s-Hertogenbosch (Netherlands)

- G. López, P. Ortega, C. Voz, I. Martín, A. Morales-Vilches, A. Orpella, R. Alcubilla, " Emitter formation using laser doping technique on n- and p-type c-Si substrates" E-MRS Spring Meeting 2014, 26-30 May 2014, Lille (France)

- M. Colina, I. Martín, C. Voz , A. Morales-Vilches , P. Ortega, G. López, A. Orpella, M. García-Molina, D. Muñoz-Martín, M.I. Sánchez-Aniorte, C. Molpeceres, R. Alcubilla. " Optimization of Laser Processes for Local Rear Contacting of Passivated Silicon Solar Cells", E-MRS Spring Meeting 2013, 27-31 May 2013, Strasbourg (France)

- A. Morales-Vilches, C. Voz, M. Colina, G. López, I. Martín, P. Ortega, A. Orpella, R. Alcubilla. "Recovery of Indium-tin-oxide/silicon Heterojunction Solar Cells by Thermal Annealing", E-MRS Spring Meeting 2013, 27-31 May 2013, Strasbourg (France)

- G. López, P. Ortega, C. Voz, I. Martín, M. Colina, A. Morales-Vilches, A. Orpella, and R. Alcubilla. "Surface passivation and optical characterization of $Al_2O_3/a-SiC_x$ stacks on c-Si substrates", E-MRS Spring Meeting 2013, 27-31 May 2013, Strasbourg (France)

- D. Carrió, P. Ortega, G. López, J. Lopez-Gonzalez, I. Martin, C. Voz, R. Alcubilla. "3D simulations of back-contact back-junction c-Si(P) solar cells with doped point contacts". European Photovoltaic Solar Energy Conference and Exhibition, 28th PVSEC, 30 September 2013, Paris (France)

- G. Masmitja, P. Ortega, G. López, E. Calle, M. García, I. Martín, A. Orpella, C. Voz, R. Alcubilla. "Boron diffused emitters passivated with Al_2O_3 films, 9th Spanish Conference on Electron Devices, CDE 2013, 12-14 February, Valladolid (Spain)

- P. Ortega, R. Jové, A. Pedret, G. Gonzalvez, G. López, I. Martín, M. Domínguez, R. Alcubilla, A. Camps." An IBC solar cell for the UPC CubeSat-1 mission". 9th Spanish Conference on Electron Devices, CDE 2013, 12-14 February, Valladolid (Spain)

- A. Morales-Vilches, C. Voz, M. Colina, G. Lopez, I. Martin, A. Orpella, J. Puigdollers, M. Garcia, and R. Alcubilla. "Progress in silicon heterojunction solar cell fabrication with rear laser-fired contacts". 9th Spanish Conference on Electron Devices, CDE 2013, 12-14 February, Valladolid (Spain)

- C. Molpeceres, M. Colina, D. Muñoz-Martin, I. Martín, P. Ortega, I. Sánchez, M. Morales, S. Lauzurica, J. García-Ballesteros, C. Voz, G. López, A. Morales, R. Alcubilla. " New laser-based approaches to improve the passivation and rear contact quality in high efficiency crystalline silicon solar cells", SPIE Optics+Photonics. Proceedings SPIE Vol. 8826". San Diego: 2013, p. 882603-1-882603-11

- M. Colina, I. Martín, C. Voz, A. Morales-Vilches, P. Ortega, G. López, A. Orpella, R. Alcubilla, I. Sánchez-Aniorte, C. Molpeceres. "Optimiza-

tion of laser doping processes for the creation of p+ regions from solid dopant sources", European Photovoltaic Solar Energy Conference and Exhibition,27th PVSEC, 24-28 September 2012, Frankfurt (Germany)

- G.Lopez, P. Ortega, I. Martin, M. Colina, A. Orpella, R. Alcubilla. "Optimization of Al_2O_3 films obtained by ALD to passivate p-type c-silicon wafers", European Photovoltaic Solar Energy Conference and Exhibition, 27th PVSEC, 24-28 September 2012, Frankfurt (Germany)